Czech Technical University in Prague
Faculty of Electrical Engineering

**Intensification of ozone generation through multi-criteria optimization
of dielectric barrier discharge**

by

Ing. Jan Mikeš, Ph.D.

Habilitation Thesis

June 2023

Faculty of Electrical Engineering
Czech Technical University in Prague
Technická 2
166 27 Prague 6
Czech Republic

Acknowledgements

Abstract

This habilitation thesis comprises an annotated collection of articles published in the years 2014-2023, while exploring possibilities of efficient intensification of ozone generators, operating on the principles of dielectric barrier discharges through multi-criteria optimizations focused on the impact of the environment within which they originate. Top-priority accent was laid on optimizing the direction of the flow of feeding gas (air) in an ozone generator in relation to the microdischarges being generated, to the environmental impacts in which they occur, and the introduction of photocatalytic materials to their vicinity.

Keywords: Surface dielectric barrier discharge (SDBD), Ozone (O_3), Ozone generator, Non-thermal plasma, Airflow, Numerical simulations, Photocatalysts

Abstrakt

Habilitační práce je komentovaným souborem článků publikovaných v letech 2014-2023 zabývajících se možnostmi efektivního zvýšení účinnosti generátorů ozónu pracujících na principech dielektrických bariérových výbojů prostřednictvím vícekriteriálních optimalizací zaměřených na vliv prostředí, ve kterém jsou formovány. Převážný důraz je kladený na směrovou optimalizaci proudění pracovního plynu generátoru ozónu vůči vznikajícím mikrovýbojům, vlivům prostředí, ve kterém jsou generovány, a implementaci fotokatalytických látek do jejich blízkosti.

Klíčová slova: Povrchový dielektrický barierový výboj (SDBD), Ozón (O_3), Generátor ozónu, Netermální plazma, Proudění vzduchu, Numerické simulace, Fotokatalyzátory

Contents

List of Figures

Introduction

1.1 Motivation

The usage of dielectric barrier discharge (DBD) [1] has been on the rise in many applications, such as active particles, ozone, and ultraviolet (UV) generation [2] (available in Appendix A.1), pollution control [3], surface treatment [4], [5], plasma-chemical vapour deposition [6], in medical, biological and chemical applications (sterilization, deodorization, bacterial deactivation, and prolongation of food storage) [7], and air-flow control [8], [9].

The chemically reactive species, together with UV radiation generated by electrical discharges, are responsible for high nonthermal plasma reactivity, which can be utilized for a variety of above-mentioned applications [10], [11].

From all of the properties of DBD, we have selected generation of ozone as it offers the strongest oxidizing effects and can be quantified well. UV radiation can be further employed for the inactivation of bacteria and viruses, sterilization, disinfection and surface treatment [12]. UV radiation can also serve for photocatalytic activation [13].

Ozone is produced by DBD or corona discharges (CD) from oxygen or air. Our study prioritizes efficient ozone production and UV radiation of DBD in air. Another method of ozone production is the photochemical method, which makes use of UV radiation. Chemical, thermal or electrochemical methods can be also applied. The individual methods differ in the type of energy needed to dissociate the oxygen bonds during ozone production. In spite of the fact that ozone production from air is accompanied by occurrence of nitrogen oxides, many types of commercial ozonizers use air as a feeding gas, as is the case in this study.

Ozone generation in a DBD in air at atmospheric pressure constitutes a complex process involving a number of ozone generation as well as ozone decomposition reactions [14]–[17]. In a DBD, current flow is brought about by a large number of statistically distributed microdischarges [18]. Since ozone, mainly formed in the microdischarge channels, diffuses immediately after its generation into the discharge volume [14], [19], its production is affected by the number and distribution of microdischarge channels as well as their properties. These properties can be influenced by the electrical parameters of the discharge, gap

spacing, or properties of the dielectric layer and the metal active electrode used (see examples in Fig. 1.1). Consequently, discharge ozone production is a result of a combination of all these factors.

(a) Honeycomb.   (b) Strips.   (c) Mesh.
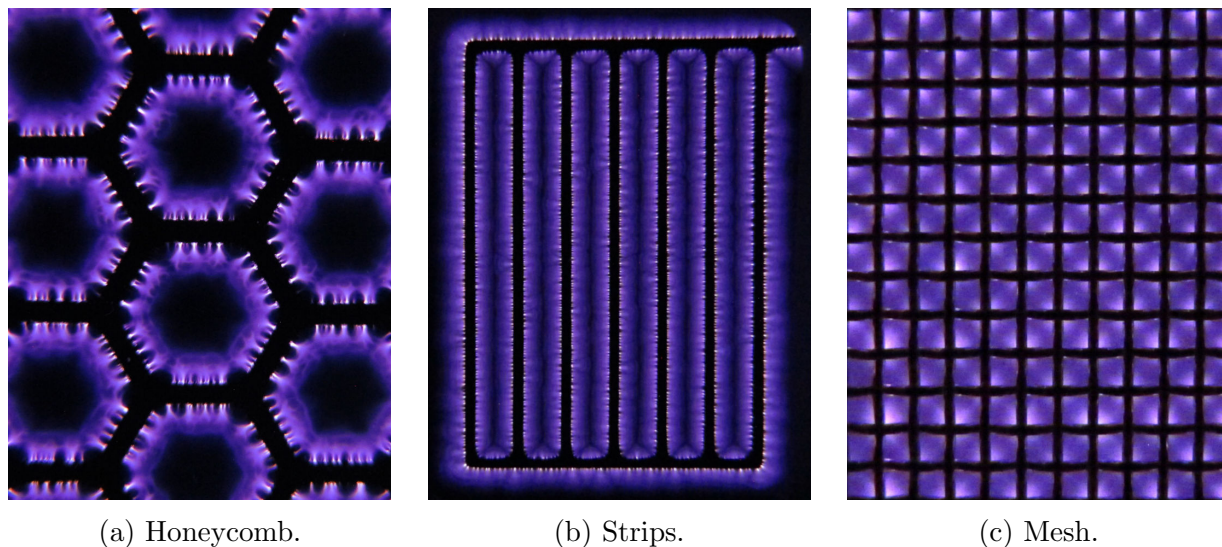
Figure 1.1: Electrodes with burning discharge.

1.2   Importance and objectives of studied phenomena

Ozone generation by means of dielectric discharges figures among the most efficient and competent methods of its preparation. However, seen from an economic point of view, it also ranks among the most expensive methods. Viewed against the current trend in society seeking widespread sanitization in its various segments, the stage has now been set for the vital need to produce and introduce a wide scale of devices, ranging from stationary high-capacity generators to mobile as well as hand-held battery-operated generators.

The research results summed up in this habilitation thesis respond to the specific needs of the commercial sectors, reflecting the current issues pertaining to the energy, materials as well as electronic crisis; this research concentrated on multi-criteria optimization of ozone generation, primarily through optimization of the direction of the flow of feeding gas in relation to microdischarges resulting from DBD.

Even though ozone´s indisputable advantage during dissociation is its decomposition into atomic or rather molecular oxygen, the remaining negative aspect is its non-selective oxidation interaction with surrounding surfaces and objects, and concurrent generation of nitrogen oxides. These factors have to be taken into consideration in the actual design and construction of ozone generators.

Proceeding from targeted studies of the issues concerning dielectric barrier discharges based on the preparation of ozone, multi-criteria optimization methods leading to intensification of ozone generation have been proposed. The hitherto frequently neglected factors

2

– optimizing the direction of the flow of feeding gas in ozone generator´s chamber, adequate provision of environmental conditions on the site of their origin, and introduction of photocatalytic materials to their vicinity – were primarily reflected in this research. The procedures outlined here are conducive not only to enhancing the overall efficiency of ozone generators by as much as dozens of percent, but – at the same time – to providing a vital context for continuing basic research in the physics of nonthermal plasma. The motivations of the results presented in this thesis are therefore both technical (practical) and fundamental.

1.3   Structure of the habilitation thesis

This habilitation thesis is divided into three interconnected thematic units describing – on the basis of long-term investigation of the interactions of DBD with external environment – the possibilities of upgrading the efficiency of ozone generation by means of multi-criteria optimization.

The first part analyzes the general electrical parameters of dielectric discharge in a stationary environment of an immobile feeding gas. Also under scrutiny is the importance of the geometry of the electrode itself, together with the impact on amplitude and frequency of the applied electric voltage, current peaks and phase shifts of currents originating during microdischarges. Our own numerical 3D model simulating behaviour of a dielectric discharge reflecting the geometry of the mutual position of electrode systems has been designed, constructed and tested for the options of multi-criteria optimizations. The results thus gained by the model facilitate their direct implementation in the process of practical design of ozone generators.

Follow-up investigation focused on the impact of the vicinity on the microdischarges being generated, primarily on the effect of ambient temperature and directionally oriented low-speed airflow of feeding gas on the microdischarges occurring during a DBD. These phenomena were studied both in planar and cylindrical configurations of the electrode systems. The chief outcome of this section of my habilitation thesis is a body of findings applicable in the practical designing of ozone generators, with systematic optimization of the flow of feeding gas in relation to the orientation of microdischarges being capable of enhancing their efficiency.

The final, third part of the thesis discusses the importance of introducing photocatalytic substances into the environment of electrical discharges, as seen from a theoretical, experimental as well as practical point of view. UV radiation, which is also generated by SDBD, may be utilized for the activation of photocatalytic materials participating in the generation of other excited particles, and thus increasing the amount of generated ozone. Significance of the following photocatalysts: TiO_2, ZnO, $BaTiO_3$ a WO_3 was examined in particular.

Phenomenology of dielectric barrier discharge

Dielectric barrier discharge is an electrical discharge created between a minimum of two electrodes, at least one of which is covered by an insulant. The distance between electrodes is typically several millimetres (defined by the thickness of the dielectric material).

By connecting these electrodes to alternating high voltage sources and under the pressure of surrounding feeding gas ranging from 0.01 to 10 MPa will give rise to generation of strong local electric fields and thus surface and spatial separation of the electric charge which may cause the generation of electron avalanches resulting in the origin of microdischarges. Microdischarges with a diameter of 100 μm cover the entire area of the electrodes and last for a period from 1 to 100 ns. During each discharge, an electric charge of the size 10^2-10^3 pC with current density up to 10^5 A/m^2 is transferred. This generates a nonthermal plasma showing the characteristics of electron density from approximately 10^{14} cm^{-3} to values higher than 10^{15} cm^{-3}, and with mean electron energies ranging from 1 eV to values higher than 15 eV. Plasma originating under such circumstances is also accompanied by the generation of UV radiation.

2.1 Dielectric barrier discharge behaviour

According to the space in which dielectric discharges are generated (regarding the configuration of electrodes), they can be further classified into the Surface Dielectric Barrier Discharge (SDBD), providing the surface of the active electrode is covered by an additional dielectric layer, the Coplanar Dielectric Barrier Discharge (CDBD), and finally the Volume Dielectric Barrier Discharge (VDBD) types. VDBD has been the most frequently investigated type because it is easier to perform in technical terms. The applied voltage and its frequency, just as the thickness and type of dielectric layer, and the configuration of the electrode motive determine and directly affect the type of discharge that occurs on the surface of the dielectric material.

In my research I have zeroed in on SDBDs, originating on the surface of an active electrode, which was driven by the sinusoidal low-frequency voltage.

2.2 Dielectric barrier discharge features

2.2.1 Active electrode geometry

2.2.1.1 Properties of dielectrics layers

SDBD has been frequently studied within a planar experimental configuration, where one electrode connected to an alternating high-voltage power supply system and serving as a high-voltage (active) electrode is applied to one side of a planar dielectric plate (barrier) by means of screen printing, steaming, and dusting or, eventually, is cut out of a thin foil made of an electrically conductive material (copper, aluminium, stainless steel, special steel) and is glued by conductive glue. An optional procedure could be the use of a thin conductive mesh.

A grounded electrode, often made of the same material in an oblong or square shape and overlapping the active electrode surface by several millimetres, is located on the lower (opposite) side. The actual shape of the active electrode is usually selected in keeping with the purpose to be served by the designed generator of active particles and ozone (it can also be a source of ultraviolet radiation). The configuration frequently features thin parallel strips, circles, and segments shaped as a honeycomb, but it can also take the shape of a mesh (see Fig. 1.1).

In case of my study, dielectric barrier discharge was gradually investigated on several types of configurations of dielectric systems. The first two configurations were planar, made of Alumina, produced by the company Elceram. The Alumina plate contained 96% Al_2O_3, mass density of 3.7 g/cm^3, roughness 0.25-0.7 µm, the dielectric constant for 1 MHz of 9.6, electric strength of 14 kV/mm and heat conductivity for a temperature of 25°C of 24 W/m·K. The dimensions of this plate were $50 \times 50 \times 0.635$ mm, and $110 \times 110 \times 0.635$ mm, respectively. Both types, laboratory-prepared and also commercially available electrodes used in industrial ozone generators, were tested.

The last assembly was a cylindrical dielectric tube made of Simax glass with an outer diameter of 20 mm and an inner diameter of 17.4 mm, and length of 150 mm. The relative permittivity of Simax glass, at temperature 20°C and frequency 1 MHz, amounted to 4.6.

2.2.1.2 Electrically conductive material of active electrode geometry

In the first example, the active electrode system was produced by screen printing, using the DuPont nickel-based paste 9538. The sheet resistivity of the layer made from this paste amounted to 30-60 mΩ/sq at 25 µm thickness.

A 0.035 mm thick copper foil, manufactured by the Elchemco company, was used in other cases. The last sample to be used was a 0.025 mm thick aluminium foil from the Anticor company. Both were glued on the Alumina plate or the Simax tube's outer side.

2.2.1.3 The shape of active electrode geometry

An electrode formed by 9 or 14 interconnected strips respectively, 1 mm thick, with a 3 mm distance between one another, was employed for planar configurations. An example of specific geometry used in the articles [20]–[25] published in Appendices A.2, A.3, A.5, A.6, A.10, A.11 is shown in Fig. 2.1 and Fig. 2.2.
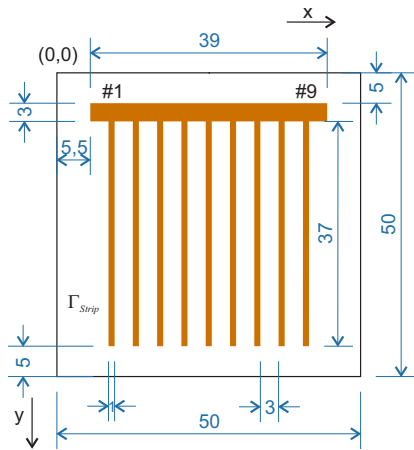
Figure 2.1: 2D geometry of the active strip electrode.
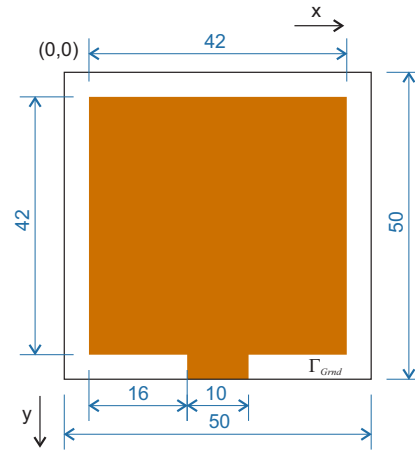
Figure 2.2: 2D geometry of the grounded electrode.

The same dimensional geometry (strip thickness 1 mm and a 3 mm distance between neighbouring electrodes) was maintained with cylindrical systems (see Fig. 2.3 and Fig. 2.4) even though the selected shape of electrodes featured interconnected rings, eventually longitudinal or inclined strips.
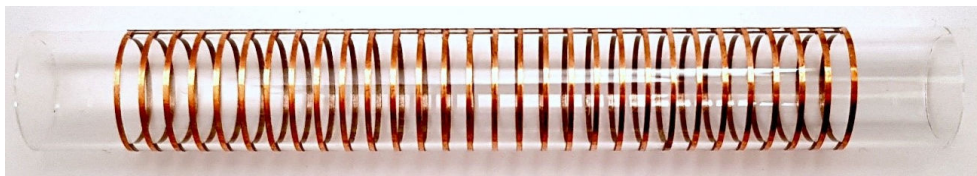
Figure 2.3: Geometry of the cylindrical active electrode - rings.

Figure 2.4: Geometry of the cylindrical active electrode - strips.

Electrodes made of stainless steel meshes, eventually with a deposition of the following metals: titanium, vanadium, zirconium, molybdenum and copper, were tested for specific purposes. The appropriate choice of dielectric material and electrode material improves the lifetime of the DBD system.

2.2.2 Commonly used measuring setup

The laboratory equipment for the evaluation of physical-engineering parameters was set up by employing an experimental system that allowed for autonomous management of experiments and data collection. The power system comprised a function generator, power amplifier with a transformer, safety features, wiring and devices for the measurement of electric quantities in the shape of voltage and current probes, and a power analyzer.

The pneumatic section of the system was composed of a compressor, equipped with a dehumidifying mechanism, devices for conducting feeding gas, a control valve and components for measuring non-electric quantities, such as gas temperature and humidity in various parts of the system, pressure and concentration of O_3. The experimental setup is depicted in Fig. 2.5.
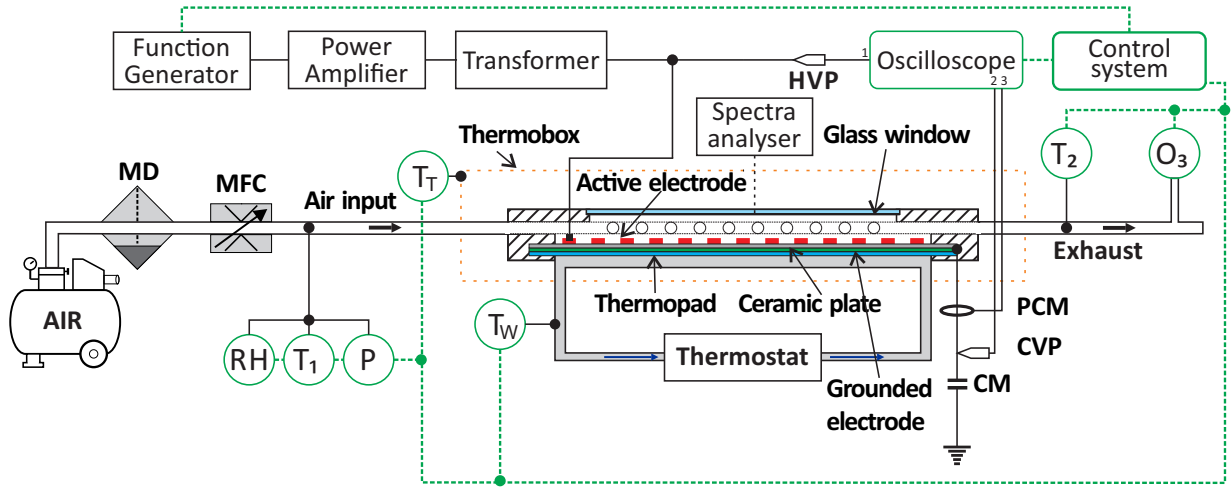
Figure 2.5: Experimental arrangement.

Two methods were used to keep the temperature of the discharge chamber constant (for reasons see the [21], [26] in Appendices A.3, A.8, and compare with Chapter 3.1). Firstly, the cooling water flowing through the radiator (for example a central brass tube) was supplied to the thermostat WCR P12. The temperature of water T_W was controlled in this way. Secondly, the discharge chamber was placed into the cooled thermo box POL-EKO-APARATURA, offering the possibility of regulating temperature from +3 to +70°C with an accuracy of ±0.1°C. The experiments were performed with the cooling water T_W temperature, and temperature in the thermo box T_T was adjusted as required.

Air is supplied from an oil-free compressor through a membrane dryer (MD) and a system of air filters and a mass flow controller (MFC). The relative humidity RH, temperature T_1, and pressure P of the air prior to discharge chamber input (see Fig. 2.5) were monitored. Also measured was temperature T_2 of the air at the discharge chamber output. An RH sensor was installed to monitor relative humidity. A digital manometer detected the pressure Siemens Sitrans P. Finally, air temperature was measured by the optical fibre thermometer Neoptix. BMT 964 or API 450 ozone analyzers measured the concentration of generated ozone at the discharge chamber output.

The power supply system consisted of the function generator KEYSIGHT 33500B, wide-band AC power amplifier AL-1400-HF-A (1000 W, frequency response 5 Hz to 800 kHz), and a high-frequency high-voltage transformer AL-T1000.7 (1000 W, frequency response 3.5 to 11 kHz).

The electrical parameters of the discharge were recorded by a digital four-channel oscilloscope Tektronix MDO4054B-3 (3 GHz, 2.5 GS/s). Discharge voltage signal $V_j(t)$ was measured by a high-voltage probe Pintek HVP-28HF (division ratio 1000/1, frequency up to 200 MHz) and discharge current was monitored by a Pearson current monitor (PCM – model 2877, bandwidth up to 200 MHz).

The measuring system is controlled by a Raspberry Pi 4 single-board computer. This computer runs on a dedicated software, created during the course of experimental setup design. Using the Modbus TCP bus, the proposed software collects and stores sensor data and manages individual devices connected to the experimental chain utilizing SCPI commands. The course of the experiment depends on predefined parameters. These include the total duration of the experiment, its duty cycles and the number of their repetitions, setting the resolution of the oscilloscope and setting the fixed input voltages on the function generator. In addition, it is possible to perform power regulation or input voltage to the ozone generator chamber, using active control of the function generator and feedback measurement of electrical quantities on the power analyzer. The software is responsible for the synchronous collection of non-electrical and electrical data. The computer measures the non-electrical quantities; meanwhile, electrical data are collected by oscilloscope. Both outputs are stored in CSV files and prepared for later fusion and processing.

Figure 2.6: Particle injector for flow visualisation.

The laboratory equipment for checking the shape and direction of feeding gas (see Fig.

2.7) flowing through the chamber and the validity of the real preparation with a numerical model (depicted in Fig. 2.6) was set up by a pneumatic system, supplemented with an active particles injector. The streamlines of the feeding gas were monitored by means of small TiO_2 granules carried by gas, and their movement was recorded by a high-speed camera Photron SA-Z 2100 and the necessary accessories, such as software for high-speed recording, light sources and high-speed memory modules. Experiments involving flow monitoring on the real equipment helped in verifying the model´s reliability from the Comsol Multiphysics environment, and thus confirmed the importance of implementing the designed solution.
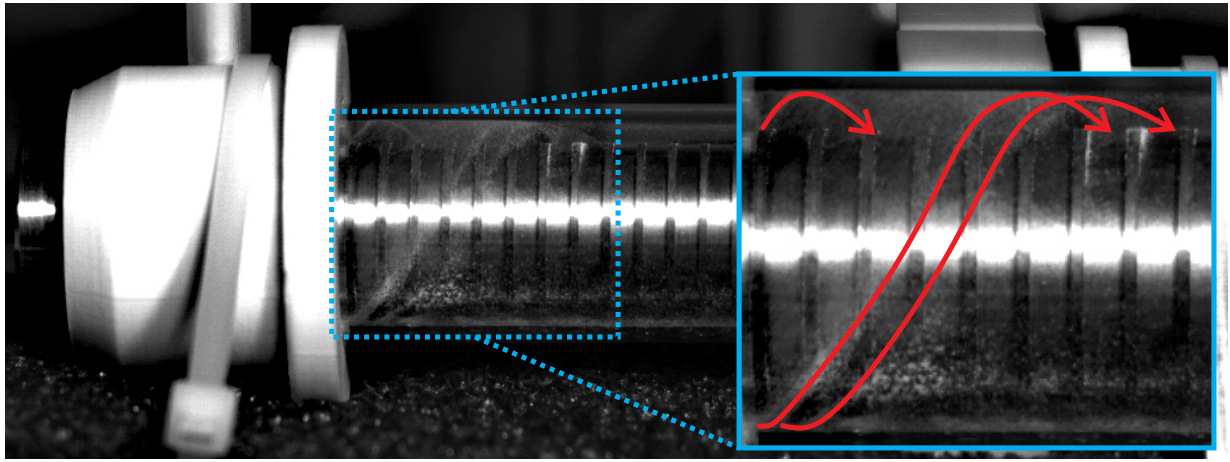
Figure 2.7: Detail of visualised flow patterns.

2.2.3 Electrical parameters of dielectric barrier discharge

At atmospheric pressure, SDBDs tend to display a strong trend of filamentary development exceeding the areas with homogeneous nonthermal plasma (atmospheric glow discharge). Typical diameter of the transient microdischarge is 100 µm in air at atmospheric pressure, and a 1 mm discharge gap and durations at the order 10-100 ns [27]. The principle of SDBD is based on regularly alternating positive and negative potential conducted to an active, or rather grounded electrode. During a negative half-period, active electrode generates electrons that are accelerated by a powerful surface electric field in the direction from the dielectric material. In a positive half-period, electrons are desorbed from the surface and accelerated in the opposite direction. The given situation is shown in Fig. 2.8.

DBDs are normally characterized by a large number of microdischarges per unit of electrode area and per period of driving voltage. Their existence is accompanied by current pulses. Under certain conditions, microdischarges increase their cross-section and merge, while discharge appears to be homogeneous. The occurrence of microdischarges and their pattern are determined not only by the amplitude and frequency of driving voltage, type of gas, its humidity, and presence of admixtures in the gas, but also by the surface properties and, of course, the electrode geometry (see [20] in Appendix A.2).

10
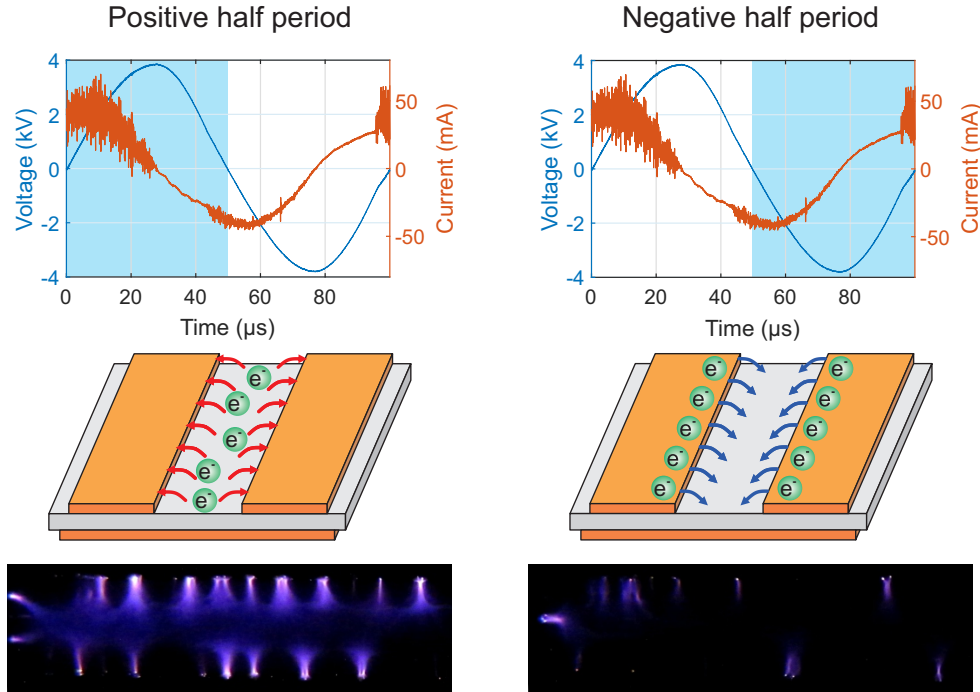
Figure 2.8: Principle of the surface dielectric barrier discharge.

Depending on the electrode layout, applied voltage and its frequency, pressure, and the type of feeding gas, SDBDs may occur both in a filament and homogenous regime with the typical Townsend or streamer properties.

The electrical supply voltage frequency is of smaller importance for the change of the character of discharge. Rising frequency slightly reduces the burning voltage of the discharge, i.e. the state whereby discharge is burning all over the entire surface of the electrode.

This is understandable if we assume that charge density does not completely vanish from one period to the other. In that case, charges at higher frequencies have less time to recombine, giving a higher charge build-up and allowing for lower burning voltages [9].

The explanation of the change in the number of current pulses per unit of time with the change of frequency [17] is mainly based on the accumulated charges of the microdischarges over the dielectric material from the preceding half cycle of the applied voltage, which enhances the electric field and subsequently the discharge in the next half cycle of the applied voltage.

Growing amplitude of supply voltage results in mounting current peaks, representing growth of discharge filaments, just as of continual current. A higher supply voltage is also reflected in earlier occurrence of individual filaments and in their greater numbers. The amplitude of the current peaks is about ten times larger in the positive half-period than in the negative half-period.

Electrode geometry itself has its significance for a higher growth of filaments when the active electrode is longer or the effect of a smaller number of mutual electrode motives is

applied (edge effect is prevalent). The amplitude of current peaks representing microdischarges is dependent on the space filaments can fill up. In the case of individual electrode strips being at a short distance from one another, mutual electric fields overlap and influence each other, while filament density decreases (Cf. [28]). When the distance between individual strips is smaller, the number of filaments drops as a result of Paschen´s law, but their frequency remains unchanged. Study on the impact of frequency and amplitude of the supply voltage depending on the generation of the amount of O_3 was published in the article [20] in Appendix A.2. The details are shown through the relationship between Fig. 9 and Fig. 10 in [20] in Appendix A.2.

2.3 Representation of the microdischarge channel development based on 3D numerical study

Recently published articles offer a predominance of studies describing the origin and behaviour of dielectric barrier discharge from an experimental point of view [21], [29]–[32], while phenomena characterized by physical-mathematical models are treated less frequently [33]–[38]. The past few decades have seen the development of mathematical models describing – with a certain, smaller, or greater precision and success rate – the specific configuration of the phenomenon being modelled [39]–[43]. The authors [17], [21], [31], [44] classify such models into simplified (phenomenological) ones and first-principles ones that employ mathematical approaches to solving the given task. The category of simplified models comprises, for instance, *Electrostatic models*, *Linearized force models*, or *Potential flow models*. For their part, first-principles-based models include *Kinetics models* and *Fluid models* [35], [45], [46]. The latter ones, in particular, are the subject of our studies.

As long as our research is oriented towards the discharge generation of various active species like ozone [22] (available in Appendix A.5), the critical quantity which determines the efficiency of this generation is the dimension of the active volume in which the processes of species generation occur. In the case of SDBD, discharge develops along the dielectric surface. At critical field strength, a set of microdischarges appears on the dielectric surface, which is accompanied by the luminosity of the discharge near the strip electrodes. This luminosity area and, consequently, the active discharge volume do not cover the whole area of the dielectric.

The physics of the discharge, leading to the formation of the active volume, is rather complex; therefore, we had to make essential simplifications. Thus, we restricted ourselves to the positive half-period of the driving voltage only, used solely one type of positive ions-electrons model, and restricted ourselves to a time interval $T = 46$ ns. This assumption is associated with the processes of electron production from the electrodes. In the case of the strip electrode's positive polarity, the photoemission current plays a decisive role. The ion emission current is less significant [47]. According to this paper, the photoemission starts after more than $T = 15$ ns. In fact, for the negative polarity of the strip electrode, the photoemission current reaches a maximum at about $T = 6$ ns. Thus, the photoemission

and the ion emission from electrodes in the chosen simulation time interval can be neglected. Besides, this time interval limitation allows us to ignore the heating of electrodes, gas heating, and heat-related effects on electrodes and gas properties.

2.3.1 Physical description of the SDBD phenomena

This chapter is based on the author's works [22], [23] in Appendices A.5 and A.6. We use a two-species model with electrons and one type of ions, notably for positive ions. Moreover, we restrict ourselves to the initial phase of the positive half-period of the applied voltage and disregard different ionic reactions.

Note: Definitions of electrode areas and labeling of the bounded domains are based on [22], [23] in Appendices A.5 and A.6.

Therefore, the definition of the model follows from [22], [38], [43], [48]–[50]. Hence, we first model the relation between the electric field $\mathbf{E} : Q_T \to \mathbb{R}^3$ and the electric potential $\Phi : Q_T \to \mathbb{R}$ by means of the Poisson equation as follows

$$\mathbf{E} = -\nabla \Phi \quad \text{in } Q_T, \tag{2.1}$$

where ∇ represents the gradient with respect to the space variable. Further, we assume the electric potential to be decomposed into two parts: $\phi : Q_T \to \mathbb{R}$ being induced by the external electric field and $\varphi : \Omega_{Air} \times (0, T) \to \mathbb{R}$ being induced by the net charge density in the plasma, i.e. $\Phi = \phi + \varphi$ and

$$\nabla \cdot (\varepsilon_{Air}\varepsilon_0 \nabla \varphi) = -e_c(n_e - n_i) \quad \text{in } \Omega_{Air} \times (0, T), \tag{2.2}$$

$$\nabla \cdot (\varepsilon_r \varepsilon_0 \nabla \phi) = 0 \quad \text{in } Q_T, \tag{2.3}$$

where ∇ represents the divergence operator, $n_e : \Omega_{Air} \times (0, T) \to \mathbb{R}$ denotes the electron density, $n_i : \Omega_{Air} \times (0, T) \to \mathbb{R}$ denotes the ion density, ε_0 is the vacuum permittivity, ε_r is a piecewise constant function designating the relative permittivity of air ($\varepsilon_r = \varepsilon_{Air}$ on Ω_{Air}) and dielectric material ($\varepsilon_r = \varepsilon_{Die}$ on Ω_{Die}) and e_c is the elementary charge.

Further, the time evolution of electrons and ions concentrations are determined by the continuity equations where the ionic reactions are defined using the Townsend coefficients [51], i.e., the time evolution equations are described as follows

$$\frac{\partial n_i}{\partial t} + \nabla \cdot (n_i \mathbf{V}_i) = A p_c \exp\{-\frac{B p_c}{\|\mathbf{E}\|}\} \|n_e \mathbf{V}_e\| - r_{i \leftrightarrow e} n_i n_e \tag{2.4}$$

in $\Omega_{Air} \times (0, T)$.

Summing up, the used assumptions, including chosen simulation time interval, allowed us to write a continuity equation for electrons in the form of (2.5),

$$\frac{\partial n_e}{\partial t} + \nabla \cdot (n_e \mathbf{V}_e) = A p_c \exp\{-\frac{B p_c}{\|\mathbf{E}\|}\} \|n_e \mathbf{V}_e\| - r_{i \leftrightarrow e} n_i n_e, \tag{2.5}$$

in $\Omega_{Air} \times (0, T)$, where $\mathbf{V}_i : \Omega_{Air} \times (0, T) \to \mathbb{R}^3$ is the ion velocity field, $\mathbf{V}_e : \Omega_{Air} \times (0, T) \to \mathbb{R}^3$ is the electron velocity field, p_c is the constant air pressure, $r_{i \leftrightarrow e}$ denotes the electron-ion recombination rate, A and B are pre-exponential and exponential constants, respectively. For the sake of completeness, let us note that $\| \cdot \|$ represents the usual Euclidean norm.

Note: Let us comment on the assumption of constant air pressure. Since we are set to work within a very small time range ($\approx$ ns), it seems reasonable to assume the air pressure to be constant. Though it is still by no means obvious that this simplification is insignificant, we are also unable to compute an approximate solution without this assumption as yet.

Further, using the so-called Drift-Diffusive model (see [51], [52]), we rewrite electronic and ionic fluxes as

$$n_i \mathbf{V}_i = n_i \mu_i \mathbf{E} - D_i \nabla n_i \quad \text{in } \Omega_{Air} \times (0, T), \tag{2.6}$$
$$n_e \mathbf{V}_e = -n_e \mu_e \mathbf{E} - D_e \nabla n_e \quad \text{in } \Omega_{Air} \times (0, T), \tag{2.7}$$

where μ_e and μ_i are the electron and ion mobility coefficients, respectively, and D_e and D_i are the electron and ion diffusion coefficients, respectively.

Now we observe that the numerical solution of equation (2.3) can be computed independently of the remaining equations. Therefore, by substituting (2.1), (2.6), and (2.7) into (2.4) and (2.5) and using the results of (2.3), we can reduce the remaining equations to three scalar equations for three scalar unknowns (φ, n_i, n_e) and compute the remaining entities afterwards. All in all, we, therefore, focus on finding a solution (ϕ) of equation (2.3) in Q_T and solution (φ, n_i, n_e) for equation (2.2) coupled with the following equations

$$
\begin{aligned}
\frac{\partial n_i}{\partial t} &+ \nabla \cdot (-n_i \mu_i \nabla(\phi + \varphi) - D_i \nabla n_i) \\
&= A p_c \exp\{-\frac{B p_c}{\|\nabla(\phi + \varphi)\|}\} \|n_e \mu_e \nabla(\phi + \varphi) - D_e \nabla n_e\| \\
&- r_{i \leftrightarrow e} n_i n_e
\end{aligned}
\tag{2.8}
$$

$$
\begin{aligned}
\frac{\partial n_e}{\partial t} &+ \nabla \cdot (n_e \mu_e \nabla(\phi + \varphi) - D_e \nabla n_e) \\
&= A p_c \exp\{-\frac{B p_c}{\|\nabla(\phi + \varphi)\|}\} \|n_e \mu_e \nabla(\phi + \varphi) - D_e \nabla n_e\| \\
&- r_{i \leftrightarrow e} n_i n_e,
\end{aligned}
\tag{2.9}
$$

in $\Omega_{Air} \times (0, T)$.

Thus, formulating the initial and boundary conditions for (ϕ) and (φ, n_i, n_e) remains.

We assume the following setting [22]

$$\phi(x,0) = 0 \quad \text{in } \Omega, \tag{2.10}$$

$$\phi(x,t) = 0 \quad \text{on } \Gamma_{Grnd} \times (0,T), \tag{2.11}$$

$$\phi(x,t) = U_{amp}\sin(\omega t) =: \phi_{Strip}(x,t) \quad \text{on } \Gamma_{Strip} \times (0,T) \tag{2.12}$$

$$\frac{\partial \phi}{\partial \boldsymbol{n}}(x,t) = 0 \quad \text{on } \Gamma_{Walls} \times (0,T) \tag{2.13}$$

$$\varphi(x,0) = 0, \quad \text{in } \Omega_{Air}, \tag{2.14}$$

$$\varphi(x,t) = 0 \quad \text{on } \Gamma_{Strip} \times (0,T), \tag{2.15}$$

$$\frac{\partial \varphi}{\partial \boldsymbol{n}}(x,t) = 0 \quad \text{on } \Gamma_{TopWalls} \cup \Gamma_{AirToDie} \times (0,T), \tag{2.16}$$

$$n_i(x,0) = n_i^0(x) \quad \text{in } \Omega_{Air}, \tag{2.17}$$

$$n_i(x,t) = 0, \quad \text{on } \Gamma_{Strip} \times (0,T), \tag{2.18}$$

$$\frac{\partial n_i}{\partial \boldsymbol{n}}(x,t) = 0 \quad \text{on } \Gamma_{TopWalls} \cup \Gamma_{AirToDie} \times (0,T), \tag{2.19}$$

$$n_e(x,0) = n_e^0(x) \quad \text{in } \Omega_{Air}, \tag{2.20}$$

$$\frac{\partial n_e}{\partial \boldsymbol{n}}(x,t) = 0 \quad \text{on } \partial\Omega_{Air} \times (0,T), \tag{2.21}$$

where $\phi_{Strip} : \Gamma_{Strip} \times (0,T) \to \mathbb{R}$ is an electric potential boundary function, $\boldsymbol{n}$ denotes the outer unit normal vector to $\partial\Omega$, $n_i^0 : \Omega_{Air} \to \mathbb{R}$ and $n_e^0 : \Omega_{Air} \to \mathbb{R}$ is the initial ion density and electron density, respectively, U_{Amp} is the discharge voltage, $\omega = 2\pi f$ is the angular velocity and f is the frequency.

   Note: Let us comment on boundary conditions for ions and electrons. Although there are several theories regarding a proper setting of boundary conditions for them [35], [53], we prefer to assume the homogeneous Neumann condition on the whole boundary. An exception will be for the Γ_{Strip} for ions, where it is clear and physically reasonable to assume a homogeneous Dirichlet condition for the positive half-period of the discharge. Since there is uncertainty as to the proper setting of those boundary conditions, we instead implement the general condition even though, numerically, it renders the computations less stable.

2.3.2 Formulation of the problems

In this section, we start with the process of partial non-dimensionalization and then introduce the weak formulations of the studied problems. The partial non-dimensionalization is motivated by better numerical stability due to the appropriate rescaling of the quantities we are simulating.

2.3.2.1 Non-dimensionalization and weak formulations

Inspired by the non-dimensionalization scheme presented in [40], we introduce new variables and new dimensionless quantities as follows

$$\tau = \frac{t}{t_0}, \quad z_i = \frac{x_i}{L}, \ i = 1, 2, 3,$$

$$N_e = \frac{n_e}{n_0}, \quad N_i = \frac{n_i}{n_0}, \quad \Phi_{nd} = \frac{e_c}{k_B T_e}\Phi, \tag{2.22}$$

where t_0 is reference time, L is characteristic length, n_0 is reference particle density, k_B is Boltzmann's constant and T_e is electron temperature.

Let us now define

$$\mathcal{D}^G = \{\tilde{\phi} \in H^1(\Omega) : \tilde{\phi} = 0 \text{ on } \Gamma_{Grnd}\}$$

$$\mathcal{D}^{SG} = \{\tilde{\phi} \in H^1(\Omega) : \tilde{\phi} = 0 \text{ on } \Gamma_{Strip} \cup \Gamma_{Grnd}\}$$

$$\mathcal{D}^S_{Air} = \{\tilde{\varphi} \in H^1(\Omega_{Air}) : \tilde{\phi} = 0 \text{ on } \Gamma_{Strip}\}$$

and assume there exists $\phi^*_{Strip} \in \mathcal{C}(0, T; \mathcal{D}^G)$ such that ϕ_{Strip} is its trace on $\Gamma_{Strip} \times (0, T)$. Now we are ready to introduce the weak formulation of the problem governed by equation (2.3) and boundary conditions (2.10)-(2.13). Let us denote this weak formulation as (*SDBD-0*): Find $\phi \in L^2(0, T; \mathcal{D}^G)$ such that holds:

$$\phi - \frac{e_c}{k_B T_e}\phi^*_{Strip} \in L^2(0, T; \mathcal{D}^{SG}),$$

$$a(\phi, \tilde{\phi}) = 0 \text{ for a.e. } t \in (0, T), \forall \tilde{\phi} \in \mathcal{D}^{SG},$$

$$\lim_{t \to 0} \|\phi(\cdot, t)\|_{L^2(\Omega)} = 0, \tag{2.23}$$

where

$$a(\phi, \tilde{\phi}) = \varepsilon_{Air} \int_{\Omega_{Air}} \nabla\phi\nabla\tilde{\phi}dx + \varepsilon_{Die} \int_{\Omega_{Die}} \nabla\phi\nabla\tilde{\phi}dx. \tag{2.24}$$

Further, let us as well introduce the weak formulation to a problem governed by equations (2.2), (2.8), (2.9) and conditions (2.14)-(2.21). Let $\phi \in L^2(0, T; \mathcal{D}^G)$ be a weak solution of problem (*SDBD-0*). We denote the weak formulation as (*SDBD-1*): Find $\varphi \in L^2(0, T; \mathcal{D}^S_{Air})$, $N_i \in L^2(0, T; \mathcal{D}^S_{Air})$ and $N_e \in L^2(0, T; H^1(\Omega_{Air}))$ such that for a.e. $t \in (0, T)$, $\forall \tilde{\varphi} \in \mathcal{D}^S_{Air}$, $\forall \tilde{N}_i \in \mathcal{D}^S_{Air}$ and $\forall \tilde{N}_e \in \mathcal{H}^1(\Omega_{Air})$

$$a_{Air}(\varphi, \tilde{\varphi}) = L(N_i, N_e, \tilde{\varphi}),$$

$$\int_{\Omega_{Air}} \frac{\partial N_i}{\partial \tau}\tilde{N}_idx + \mu_i c(N_i, \varphi, \phi, \tilde{N}_i) + D_i d(N_i, \tilde{N}_i)$$

$$- f_e(N_e, \varphi, \phi, \tilde{N}_i) = R(N_i, N_e, \tilde{N}_i),$$

$$\int_{\Omega_{Air}} \frac{\partial N_e}{\partial \tau}\tilde{N}_edx - \mu_e c(N_e, \varphi, \phi, \tilde{N}_e) + D_e d(N_e, \tilde{N}_e)$$

$$- f_e(N_e, \varphi, \phi, \tilde{N}_e) = R(N_i, N_e, \tilde{N}_e), \tag{2.25}$$

16

and

$$\lim_{t\to 0} \|\varphi(\cdot, t)\|_{L^2(\Omega_{Air})} = 0,$$

$$\lim_{t\to 0} \|N_i(\cdot, t) - \frac{1}{n_0} n_i^0(\cdot)\|_{L^2(\Omega_{Air})} = 0,$$

$$\lim_{t\to 0} \|N_e(\cdot, t) - \frac{1}{n_0} n_e^0(\cdot)\|_{L^2(\Omega_{Air})} = 0,$$

where (for $N, \tilde{N} \in \mathcal{H}^1(\Omega_{Air})$)

$$a_{Air}(\varphi, \tilde{\varphi}) = \int_{\Omega_{Air}} \nabla\varphi \nabla\tilde{\varphi} dx,$$

$$c(N, \varphi, \phi, \tilde{N}) = \frac{k_B T_e t_0}{e_c L} \int_{\Omega_{Air}} N(\nabla\varphi + \nabla\phi)\nabla\tilde{N} dx,$$

$$d(N, \tilde{N}) = \frac{t_0}{L} \int_{\Omega_{Air}} \nabla N \nabla\tilde{N} dx,$$

$$\cdot \|\frac{\mu_i k_B T_e t_0}{e_c L} N(\nabla\varphi + \nabla\phi) + \frac{D_i t_0}{L}\nabla N\| \cdot \tilde{N} dx,$$

$$f_e(N, \varphi, \phi, q) = A p_c \int_{\Omega_{Air}} \exp\{-\frac{B p_c e_c L}{k_B T_e \|\nabla\varphi + \nabla\phi\|}\}$$

$$\cdot \|\frac{\mu_e k_B T_e t_0}{e_c L} N(\nabla\varphi + \nabla\phi) - \frac{D_e t_0}{L}\nabla N\| \cdot \tilde{N} dx,$$

$$L(N_i, N_e, \tilde{\varphi}) = \frac{e_c^2 L^2 n_0}{\varepsilon_{Die} k_B T_e} \int_{\Omega_{Air}} \tilde{\varphi}(N_i - N_e) dx,$$

$$R(N_i, N_e, \tilde{N}) = -r_{i\leftrightarrow e} n_0 t_0 \int_{\Omega_{Air}} \tilde{N} N_i N_e dx.$$

2.3.3 Discretization

We suppose that the domain Ω is polyhedral with the Lipschitz boundary. By $\mathcal{T}_h$, we denote a regular partition of the domain Ω, and by $\mathcal{T}_h^{Air} \subset \mathcal{T}_h$, we denote a regular partition of the domain Ω_{Air}. Let us define

$$\mathcal{D}_h^G = \{\tilde{\phi}_h \in \mathcal{D}^G : \tilde{\phi}_h|_K \in P_r(K), K \in \mathcal{T}_h\},$$

$$\mathcal{D}_h^{SG} = \{\tilde{\phi}_h \in \mathcal{D}^{SG} : \tilde{\phi}_h|_K \in P_r(K), K \in \mathcal{T}_h\},$$

$$\mathcal{D}_{Air,h}^S = \{\tilde{N}_h \in \mathcal{D}_{Air}^S : \tilde{N}_h|_K \in P_r(K), K \in \mathcal{T}_h^{Air}\},$$

$$\mathcal{D}_{Air,h} = \{\tilde{N}_h \in H^1(\Omega_{Air}) : \tilde{N}_h|_K \in P_r(K), K \in \mathcal{T}_h^{Air}\},$$

$$\boldsymbol{L}_h = \{\mathbf{E}_h \in L^2(\Omega)^3 : \mathbf{E}_h|_K \in P_{r-1}(K)^3, K \in \mathcal{T}_h\},$$

$$\boldsymbol{L}_h^{Air} = \{\mathbf{V}_h \in L^2(\Omega_{Air})^3 : \mathbf{V}_h|_K \in P_{r-1}(K)^3, K \in \mathcal{T}_h^{Air}\},$$

where $P_r(K)$, $P_s(K)$ and $P_q(K)$ denote the space of all polynomials on K of a degree less or equal to r, s and q, respectively. Moreover, we assume $r \geq 2$, $s \geq 1$ and $q \geq 1$.

For the time discretization of $(SDBD\text{-}0)$ and $(SDBD\text{-}1)$ we consider a uniform partition of the time interval $[0, T]$ formed by the time instants $t_j = j\Delta t$, $j = 0, 1, \ldots, j_{max}$, with a time step $\Delta t = T/j_{max}$.

2.3.3.1 Approximate solution for (SDBD-0)

Let $\boldsymbol{g}_h^j \in \mathcal{D}_h^G \approx U_{amp}\sin(\omega t_j)$ on Γ_{Strip}, $j = 0, \ldots, j_{max}$. We define the approximate solution of $(SDBD\text{-}0)$ problem obtained by the Finite Elements Method as a set of functions $\phi_h^j \in \mathcal{D}_h^G$, $j = 0, \ldots, j_{max}$, satisfying

$$
\begin{aligned}
&\phi_h^j - \boldsymbol{g}_h^j \in \mathcal{D}_h^{SG} \quad \forall j = 0, \ldots, j_{max}, \\
&a(\phi_h^j, \tilde{\phi}_h) = 0 \quad \forall j = 0, \ldots, j_{max}, \forall \tilde{\phi}_h \in \mathcal{D}_h^{SG} \\
&\|\phi_h^0\|_{L^2(\Omega)} = 0.
\end{aligned}
\tag{2.26}
$$

2.3.3.2 Approximate solution for (SDBD-1)

Let $\{\phi_h^j\}_{j=0}^{j_{max}}$ be an approximate solution of $(SDBD\text{-}0)$. We define the approximate solution of the $(SDBD\text{-}1)$ problem obtained by the BDF-2 method (BDF stands for Backward differentiation formula) and the Finite Elements Method as functions $(\varphi_h^j, N_{ih}^j, N_{eh}^j) \in \mathcal{D}_{Air,h}^S \times \mathcal{D}_{Air,h}^S \times \mathcal{D}_{Air,h}$, $j = 0, \ldots, j_{max}$, satisfying for all $j = 1, \ldots, j_{max}$

$$
\begin{aligned}
&a_{Air}(\varphi_h^j, \tilde{\varphi}_h) = L(N_{eh}^j, N_{ih}^j, \tilde{\varphi}_h) \quad \forall \tilde{\varphi}_h \in \mathcal{D}_{Air,h}^S \\
&\frac{1}{\Delta\tau} \int_{\Omega_{Air}} (N_{ih}^j - \frac{4}{3}N_{ih}^{j-1} + \frac{1}{3}N_{ih}^{j-2})\tilde{N}_{i,h}dx \\
&\qquad = \frac{2}{3}\mathbf{F}_i(N_{ih}^j, N_{eh}^j, \varphi_h^j, \phi_h^j, N_{ih}^{j-1}, \varphi_h^{j-1}, \phi_h^{j-1}, \tilde{N}_{i,h}) \\
&\qquad \forall \tilde{N}_{i,h} \in \mathcal{D}_{Air,h}^S, \\
&\frac{1}{\Delta\tau} \int_{\Omega_{Air}} (N_{eh}^j - \frac{4}{3}N_{eh}^{j-1} + \frac{1}{3}N_{eh}^{j-2})\tilde{N}_{e,h}dx \\
&\qquad = \frac{2}{3}\mathbf{F}_e(N_{ih}^j, N_{eh}^j, \varphi_h^j, \phi_h^j, N_{eh}^{j-1}, \varphi_h^{j-1}, \phi_h^{j-1}, \tilde{N}_{e,h}) \\
&\qquad \forall \tilde{N}_{e,h} \in \mathcal{D}_{Air,h},
\end{aligned}
\tag{2.27}
$$

where $\Delta\tau = \frac{\Delta t}{t_0}$, $(\varphi_h^0, N_{ih}^0, N_{eh}^0)$ and $(\varphi_h^{-1}, N_{ih}^{-1}, N_{eh}^{-1})$ are defined as the $L^2(\Omega)$ projections of the initial data $(0, \frac{n_i^0}{n_0}, \frac{n_e^0}{n_0})$ and $(0,0,0)$, respectively, on $\mathcal{D}_{Air,h}^S \times \mathcal{D}_{Air,h}^S \times \mathcal{D}_{Air,h}$ and

$$
\begin{aligned}
\mathbf{F}_i(N_{ih}^j, & N_{eh}^j, \varphi_h^j, \phi_h^j, N_{ih}^{j-1}, \varphi_h^{j-1}, \phi_h^{j-1}, \tilde{N}_{i,h}) \\
&= \mu_i c(N_{ih}^j, \varphi_h^j, \phi_h^j, \tilde{N}_{i,h}) - D_i d(N_{ih}^j, \tilde{N}_{i,h}) \\
&\quad + \tilde{f}_e(N_{eh}^j, \varphi_h^j, \phi_h^j, N_{eh}^{j-1}, \varphi_h^{j-1}, \phi_h^{j-1}, \tilde{N}_{i,h}) \\
&\quad + R(N_{ih}^j, N_{eh}^j, \tilde{N}_{i,h}) \\
\mathbf{F}_e(N_{ih}^j, & N_{eh}^j, \varphi_h^j, \phi_h^j, N_{eh}^{j-1}, \varphi_h^{j-1}, \phi_h^{j-1}, \tilde{N}_{e,h}) \\
&= -\mu_e c(N_{eh}^j, \varphi_h^j, \phi_h^j, \tilde{N}_{e,h}) - D_e d(N_{eh}^j, \tilde{N}_{e,h}) \\
&\quad + \tilde{f}_e(N_{eh}^j, \varphi_h^j, \phi_h^j, N_{eh}^{j-1}, \varphi_h^{j-1}, \phi_h^{j-1}, \tilde{N}_{e,h}) \\
&\quad + R(N_{ih}^j, N_{eh}^j, \tilde{N}_{e,h})
\end{aligned}
$$

where $\tilde{f}_e$ is linear approximation of f_e, defined in the following section 2.3.3.3.

2.3.3.3   Linear approximation of ionization rate

Even though it might seem that we should directly use the Newton method to solve the presented non-linear problem, we rather introduce a linear approximation of ionization rate separately and with extra care. As we will show below, it is necessary to carefully treat the possibility of division by zero and problems with finite machine precision. Most importantly, identical problems have to be overcome even if we skip the linearization process and use directly the Newton method since the derivatives performed in the Newton method will introduce similar "controversial" terms.

Let us define the following operator f acting on $\mathcal{D}_{Air,h} \times \mathcal{D}_{Air,h}$

$$
f(\varphi_h, N_h) = \alpha \exp\{-\frac{\beta}{\|\nabla\varphi_h\|}\}\|\gamma N_h \nabla\varphi_h - \delta\nabla N_h\| : \Omega \to \mathbb{R}, \qquad (2.28)
$$

where $\alpha, \beta, \gamma, \delta$ are generic constants. It is obvious that $f(\varphi_h, N_h)$ is not defined on set $\Theta = \{\boldsymbol{x} \in \Omega_{Air} : \|\nabla\varphi_h(x)\| = 0\}$ for given $\varphi_h \in \mathcal{D}_{Air,h}$. Nevertheless, we can set $f(\varphi_h, N_h) \equiv 0$ on Θ and then for such $f(\varphi_h, N_h)$ holds that $f(\varphi_h, N_h) \in \mathcal{C}(\Omega_{Air})$.

Now, we present the linearization of the operator (2.28) for any $(\varphi_h, N_h) \in \mathcal{D}_{Air,h} \times \mathcal{D}_{Air,h}$ from which one can easily deduce the linear approximation of ionization rate.

Let $\vec{\psi}_h = \{\psi_h^i\}_{i=1}^{m_d}$ be the basis of space $\mathcal{D}_{Air,h}$, $m_d = dim(\mathcal{D}_{Air,h})$. Now, any $\varphi_h \in \mathcal{D}_{Air,h}$ can be uniquely represented as $\varphi_h = \vec{\Psi} \cdot \vec{\psi}_h = \sum_{i=1}^{m_d} \Psi_i \psi_h^i$, where $\vec{\Psi} \in \mathbb{R}^{m_d}$.

Consequently, operator f can be understood as an operator acting on $\mathbb{R}^{m_d} \times \mathbb{R}^{m_d}$, i.e.

$$
\begin{aligned}
f(\varphi_h, N_h) &= f(\vec{\Psi}_\varphi, \vec{\Psi}_N) \\
&= \alpha \exp\{-\frac{\beta}{\|\vec{\Psi}_\varphi \cdot \nabla\vec{\psi}_h\|}\}\|\gamma\vec{\Psi}_N \cdot \vec{\psi}_h \vec{\Psi}_\varphi \cdot \nabla\vec{\psi}_h - \delta\vec{\Psi}_N \cdot \nabla\vec{\psi}_h\|
\end{aligned}
$$

Using the Taylor series, we introduce a linear approximation of $f(\vec{\Psi}_\varphi, \vec{\Psi}_N)$ near point $(\vec{\Psi}_\varphi^0, \vec{\Psi}_N^0) \in (\mathbb{R}^{m_d} \times \mathbb{R}^{m_d})$ as follows

$$
\begin{aligned}
f(\vec{\Psi}_\varphi, \vec{\Psi}_N) \approx f(\vec{\Psi}_\varphi^0, \vec{\Psi}_N^0) &+ \frac{\partial f}{\partial \vec{\Psi}_\varphi}(\vec{\Psi}_\varphi^0, \vec{\Psi}_N^0) \cdot (\vec{\Psi}_\varphi - \vec{\Psi}_\varphi^0) \\
&+ \frac{\partial f}{\partial \vec{\Psi}_N}(\vec{\Psi}_\varphi^0, \vec{\Psi}_N^0) \cdot (\vec{\Psi}_N - \vec{\Psi}_N^0),
\end{aligned}
$$

where using marking $\mathbb{J} = \gamma \vec{\Psi}_N^0 \vec{\psi}_h \vec{\Psi}_\varphi^0 \nabla \vec{\psi}_h - \delta \vec{\Psi}_N^0 \nabla \vec{\psi}_h$

$$
\begin{aligned}
\frac{\partial f}{\partial \vec{\Psi}_\varphi}(\vec{\Psi}_\varphi^0, \vec{\Psi}_N^0) &= \nabla \vec{\psi}_h \left[\alpha \exp\{-\frac{\beta}{\|\vec{\Psi}_\varphi^0 \nabla \vec{\psi}_h\|}\} \gamma \vec{\Psi}_N^0 \vec{\psi}_h \frac{\mathbb{J}}{2\|\mathbb{J}\|} \right. \\
&\left. + \|\mathbb{J}\| \beta \exp\{-\frac{\beta}{\|\vec{\Psi}_\varphi^0 \nabla \vec{\psi}_h\|}\} \frac{\vec{\Psi}_\varphi^0 \nabla \vec{\psi}_h}{2\|\vec{\Psi}_\varphi^0 \nabla \vec{\psi}_h\|^3} \right] \\
\frac{\partial f}{\partial \vec{\Psi}_N}(\vec{\Psi}_\varphi^0, \vec{\Psi}_N^0) &= \left[\alpha \exp\{-\frac{\beta}{\|\vec{\Psi}_\varphi^0 \nabla \vec{\psi}_h\|}\} \frac{\mathbb{J}}{2\|\mathbb{J}\|} \right] \\
&\cdot \left(\gamma \vec{\Psi}_\varphi^0 \nabla \vec{\psi}_h \cdot \vec{\psi}_h - \delta \nabla \vec{\psi}_h \right),
\end{aligned}
$$

under the assumption that every term on the right-hand side makes sense.

Here, we can observe that we should take care of possible divisions by zero and potential problems introduced by the machine precision limitations, as mentioned earlier.

Let us now switch back to the equivalent representation of operator f by (2.28). We finally present the approximation of f at the point $(\varphi_h, N_h) \in \mathcal{D}_{Air,h} \times \mathcal{D}_{Air,h}$ near point $(\varphi_h^0, N_h^0) \in \mathcal{D}_{Air,h} \times \mathcal{D}_{Air,h}$

$$
\begin{aligned}
f(\varphi_h, N_h) &\approx \tilde{f}(\varphi_h, N_h, \varphi_h^0, N_h^0) & (2.29) \\
&= \tilde{f}_{00}(\varphi_h^0, N_h^0) + \tilde{f}_{10}(\varphi_h^0, N_h^0) \cdot \nabla(\varphi_h - \varphi_h^0) & (2.30) \\
&+ \tilde{f}_{01}(\varphi_h^0, N_h^0) \cdot \left[\gamma \nabla \varphi_h^0(N_h - N_h^0) - \delta \nabla(N_h - N_h^0) \right],
\end{aligned}
$$

where using marking $\mathbb{K} = \gamma N_h^0 \nabla \varphi_h^0 - \delta \nabla N_h^0$

$$\tilde{f}_{00}(\varphi_h^0, N_h^0) = 0, \qquad\qquad \text{if } \|\nabla\varphi_h^0\| < \frac{10^{-2}}{\beta},$$

$$= \alpha \exp\{-\frac{\beta}{\|\nabla\varphi_h^0\|}\}\|\mathbb{K}\|, \quad \text{else}$$

$$\tilde{f}_{10}(\varphi_h^0, N_h^0) = 0, \qquad\qquad \text{if } \|\nabla\varphi_h^0\| < \frac{10^{-2}}{\beta},$$

$$= \|\mathbb{K}\|\beta \exp\{-\frac{\beta}{\|\nabla\varphi_h^0\|}\}\frac{\nabla\varphi_h^0}{2\|\nabla\varphi_h^0\|^3},$$

$$\text{if } \|\nabla\varphi_h^0\| \geq \frac{10^{-2}}{\beta}, \ \|\mathbb{K}\| < \frac{1}{2}\alpha\gamma\exp\{-\frac{\beta}{\|\nabla\varphi_h^0\|}\}$$

$$= \alpha \exp\{-\frac{\beta}{\|\nabla\varphi_h^0\|}\}\gamma N_h^0 \frac{\mathbb{K}}{2\|\mathbb{K}\|}$$

$$+ \|\mathbb{K}\|\beta\exp\{-\frac{\beta}{\|\nabla\varphi_h^0\|}\}\frac{\nabla\varphi_h^0}{2\|\nabla\varphi_h^0\|^3}, \qquad \text{else}$$

$$\tilde{f}_{01}(\varphi_h^0, N_h^0) = 0,$$

$$\text{if } \|\nabla\varphi_h^0\| < \frac{10^{-2}}{\beta} \text{ or } \|\mathbb{K}\| < \frac{1}{2}\alpha\exp\{-\frac{\beta}{\|\nabla\varphi_h^0\|}\}$$

$$= \alpha\exp\{-\frac{\beta}{\|\nabla\varphi_h^0\|}\}\frac{\gamma N_h^0 \nabla\varphi_h^0 - \delta\nabla N_h^0}{2\|\gamma N_h^0 \nabla\varphi_h^0 - \delta\nabla N_h^0\|}, \text{ else.}$$

It is clear that $\tilde{f}$ is linear. Taking here $\varphi_h^j + \phi_h^j$ instead of φ_h, N_{eh}^j instead of N_h, $\varphi_h^{j-1} + \phi_h^{j-1}$ instead of φ_h^0, N_{eh}^{j-1} instead of N_h^0 and by proper choice of α, β, γ and δ, one easily gets the linear approximation of the ionization rate.

2.3.4 The reconstruction of $\mathbf{E}$, $\mathbf{V}_i$ and $\mathbf{V}_e$

In order to reconstruct the entities $\mathbf{E}$, $\mathbf{V}_i$ and $\mathbf{V}_e$, we use equations (2.1), (2.6) and (2.7), respectively. First, we define the approximate solution to (2.1) as a projection of $(\nabla(\phi_h^j + \varphi_h^j))$ on $\boldsymbol{L}_h$, i.e. as a function $\mathbf{E}_h^j \in \boldsymbol{L}_h$, $j = 0, \ldots, j_{max}$, satisfying for all $\tilde{\mathbf{E}}_h \in \boldsymbol{L}_h$

$$\int_\Omega \mathbf{E}_h^j \tilde{\mathbf{E}}_h dx = -\frac{k_B T_e}{e_c L}(\int_\Omega \nabla\phi_h^j \tilde{\mathbf{E}}_h dx + \int_{\Omega_{Air}} \nabla\varphi_h^j \tilde{\mathbf{E}}_h dx),$$

where ϕ_h^j is the approximate solution of (SDBD-0) and φ_h^j is the first component of approximate solution of (SDBD-1).

Now, we have to proceed more cautiously in reconstructing $\mathbf{V}_i$ and $\mathbf{V}_e$ has to be more cautious. Since the precomputed particle densities N_{ih}^j and N_{eh}^j may be of zero value, equations (2.6) and (2.7) become meaningless at some parts of the domain (there might be no particles to track). This may make our task harder since we work within computer

arithmetic: the values might not be equal to zero but just close to the machine epsilon. This may lead to absurd values of particle velocities.

Therefore, we employ a simple heuristic "where there are a few particles, there is no movement." We define a minimal amount of particle coefficient N_{min}. Further, we define the approximate solution to (2.6) as a function $\mathbf{V}_i^{hj} \in \boldsymbol{L}_h^{Air}$, $j = 0, \ldots, j_{max}$, satisfying for all $\tilde{\mathbf{E}}_h \in \boldsymbol{L}_h^{Air}$ and for all $K \in \mathcal{T}_h^{Air}$

$$\int_K \mathbf{V}_i^{hj} \tilde{\mathbf{E}}_h dx = \int_K \left(\mu_i \mathbf{E}_h^j - \frac{D_i}{L} (\nabla N_{ih}^j / N_{ih}^j) \right) \tilde{\mathbf{E}}_h dx,$$
$$\text{if } \int_K N_{ih}^j dx > N_{min}$$
$$= 0,$$
$$\text{if } \int_K N_{ih}^j dx <= N_{min}.$$

Analogously, we define the approximate solution to (2.7) as the function $\mathbf{V}_e^{hj} \in L_h^{Air}$, $j = 0, \ldots, j_{max}$.

2.3.5 Implementation of the numerical scheme

As stated in the introduction, we carried out the implementation in FEniCS environment, and we will describe the numerical scheme using pseudocode based on FEniCS libraries.

We start by describing of the numerical solution (*SDBD-0*) and (*SDBD-1*). First, let us note that all presented discrete problems are equivalent to a system of linear algebraic equations.

SDBD-0

We use the FEniCS in-built GMRES (Generalized Minimal RESidual) iteration method with ILU preconditioner to solve the system of linear algebraic equations. The absolute convergence criterion (based on the norm of residuum) for GMRES is set to 10^{-9} with a maximum of 200 iterations [22].

SDBD-1

We use a similar setting as for (*SDBD-0*), i.e. the FEniCS in-built GMRES iteration method with ILU preconditioner with the same criterion settings.

Reconstructions

Using the FEniCS method *project* (from *dolfin.fem.projection*), we implement the reconstruction algorithms and obtain approximative solutions.

2.3.6 Pseudocode of main scheme

Now the main algorithm scheme is as follows:

timestamp$_{\text{SDBD}}$ = $\Delta \tau$

while timestamp$_{\text{SDBD}} \leq T$:

    Solve (*SDBD-0*) at timestamp$_{\text{SDBD}}$

    Compute coefficients for $\tilde{f}_e$

    Solve (*SDBD-1*) at timestamp$_{\text{SDBD}}$

    Compute reconstructions at timestamp$_{\text{SDBD}}$

    timestamp$_{\text{SDBD}}$ += $\Delta\tau$

2.3.7 Numerical results

Numerical examples illustrating the above-described approach can be found in [22], [23], see also Appendices A.5 and A.6. Figs. 2.9 - 2.10 show calculated trajectories of electrons and ions at the time, $T = 18$ ns, with corresponding V_i and V_e velocities. The colour of individual parts of the trajectories signifies the magnitude of velocity. For better clarity, only trajectories between two neighbouring strips are shown close to their tips.

It should be pointed out that these trajectories depict only the state during the initial phase of the positive half-period of driving voltage. Proceeding from a comparison of the trajectories of electrons and ions, it can be concluded (see Fig. 2.11) that electrons do not extend as much from the edge of the strips as ions do.
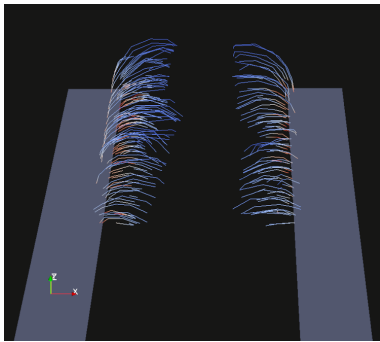
Figure 2.9: Trajectories and velocities of ions V_i at time 18 ns.
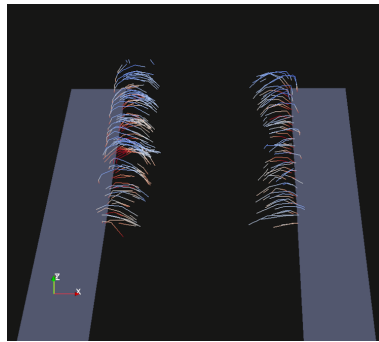
Figure 2.10: Trajectories and velocities of electrons V_e at time 18 ns.
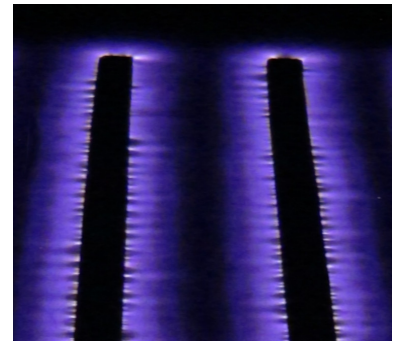
Figure 2.11: Luminous region around the strip electrode.

This trajectory of the relevant particles could be associated with the luminous region around the strip electrode, depicting the active volume of the discharge. Therefore, this result could be used to optimize the distance among neighbouring strips. This, in turn, would have a strong impact on the design of the electrode system. The practical implications are apparent in Section 2.4 and Chapter 3.

2.4 Comparison of the suitability electrode systems for O_3 and UV generation

In the following text, the appropriate choice of the relevant electrode system for O_3 and UV generation is introduced. This chapter is based on the knowledge published in [20] and available in Appendix A.2, where we tested two active electrode setups created on the upper side of the Alumina plate. The first one, the strip active electrode was formed by 14 strips, each 59 mm long and 1 mm wide, made of a 0.035 mm thin copper foil. The distance between adjacent strips was 3 mm. This electrode was glued to the Alumina plate. The capacitance of the electrode system containing this active electrode was 202 pF.

The second active electrode setup consisted of a stainless steel wire mesh with square cells of inner dimensions 1×1 mm. The wire used for the mesh had a diameter of 0.4 mm. Due to the structure of the mesh the wires touched the Alumina plate surface at points of intersections of the orthogonal wires. The capacitance of the electrode system with the mesh active electrode totalled 103 pF.

Sinusoidal driving voltage of frequencies 4, 7 or 10 kHz was applied. The concentration of ozone at the output of the discharge chamber was measured by the absorption of a 254 nm UV spectral line with an API 450 ozone monitor. The accuracy of ozone concentration measurements was $\pm 0.5\%$. We measured discharge UV emission for the wavelengths of 320 to 420 nm, using the AccuMAX UV monitor. An XS-365 sensor of the diameter of 21.6 mm was employed for a range of intensities of 0-100 mW/cm². For UV intensities measurements, the upper Plexiglas window of the discharge chamber was removed and replaced with a window with an opening in which a tube of the inner diameter of 36.5 mm was inserted. The centre of this tube coincided with the centre of the active electrode. A UV sensor was placed at the end of this tube at a distance of 63.5 mm from the upper side of the Alumina plate so that the UV peak intensities were obtained by registering the radiation emitted directly by the discharge. Full description of the setup was published in [20] and is available in Appendix A.2.

The microdischarges originating at the strips can freely develop and terminate between the strips. This is shown by the occurrence of the dark region in the middle between adjacent strips (see Section 2.3 in Chapter 2 and Appendices A.5 and A.6 and Fig. 2.12). However, partial suppression of microdischarges originating from the strips and the perpendicular part of the electrode connecting the strips can be observed at the corners when the strips meet with the connecting part of this active electrode (see Fig. 2.12). This suppression is illustrated by the darker triangle-shaped regions at these corners.

These triangles and darker regions between two adjacent strips could be seen in the zoom image of the discharge in Fig. 2.12a and also appeared in [20], available in Appendix A.2. If consecutive strips are close to each other or the electric field is too strong (see Fig. 2.12b), their electric fields overlap and the homogeneous dark region is damaged together with the microdischarges.

As for the discharge with the mesh active electrode setup, the electrode was made of stainless steel wire. Due to the structure of the mesh, the wires touched the Alumina plate

(a) Homogeneous region.

(b) Region with overlapped electric fields.
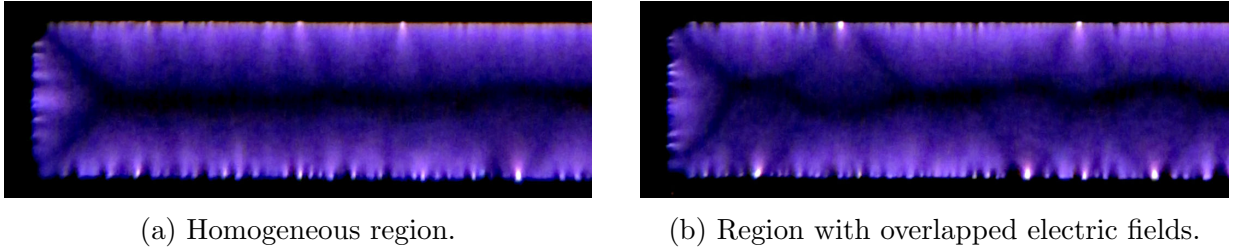
Figure 2.12: Darker regions between two adjacent strips.

surface at points of intersections of orthogonal wires, which resulted in the production of plasma, manifested not only by the surface but also by the volume dielectric barrier discharge. The detailed analysis of the physics of various configurations of the dielectric barrier discharges is given in [47].

In most gases at about atmospheric pressure, the typical DBD systems are characterized and initiated by a large number of independent current filaments or microdischarges. Their existence is accompanied by current pulses.

These microdischarges can be described as weakly ionized plasma channels (Cf. Chapter 2.3 and published in [22], [23] in Appendices A.5 and A.6). The number of microdischarges per unit of electrode area and time depends on discharge voltage. The strength of the microdischarge, which can be defined by the energy deposition in the microdischarge channel, is determined by discharge energizing, the type and properties of the feeding gas, gap spacing, and the properties of the dielectric or the metal electrode. In addition to radiation and collisional gain and loss, drift and diffusion, the convection of particles due to the neutral gas flow also contributes to the particle balance of charged and excited species in the microdischarge. Thus, temperature and gas flow are also important control parameters of the microdischarges. We focused on these quantities in [21], [26], available in Appendices A.3 and A.8. These articles are discussed in Chapter 3.

2.5 Summary

The obtained findings can be summarized as follows:

○ When applied voltage amplitude or applied voltage frequency increases, the filament rate, current peak amplitude, and simultaneously the dissipated energy in the DBD system rise as well.

○ The amplitude of the filaments seems to be strongly dependent on the space available to plasma for expanding laterally around the electrodes. Indeed, if consecutive strips are close to each other, their electric fields overlap (see Fig. 2.12b).

○ Due to the small dimensions of the mesh cells, the development of microdischarges from each side of the square cell was suppressed. It could be, therefore, said that when the geometry of the active electrode does not allow for full development of

microdischarges, and volume and surface discharge occurs concurrently, the visual appearance of the discharge is changed in comparison with the discharge featuring the geometry of the active electrode with fully developed microdischarges; at the same time, generation of O_3 by the mesh electrode decreases.

Non-electrical parameters of the discharge

Generation of ozone from air by an electric discharge is a complex process, which, apart from electrical parameters of the discharge, material of electrodes, pressure, humidity, and so on, depends mainly on air temperature and air flow in the discharge chamber. Out of the many fundamental non-electrical phenomena, we focused on the two quantities most heavily influencing the formation of microdischarges: on the temperature, and direction (character) of airflow.

3.1   Temperature effect on SDBD

Air temperature in the reaction space depends on the temperature and efficiency of the cooling system, heat transfer conditions (heat removal, direction of input, output, airflow through the chamber), and the total energy channelled into the SDBD system. Air temperature determines not only its thermodynamic properties but also the coefficients of reactions leading to both ozone generation as well as to its destruction in air-fed ozone generators. This Chapter 3.1 is based on our published articles [21], [26] in Appendices A.3 and A.8.

Ozone generation from air by SDBD constitutes a complex process involving many ozone formation and ozone destruction reactions. There are different models of this mechanism, which differ mainly by the number of species and reactions involved ([15], [54]–[56]).

Generally speaking, the mechanism of ozone generation by an electric discharge in air is rather complex due to the presence of nitrogen in the air. The presence of nitrogen causes ozone destruction processes because of the existence of nitrogen oxides. The simple model of ozone formation from air involves the following reactions. The initial step is the electron impact dissociation of molecular O_2 and N_2.

The initial step in the formation of O_3 and NO_x is the electron impact dissociation of molecular O_2 and N_2:

$$e + O_2 \rightarrow O + O + e \tag{3.1}$$

$$e + N_2 \rightarrow N + N + e \tag{3.2}$$
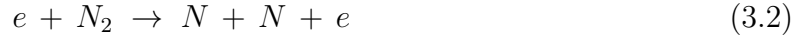
The threshold electron energy for molecular oxygen dissociation is 6 eV or 8.4 eV. Similarly, the threshold electron energy for nitrogen molecular dissociation is 6.17 eV or 7.35 eV [57].

Atomic nitrogen reacts with O_2 and O_3 to form NO by the reactions:

$$N + O_2 \rightarrow NO + O \tag{3.3}$$

$$N + O_3 \rightarrow NO + O_2 \tag{3.4}$$

NO and NO_2 form a cycle for ozone destruction by the reactions:

$$O + NO_2 \rightarrow NO + O_2 \tag{3.5}$$

$$NO + O_3 \rightarrow NO_2 + O_2 \tag{3.6}$$

NO_2 is consumed by the following reactions:

$$NO_2 + O_3 \rightarrow NO_3 + O_2 \tag{3.7}$$

$$NO_2 + NO_3 \rightarrow N_2O_5 \tag{3.8}$$
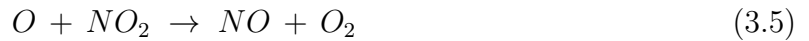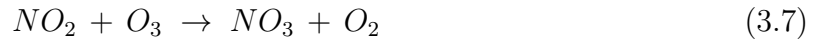
and regenerated by the reactions:

$$NO + NO_3 \rightarrow NO_2 + NO_2 \tag{3.9}$$

$$N_2O_5 \rightarrow NO_2 + NO_3 \tag{3.10}$$

$$O + N_2O_5 \rightarrow NO_2 + NO_2 + O_2 \tag{3.11}$$
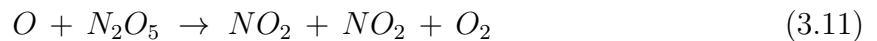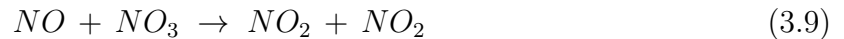
The principal ozone formation reaction dominant at high pressures (atmospheric) is given below:

$$O + O_2 + M \rightarrow O_3 + M \tag{3.12}$$

An undesirable reaction, which determines the upper limit of O concentration, is as follows:

$$O + O + M \ \rightarrow \ O_2 + M \tag{3.13}$$

M is the third collision partner. In case of discharge in air M represents molecular oxygen or nitrogen.

There are definitely other different reactions destroying ozone. One example of catalytic reaction destroying ozone is:

$$NO_2 + O_3 \ \rightarrow \ NO_3 + O_2 \tag{3.14}$$

$$O + NO_3 \ \rightarrow \ O_2 + NO_2 \tag{3.15}$$

The presented enumeration is simplified as it does not include the reactions involving excited species, other molecules or other ozone self-destruction reactions.

Appropriate rates of individual reactions depend on various parameters, for example, on electric field, temperature or pressure. Temperature, or more precisely temperature distribution in the discharge chamber, can be affected by varying air input into the discharge chamber. Thus, for example the main ozone formation reaction dominant at atmospheric pressure is reaction No. (3.12). In this particular case, the reaction rate dependence on gas temperature T_g is given by the following expression:

$$k = 2.5 \cdot 10^{-35} \cdot \exp^{\left(\frac{970}{T_g}\right)} \tag{3.16}$$

where k is in $cm^6 \cdot s^{-1}$.

This expression 3.16 shows that the reaction rate of ozone generation decreases with rising gas temperature.

Unlike ozone generation, NO_x formation is expedited by heat and is linked with discharge path temperature. Thus, for instance, reaction No. (3.6) is significantly enhanced by increasing gas temperature.

$$k = 1.5 \cdot 10^{-12} \cdot \exp^{-\left(\frac{300}{T_g}\right)} \tag{3.17}$$

where k is in $cm^3 \cdot s^{-1}$.

For example: for the ozone formation reaction No. (3.12), an increase in temperature from 10°C to 20°C causes a 10% decrease of this reaction rate. On the other hand, the same change of temperature for the NO_x formation reaction No. (3.6) gives rise to an increase of this reaction rate by 16%. Obviously, discharge ozone production results from the reaction rates of all the individual reactions involved in the process. Increasing gas temperature substantially reduces ozone generation processes.

In the context of the dominant reactions leading to ozone generation and destruction, it should be pointed out, however, that the role of particular reactions resulting in ozone generation and destruction varies with the temperature of the gas used. Thus, according to [56], for a temperature of air gas lower than 350 K, the dominant reaction for ozone loss is described by the following reaction:

(a) Ozone formation. (b) Ozone depletion.
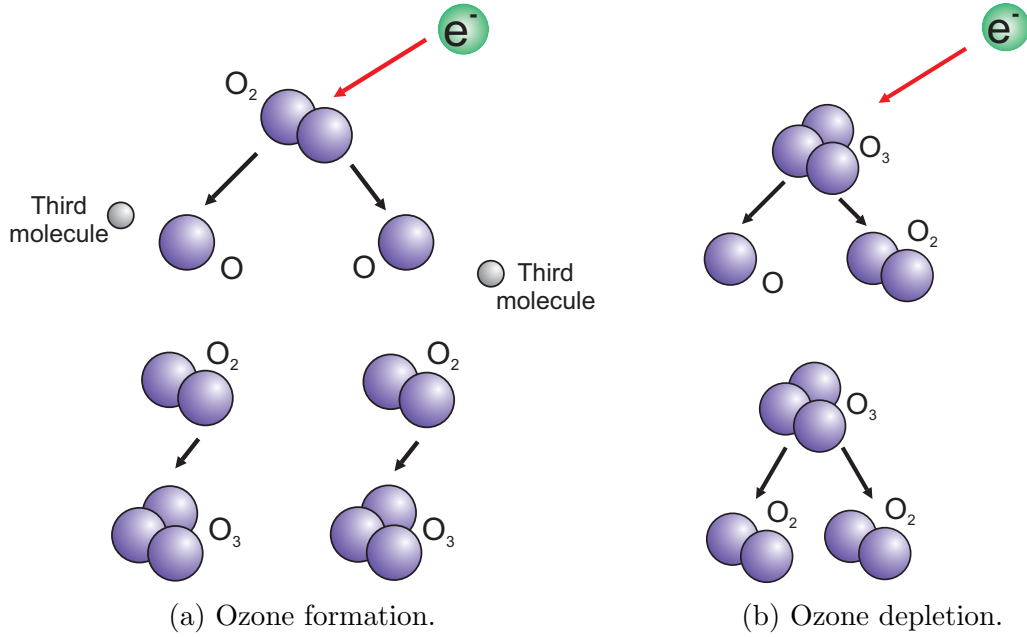
Figure 3.1: The main reactions leading to ozone generation and depletion.

$$e + O_3 \rightarrow O + O_2 + e \qquad (3.18)$$

for which the reaction rate coefficient is $k = 5.88 \cdot 10^{-9}$ in $cm^3 \cdot s^{-1}$ [58].
An extremely fast reaction that depends steeply on temperature is:

$$O_3 + O \rightarrow O_2 + O_2 \qquad (3.19)$$

for which the reaction rate coefficient according to [59] is:

$$k = 1.8 \cdot 10^{-11} \cdot \exp^{-(\frac{2300}{T_g})} \qquad (3.20)$$

.

The dissociation rate coefficients of O_2, N_2, and O_3 by electron impact depend on the energy distribution of electrons in the discharge (both in space and time). These coefficients are represented as a function of electric field strength per unit gas density (E/N) [15]. According to [12], the optimum reduced electric field for ozone generation from air at atmospheric pressure is about (E/N) $\sim$ 200 Td; this process takes about 100 µs.

The process of ozone synthesis (and its decomposition) occurs at temperatures higher than the temperature of the gas involved. It proceeds in the discharge channels in which the temperature T (see reactions No. (3.12), No. (3.19), and No. (3.13)) during the short time after the decay of the electron passage is several dozens of degrees higher [59]. More details about the temperature effect with related links to the cited articles can be found in [21], [26] in Appendix A.3 and A.8.

3.2   Interaction of SDBD with low speed airflow

Interaction of DBD with the surrounding environment represented by feeding gas has a non-negligible effect not only on ozone generation but also on the formation of other active ionized species and on discharge stability.

Since ozone is formed mainly in microdischarges [14], the change in the number of microdischarges and their properties will result in a change of discharge ozone production. Therefore, controlling plasma conditions inside the microdischarge columns is of great importance for optimizing the reaction kinetics of ozone formation.

The overall yield of plasma processes in DBDs is determined by the multitude of discharges, while the properties of a single discharge determine the main processes. That is why it can be said that DBD is characterized by conversion of electric field energy to chemical or physical processes or heating of the gas or surfaces, and the effectiveness of special application of DBD crucially depends on the dynamics of charge transfer within the discharge [1]. While the energy of the electrons is put to use for chemical and physical purposes, the energy of ions controls the stability of the discharge. This energy conversion efficiency is governed by the total amount of energy released in the discharge volume per unit of time. This quantity, expressed as power density, depends on electric field strength and on current density, and is described by the following equation 3.21.

$$p = \mathbf{j}.\mathbf{E} \;\; (W/m^3) \tag{3.21}$$

The current density $\mathbf{j}$ can be expressed by the following equation:

$$\mathbf{j} = \pm \mu N \mathbf{E} - D \nabla N + \mathbf{v} N \;\; (A/m^2) \tag{3.22}$$

In this expression 3.22, $N = e.n$, denotes the density of charged particles, μ refers to charged particles mobility, $\mathbf{E}$ designates electric field, $\mathbf{v}$ denotes local velocity, and D stands for the diffusion coefficient.

Application of the flow to the discharge can affect all three terms in the expression for current density and, consequently, energy transformations in the microdischarges. The airflow through collisions of the neutral particles with ions affects microdischarges dimensions as well as the mixing of the gas. This influences the size of the region in which the plasma-chemical processes occur. Obviously, an important role in these processes is played by flow velocity, uniformity of the flow in the discharge chamber, number of microdischarges (which is determined by the electrical parameters of the discharge and geometry of the active electrode), and also orientation of the flow with respect to the microdischarges. When airflow is oriented perpendicularly to the microdischarges, their radius is effectively influenced, and, proceeding from our published results in [21], [22], [26], [60] in Appendicies A.5, A.3, A.7, A.8, there is a maximum impact of the flow on plasma-chemical processes. Unfortunately, as is often the case with plasmas, one external parameter, such as orientation of gas flow with respect to the microdischarges, affects multiple aspects of the discharge simultaneously [61]. Thus, the overall yield of plasma-chemical processes in the discharge is given by the synergy among all the above-mentioned properties.

As a result, we focused on exploring the impact of airflow direction on the amount of generated microdischarges, and thus on affecting the plasma-chemical reactions leading to the development of O_3 concentration.

3.2.1 Perpendicular versus parallel airflow with respect to the microdischarges

Based on the above-mentioned facts, we tested in [21]–[23], available in Appendices A.3, A.5, and A.6 different directions of the feeding gas with respect to the geometry of the high-voltage active electrode.

Subsequently, for two mutually orthogonal directions of the feeding gas flow, i.e. the parallel direction and the perpendicular direction to the electrode geometry (or more precisely, perpendicular to the microdischarges and parallel to the microdischarges), we carried out a detailed verification of its effect.

An axisymmetric geometry, cut from aluminium foil (see Fig. 3.2) and glued with electroconductive glue to an Alumina plate, served as a high-voltage electrode. In order to comply with the conditions of orthogonality, a chamber with eight inputs and outputs of the feeding gas was printed, using 3D printing to make sure that the inputs and outputs were directed into the eight spaces equally between the individual electrode strips (see Fig. 3.3 and 3.4). For all our experiments we used 3D-printed PLA chambers that were tested for ozone resistance in [2], available in Appendix A.1.

The dependence of O_3 on the discharge power was measured for both configurations and is shown in Fig. 3.5. A striking difference between the parallel (blue curves) and perpendicular (red curves) flow to the given configuration of the electrode geometry can be seen in Fig. 3.5. This effect is significant up to the value of feeding gas flow of less than 6 l/min.

There are several contexts that can explain the impact of the difference in the parallel and perpendicular airflow orientation.

It is important to mention that the effects first published in [22] were observed in stronger electric fields represented by higher applied voltage when the discharge burned completely filamentarily. The electrode geometry was also not absolutely symmetrical. The ends of the electrode were not encapsulated (interconnected). To correct these inaccuracies, we repeated the experiment with an absolutely symmetrical electrode.

Fig. 3.7 shows the dependence on ozone concentration versus effective discharge voltage for an airflow of 2 slm, while Fig. 3.8 depicts the same situation with an 8 slm airflow. In both cases, both feeding gas directions were measured. The profound effect on ozone production in relationship with parallel or perpendicular airflow can be seen in Fig. 3.7. Vice versa, the second case is depicted in Fig. 3.8.

The species important for ozone formation include, among others, nitrogen ions involved, e.g., in the second positive system of nitrogen $C^3\Pi_u \rightarrow B^3\Pi_b$ and in the first positive system of nitrogen $B^3\Pi_b \rightarrow A^3\Sigma_u^+$. The lifetime of $A^3\Sigma_u^+$ is of the order of around 10^{-2} s and is much longer than the half-period of the discharge voltage. In our experiment,
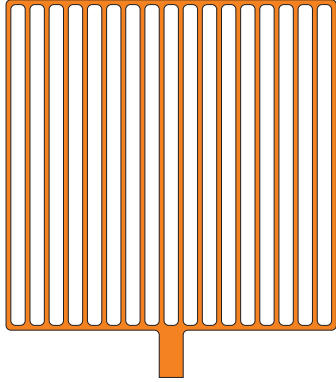
Figure 3.2: Symmetrical electrode.
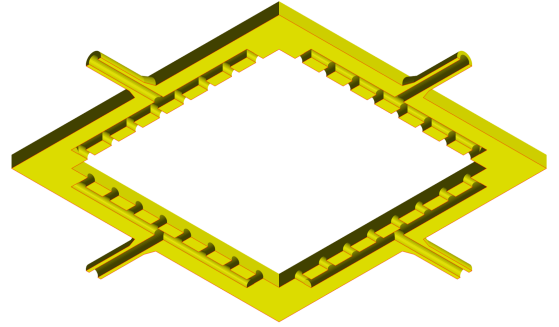
Figure 3.3: Horizontal cross-section of the symmetrical chamber.
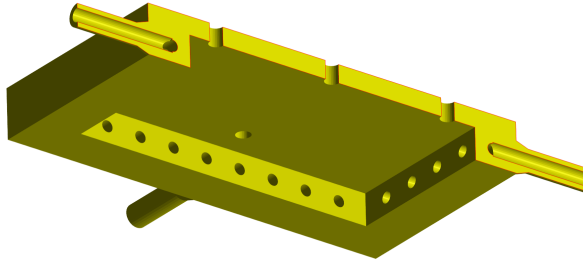
Figure 3.4: Vertical cross-section of the symmetrical chamber.

we used a 10 kHz alternating high-voltage signal. The metastable ions $A^3\Sigma_u^+$ form a reservoir of energy during discharge generation [9]. If airflow orientation is parallel with respect to the strip electrode (i.e., perpendicular to the microdischarge channels), the ions in this metastable state are removed from the area of discharge and are reused in a neighbouring microdischarge. The metastables move at a velocity equal to the speed of neutral molecules represented by airflow velocity.

If airflow is oriented perpendicularly with respect to the strip electrode, the ions in these metastable states are transferred within individual microdischarges (particles move in a parallel direction along the microdischarge length), they are not removed, but they can be absorbed by the dark region between the neighbouring strips. In our example, with airflow amounting to 2 slm and 12 slm, respectively, they moved in one half-period of applied voltage for a distance between 0.05 mm - 0.25 mm. These metastables further participate in subsequent collisions leading to ozone formation. We supported our conclusions by calculating the velocity field inside the symmetrical chamber (see Fig. 3.6).

The metastables also contribute to the coefficient of secondary electron emission γ, through the bombardment of the dielectric. If metastables are depleted, this results in a reduction of γ [9]. When γ decreases, filaments start at higher voltage values.

The second effect could be associated with the influence of airflow orientation on mi-
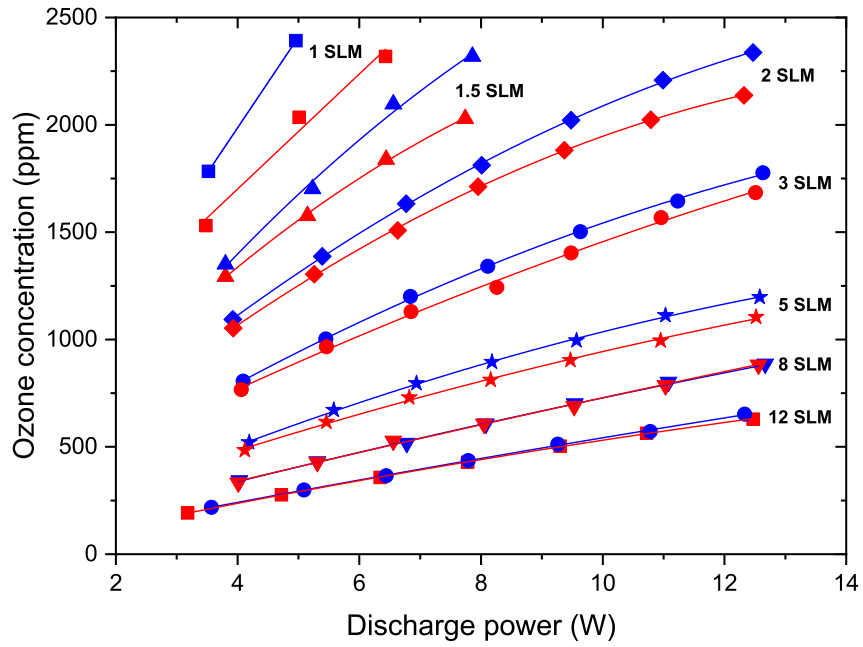
Figure 3.5: Ozone concentration versus discharge power for symmetrical electrode and relevant airflows.

(a) 2 SLM.

(b) 8 SLM.
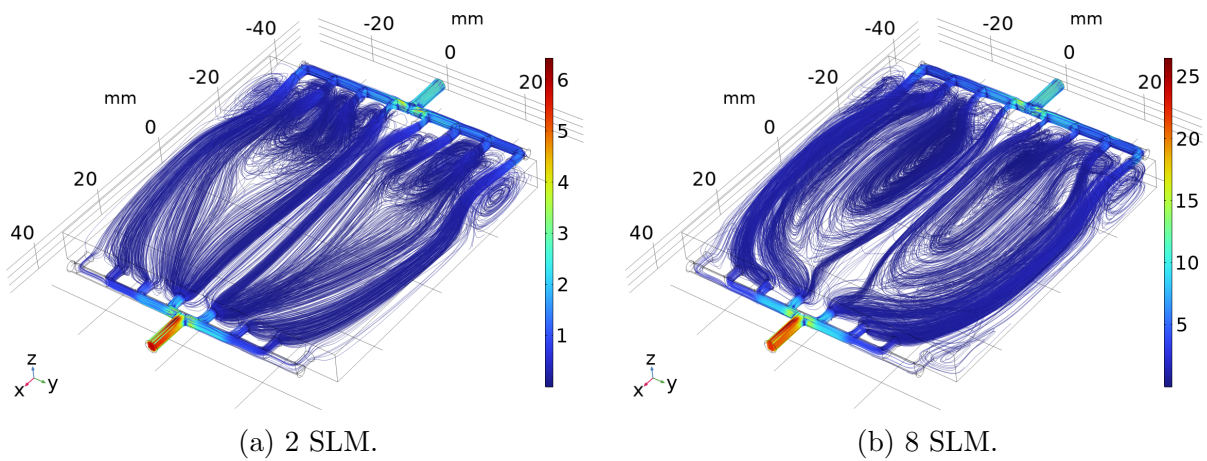
Figure 3.6: Numerical simulation of the velocity field in the symmetrical chamber.
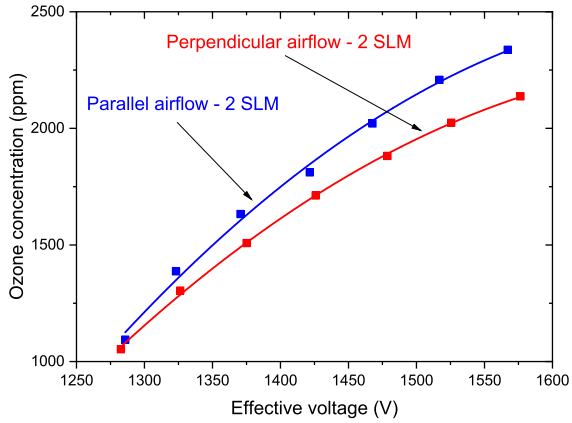
Figure 3.7: Ozone concentration versus effective discharge voltage for the airflow 2 slm.
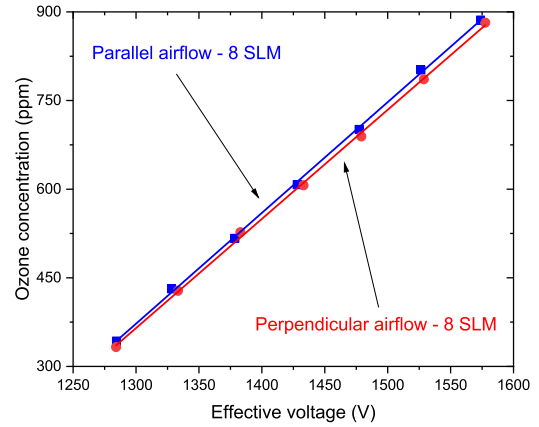
Figure 3.8: Ozone concentration versus effective discharge voltage for the airflow 8 slm.

crodischarge dimensions and consequently on the residence time. The longer the residence time, the higher the probability of dissociation of oxygen molecules into atomic oxygen, and hence the higher ozone generation. The residence time can be taken as a ratio of the dimensions of the region in which ozone generation occurs and air velocity. According to [14], ozone generation in dielectric barrier discharge takes place mainly in microdischarges. The microdischarge radius is approximately 100-200 µm and its length (depending on the polarity of the surface electrode) is of the order of a millimetre. As long as the magnitude of air velocity at a particular point of the discharge chamber is the same for both orientations of airflow, the residence time is influenced only by the dimensions of the microdischarge channels. The dimensions of the microdischarge channels could be changed due to the fact that the particles are carried by airflow. Thus, the relative change of the radius of the microdischarge for the case of parallel airflow with respect to the strip electrode is greater than the relative change of the length of the microdischarge channel for the case of perpendicular airflow with respect to the strip electrode.

As shown in Fig. 3.9, there is no substantial change in applied voltage by the constant input power as compared with our results published in [22]. It is vital to mention that we perform our experiment in a lower-applied voltage than in [22], because of the ozone monitor range. At low speeds and low applied voltage, the filament duration is very sensitive to the flow conditions and the charge transfer and management. The measured current contains the current associated with charge transfer and the displacement current in the gas gap. Complete ignition of the discharge cannot occur at low amplitude of the applied voltage. The electrical capacity, as well as the phase shift, change due to charge transfer. This situation is also obvious in Fig. 3.10 (C.f. [26] in A.8).

35
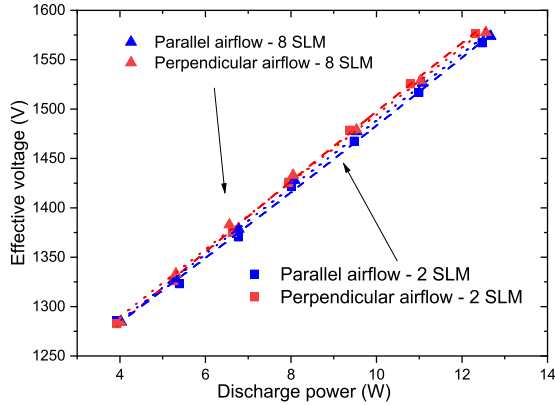
Figure 3.9: Effective voltage versus discharge power for the airflow 2 slm and 8 slm, respectively.
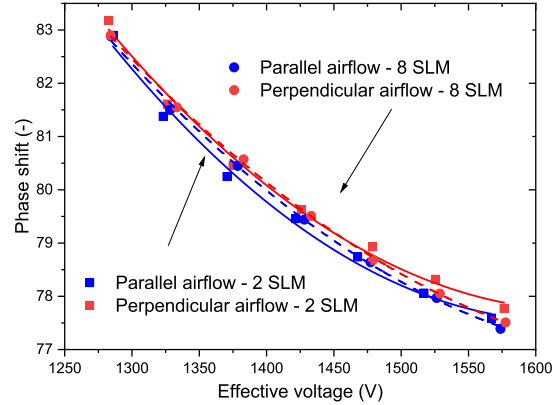
Figure 3.10: Phase shift versus effective discharge voltage for the airflow 2 slm and 8 slm, respectively.

3.3 Practical outcome for cylindrical ozone generators

Many commercial cylindrical ozonizers use only one air input – radial or axial. We, therefore, performed a detailed investigation of various air input effects on ozone synthesis in SDBD in a cylindrical configuration. Three different air inputs – radial, axial or tangential – were employed (see [26], [60] in Appendicies A.7 and A.8). We also investigated the role of changing the number of air input nozzles in the discharge volume from one to four (see Fig. 3.11 and 3.12). Furthermore, we also altered the geometry of the active electrode of the discharge from rings to strips, and finally, the experiments were performed with two different temperatures of cooling water and in the thermo box: 10°C, and 20°C, respectively.

Our experiments with both geometries (strips and rings) of the active electrode and all the air inputs were performed with the same discharge chamber. For both active electrode geometries, the tenet to keep the width of the active electrode and the distance between neighbouring strips/rings constant resulted in the different lengths of the strips and rings active electrode. The number of microdischarges originating from the active electrode increases with the discharge voltage, but it also depends on the active electrode's length [62]. The production of ozone and the number of microdischarges depend on the electrical parameters of the discharge.

Burning voltage is dependent on the speed and direction of airflow, especially if its streamline pattern is parallel to the electrode motive. Consequently, the relative change of radius of the microdischarge channels for the case of parallel airflow with respect to the ring electrode is also greater than the relative change of the length of the microdischarge channel for the case of perpendicular airflow with respect to this electrode, which results in different discharge ozone production (contrary to a strips electrode). Concurrently with the relative change of radius of the microdischarge channels, the type of discharge burning in the given channel changes as well.

36
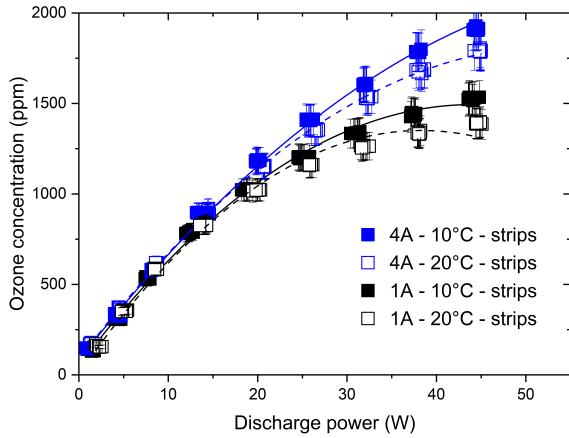
Figure 3.11: Ozone concentration for the strips active electrode, air inputs 1A and 4A and temperatures 10°C (full symbols) or 20°C (empty symbols).
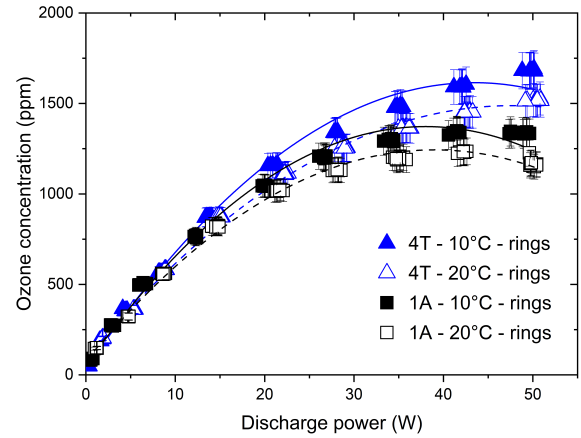
Figure 3.12: Ozone concentration for the rings active electrode, air inputs 1A and 4T and temperatures 10°C (full symbols) and 20°C (empty symbols).
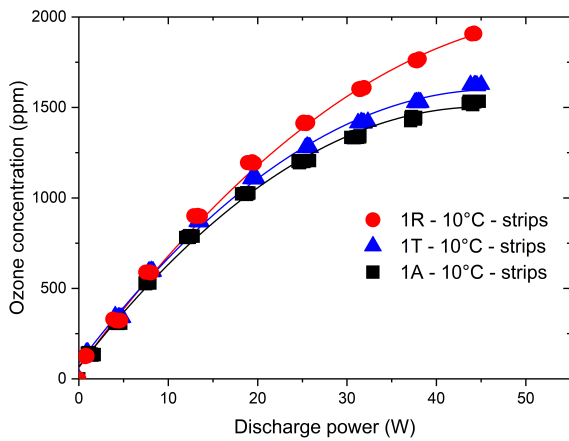
Figure 3.13: Ozone concentration versus instantaneous discharge power for the strips active electrode and one air input nozzle oriented radially (R), axially (A), and tangentially (T).
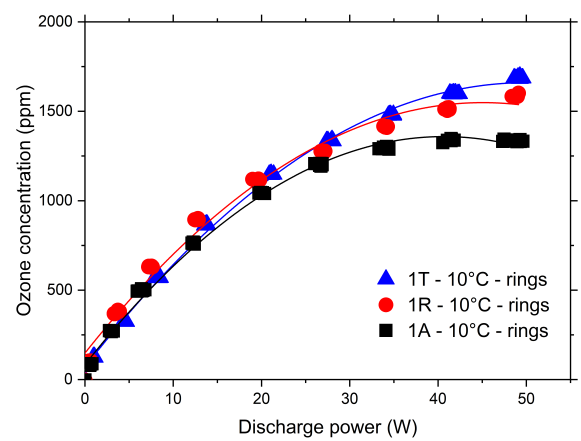
Figure 3.14: Ozone concentration versus instantaneous discharge power for the rings active electrode and one air input nozzle oriented radially (R), axially (A), or tangentially (T).

As long as the lengths of the rings and strips active electrode are different, it is impossible to compare ozone concentration and the electrical parameters of the discharge for the strips and rings active electrodes quantitatively (see Figs. 3.11, 3.12, 3.13, and 3.14). On the other hand, it is justified to compare quantitatively the effect of the way of air input (tangential, radial, or axial) through one or four nozzles for the strips or rings active electrode separately.

In keeping with the conclusion that for optimal ozone generation by dielectric barrier discharge, the streamlines should be perpendicular to the microdischarges, this fact should be reflected by the active electrode geometry. We, therefore, proposed two types of comparable active electrodes consisting of rings, inclined rings and axial strips (A-type – see Fig. 3.15 and B-type – see Fig. 3.16). Both electrodes have the same total length consisting of all individual segments, but a different proportion of parallel and perpendicular parts. The electrical capacity was, in both cases, also identical.
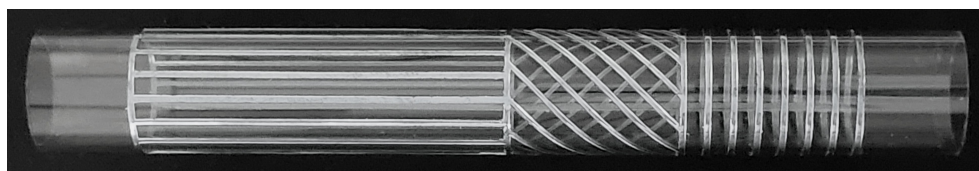
Figure 3.15: Geometries of the optimized cylindrical active electrode - A-type.
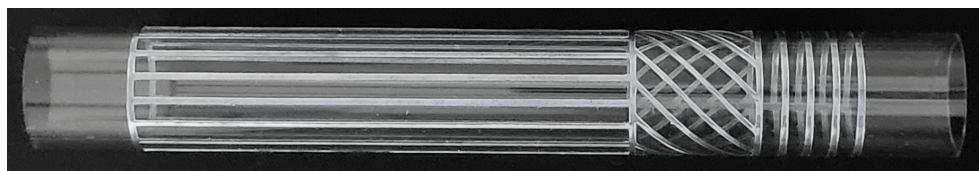
Figure 3.16: Geometries of the optimized cylindrical active electrode - B-type.

We monitored the importance of the longitudinal and transverse components of the flow on the amount of generated ozone. We used the tangential input of the feeding gas (air) into the cylindrical discharge chamber in order to create helical flow in its annular volume. Depending on airflow, the helical structure of the flow extends axially along the length of the discharge tube.

This study has been inspired by the results of numerical modelling of airflow with the help of COMSOL Multiphysics programme in the annular space in a cylindrical discharge tube with one tangential input. The following Fig. 3.17 shows the streamlines for airflow of 5 slm.

To make a proper choice of ozone generator it is necessary to perform a thoroughgoing analysis of the obtained results. For this purpose, it is important to fall back on the decisive parameters which turn out to be most useful for the particular applications. For some applications, these parameters involve the concentration of generated ozone, the mass
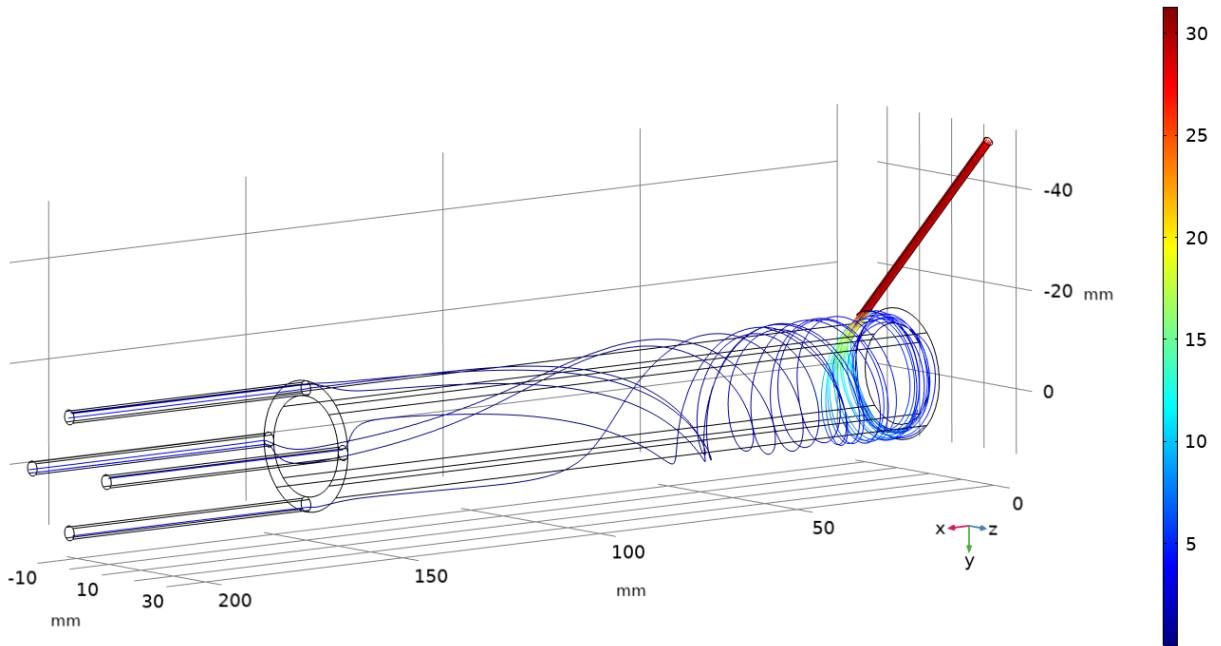
Figure 3.17: COMSOL Multiphysics streamline simulation for 5 SLM.
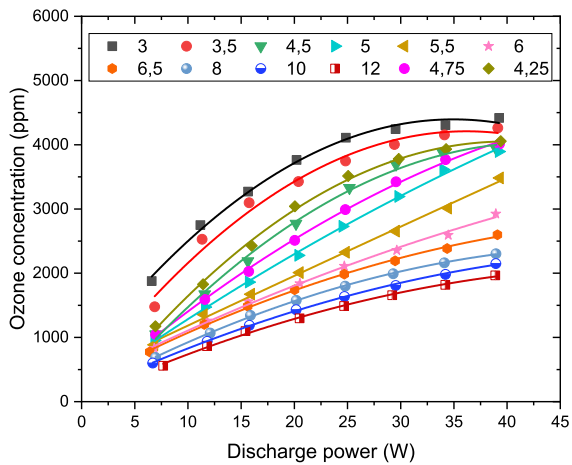
Figure 3.18: Ozone concentration versus instantaneous discharge power for the A-type electrode.
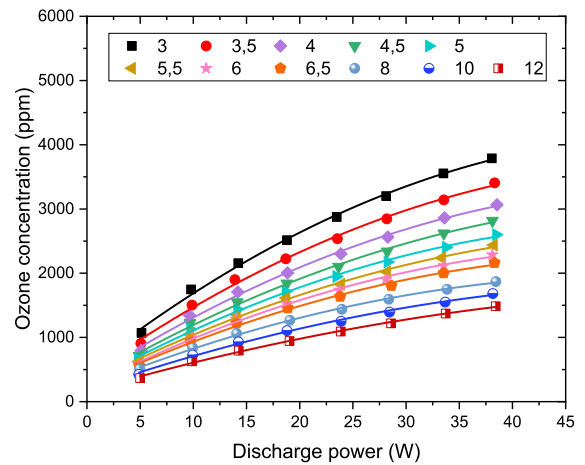
Figure 3.19: Ozone concentration versus instantaneous discharge power for the B-type electrode.

of the ozone produced per unit of time or the mass of the ozone produced per unit of energy. For other applications, the most important quantity is the ozone production yield, which spells out the mass of the generated ozone per unit of energy.

In many situations, these quantities are presented as a function of one of the independent parameters, e.g. concentrations of generated ozone as a function of discharge power. In our case, we examine generated ozone as a function of two parameters. Thus, we analyze the mass of the ozone generated per unit of time as a function of airflow through the discharge chamber and discharge power. The properties of the feeding gas are constant.

Proceeding from Fig. 3.18 and Fig. 3.19, it can be concluded that at lower feeding gas flow rates, when the significant effect of the difference between parallel and perpendicular flow still prevails, but at the same time, when the influence of helical flow at the beginning of the discharge chamber of the generator is still visible, a higher concentration of generated ozone can be achieved with an A-type electrode (Fig. 3.18) than under the same conditions with a B-type electrode (Fig. 3.19).
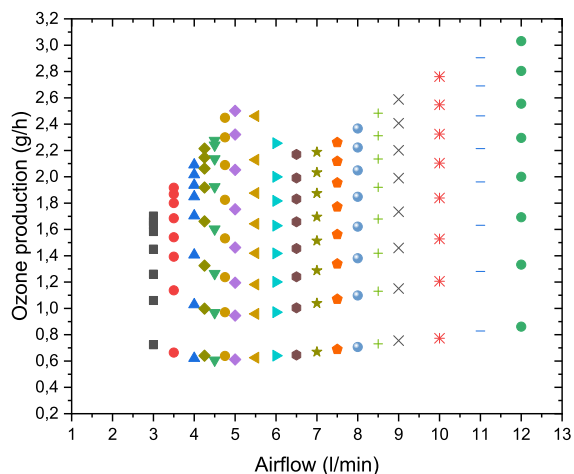
Figure 3.20: Ozone production versus airflow for the A-type electrode.
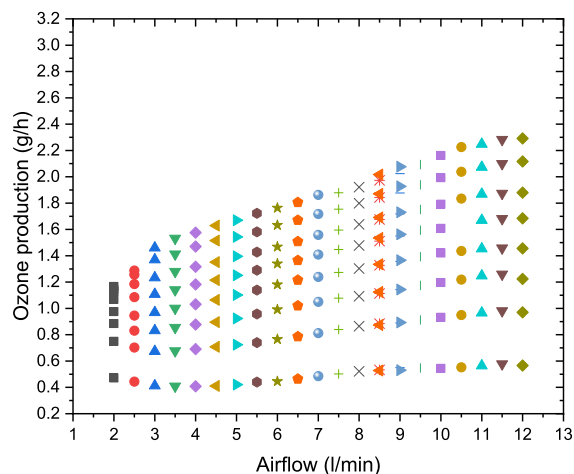
Figure 3.21: Ozone production versus airflow for the B-type electrode.

For A-type electrode, the first local maximum of ozone production occurs at about 5 slm (see Fig. 3.20). This situation was simulated by flow in the COMSOL Multiphysics programme (C. f. with Fig. 3.17). For A-type electrode, the geometry of the electrode in the radial and directionally orientated parts corresponds to the position of the transition from tangential to axial flow. In this way, all segments of A-type electrode are fully utilized. Meanwhile, under the same conditions, the radial part of the B-type electrode is significantly smaller and the local maximum would occur in the part before 1 slm (see Fig. 3.21).

Finally, Fig. 3.22 shows the difference in ozone production in time between two types of electrodes (blue area – A-type, red area – B-type). Proceeding from this particular Fig. 3.22, we can conclude that through the appropriate choice of all the electrode segments we can obtain significantly more of generated ozone per time unit under the same conditions

40
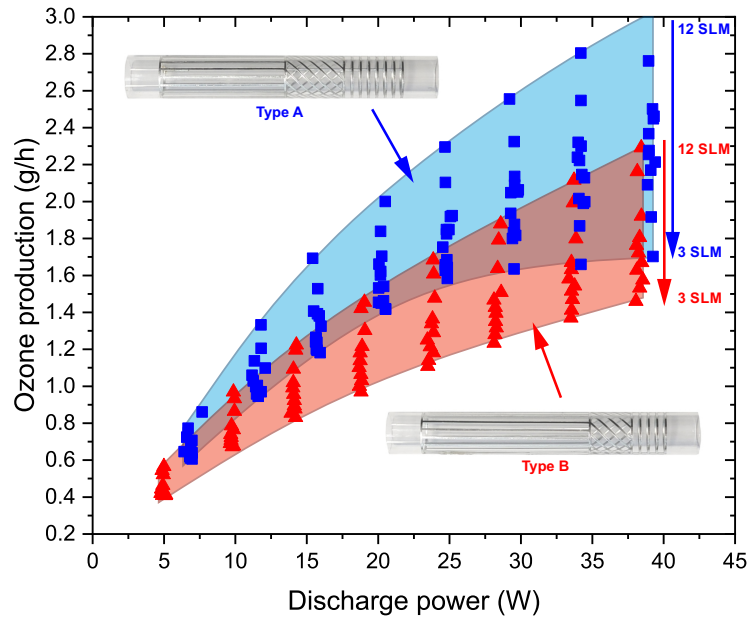
Figure 3.22: Difference in ozone production between two types of electrode systems (blue area - A-type, red area - B-type).

than by the same type B-type electrode. These conclusions are important for practical outcomes.

The effect of directional airflow in a cylindrical ozone generator with a tangential input was patented under Czech patent No. 308279, which is available in Appendix A.12

It is crucial to mention that, when feeding gas velocity is increased in a DBD system (after the disappearance of the effect of longitudinal and transverse flow), photoionization and photoemission are likely to become the predominant electron production mechanisms rather than ion or metastable bombardment of the cathode.

The overall schematic shape of the generator chamber is presented in Fig. 3.23, while the open final ozone generator prototype is shown in 3.24.
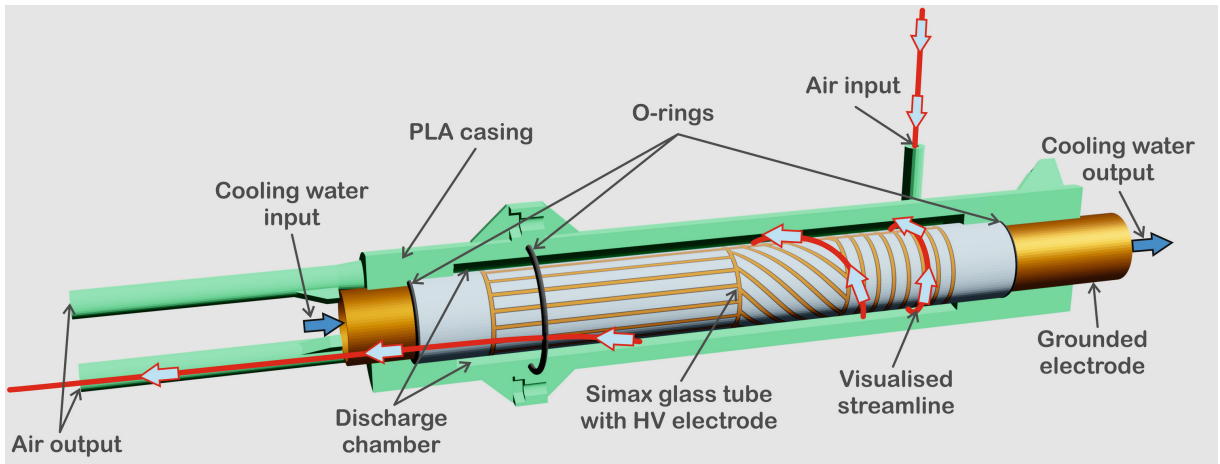
Figure 3.23: Ozone generator with optimized airflow patterns with microdischarge orientation.
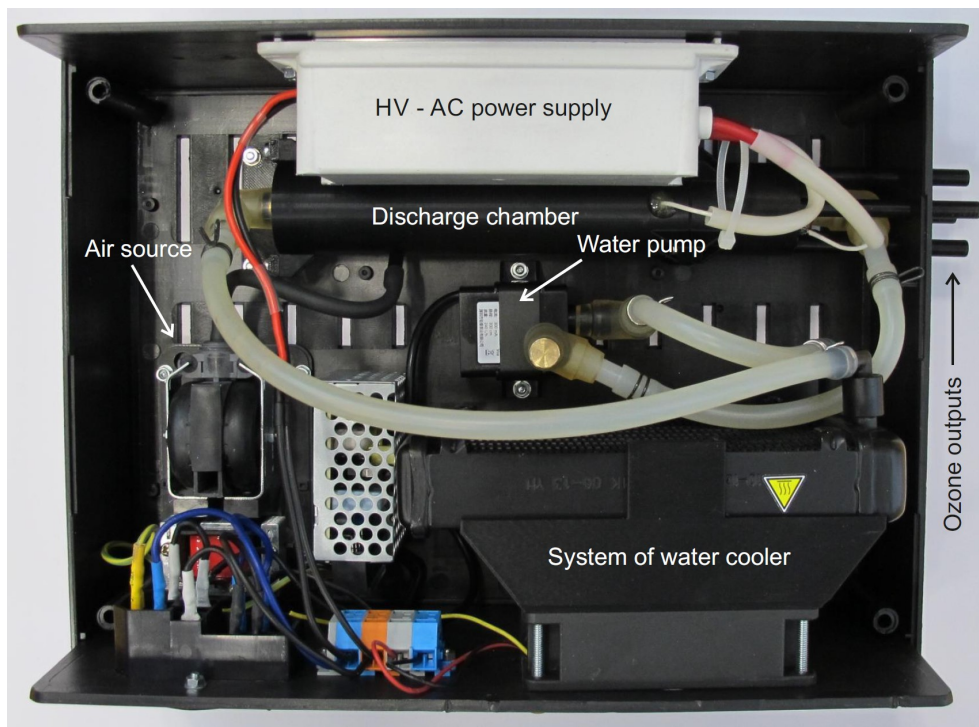
Figure 3.24: Proposal of ozone generator prototype.

3.4   Summary

We studied the effect of airflow orientation concerning the microdischarges and the impact of the number of air input nozzles, the direction of the input and output of air on ozone production, the shape of the electrode motive, and the electrical parameters of the surface dielectric barrier discharge in a planar and cylindrical configuration. Considerable attention was devoted to the most commercially available cylindrical ozone generators with one input dislocated axially, radially or tangentially.

The obtained findings can be summarized as follows:

- For the maximum effect of the flow on ozone concentration produced by the surface dielectric barrier discharge, the streamlines patterns should be predominantly oriented perpendicular to the majority of microdischarges.

- The streamlines patterns should be uniformly distributed in the discharge chamber volume. Their distribution can be controlled by the number and orientation of the input nozzles.

- Electrical parameters of the discharge are not so radically affected by air input for a particular geometry of the active electrode.

- Increase of temperature decreases discharge ozone production.

- The precise optimization of the interaction between the flow and microdischarges can help in designing more efficient ozone generators.

Photocatalytical effect on ozone generation by SDBD

Plasma-chemical processes occurring in non-equilibrium plasma of DBD are responsible for the generation of various active species, as well as electromagnetic radiation of various wavelengths. These discharge products, consisting of photons, electrons, positive and negative ions, free radicals, atoms, and molecules of gas, as well as electromagnetic radiation (visible light, photons, and UV) in excited and non-excited states, affect the efficiency of the aforementioned applications, and the process viability should be maximized in terms of energy efficiency and product selectivity.

There are several above-mentioned methods designed to boost the efficiency of ozone generation by DBD. Last but not least, an interesting alternative to these approaches is to use various catalysts that trigger plasma-catalyst interactions. In our published papers [24], [25], [63] in Appendices A.9, A.10, A.11 we focused our attention predominantly on TiO_2, ZnO, and $BaTiO_3$ photocatalysts.

Heterogeneous catalysts can be combined with nonthermal plasma produced by electrical discharge in two ways: by introducing the catalyst in the discharge zone [64], or by placing the catalyst behind the discharge zone [65], [66]. In both cases, the catalyst material can be in the form of coating, powder, granulates, coated fibres, or pellets.

The principle of this reaction, see Fig. 4.1, consists of the irradiation of the photocatalyst by electromagnetic radiation with the energy of photons higher than the forbidden energy gap. This irradiation can promote electrons from the valance band to the largely vacant conduction band. Simultaneously, a positive hole with strong oxidizing capability is formed. Electrons are capable of performing reduction reactions and holes can carry out oxidation reactions [67]. The chemical structure of the photocatalyst remains unchanged.

In the case of discharges in the presence of photocatalysts, the contribution of the surface reactions due to the activation of the photocatalysts by UV radiation emitted by the discharge should be added to the volume reactions.

For the discharges in air, the strongest emissions originate from the second positive system of nitrogen $C^3\Pi_u \rightarrow B^3\Pi_b$ which emits photons at a wavelength of 337.1 nm.
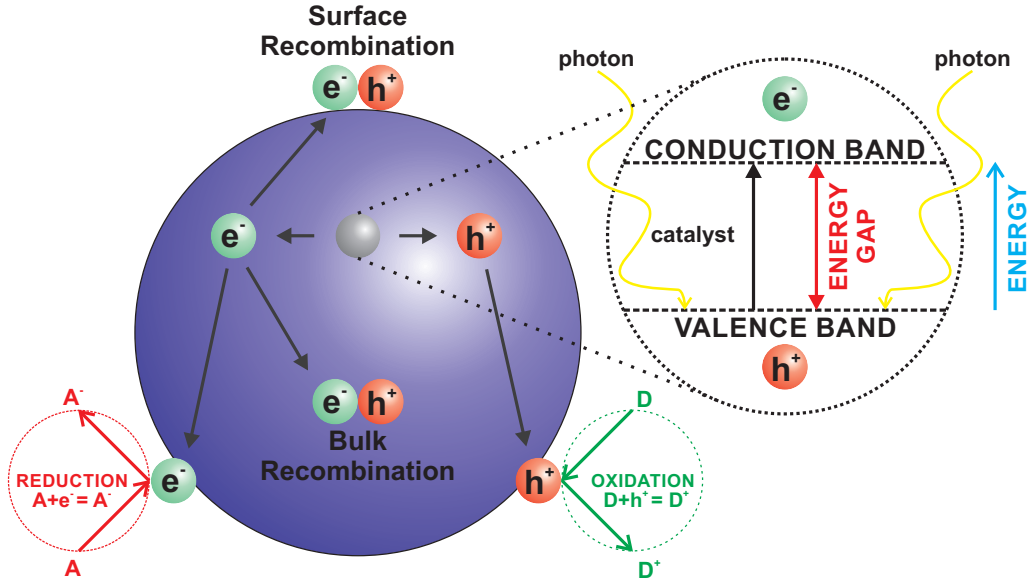
Figure 4.1: Basic mechanism of photocatalyst effect.

Thus, when the photocatalyst is illuminated by the UV light of these wavelengths, it becomes activated and the electron and positive hole can then react with the molecules in the vicinity of the catalyst. An example of the reaction of an electron with an oxygen molecule is the formation of the superoxide anion O_2^-:

$$e^- + O_2 \rightarrow O_2^- \tag{4.1}$$

From the equation 4.1 additional superoxide anions, other active oxygen species, such as O^-, O_3^{--}, and O_2^{--}, can be generated.

4.1 Most frequently used photocatalyst

The most frequently used photocatalyst for the enhancement of discharge ozone generation is TiO_2. This photocatalyst is an n-type semiconductor that can exist in several phases: TiO_2 in an anatase phase has a forbidden energy gap of 3.2 eV, TiO_2 in a rutile phase has a forbidden energy gap of 3.02 eV, and TiO_2 in a brookite phase has a forbidden energy gap of 2.96 eV [68]. The energy gaps of 3.2 eV and 2.96 eV correspond to electromagnetic radiation of the wavelengths of 387 nm and 414 nm, respectively.

Zinc oxide ZnO is an n-type semiconductor with an energy gap of 3.37 eV at room temperature [69]. This energy gap corresponds to electromagnetic radiation at a wavelength of 376 nm.

Barium titanate, $BaTiO_3$, is an electrical insulator in its pure form. However, when doped with small amounts of metals, it becomes an n-type semiconductor with an energy gap of 3.3–3.5 eV [70]. This energy gap corresponds to electromagnetic radiation wavelength of 375–353 nm.

46

Tungsten trioxide WO_3 is an n-type semiconductor with a bandgap of 2.6 eV (highly crystalline) to 3.3 eV (amorphous) [71]. The corresponding wavelengths are 476 and 374 nm. Moreover, the electrical and optical properties of the WO_3 can be changed by adding dopants, including metallic.

In addition to the selection of a suitable type of photocatalyst with an appropriate width of the forbidden band in relation to the emitted radiation, we also dealt with the issue involving the position of the photocatalyst in relation to the DBD in [24], [25]. The wavelengths contributing to the given photocatalysts are shown in Fig. 4.2.
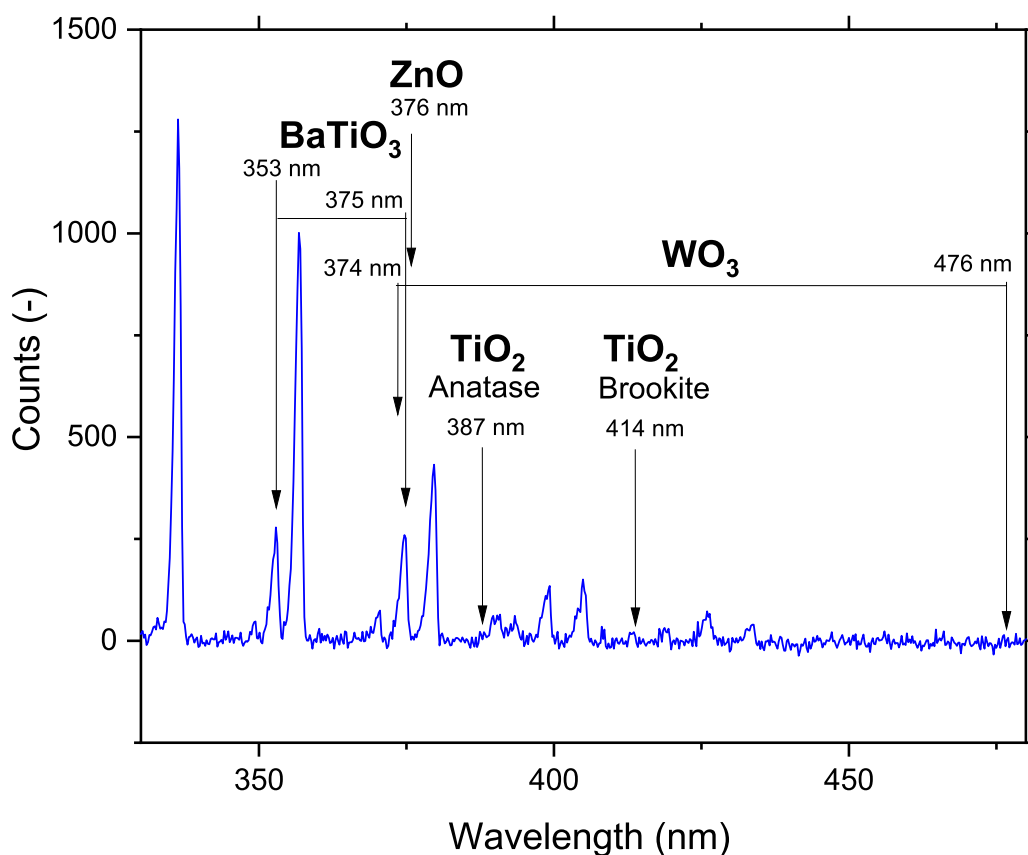
Figure 4.2: The surface dielectric barrier discharge spectrum in air for the wavelengths of 330 to 480 nm.

4.2 Photocatalyst adjustment

4.2.0.1 Area of catalyst interaction

To evaluate the photocatalytic activity of the catalysts, we compared the increment in the ozone concentration produced by the discharge, having placed the photocatalyst in the discharge chamber, in the first example on a plane parallel plate, and in the second case on

the plate with small pyramids compared with the state containing no photocatalyst. For more detail see [25] in Appendix A.11.

We concluded that the increment of the discharge ozone production is higher for plate with pyramids than for plates without pyramids, because of the larger active area with a photocatalyst. This situation is demonstrated by Fig. 4.3 and Fig. 4.4.
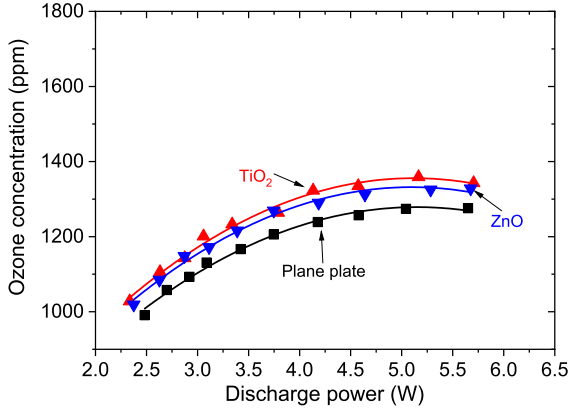
Figure 4.3: Ozone concentration versus discharge power for plate with introduced photocatalysts.
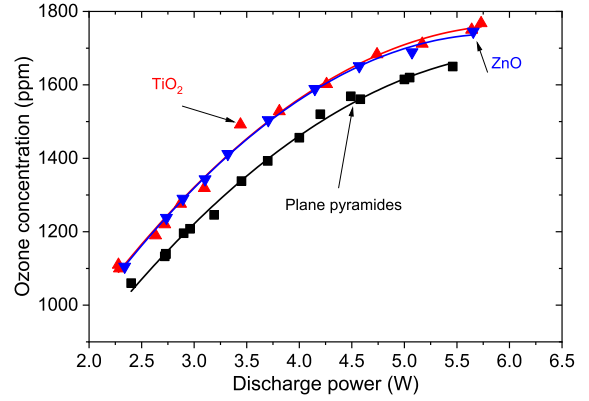
Figure 4.4: Ozone concentration versus discharge power for plate with pyramides and introduced photocatalysts.

4.2.0.2 Effect of TiO$_2$ on various regions of the active electrode

As a second factor affecting the generation of ozone concentration due to the presence of a photocatalyst, we studied the effect of TiO_2 on various regions of the active electrode on the electrical parameters of discharge, and on its emission spectra. When investigating the impact of TiO_2 on various regions of the active strip electrode on properties of the discharge, the TiO_2 layer covered either only the strips, the region between the strips, or the entire active electrode. All these cases are described by the Fig. 4.5.

We observed spectral lines attributed to the first positive system of nitrogen $B^3\Pi_b \rightarrow A^3\Sigma_u^+$ and we measured its intensity (see Fig. 4.6). For this system, the most intense peak is observed at the wavelength of 336.7 nm. It can be concluded that for all four situations, the emission spectra contain the same spectral lines, however with varying intensities. It is seen from Fig. 4.6 that the highest intensity is obtained for discharge with a layer of TiO_2 on the strip electrode (1988 a.u.); the second highest intensity is gained for discharge without any TiO_2 on the active electrode (1249 a.u.); this is followed by discharge with a layer of TiO_2 between strip electrodes (1013 a.u.); and the smallest intensity is obtained for discharge with a layer of TiO_2 on the entire area of the active electrode (807 a.u.).

Finally, covering the strips of the active electrode with a layer of TiO_2 increases average discharge current, enhances the intensity of spectral lines, and boosts the concentration of ozone produced by the discharge. This particular finding has an important practical impact for the construction of more efficient ozone generators. The concentration of ozone
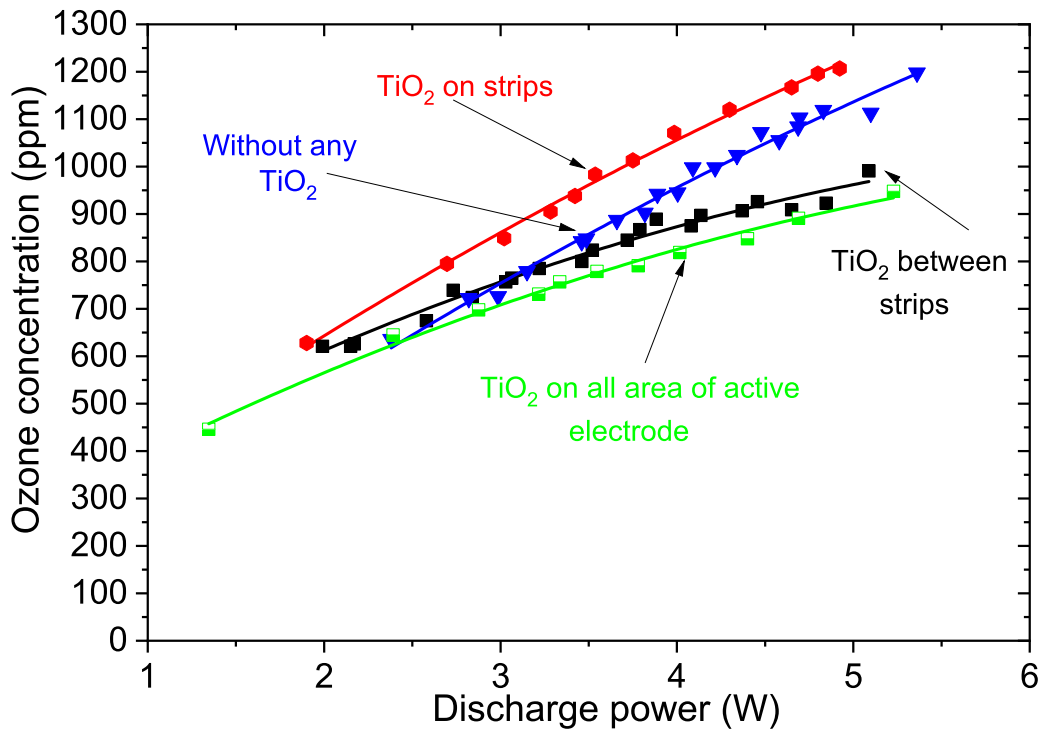
Figure 4.5: Ozone concentration versus discharge power for places with introduced photocatalysts.
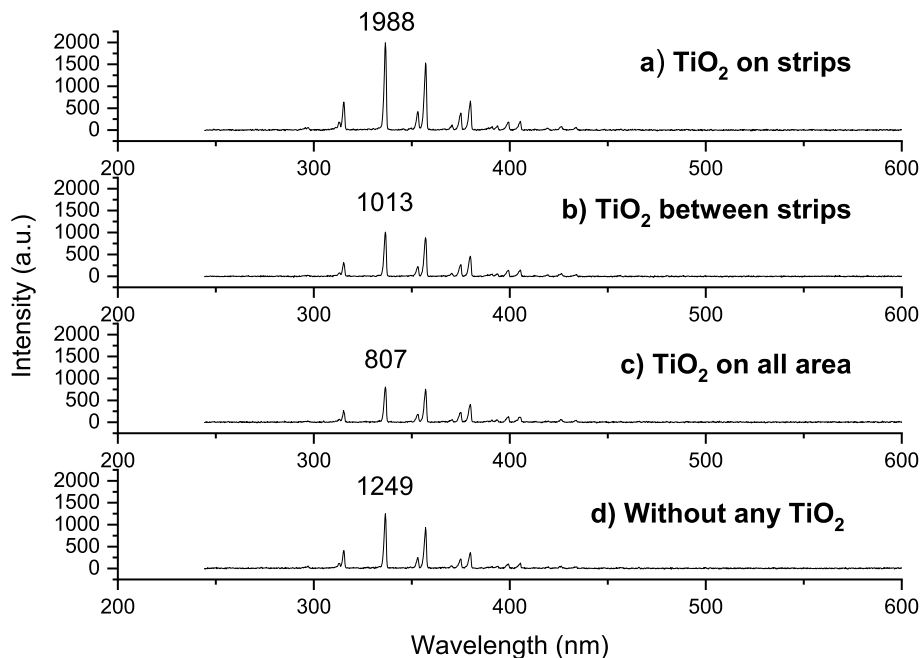
Figure 4.6: Emission spectra of the discharge with various regions of the active electrode covered by TiO_2.

produced by the discharge as well as discharge emission is the biggest among all the investigated cases. Similar results were also obtained in [72] in Appendix A.4, where we used a diamond layer on the mesh active electrode.

Covering the region between the strips of the active electrode with a layer of TiO_2 increases average discharge current, decreases the intensity of spectral lines, and reduces the concentration of ozone produced by the discharge. The average discharge current is the highest among all the investigated cases. In this example, an important role is played by the distribution of the electric field. Change of the dielectric constant of the Alumina plate in the region between the strips of the active electrode also acts on the expansion of the positive ion cloud in the positive half-period of the driving voltage.

Covering the entire area of the active electrode with a layer of TiO_2 increases average discharge current. Intensity of the spectral lines, as well as the concentration of ozone produced by the discharge, are the smallest among all the investigated cases.

The last two cases are close to CDBD with their properties, but the mechanical stability of the coplanar layer is low and unsuitable for a practical long-term use.
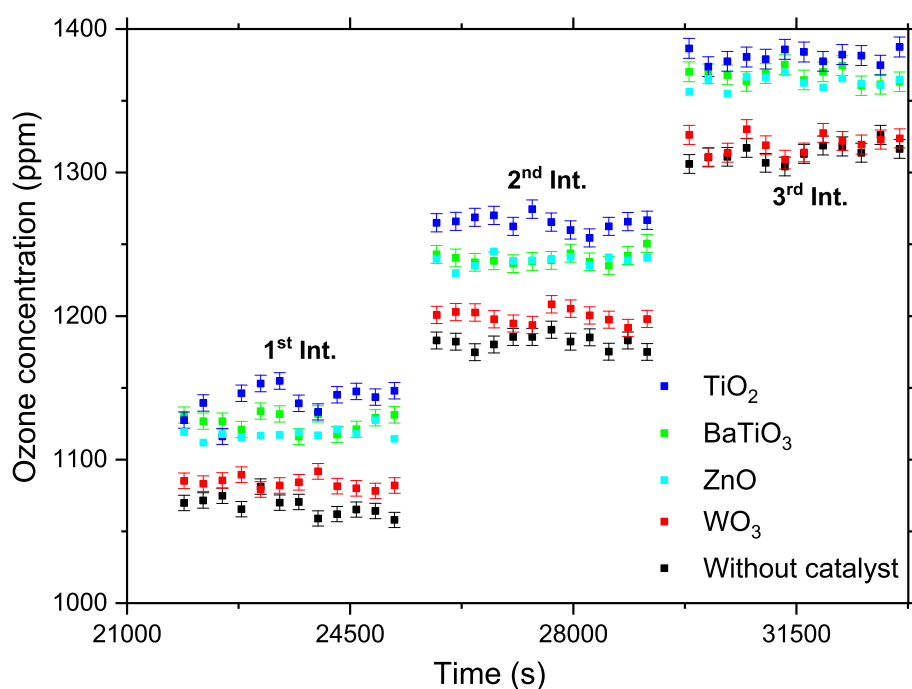
Figure 4.7: Time dependences of ozone concentrations generated by the discharge without and with photocatalysts.

4.2.1 Stability of photocatalytic activity

One of the most important parameters in ozone generation by electrical discharges in the presence of photocatalysts is the stability of photocatalytic activity. However, a comparative study of the catalytic activity and the stability of various catalysts in low-temperature

plasma produced by the dielectric barrier discharge is still missing. In our paper [63] we studied various photocatalysts, TiO_2, $BaTiO_3$, ZnO, and WO_3, to compare their effects on ozone generation by the surface dielectric barrier discharge in air. These catalysts were placed in the discharge chamber in their fixed position (at a distance of 4 mm from the active electrode). All catalysts were deposited on the inner part of the glass window and exposed to the active electrode.

Figs. 4.7 show that in contrast to TiO_2, ZnO, and $BaTiO_3$, the presence of WO_3 does not increase the concentration of ozone generated by the discharge. This result can be explained on the basis of the following considerations. The WO_3 behaves as a typical n-type semiconductor, with a bandgap of 2.6 eV (highly crystalline) to 3.3 eV (amorphous). These bandgaps correspond to electromagnetic radiation of the wavelengths of 476 and 374 nm, respectively. In our case, the layer of WO_3 is formed by highly crystalline nanoparticles of the dimensions of 100–200 nm. Consequently, the forbidden bandgap corresponds to the radiation wavelength of 476 nm. Considering the spectrum emitted by the discharge, see Fig. 4.2, it is seen that the intensity of radiation of this wavelength is negligibly small in comparison with the radiation emitted at shorter wavelengths. It can be consequently concluded that ozone generation processes will not be enhanced by the presence of a WO_3 layer.

There are only small differences in these concentrations for the following three catalysts, TiO_2, $BaTiO_3$, ZnO, and for WO_3, catalyst. On the other hand, the presence of WO_3 in the discharge does not affect the concentration of generated ozone compared with the discharge without catalysts. Approximately the same increase of ozone concentration produced in the discharge, observed in the presence of TiO_2 and ZnO catalysts, concurs with our earlier results [24], [25].

Finally, the discharge power is given by the discharge voltage and current product. The presence of photocatalysts for a particular voltage does not substantially affect the discharge current. For a capacitive load, it also depends on the phase shift between applied voltage and current. Based on the analysis of the discharge voltage and current waveforms, we calculated the phase shift for the discharge without and with different photocatalysts. The dependence of the phase shift versus the effective value of the discharge voltage for different photocatalysts is shown in Fig. 4.8.

4.3   Summary

○ Increase in discharge ozone production is higher for larger exposed area of the catalyst placed into the discharge chamber.

○ Layers of TiO_2, ZnO, and $BaTiO_3$ catalysts for particular discharge power increase the ozone concentration generated by the discharge. There are only small differences in the effect of these catalysts on ozone concentration.

○ Layers of catalysts show no substantial effects on the electrical parameters of the discharge. It can be concluded that the effect of catalysts on the phase shift between
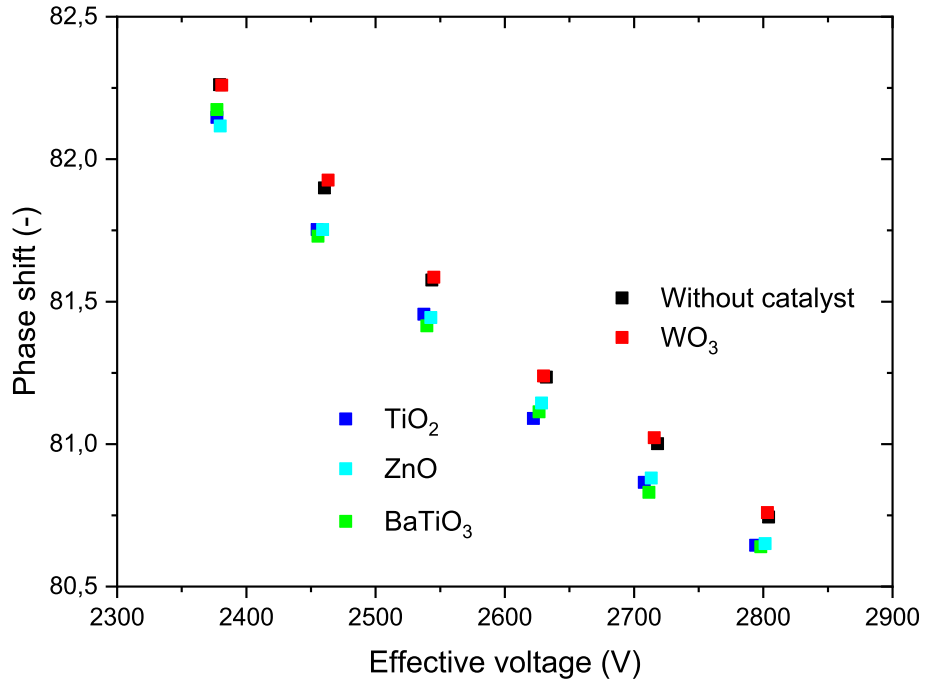
Figure 4.8: Phase shifts between applied voltage and current for the discharge without and with various photocatalysts as a function of the effective voltage.

voltage and current waveforms can be grouped into two families; the first one involves the discharge with TiO_2, $BaTiO_3$, and ZnO photocatalysts. The second group comprises cases of the discharge without photocatalyst and with WO_3. For each of these groups, the effect of photocatalysts is the same, but for the discharge without photocatalyst and the discharge with WO_3, the phase shift is higher than for the discharge with TiO_2, $BaTiO_3$, and ZnO photocatalysts. Thus, we can say that for our experimental conditions, for the constant discharge voltage, the photocatalysts have no substantial effect on the effective value of the discharge current, while the presence of TiO_2, ZnO, and $BaTiO_3$ slightly increases discharge power, and also decreases the phase shift between voltage and current.

○ As for the effect of TiO_2 catalyst on various regions of the strips active electrode, maximum generated ozone was observed in the case of a TiO_2 layer covering only the strips active electrode.

○ The concentration of ozone generated by the discharge with individual catalysts and the discharge without catalyst shows good time stability.

General conclusions

5.1   Conclusion

In this habilitation thesis, I summarized parts of the work on which I have been collaborating with my colleagues over the past ten years, a project that sets its sights on contributing to efficient ozone generation by dielectric barrier discharges.

These are the main results we have achieved:

- We presented a systematic and comprehensive approach to designing ozone generators that allows for their optimal configuration aimed at maximizing the amount of generated ozone.

- Based on the study of electrical and non-electrical properties of dielectric barrier discharges, the possibilities of their further optimization were identified.

- We proposed a numerical method for solving optimal strips (segment) distance of individual electrode parts, and verified this method experimentally.

- We studied the significance of parallel and perpendicular airflow with respect to ozone generator´s active electrode parts, with the ultimate goal of maximizing the generation of ozone.

- We managed to prove that the direction of feeding gas in relation to the direction of emerging microdischarges is absolutely essential for the amount of ozone generated.

- By combining airflow and dimensions of the different parts of the active electrode, we are able to determine – for each particular airflow – the optimal length of the rings part, inclined rings part and strips part of the active electrode in order to ensure the most efficient discharge ozone production.

- We presented the possibilities of the additional impact of photocatalytic substances on the amount of generated ozone.

○ With this knowledge, we designed and experimentally verified modifications of cylindrical generators with a single tangential feeding gas inlet that are frequently commercially used.

5.2 Future outlooks

Our research project, concentrated on direct application of ozone and other ionized particles, is conducive to generating them in a more economical and less energy-intensive manner. Taking into account the wide range of potential applications of generated ozone (in time and space), mentioned in the introduction to this habilitation thesis, each and every increase of the efficiency of a generator is concurrent with their use.

It is anticipated that our research of DBDs and their practical applications will be continued by a team of Ph.D. students, postdoctoral researchers and undergraduates of the Faculty of Electrical Engineering of the Czech Technical University in Prague, especially in cooperation with the Department of Physics of the Czech Technical University in Prague and the Institute of Macromolecular Chemistry of the Academy of Sciences of the Czech Republic in several integrated spheres of application; at the same time, we would definitely like to focus on the field of basic research as well.

○ Our intention is to centre primarily on non-trivial applications where the optimized parameter affecting the nature of DBD concurrently constitutes the quantity exerting significant impact in the process of application itself. A case in point may be application of DBD under extremely high or low temperatures, in the presence of increased relative humidity or environment of specific gases.

○ We plan to use the fundamental results achieved during our investigation of ozone generation in what is a joint research already in progress, which is focused on the Sabatier reaction offering promising production of methane that can be used for energy purposes during the catalytic processing of the continuously increasing worldwide concentration of carbon dioxide.

○ As for extremely low temperatures, we plan to study the application and primarily the behaviour of DBD in removing ice deposits on aircraft wings – hence we strive to solve combined tasks integrating such factors as flow and temperature as well as direct impact of relative humidity, or rather presence of water in the discharge. DBD is considerably sensitive to changes of all the mentioned quantities (flow, temperature, humidity and concentration).

○ Judging by experience, materials research now figures – and is bound to figure more and more prominently in the future – as a major additional boost of the efficiency of appliances and devices operating on the DBD principles. Using materials for electrodes that resist strong oxidation processes and other degrading effects, represented by strong electric fields and heat stress, can offer us good prospects not only for

prolonging the service life of designed equipment but also for boosting the generation of ionized particles and ozone.

○ The last – but in no case negligible – research direction we seek to promote is incorporation of experimentally obtained results into more sophisticated numerical models, better suited to reflect the real processes occurring during the formation of DBD, but also models incorporating into their solutions – at higher electrical voltages and velocities of feeding gases – the prevailing effects of photoionization and photoemission mechanisms.

Bibliography

[1] V. I. Gibalov and G. J. Pietsch, 'The development of dielectric barrier discharges in gas gaps and on surfaces,' *Journal of Physics D: Applied Physics*, vol. 33, no. 20, pp. 2618–2636, Sep. 2000. DOI: `10.1088/0022-3727/33/20/315`.

[2] J. Mikeš, S. Pekárek, O. Babčenko, O. Hanuš, J. Kákona and P. Štenclová, '3d printing materials for generators of active particles based on electrical discharges,' *Plasma Processes and Polymers*, vol. 17, no. 1, Jan. 2020. DOI: `10.1002/ppap.201900150`.

[3] U. Kogelschatz, 'UV production in dielectric barrier discharges for pollution control,' in *Non-Thermal Plasma Techniques for Pollution Control*, Springer Berlin Heidelberg, 1993, pp. 339–354. DOI: `10.1007/978-3-642-78476-7_24`.

[4] G. Borcia, C. A. Anderson and N. M. D. Brown, 'Dielectric barrier discharge for surface treatment: Application to selected polymers in film and fibre form,' *Plasma Sources Science and Technology*, vol. 12, no. 3, pp. 335–344, May 2003. DOI: `10.1088/0963-0252/12/3/306`.

[5] N. Bednar, J. Matovič and G. Stojanovič, 'Properties of surface dielectric barrier discharge plasma generator for fabrication of nanomaterials,' *Journal of Electrostatics*, vol. 71, no. 6, pp. 1068–1075, Dec. 2013. DOI: `10.1016/j.elstat.2013.10.010`.

[6] N. D. Boscher, F. Hilt, D. Duday, G. Frache, T. Fouquet and P. Choquet, 'Atmospheric pressure plasma initiated chemical vapor deposition using ultra-short square pulse dielectric barrier discharge,' *Plasma Processes and Polymers*, vol. 12, no. 1, pp. 66–74, Aug. 2014. DOI: `10.1002/ppap.201400094`.

[7] P. F. Ambrico, M. Šimek, C. Rotolo *et al.*, 'Surface dielectric barrier discharge plasma: A suitable measure against fungal plant pathogens,' *Scientific Reports*, vol. 10, no. 01, 2020. DOI: `10.1038/s41598-020-60461-0`.

[8] S. Pavon, J. L. Dorier, C. Hollenstein, P. Ott and P. Leyland, 'Effects of high-speed airflows on a surface dielectric barrier discharge,' *Journal of Physics D: Applied Physics*, vol. 40, no. 6, pp. 1733–1741, Mar. 2007. DOI: `10.1088/0022-3727/40/6/021`.

[9] S. Pavón, 'Interaction between a surface dielectric barrier discharge and transonic airflows,' Ph.D. dissertation, École Polytechnique Fédérale de Lausanne, École polytechnique fédérale de Lausanne, 2008, p. 178. DOI: 10.5075/epfl-thesis-4201.

[10] I. Adamovich, S. D. Baalrud, A. Bogaerts *et al.*, 'The 2017 plasma roadmap: Low temperature plasma science and technology,' *Journal of Physics D: Applied Physics*, vol. 50, no. 32, p. 323 001, Jul. 2017. DOI: 10.1088/1361-6463/aa76f5.

[11] K.-D. Weltmann, J. F. Kolb, M. Holub *et al.*, 'The future for plasma science and technology,' *Plasma Processes and Polymers*, vol. 16, no. 1, p. 1 800 118, 2019. DOI: 10.1002/ppap.201800118.

[12] U. Kogelschatz, B. Eliasson and W. Egli, 'Dielectric-Barrier Discharges. Principle and Applications,' *Journal de Physique IV Proceedings*, vol. 07, no. C4, pp. C4-47-C4–66, 1997. DOI: 10.1051/jp4:1997405.

[13] N. Allen, 'Photocatalysis: Science and technology,' *Journal of Photochemistry and Photobiology A: Chemistry*, vol. 160, pp. 225–225, Aug. 2003. DOI: 10.1016/S1010-6030(03)00234-X.

[14] U. Kogelschatz, 'Dielectric-barrier discharges: Their history, discharge physics, and industrial applications,' *Plasma Chemistry and Plasma Processing*, vol. 23, pp. 1–46, Mar. 2003. DOI: 10.1023/A:1022470901385.

[15] S. Yagi and M. Tanaka, 'Mechanism of ozone generation in air-fed ozonisers,' *Journal of Physics D: Applied Physics*, vol. 12, no. 9, pp. 1509–1520, Sep. 1979. DOI: 10.1088/0022-3727/12/9/013.

[16] S. Pekárek, 'DC corona discharge ozone production enhanced by magnetic field,' *The European Physical Journal D*, vol. 56, no. 1, pp. 91–98, Nov. 2009. DOI: 10.1140/epjd/e2009-00276-4.

[17] A. A. Abdelaziz, T. Ishijima, T. Seto, N. Osawa, H. Wedaa and Y. Otani, 'Characterization of surface dielectric barrier discharge influenced by intermediate frequency for ozone production,' *Plasma Sources Science and Technology*, vol. 25, no. 3, p. 035 012, Apr. 2016. DOI: 10.1088/0963-0252/25/3/035012.

[18] A. Fridman, A. Chirokov and A. Gutsol, 'Non-thermal atmospheric pressure discharges,' *Journal of Physics D: Applied Physics*, vol. 38, no. 2, R1, Jan. 2005. DOI: 10.1088/0022-3727/38/2/R01.

[19] G. Vezzu, J. L. Lopez, A. Freilich and K. H. Becker, 'Optimization of large-scale ozone generators,' *IEEE Transactions on Plasma Science*, vol. 37, no. 6, pp. 890–896, 2009. DOI: 10.1109/TPS.2009.2015452.

[20] S. Pekárek and J. Mikeš, 'Driving voltage frequency and active electrode setup effects on ozone and UV generation of dielectric barrier discharge in air,' *The European Physical Journal D*, vol. 74, no. 3, Mar. 2020. DOI: 10.1140/epjd/e2020-100332-3.

[21] S. Pekárek and J. Mikeš, 'Temperature-and airflow-related effects of ozone production by surface dielectric barrier discharge in air,' *The European Physical Journal D*, vol. 68, no. 10, Oct. 2014. DOI: `10.1140/epjd/e2014-50393-x`.

[22] J. Mikeš, S. Pekárek and I. Soukup, 'Experimental and modelling study of the effect of airflow orientation with respect to strip electrode on ozone production of surface dielectric barrier discharge,' *Journal of Applied Physics*, vol. 120, no. 17, p. 173 301, Nov. 2016. DOI: `10.1063/1.4966603`.

[23] J. Mikeš, I. Soukup and S. Pekárek, 'A 3d numerical study of the surface dielectric barrier discharge initial phase,' *Mathematics*, vol. 11, no. 4, 2023, ISSN: 2227-7390. DOI: `10.3390/math11041025`.

[24] S. Pekárek, J. Mikeš, I. Beshajová-Pelikánová, F. Krčma and P. Dzik, 'Effect of TiO_2 on various regions of active electrode on surface dielectric barrier discharge in air,' *Plasma Chemistry and Plasma Processing*, vol. 36, no. 5, pp. 1187–1200, Jun. 2016. DOI: `10.1007/s11090-016-9723-4`.

[25] S. Pekárek, J. Mikeš and J. Krýsa, 'Comparative study of TiO_2 and ZnO photocatalysts for the enhancement of ozone generation by surface dielectric barrier discharge in air,' *Applied Catalysis A: General*, vol. 502, pp. 122–128, 2015, ISSN: 0926-860X. DOI: `10.1016/j.apcata.2015.06.003`.

[26] J. Mikeš, S. Pekárek and O. Hanuš, 'Surface dielectric barrier discharge in a cylindrical configuration – effect of airflow orientation to the microdischarges,' *Ozone: Science & Engineering*, vol. 45, no. 1, pp. 2–18, Jan. 2023. DOI: `10.1080/01919512.2021.2016369`.

[27] R. Brandenburg, 'Dielectric barrier discharges: Progress on plasma sources and on the understanding of regimes and single filaments,' *Plasma Sources Science and Technology*, vol. 26, no. 5, p. 053 001, Apr. 2017. DOI: `10.1088/1361-6595/aa6426`.

[28] S. Pekárek, 'Asymmetric properties and ozone production of surface dielectric barrier discharge with different electrode configurations,' *The European Physical Journal D*, vol. 67, May 2013. DOI: `10.1140/epjd/e2013-30723-4`.

[29] K. Shimizu and M. Blajan, 'Dielectric barrier discharge microplasma actuator for flow control,' in *Actuators*, InTech, Jul. 2018. DOI: `10.5772/intechopen.75802`.

[30] L.-S. Wei, D.-K. Yuan, Y.-F. Zhang, Z.-J. Hu and G.-P. Dong, 'Experimental and theoretical study of ozone generation in pulsed positive dielectric barrier discharge,' *Vacuum*, vol. 104, pp. 61–64, Jun. 2014. DOI: `10.1016/j.vacuum.2014.01.009`.

[31] S. Xie, Y. He, D. Yuan *et al.*, 'The effects of gas flow pattern on the generation of ozone in surface dielectric barrier discharge,' *Plasma Science and Technology*, vol. 21, no. 5, p. 055 505, Mar. 2019. DOI: `10.1088/2058-6272/aafc50`.

[32] L. Wei, D. Yuan, Y. Zhang *et al.*, 'An analysis of the effect of inert gases on ozone generation using dielectric barrier discharge in oxygen,' *The European Physical Journal D*, vol. 68, no. 1, Jan. 2014. DOI: `10.1140/epjd/e2013-40556-8`.

[33] A. Ahmadi, J. Labadin, P. Piau and A. R. Rigit, 'Numerical modeling of the dielectric barrier discharges plasma flow,' in *2010 Fourth Asia International Conference on Mathematical/Analytical Modelling and Computer Simulation*, IEEE, 2010. DOI: `10.1109/ams.2010.88`.

[34] B. Jayaraman, Y.-C. Cho and W. Shyy, 'Modeling of dielectric barrier discharge plasma actuator,' *Journal of Applied Physics*, vol. 103, no. 5, p. 053 304, Mar. 2008. DOI: `10.1063/1.2841450`.

[35] B. Jayaraman and W. Shyy, 'Modeling of dielectric barrier discharge-induced fluid dynamics and heat transfer,' *Progress in Aerospace Sciences*, vol. 44, no. 3, pp. 139–191, Apr. 2008. DOI: `10.1016/j.paerosci.2007.10.004`.

[36] B. Jayaraman, W. Shyy and S. Thakur, 'Modeling of dielectric barrier discharge and resulting fluid dynamics,' in *44th AIAA Aerospace Sciences Meeting and Exhibit*, American Institute of Aeronautics and Astronautics, Jan. 2006. DOI: `10.2514/6.2006-686`.

[37] B. Jayaraman, S. Thakur and W. Shyy, 'Modeling of fluid dynamics and heat transfer induced by dielectric barrier plasma actuator,' *Journal of Heat Transfer*, vol. 129, no. 4, p. 517, 2007. DOI: `10.1115/1.2709659`.

[38] J. S. Shang and G. P. Huang, 'Modeling of ac dielectric barrier discharge,' *Journal of Applied Physics*, vol. 107, no. 11, p. 113 302, Jun. 2010. DOI: `10.1063/1.3415526`.

[39] M. Abdollahzadeh, J. C. Pascoa and P. J. Oliveira, 'Implementation of the classical plasma–fluid model for simulation of dielectric barrier discharge (DBD) actuators in OpenFOAM,' *Computers & Fluids*, vol. 128, pp. 77–90, Apr. 2016. DOI: `10.1016/j.compfluid.2016.01.012`.

[40] H. Kumar and S. Roy, 'Multidimensional hydrodynamic plasma-wall model for collisional plasma discharges with and without magnetic-field effects,' *Physics of Plasmas*, vol. 12, no. 9, p. 093 508, Sep. 2005. DOI: `10.1063/1.2044747`.

[41] S. Roy, 'Flow actuation using radio frequency in partially ionized collisional plasmas,' *Applied Physics Letters*, vol. 86, no. 10, p. 101 502, Mar. 2005. DOI: `10.1063/1.1879097`.

[42] K. P. Singh and S. Roy, 'Force approximation for a plasma actuator operating in atmospheric air,' *Journal of Applied Physics*, vol. 103, no. 1, p. 013 305, Jan. 2008. DOI: `10.1063/1.2827484`.

[43] C.-C. Wang and S. Roy, 'Geometry effects of dielectric barrier discharge on a flat surface,' *49th AIAA Aerospace Sciences Meeting including the New Horizons Forum and Aerospace Exposition*, Apr. 2011. DOI: `10.2514/6.2011-732`.

[44] D. Yuan, Z. Wang, C. Ding, Y. He, R. Whiddon and K. Cen, 'Ozone production in parallel multichannel dielectric barrier discharge from oxygen and air: The influence of gas pressure,' *Journal of Physics D: Applied Physics*, vol. 49, no. 45, p. 455 203, Oct. 2016. DOI: `10.1088/0022-3727/49/45/455203`.

[45] A. Bouchmal, 'Modeling of dielectric-barrier discharge actuator: Implementation, validation and generalization of an electrostatic model,' M.S. thesis, Delft University of Technology, 2011.

[46] C. Liu, D. Dobrynin and A. Fridman, 'Uniform and non-uniform modes of nanosecond-pulsed dielectric barrier discharge in atmospheric air: Fast imaging and spectroscopic measurements of electric fields,' *Journal of Physics D: Applied Physics*, vol. 47, no. 25, p. 252 003, May 2014. DOI: 10.1088/0022-3727/47/25/252003.

[47] V. I. Gibalov and G. J. Pietsch, 'Dynamics of dielectric barrier discharges in different arrangements,' *Plasma Sources Science and Technology*, vol. 21, no. 2, p. 024 010, Apr. 2012. DOI: 10.1088/0963-0252/21/2/024010.

[48] F. Roveda, 'Numerical analysis of dielectric barrier discharge,' Ph.D. dissertation, Università degli Studi di Bologna, 2012.

[49] E. Bogdanov, A. A. Kudryavtsev, A. L. Kuranov, I. E. Kozlov and T. L. Tkachenko, '2d simulation and scaling of dbd plasma actuator in air,' *American Institute of Aeronautics and Astronautics*, Jan. 2008. DOI: 10.2514/6.2008-1377.

[50] H. Luo, K. Liu, R. Junxia *et al.*, 'Study of dielectric barrier townsend discharge in 3-mm air gap at atmospheric pressure,' *Plasma Science, IEEE Transactions on*, vol. 42, pp. 1211–1215, May 2014. DOI: 10.1109/TPS.2014.2312543.

[51] Y. P. Raizer, *Gas discharge physics*. Springer, 1997.

[52] S. T. Surzhikov, *Computational physics of electric discharges in gas flows*. De Gruyter, 2013.

[53] J. Yu, F. Chen, H. Liu and Y. Song, 'Numerical study of fluid dynamics and heat transfer induced by plasma discharges,' *Plasma Science and Technology*, vol. 17, no. 1, pp. 41–49, Jan. 2015. DOI: 10.1088/1009-0630/17/1/09.

[54] U. Kogelschatz, B. Eliasson and M. Hirth, 'Ozone generation from oxygen and air: Discharge physics and reaction mechanisms,' *Ozone: Science & Engineering*, vol. 10, no. 4, pp. 367–377, 1988. DOI: 10.1080/01919518808552391.

[55] J. Kitayama and M. Kuzumoto, 'Analysis of ozone generation from air in silent discharge,' *Journal of Physics D: Applied Physics*, vol. 32, no. 23, pp. 3032–3040, Nov. 1999. DOI: 10.1088/0022-3727/32/23/309.

[56] H. Y. Kim, S. K. Kang, H. C. Kwon, H. W. Lee and J. K. Lee, 'Gas temperature effect on reactive species generation from the atmospheric pressure air plasma,' *Plasma Processes and Polymers*, vol. 10, no. 8, pp. 686–697, May 2013. DOI: 10.1002/ppap.201200163.

[57] L. Wei, H. Deng, G. Neretti and Y. Zhang, 'Ozone yield limit in low temperature plasmas based on thermodynamics,' *The European Physical Journal D*, vol. 73, no. 7, Jul. 2019. DOI: 10.1140/epjd/e2019-90560-y.

[58] F. J. Gordillo-Vázquez, 'Air plasma kinetics under the influence of sprites,' *Journal of Physics D: Applied Physics*, vol. 41, no. 23, p. 234 016, Nov. 2008. DOI: `10.1088/0022-3727/41/23/234016`.

[59] S. Jodzis, T. Smolinski and P. Sowka, 'Ozone synthesis under surface discharges in oxygen: Application of a concentric actuator,' *IEEE Transactions on Plasma Science*, vol. 39, no. 4, pp. 1055–1060, Apr. 2011. DOI: `10.1109/tps.2011.2105285`.

[60] S. Pekárek, J. Mikeš, M. Červenka and O. Hanuš, 'Air supply mode effects on ozone production of surface dielectric barrier discharge in a cylindrical configuration,' *Plasma Chemistry and Plasma Processing*, vol. 41, no. 3, pp. 779–792, Jan. 2021. DOI: `10.1007/s11090-021-10154-x`.

[61] P. J. Bruggeman, F. Iza and R. Brandenburg, 'Foundations of atmospheric pressure non-equilibrium plasmas,' *Plasma Sources Science and Technology*, vol. 26, no. 12, p. 123 002, Nov. 2017. DOI: `10.1088/1361-6595/aa97af`.

[62] M. A. Malik and D. Hughes, 'Ozone synthesis improves by increasing number density of plasma channels and lower voltage in a nonthermal plasma,' *Journal of Physics D: Applied Physics*, vol. 49, no. 13, pp. 135–202, Mar. 2016. DOI: `10.1088/0022-3727/49/13/135202`.

[63] J. Mikeš, S. Pekárek and P. Dzik, 'Catalytic and time stability effects of photocatalysts on ozone production of a surface dielectric barrier discharge in air,' *Catalysis Communications*, vol. 174, p. 106 576, 2023, ISSN: 1566-7367. DOI: `10.1016/j.catcom.2022.106576`.

[64] K. Ollegott, P. Wirth, C. Oberste-Beulmann, P. Awakowicz and M. Muhler, 'Fundamental properties and applications of dielectric barrier discharges in plasma-catalytic processes at atmospheric pressure,' *Chemie Ingenieur Technik*, vol. 92, no. 10, pp. 1542–1558, 2020. DOI: `10.1002/cite.202000075`.

[65] F. Thevenet, L. Sivachandiran, O. Guaitella, C. Barakat and A. Rousseau, 'Plasma - catalyst coupling for volatile organic compound removal and indoor air treatment: A review,' *Journal of Physics D: Applied Physics*, vol. 47, no. 22, p. 224 011, May 2014. DOI: `10.1088/0022-3727/47/22/224011`.

[66] U. Roland, F. Holzer and F.-D. Kopinke, 'Combination of non-thermal plasma and heterogeneous catalysis for oxidation of volatile organic compounds: Part 2. ozone decomposition and deactivation of γ-al2o3,' *Applied Catalysis B: Environmental*, vol. 58, no. 3, pp. 217–226, 2005, ISSN: 0926-3373. DOI: `10.1016/j.apcatb.2004.11.024`.

[67] S. Zhu and D. Wang, 'Photocatalysis: Basic principles, diverse forms of implementations and emerging scientific opportunities,' *Advanced Energy Materials*, vol. 7, no. 23, p. 1 700 841, 2017. DOI: `10.1002/aenm.201700841`.

[68] A. Fujishima, T. N. Rao and D. A. Tryk, 'Titanium dioxide photocatalysis,' *Journal of Photochemistry and Photobiology C: Photochemistry Reviews*, vol. 1, no. 1, pp. 1–21, 2000, ISSN: 1389-5567. DOI: `10.1016/S1389-5567(00)00002-2`.

[69]   A. Janotti and C. G. V. de Walle, 'Fundamentals of zinc oxide as a semiconductor,'
        Reports on Progress in Physics, vol. 72, no. 12, p. 126 501, Oct. 2009. DOI: `10.1088/`
        `0034-4885/72/12/126501`.

[70]   B. Ertug, 'The overview of the electrical properties of barium titanate,' *Am. J. Eng.*
        Res., vol. 2, no. 8, pp. 01–07, 2013.

[71]   A. Rydosz, K. Dyndał, K. Kollbek, W. Andrysiewicz, M. Sitarz and K. Marszałek,
        'Structure and optical properties of the WO_3 thin films deposited by the glad mag-
        netron sputtering technique,' *Vacuum*, vol. 177, p. 109 378, 2020, ISSN: 0042-207X.
        DOI: `10.1016/j.vacuum.2020.109378`.

[72]   S. Pekárek, O. Babchenko, J. Mikeš and A. Kromka, 'Effect of a diamond layer
        on the active electrode on the ozone generation of the dielectric barrier discharge
        in air,' *Journal of Physics D: Applied Physics*, vol. 53, p. 275 203, Mar. 2020. DOI:
        `10.1088/1361-6463/ab831f`.

Author's publications related to the habilitation thesis

A.1 3D printing materials for generators of active particles based on electrical discharges

J. Mikeš, S. Pekárek, O. Babčenko *et al.*, '3d printing materials for generators of active particles based on electrical discharges,' *Plasma Processes and Polymers*, vol. 17, no. 1, Jan. 2020. DOI: 10.1002/ppap.201900150.

FULL PAPER

3D printing materials for generators of active particles based on electrical discharges

Jan Mikeš[1] | **Stanislav Pekárek[1]** | **Oleg Babčenko[1]** | **Ondřej Hanuš[1]** | **Jakub Kákona[1]** | **Pavla Štenclová[2]**

[1]Faculty of Electrical Engineering, Czech Technical University in Prague, Prague, Czech Republic

[2]Institute of Physics, Czech Academy of Sciences, Prague, Czech Republic

Correspondence
Jan Mikeš, Faculty of Electrical Engineering, Czech Technical University in Prague, Technická 2, CZ-166 27 Prague 6, Czech Republic.
Email: mikes.jan@fel.cvut.cz

Abstract
In this study, we focus our attention on the impact of ozone (O_3) and ultraviolet radiation (UV) on materials usable for three-dimensional (3D) printing. Specifically, we have studied the potential degradative effect on the most commonly used filaments, such as polylactic acid (PLA) and acrylonitrile–butadiene–styrene (ABS). The effect has been examined on objects printed on a 3D printer and on the materials of discharge chambers of O_3 generators from which they were printed. For the purpose of adequate assessment of the actual impact of O_3 and UV, samples were monitored for a period of 18-hr of exposure. The methods of Raman spectroscopy, optical and scanning electron microscopy and Fourier-transform infrared spectroscopy (FTIR) have been employed for an objective evaluation of potential modifications. A generator equipped with a chamber printed from a new PLA filament and an active electrode system in the form of a stripes electrode, or more precisely, in the second case, a honeycomb-active electrode, both cut out of a thin copper foil, was used for the generation of O_3 and UV radiation. The tested materials showed substantial resistance to O_3 exposure under the test conditions. The result of measurements suggested that these materials could be used for chambers for the O_3 as well as for active particle generation.

Process of O_3 and UV treatment of ABS and PLA polymers
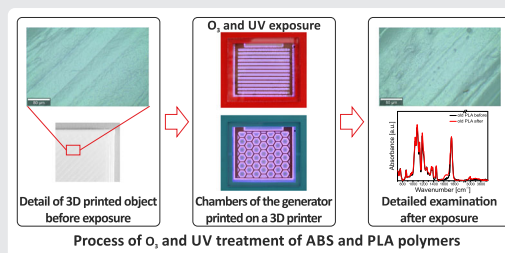
KEYWORDS
3D printing, ABS, dielectric barrier discharge, ozone, PLA, plasma treatment, surface modification, UV radiation

1 | INTRODUCTION

Prototyping of functional samples, molds, preparatory items and other developmental kits represents only a preproduction stage; but it is primarily in the domain of scientific development and research where it constitutes a

highly time-consuming and costly aspect of the process of preparing the resultant product itself. Three-dimensional (3D) printing provides a seemingly secure option for facilitation, which is, however, complicated by three fundamental factors that have to be complied with to attain the desired result. These include: (a) suitable 3D

printer, (b) suitably selected printing filament, (c) specialist experience of 3D printing (including not only the knowledge of suitable printing procedure but also correct choice of parameters for the given application). Over the past decade, 3D printing of plastics has made wide-ranging progress conducive to promoting its practical application in medicine,[1,2] chemistry,[3] food industry,[4] electronics,[5] printing of medicaments,[6] as well as medical aids and expedients,[7,8] specifically shaped for the given purposes, while also playing no small part in the arts[9] and culture.[10] Seen from a long-term perspective, it is evident that the state-of-the-art technical plastics polylactic acid (PLA), acrylonitrile–butadiene–styrene (ABS), polyethylene terephthalate, polyvinylalcohol, and so forth, have been capturing growing attention in engineering and scientific applications. A primary role in this development trend has been played by the FFF/FDM (fused filament fabrication/fused deposition modeling) technology of 3D printing, whose rapid development has set a benchmark for the present-day plastics industry, and grown to be a major competitor not only for machining but also for pressing and extruding plastic parts into molds. In addition to what are seen as highly positive aspects—which have been, quite undoubtedly, enhanced by the thoroughgoing research and development in printable materials[11]—we may also identify a great many unresolved and technologically controversial properties of the resultant printed objects. These include their fragility, porosity, deformation and especially their different chemical resistance and stability, degradability in the passage of time and frequent, hardly predictable other properties manifesting themselves, for instance, in contact with reacting agents or when exposed to specific environmental factors (temperature, pressure, ultraviolet [UV] radiation) and so forth. The actual development of printing machines, selection of most suitable filaments as well as choice of procedures pertaining to 3D printing, have not yet come to an end. According to Fattahi,[12] the properties of the individual types of filaments and their behavior in a specific environment are often objectively evaluated, but the degrees of resistance of the finished printed products for specific applications have been examined less frequently.[13,14] In our study, we have examined the usability of 3D printing and print materials for chambers of generators of active particles, produced by means of a dielectric barrier discharge, and scrutinized the impact of the concentration of ozone (O_3) and emitted UV radiation on their surface modifications, or—to be more precise— on the influence of the key parameters of a thus printed chamber. Since the development and implementation of these materials in practical usage is known to proceed very rapidly, the new materials themselves manage to be

tested for industrial applications only very rarely. The fundamental, hitherto commonly used 3D printing materials include the following. ABS,[15] to date, is one of the most frequently used materials in 3D printing. It is noted for good thermal resistance and is relatively cheap. Actually, it is a very stable plastic, displaying a high degree of tensile stress. ABS is capable of resisting temperatures of up to 100°C without great losses in strength. Its printing temperature is around 250°C. However, a major disadvantage is its thermal expansion: in comparison with other materials used, ABS comes out as the worst in this respect. It is exactly this particular property that causes deformation of objects during printing and, therefore, requires a heated pad for 3D printers. The second, and in ecological terms much more prioritized, material is PLA (polylactic acid).[16] PLA material is most likely the only one made of corn starch and thus biodegrades within a matter of months. In 3D printing, this material is considerably widespread, primarily due to its very low dilatability, which is so low that in most instances, no heated pad under 3D printer is needed for printing. In practical terms, PLA is the only one that can be used for printing large objects, over 20 cm in size. Its disadvantage lies in its fragility: printed objects can be used to the maximum temperature of 60°C, but then the material tends to plasticize. PLA filament is known for its enormous advantage in ecological properties, and is often utilized in the textile industry. It is biodegradable and even compostable. These properties, in particular, have caught our attention, most of all in view of PLA's potential resistance to enhanced concentrations of O_3 and UV radiation. To date, special attention in scientific literature has been granted only to the impact of O_3 and UV radiation on the printing filament alone, but rarely on the constructions printed from the filaments themselves. An overview of the basic physical–chemical properties of PLA filaments is contained in the article of Tsuji.[16] The life cycle of the production, disposal and eventual recycling of PLA is studied in the work of Groot and Borén.[17] Other studies dealing with the degradation of PLA may be found, for instance, in the work of Qi et al.[18] PLA and ABS monomer structures and physical and technological properties can be found in the works of Wypych.[19,20]

With regard to increasing interest to 3D printing technology our research was focused on its applicability to O_3 chamber generator fabrication. In this case, the ability of employed material to sustain combined exposure of O_3 and UV radiation (other species) produced by dielectric barrier discharge for long time is crucial. Our selection of PLA and ABS filaments was limited to these two samples of printable plastic materials due to the need to highlight items representing biodegradable filament and filaments nonbiodegradable in nature.

2 | DEGRADATION OF POLYMERS BY O_3 AND UV IRRADIATION

O_3 plays a significant role in the stability of polymer materials. Both O_3 and UV radiation rapidly damage unprotected polymers, which, in turn, may considerably shorten their lifetime. Especially, highly unsaturated polymers (i.e., rubbers) are known to suffer a great deal of degradation by O_3 since their double bonds easily react with O_3. O_3 also reacts with saturated polymers, but markedly more slowly. O_3 reacting with double bonds causes chain cracking. The general mechanism of degradation by O_3 is shown below in Figure 1.

It has been reported that UV radiation, O_3 and other oxygen related species may oxidize the polymer's surface and shorten their lifetime. According to Ramani and Ranganathaiah,[22] Koo and Jang,[23] and Eren et al.,[24] the intensity of UV radiation and the longer time of its impact lead to PLA gradual photo-oxidation of the surface, which further results in visible surface deformation. The longer effect of the concentration of O_3, atomic oxygen and UV radiation results in the disintegration of ester bonds, with PLA samples becoming hydrophilic.[23] As far as ABS is concerned, Ramani et al.[22] single out its medium-high resistance to UV radiation.

3 | EXPERIMENTAL SETUP

The experimental setup consists of generator of active particles, O_3 and UV radiation, diagnostication, and adjustment of electric parameters (voltage regulation, frequency regulation, electrical input analysis) and measurement and regulation of nonelectrical quantities (air flow through chamber, measurement of O_3 concentration, temperature, pressure, relative humidity and UV sensor and monitor).

The experimental setup used in our study is depicted in Figure 2. Its central section is formed by a chamber printed on a 3D printer from PLA material and mounted with two types of active electrode systems. In both cases, there were electrodes made of copper foil, 0.035-mm thick, manufactured by ELCHEMCo, and covered on one side by electrode acrylic glue with a very low resistivity of up to 10^{-1} Ohm/square. Copper foil was selected despite its higher mechanical degradability in contact with reaction agents, primarily because of its easy machining and yet sufficient lifetime for short-term experiments. Cutting plotter Cricut Maker was used for cutting foil matrix. In the first case, the resultant active electrode system comprised thin, 1-mm stripes, which were 3-mm far from one another; on both ends, they were
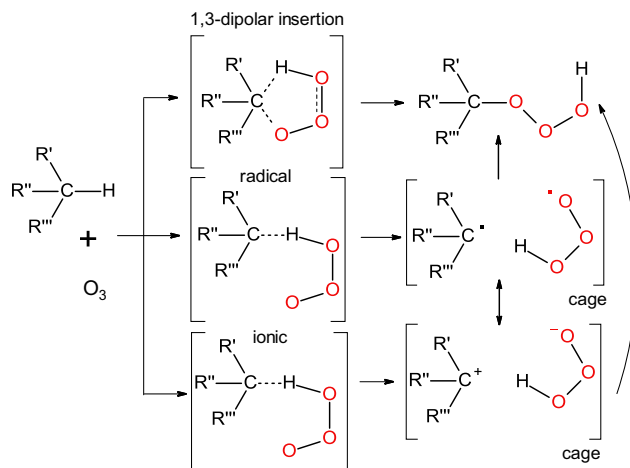
FIGURE 1 Mechanism of polymer degradation by ozone[21]

conductively connected in parallel. The active electrode system thus created was glued by conductive glue to an alumina plate, 0.635-mm thick. The structural layout of the active electrode system is shown in Figure 3a. The second case involves a honeycomb-active electrode system. This configuration is depicted in Figure 3b.

Figure 4a,b shows a dielectric barrier discharge for parameters further constantly maintained in the experiment in both types of electrodes.

The dimensions of the generator chamber were $122 \times 122 \times 18$ mm and are shown in Figures 5 and 6; a groove for inserting a high-purity alumina plate with the dimensions of $108 \times 108 \times 0.635$ mm was printed in the central part. This plate contains 96% Al_2O_3, has a dielectric constant for 1 MHz of 9.6 and an electric strength of 14 kV/mm; and the heat conductivity for the temperature of 25°C totals 24 W/m·K. A lining with the dimensions of 80×70 mm was printed in the upper section of the chamber of the O_3 generator; a window, made of translucent PMMA (poly(methyl methacrylate)), was inserted and sealed into the lining. Silicon cement produced by the Ceys company, suitable for methacrylate and polycarbonate, was used for sealing. Discharge space was created in the part of the chamber, marked off by the translucent window and alumina plate with an overall
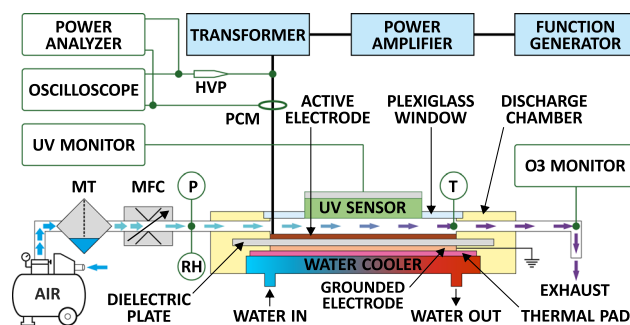
FIGURE 2 Experimental setup
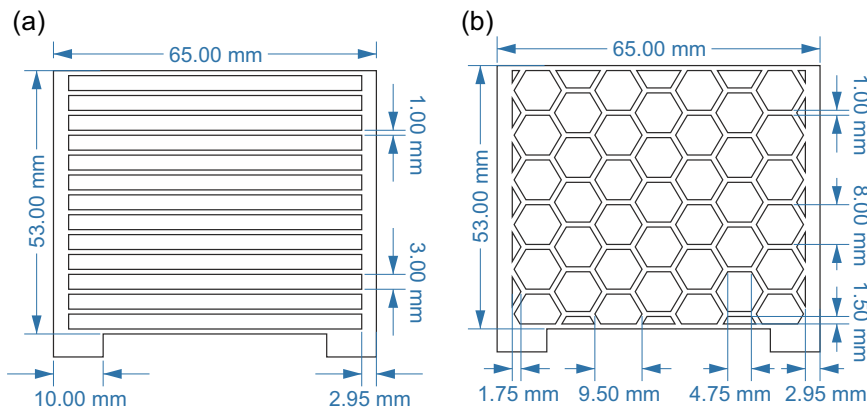
FIGURE 3 Structural layout of the active electrodes
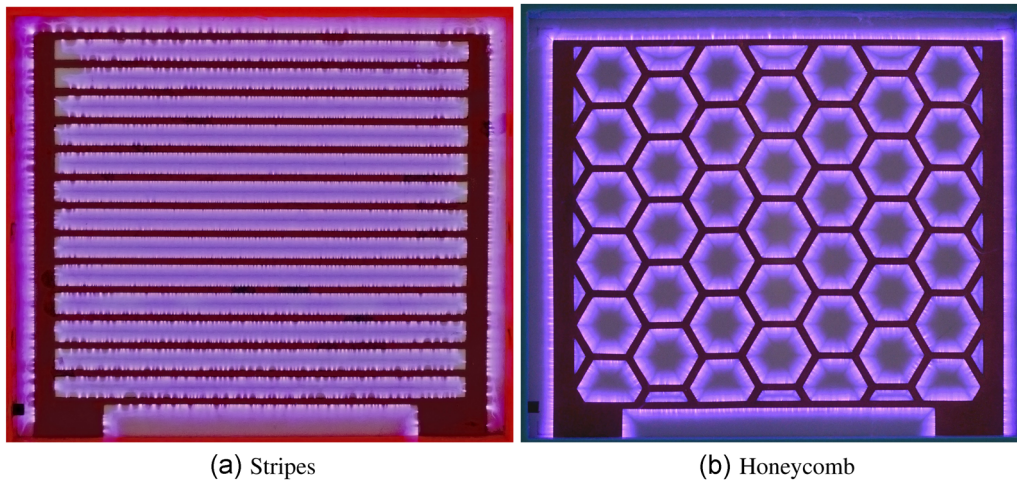
(a) Stripes

(b) Honeycomb

FIGURE 4 Discharge with stripes-active electrode (a) $P_{av} = 9.3$ W, $V_{max} = 3.2$ kV, $f = 4$ kHz, $Q_{air} = 6$ slm and honeycomb-active electrode (b) $P_{av} = 15.3$ W, $V_{max} = 4$ kV, $f = 4$ kHz, $Q_{air} = 6$ slm
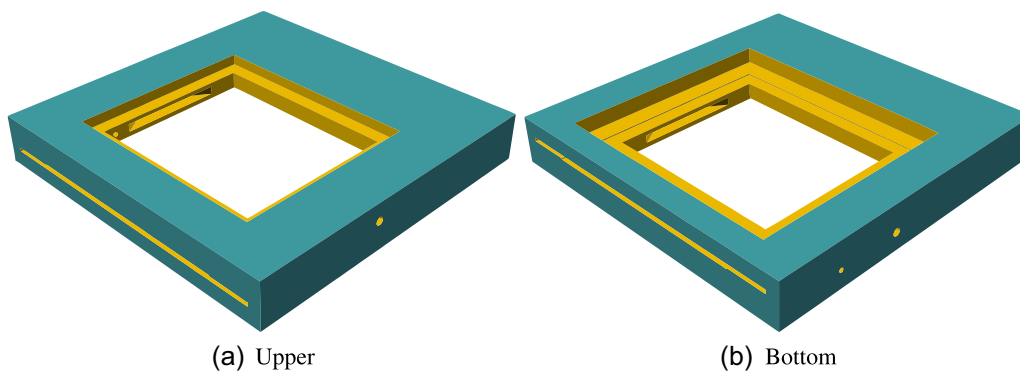
(a) Upper

(b) Bottom

FIGURE 5 View of the upper and bottom section of flat chamber of the generator printed on a 3D (three-dimensional) printer

height of 6.5 mm. A lining with the dimensions of 90×80 mm was printed in the bottom (opposite) side of the chamber for the insertion of a brass cooler, whose water circulation was secured by means of a small circulating pump with a water passage of 2 L/min. The geometry of the configuration milled into the brass block of the cooler is indicated in Figure 7a,b. The brass cooler was separated from the alumina plate by means of a heat-conducting, electrically nonconductive pad

manufactured by the company ARCTIC Thermal, with its matrix measuring $145 \times 145 \times 1$ mm; it is made of a silicon-based material with a thermal conductivity of 6.0 W/m·K, a specific weight of 3.2 g/cm^3, a range of operating temperatures from −40 to 200°C, an electric strength of 12 kV/mm and an ultimate tensile strength of 245 kPa. Two openings, shaped as suction inlets, were printed inside the chamber into its left and right sides, filling up most of the space of the shorter wall of the
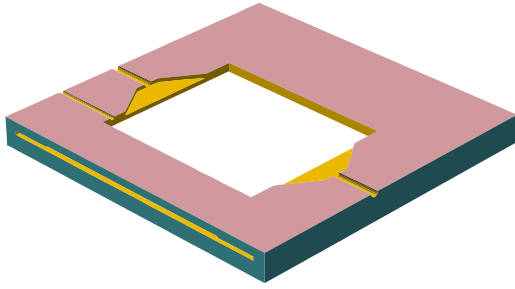
FIGURE 6 Cross-section of flat chamber of the generator printed on a 3D (three-dimensional) printer on the spot of the suction inlet

discharge space. A small opening was made on the left side for optical fiber of the Neoptix thermometer ReFlex 4 (T), which was sealed into the chamber wall by silicon cement. The grounded electrode, made of a copper foil with the dimensions of $80 \times 90 \times 0.035$ mm, was glued to the bottom side of the alumina plate and was identical for both variants of the active electrode systems; viewed in a ground plan, it overhung on each side by 0.5 mm. The overall capacitance of the configuration setup with a stripes-active electrode was 202.4 pF and in the second variant, with a honeycomb-active electrode, it was 202.8 pF.

An active electrode was connected to an AC high-voltage power supply system. This system consisted of a function/arbitrary waveform generator DG 1022, a wide-band AC power amplifier AL-600-HF-A (output power 600 W, frequency response from 20 Hz to 800 kHz) and a high-frequency high-voltage transformer AL-T1000.5 (peak voltage 10 kV, output power 1,000 W and frequency response from 4 to 12 kHz). Discharge was driven by sinusoidal voltage. The electrical parameters of discharge were registered by the four-channel oscilloscope R&S RTB2004 (350 MHz; 2.5 GSa/s) offering the option of storing and processing time behavior of voltage and current in a CSV file. The discharge voltage signal was sampled and recorded on the first channel of this oscilloscope with a high-voltage probe (HVP-28HF,

division ratio 1,000/1, frequency up to 200 MHz; Pintek). To determine the discharge current, we used a signal obtained from a Pearson current monitor (model 2877) with a bandwidth of up to 200 MHz. The voltage and current values were integrated via signal period and the mean power input into discharge was calculated and tentatively compared with the value gained by the power analyzer R&S HMC8015. The concentration of O_3 at the output of the discharge chamber was measured by the absorption of a 254 nm UV spectral line with an API 450 ozone monitor. The accuracy of O_3 concentration measurements was $\pm 0.5\%$. The intensity of the UV radiation emitted by discharge was measured by an AccuMAX UV monitor, measured from the side of the active electrode. UV radiation was measured in a wavelength range from 320 to 420 nm by an XS-365 sensor with a diameter of 21.6 mm and intensity range of 0–100 mW/cm^2. The peak values of the emitted discharge radiation were measured 63.5 mm above the surface of the alumina plate. Air for the discharge was supplied by an oil-free compressor through a moisture trap (MT) and a mass flow controller (MFC). The relative humidity of the input air was measured by a sensor (RH) and the pressure in the discharge chamber was measured by a digital manometer (P). The air temperature in the discharge volume was measured by an optical fiber thermometer, Neoptix (T).

4 | EXPERIMENTAL METHODS

4.1 | Printing properties

After a series of tests, which eventually provided the final results of this study, a chamber of the O_3 generator was fabricated from PLA material. The chamber was designed in the Open SCAD software. The specific geometry of the generator chamber is shown in Figures 5 and 6. Using the SCAD software, a Standard Tessellation Language (STL) file was prepared and employed to generate a G-code usable for the specific printer with the help of the Slic3r
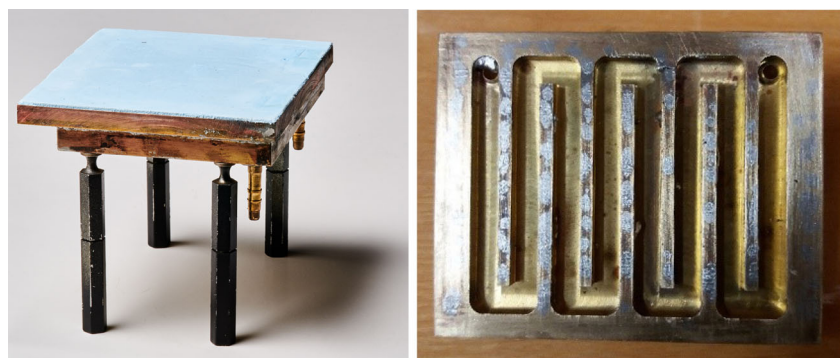
FIGURE 7 Upper side of cooler with a heat-conducting pad and its inner layout

(a) Upper

(b) Inner layout

program. Printing itself was performed on the RebeliX printer for PLA and on the Průša i3 mk3 printer for ABS. As part of printing preparation, the generator chamber was designed with adjustable parameters, reflecting the shapes and sizes of other available components (ceramic plate, cooler, inner space of discharge chamber, etc.). The infill density of printing was set to 100% to inhibit leaks of the medium from a chamber. Even though it is impossible to guarantee perfect tightness of the components printed on a 3D printer, no O_3 leaks were observed during measurements.

4.2 | Preparation of experimental plates

The experimental plates measuring $80 \times 70 \times 4$ mm were printed for both investigated materials. Photographs in Figure 8a–d show the infill of the pyramid-shaped print cavity at 15%, covered by four mutually overlapping layers printed at an angle of 60°. Plates were placed into a window in the chamber instead of the Plexiglass (see Figure 2) during the experiments. The distance between the plate and the active electrode is 6.5 mm.

4.3 | Source of O_3 and UV radiation on the basis of dielectric barrier discharge

Exposure of the testing sample was performed with the help of two sources of O_3 and UV radiation. The first chamber of the active particles, O_3 and UV radiation generator was made up of a dielectric plate with a stripes-active electrode, manufactured from a copper foil. In the second case, a honeycomb-active electrode made of the same copper foil was used. In both instances, an active electrode system was placed into a printed PLA configuration, thus constituting the backbone of the entire generator of active particles, O_3 and UV radiation.

An air flow of $Q_{air} = 6$ slm, a frequency of feeding sinusoidal voltage of 4 kHz and temperature in the range of 29.5–32.5°C were maintained for all measurements. In case of the stripes-active electrode, the average O_3

(a) Cross section

(b) new PLA

(c) old PLA

(d) ABS
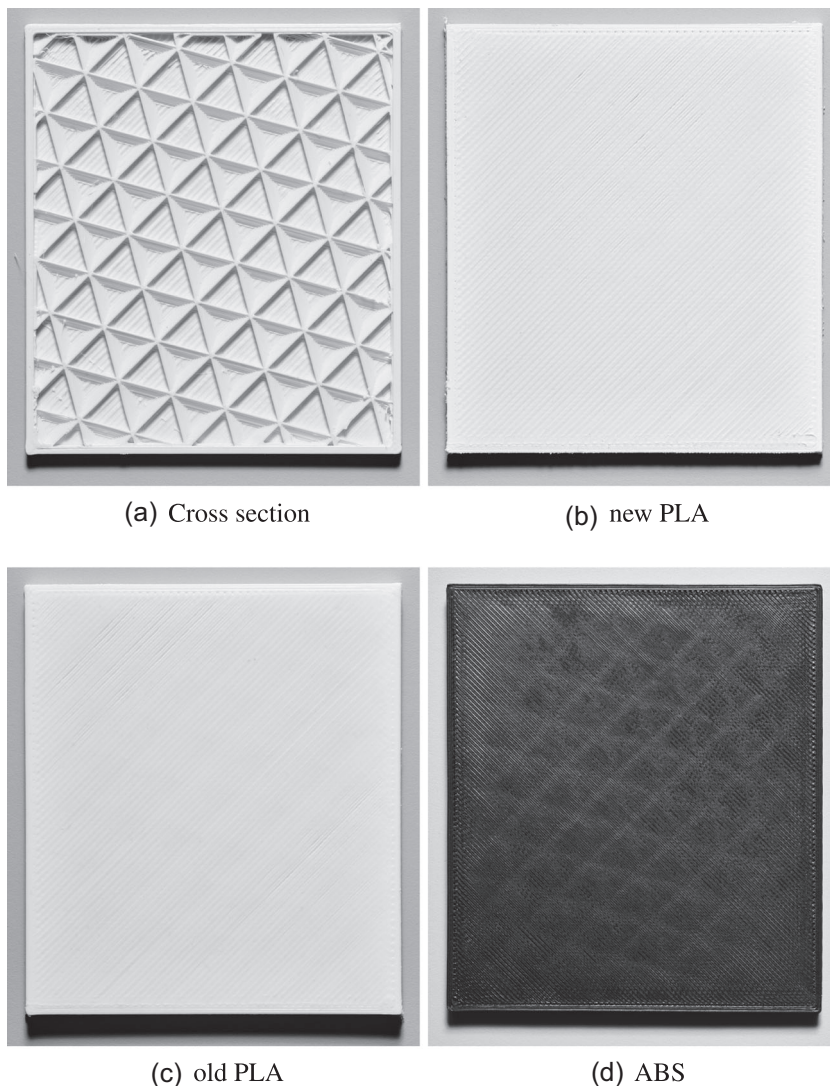
FIGURE 8 Experimental plates. ABS, acrylonitrile–butadiene–styrene; PLA, polylactic acid
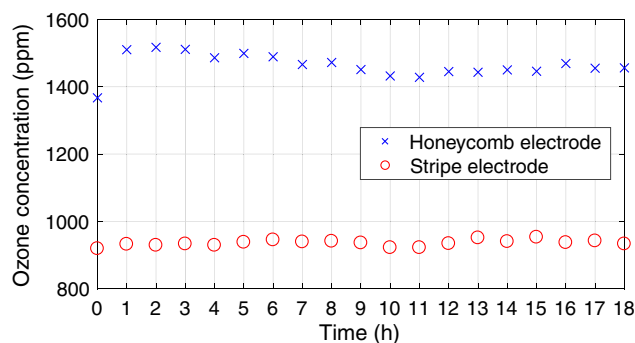
FIGURE 9 Time dependence of ozone concentration for 18 hr for both electrode configurations

concentration was 936 ppm (see Figure 9), the maximum intensity of UV radiation was $3,400\,\mu W/cm^2$ and the average discharge power was 9.3 W at $V_{max} = 3.2$ kV.

In the second instance, featuring an active electrode system with a honeycomb-active electrode, the average O_3 concentration was 1,463 ppm (see Figure 9), and the maximum intensity of UV radiation was $5,273\,\mu W/cm^2$ and average discharge power was 15.3 W at $V_{max} = 4.0$ kV.

4.4 | Material analysis

Material analyses were performed on the testing plates made of PLA and ABS materials, with two types in case of PLA: one brand-new material, unpacked from a vacuum packaging (new PLA), and a second one, which had been stored for more than a year under unstable conditions that were hard to define (fluctuating impact of temperature, humidity, dust, etc.; old PLA). A size of 80×70 mm and thickness of 4 mm was selected as the uniform testing module. The plates thus printed were placed instead of the upper cover of the chamber of active particles, O_3 and UV radiation generator. Modules were printed as lightened, structurally filled bodies (hence comprising a share of air and water vapors). The testing stage was performed with the help of three separated methods.

Scanning electron microscopy (SEM), water contact angle (WCA) measurements, and Fourier-transform infrared spectroscopy (FTIR) were carried out in the Institute of Physics of the Czech Academy of Sciences. The SEM analysis was done by means of the electron microscope MAIA3, manufactured by Tescan company.

The changes in surface wettability of tested plates were identified by the static water drop contact angle measurements. The WCA was evaluated from the drop-on-surface profile by reflection goniometry using the Surface Energy Evaluation (SEE) System (developed by Masaryk University, Brno, Czech Republic). Briefly, the $3\,\mu L$ drop of deionized water is placed on the plate's

surface while the formed drop is captured by a digital camera. The WCA is calculated by the SEE software using a multipoint fitting of the drop profile and tangent of the arc made by drop.

FTIR in the attenuated total reflection (ATR) regime was realized using a Nicolet iS50 spectrometer (Thermo Scientific, Nicolet) equipped with a single-bounced diamond ATR crystal, KBr beam splitter, and DLsTGS detector. The optical absorbance was calculated in standard absorbance units as $A = -\log(R/R_0)$, where R is the spectrum of the analyzed material, and R_0 is the reference (background) spectrum of the diamond crystal. In all cases, the spectra represent an average of 128 scans recorded with a resolution of $4\,cm^{-1}$. Published spectra are an average from six independently measured spots on polymer plates. The area $2,000–2,750\,cm^{-1}$ is omitted in the spectra due to the intrinsic absorption of diamond crystal material.

Optical microcopy and Raman spectroscopy were performed at the Faculty of Electrical Engineering, Czech Technical University in Prague, by means of the alpha 300RAS confocal microscope, manufactured by WITec company. The microscope is equipped with a set of objectives offering ×10, ×20, ×50 and ×100 magnifications and a digital camera for image capturing. All the Raman spectra were measured by an Ultra High Throughput Spectrometer 300 using a laser beam of 532 nm wavelength, a microscopic objective with ×100 magnification and numerical aperture 0.9, and a 1,800 g/mm grid. The Raman spectra of both PLA plates (new and degraded by the passage of time) were measured at the laser output of 10 mW. The Raman spectra of the ABS plate were measured at a laser power of 2 mW.

5 | RESULTS – O_3 AND UV TESTING

5.1 | Surface microscopy

The fabricated plates are macroscopic objects and the current study was focused on their ability to sustain the long-term exposure of enhanced O_3 concentrations and UV radiation. It is known that both these agents can cause degradation of organic materials while tested plates' materials are proposed to be used for 3D printed chambers. Therefore, the plates' material instability will be the main indication of mechanical demage or sealing deterioration risks. First of all, it needs to be mentioned that after the combined O_3 and UV exposure, the surface of the tested plates changes its character from hydrophobic with measured water contact angles around

75° (PLA) and 83° (ABS) to hydrophilic with the measured water contact angles around 30° (PLA) and 25° (ABS). This is in agreement with the observation of Wang et al.[8] and Eren et al.[24] and is related to the general effect of oxygen plasma species on polymers. However, the wettability itself is not able to provide information about the surface structure. Therefore, the morphology of fabricated plates was investigated by the combining of SEM at low magnifications and optical microscopy.

The SEM images of the sample surface before and after the O_3 and UV exposure are summarized in Figure 10. The SEM images of the plates' surface are in agreement with the sample photographs in Figure 8 and demonstrate that the fabricated plates are composed of well-stuck stripes. Upon comparing the PLA and
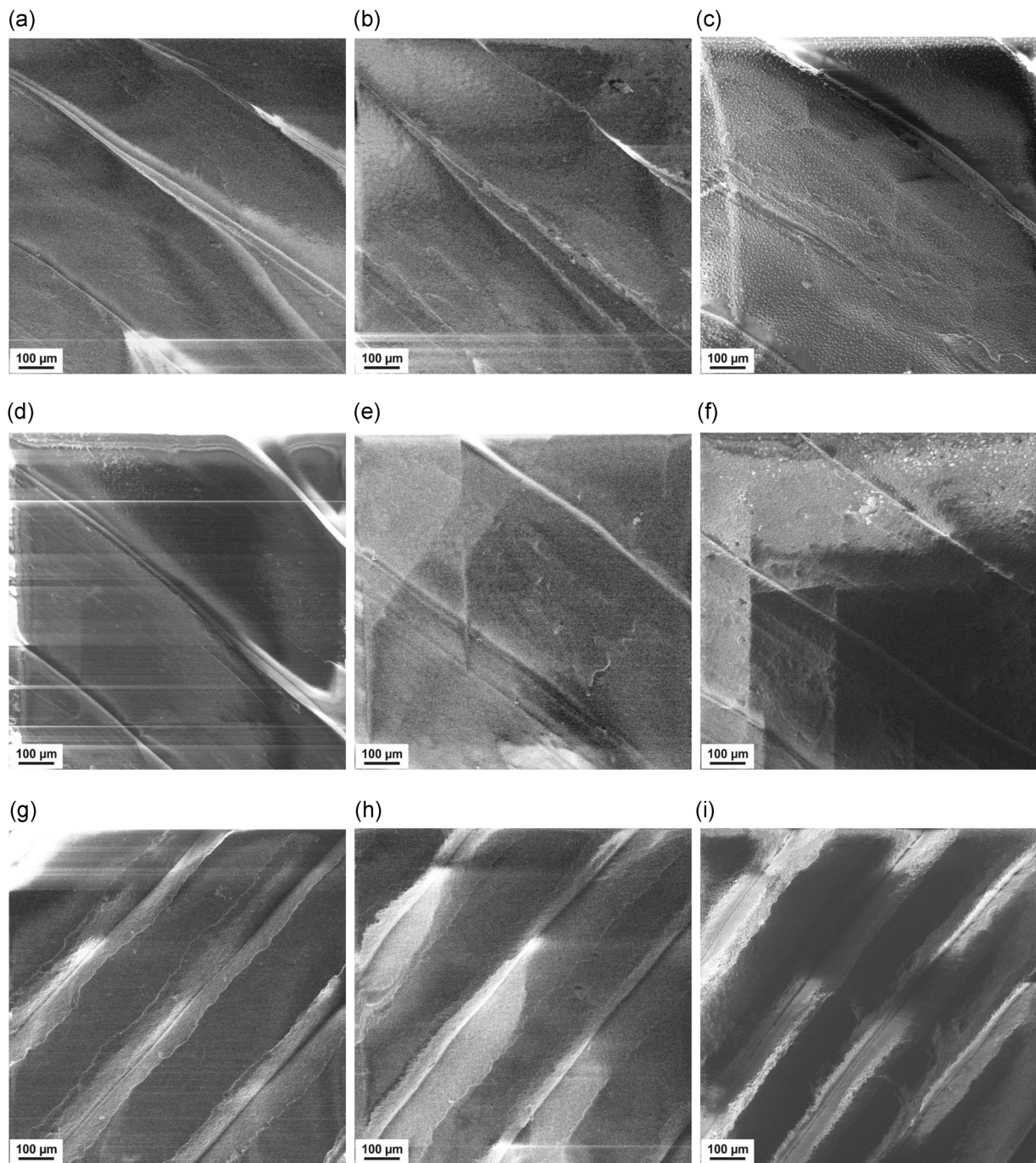
FIGURE 10 The scanning electron microscopy (SEM) images of analyzed plates made of new polylactic acid (PLA) before (a) and after (b,c) discharge treatment; old PLA before (d) and after (e,f) discharge treatment; acrylonitrile–butadiene–styrene before (g) and after (h,i) discharge treatment

ABS-made plates, it can be seen that PLA plates are more compact with narrow V-like valleys between the printed stripes. In contrast, deep valleys with wide spacing in the top part between stripes are observed for the ABS plates. Although, the ABS stripes are, in general, stuck together in the bottom part, the fractures between separate stripes were observed at a few places. This can negatively affect the sealing of the chamber and needs to be taken into consideration.

Comparing the SEM images before and after the O_3 and UV exposure, we observe formation of bubble-like features on some areas of PLA plates, whereas the ABS-made plates seems to not change their morphology. Unfortunately, the high sensitivity of both employed materials on electron beam (charging effect and degradation at high magnifications) prohibit more detailed surface analysis by the SEM. Therefore, optical microscopy was used as the nondestructive technique for plates' surface investigation. The examples of related SEM optical images captured on all plates are shown in Figure 11, while more detailed analysis was performed at higher magnification with changing of focus/microscope depth position.

As it can be seen from Figures 10 and 11, both PLA-made plates demonstrate increase of surface inhomogeneity after O_3 and UV exposure. In both cases, areas with a smooth surface and with formed bubble-like features on the surface were observed within one plate. Here, it should be noted that printed stripes for the plate made of new PLA initially contained less "cavities" than that of old PLA, and after the O_3 and UV exposure, the major part of its surface remained flat. In contrast, for the sample made of old PLA, which initially demonstrated a higher amount of cavities on printed stripes after the discharge treatment, the dominant area is the one with "flattened" bubble-like features. In case of both PLA, no fractures between stripes were observed by SEM and optical microscopy. It indicates that O_3 and UV exposure affects only the plates' surface, keeping its bulk structure intact. The last, but not the least thing to be mentioned, is that at higher optical microscope magnification, the observed PLA bubbles behave in the same way as other plate areas, that is, they are transparent enough for the laser beam of the Raman setup. Although the height of these features is lower than the observed PLA stripes surface inhomogeneities, they can be an indication of
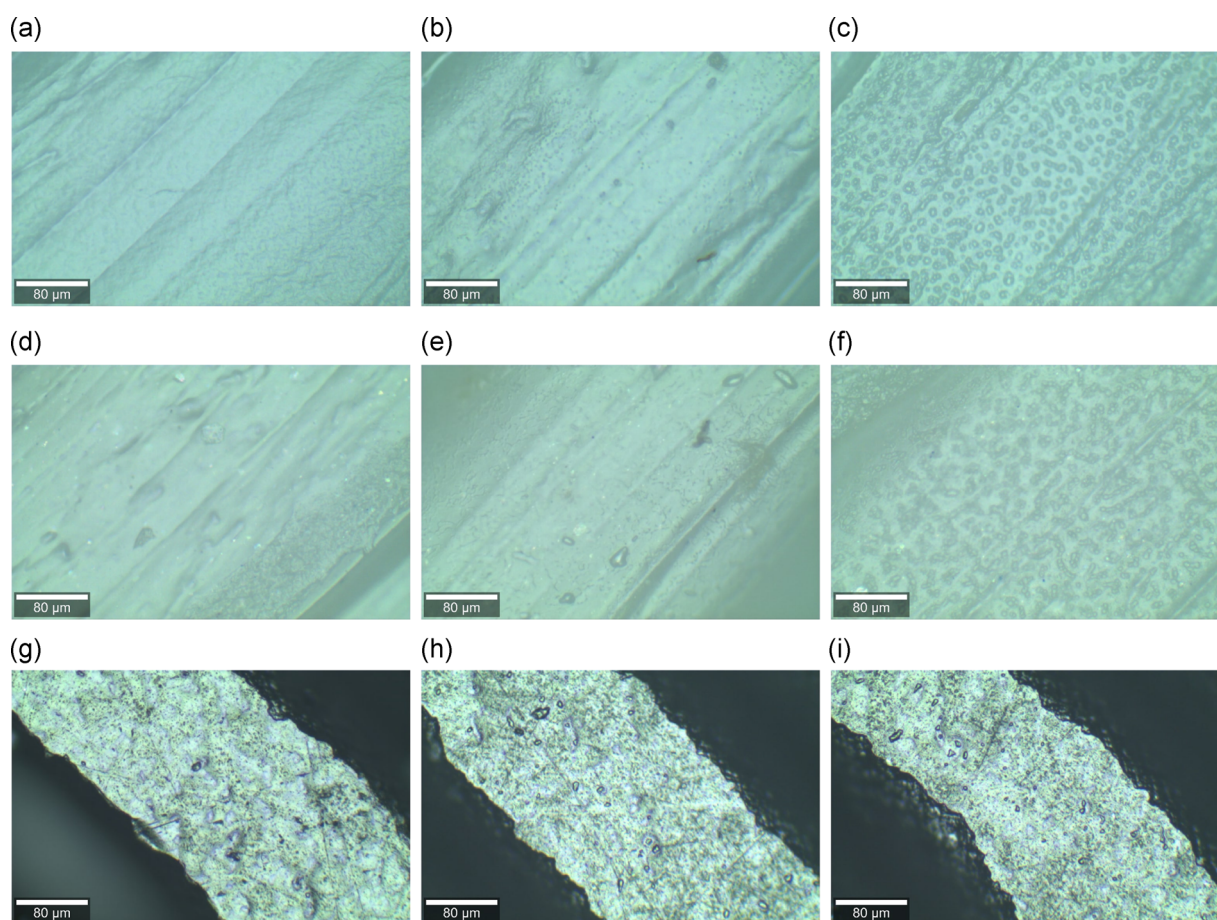
FIGURE 11 The optical images captured on plates made of new polylactic acid (PLA) before (a) and after (b,c) discharge treatment; old PLA before (d) and after (e,f) discharge treatment; acrylonitrile–butadiene–styrene before (g) and after (h,i) discharge treatment

PLA surface etching.[8,24] In spite of this etching, no evident mechanical degradation of 4 mm thick plates was observed. Thus, we propose that both PLA-made plates sustained the O_3 and UV exposure within the testing period with partial surface morphology changes only. In contrast, O_3 and UV exposure seems to have a negligible effect on the ABS plate. The morphology and microstructure of ABS-made plates remained almost the same, which resemble better material stability during the discharge treatment compared to PLA plates. However, the scratches observed by optical microscopy indicate the high softness of the ABS plates. The width of the seen ABS stripes in Figures 11g–i depends on the width of the stripes' top parts, which were in the focus of the microscope and are in agreement with SEM images Figures 10g–i.

5.2 | Raman spectra analysis

The Raman spectra of both PLA plates after the background subtraction in Figure 12 were found to be very similar. The dominant bands observed in the fingerprint region from 840 to 1,840 cm^{-1} correspond to those reported in literature: C–COO-stretching (the strongest band at 874 cm^{-1}), CH_3 asymmetric deformation (intensive band at 1,455 cm^{-1}) and C=O-stretching (band centered around 1,771 cm^{-1} with shoulder towards lower wavenumbers).[24–28] Here, it should be noted that the wide shoulder of C=O-stretching (band centered around 1,771 cm^{-1}) may be an indication of partial PLA crystallization that is resembled by the band splitting (evidence of band around 1,753 cm^{-1} in current case).[25,26,28] The other bands, assigned to C–CH_3-stretching (band at 1,046 cm^{-1}[25,26,28]), C–O–C-stretching,[25,28] and/or CH_3 out-of-plane deformation[26] (band around 1,095 cm^{-1}), CH_3-bending modes (bands at 1,129 and 1,386 cm^{-1}),[25,26,28] CH in-plane and out-of-plane bending (bands around 1,300 and 1,357 cm^{-1}, respectively),[25,26] were also resolvable. In addition to the above-mentioned bands, the spectra of old PLA plates demonstrate very weak bands around 1,184 and 1,222 cm^{-1}, which were assigned to the ester group
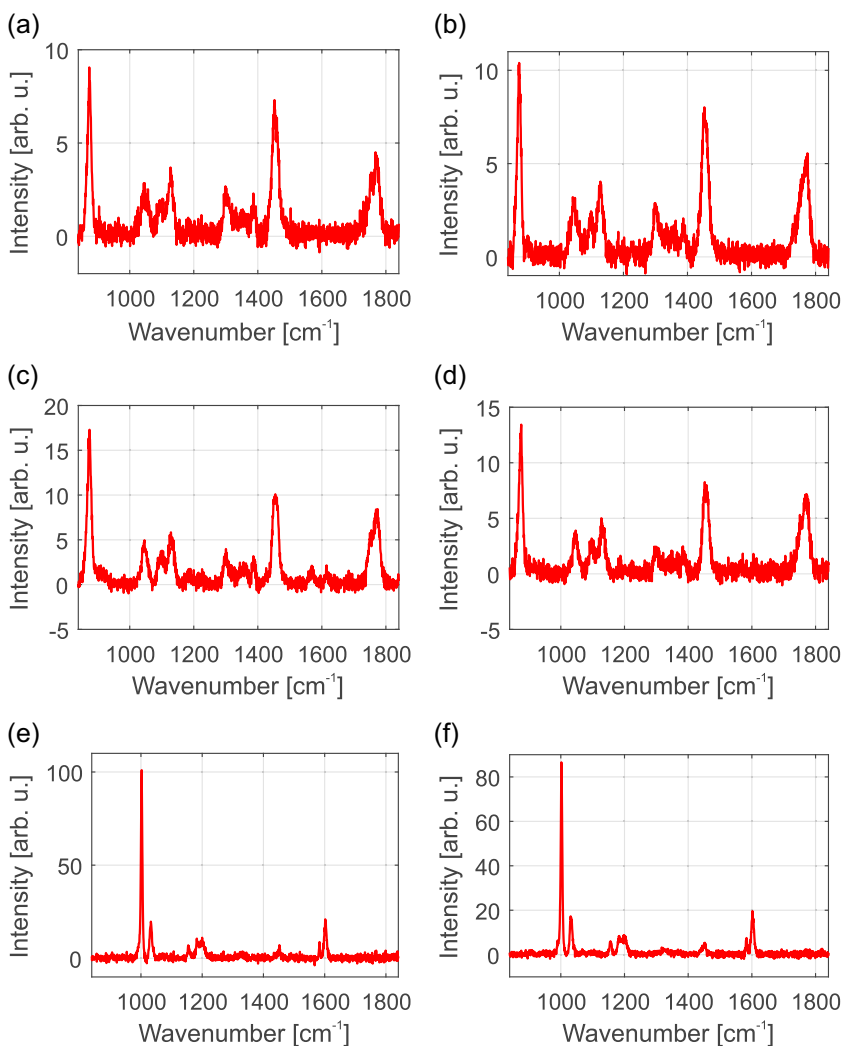
FIGURE 12 The corrected Raman shift spectra collected on plates made of new polylactic acid (PLA) before (a) and after (b) ozone and ultraviolet (UV) exposure; old PLA before (c) and after (d) ozone and UV exposure; acrylonitrile–butadiene–styrene before (e) and after (f) ozone and UV exposure

stretching,[25,28] with possible contribution of CH out-of-plane deformation[26] and weak bands around 1,568 and 1,615 cm^{-1} that are not reported to be typical for the PLA spectrum. They can be attributed to CC vibrations of the aromatic ring chain,[29] which indicate some kind of PLA filament contamination during the storing. This assumption seems to be true, because after the old PLA plates' O_3 and UV exposure processing, these bands (around 1,568 and 1,614 cm^{-1}) are significantly suppressed. The other bands, including C–H-stretching modes of CH_3 and CH_2 groups (bands in the 2,800–3,100 cm^{-1} range)[24–28] seen in the wide spectra (not shown), were not changed or changes were below the detection limit.

In contrast to PLA plates, it was found that radiation of ABS with a laser beam at power 10 mW caused fast plate degradation/damage observable by a microscope. Moreover, the fluorescent background of the as-measured spectra on ABS plates was significantly stronger. Therefore, in the case of ABS, the spectra were collected with a laser power 2 mW. The lower power was compensated by the longer integration time of spectra accumulation. The bands observed in the fingerprint region from 840 to 1,840 cm^{-1} were attributed to those reported in literature: benzene ring-breathing mode (intensive and relatively narrow band at 1,002 cm^{-1}), C–H in-plane vibration of benzene (band at 1,032 cm^{-1}) and C–C-stretching vibration modes of benzene (bands at 1,583 cm^{-1} and at 1,602 cm^{-1}), all characteristic for styrene.[30,31] Besides, the bands related to out-of-plane (1,156 cm^{-1}) and in-plane (1,183 cm^{-1}) deformations of the C–H bond of the benzene ring, C–C-stretching vibration (band centered around 1,200 cm^{-1}) and weak band (around 1,452 cm^{-1}) of CH_2 vibration with shoulder (centered around 1,440 cm^{-1}) related to C–C asymmetric stretching were observable.[30] By contrast, the band characteristic for C=C-stretching vibration of butadiene

(to be at 1,668 cm^{-1}) was not observed.[30,31] Here, it also should be noted that in the measured wide spectrum (not shown), there was no evidence of the characteristic of acrylonitrile $C \equiv N$-stretching (to be at 2,242 cm^{-1}),[30,31] whereas CH_2 and =C–H-stretching vibrations (bands in the 2,800–3,100 cm^{-1} range) were clearly seen. Whilst, this absence of the acrylonitrile band can be attributed to the presence of colouring additives in the used ABS, that can alter Raman spectra significantly,[31] the additional absence of characteristic butadiene band indicates the dominance of polystyrene component in the used ABS. The Raman shift measurements on ABS-made plates after the O_3 and UV radiation treatment are in good agreement with SEM and optical images and demonstrate no evident change in the spectrum.

5.3 | FTIR spectra analysis

The FTIR spectra of both old and new PLA before treatment revealed very similar spectra characteristics (see Figure 13).

The strong band at 1,750 cm^{-1} is related to the C=O-stretching.[32] This band is obviously a combination of several bands related to the various crystalline modifications of the PLA polymer.[33] Other oxygen-related bands are centered at 1,265 (combination of CH_3-bending and C–O stretch[28]), 1,180 (asym C–O–C stretch[32]), and 1,080 cm^{-1} (sym C–C–O stretch).[34] Other spectral bands are related to various stretching and bending vibrations of CH_X group, namely, 1,452 (CH_3-bending[34]), 1,381 (CH-bending[34]), 1,360 (CH-bending[28]), 1,130 (CH_3-rocking[34]), 1,044 (C–CH_3-stretching[34]) and 957 cm^{-1} (skeletal band[33]). The bands centered at 867 and 754 cm^{-1} are somehow related to amorphous and crystalline phase within PLA material.[28] Contrary to new PLA, the spectra of old PLA contained additional
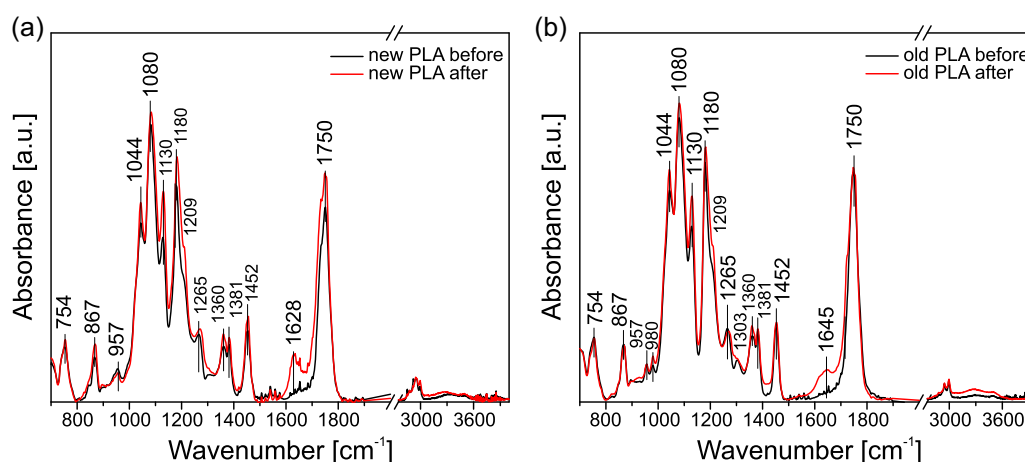
FIGURE 13 ATR–FTIR spectra of (a) new PLA; (b) old PLA before and after ozone and ultraviolet exposure. ATR, attenuated total reflection; FTIR, Fourier-transform infrared spectroscopy; PLA, polylactic acid

bands at 1,303 (CH_2 deformation[34] or CH-bending mode[28]) and 980 cm^{-1}. Since the spectra transcribe, besides CH_3-stretching vibrations, traces of other CH_X-stretching vibrations as well, we suppose, that the bands at 1,303 and 980 cm^{-1} might be somehow connected with a small contamination of old PLA plates by some hydrocarbons.

Comparison of the FTIR spectra of PLA (both new and old) plates before and after O_3 treatment revealed an additional broad band at 1,645 cm^{-1} (1,628 cm^{-1} resp.) of medium intensity. This band can be attributed to the C=C double bond[34,35] or a bending vibration of the –OH group.[32] Both effects could be possibly induced by PLA treatment. From the intensity of the band, as well as the same position and intensity of other bands, we can assume that the material did not undergo dramatic changes in its quality. With respect to the penetration depth of the evanescent wave probing the material in ATR spectroscopy, the mentioned changes are more or less related to changes in the material surface.[35]

The FTIR spectra of the ABS copolymer (see Figure 14) revealed a strong band at 695 cm^{-1} related to the out-of plane C–H vibration of the styrene aromatic ring.[36] Signals of medium intensity are localized at 1,492 (aromatic ring of styrene[36,37]), 1,451 (CH_2 scissoring mode[38]), 749 (CH deformation) and 538 cm^{-1}. Besides that, the FTIR spectra contain a number of weak signals. Signals common to both untreated and treated ABS are found at, for example, 1,601 (styrene aromatic ring[38]), 964 (C=CH deformation of polybutadiene[37]) and 907 cm^{-1} (CH deformation[39]). A few more signal of weak intensity are also found solely in the spectra of ABS after treatment, namely 1,726 (C=O stretch[29]), 1,629 (C=C stretch[38]) and 1,276 cm^{-1}.

The later-mentioned signals could be attributed to changes in the material surface by the O_3 and/or UV treatment. It is worth mentioning here that we did not observe a characteristic C ≡ N-stretching of the nitrile group in the FTIR spectra of ABS. It is unlikely, but the absence of this band can be caused by the usage of diamond crystal for ATR spectroscopy, where intrinsic diamond crystal absorption manifests itself in the area of our interest concerning the C ≡ N group.

5.4 | Material analysis summary

The observations of materials analysis are summarized as follows. The plates made of PLA (either vacuum packed or stored at ambient conditions) demonstrate better individual stripes sticking (with narrow valleys between them) than ABS-made plates. Although the top part of stripes in case of ABS plates is more flat and homogeneous than the stripes of PLA plates, the deep valleys between ABS stripes lead to
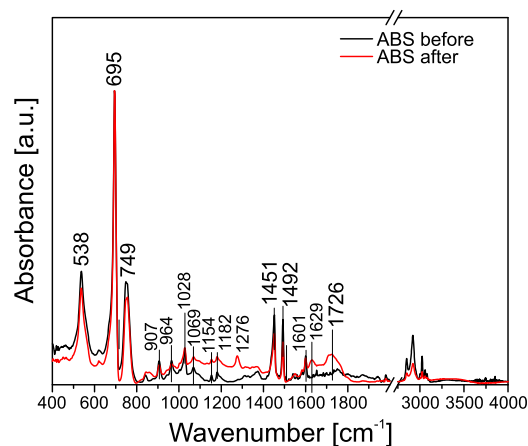
FIGURE 14 ATR–FTIR spectra of ABS polymer before and after ozone and ultraviolet exposure. ABS, acrylonitrile–butadiene–styrene; ATR, attenuated total reflection; FTIR, Fourier-transform infrared spectroscopy

fractures at some places that can negatively affect the overall chamber sealing. Moreover, the observed top ABS stripes' surface has numerous scratches, indicating higher softness of used material, whereas no scratches were evidenced on the surface of PLA plates. The 18-hr combination of O_3 exposure and UV radiation resulted in bubble-like features formation and partial surface morphology modification in case of PLA-made plates; however, the plates remained without fractures between stripes. For the plate made of ABS, no or negligible morphology change after the O_3 and UV exposure was observed. The Raman shift measurements before and after the O_3 and UV exposure demonstrate no evident changes in case of new PLA and ABS-made plates, whereas the old PLA plates show decrease in bands attributed to contamination due to storing at ambient conditions. On the contrary, the ATR–FTIR comparative analysis of plates' spectra before after O_3 discharge in all cases reveal new bands in the spectra of discharge-treated plates. These bands were attributed to changes in the plates' surface caused by exposure to 18-hr O_3 discharge. It should be noted that Raman and ATR–FTIR spectroscopy in the spectra related to ABS was not able to detect band characteristic for nitrile group stretching, while bands characteristic for butadiene were rather weak. These bands then most probably were affected by the colouring additives and high amount of polystyrene in the used ABS filament. Next, the Raman shift and ATR–FTIR spectra of old PLA plates contain the weak bands that point out storage at unstable conditions. Nevertheless, the material remains fully processable and mechanically behaves as the vacuum-stored ones. All the above-mentioned results indicate that within the 18-hr period, the used material (both PLA and ABS) was able to sustain the O_3 and UV exposure with minor morphology

and chemical composition changes that, however, had no effect on the plates bulk and sealing properties. Nevertheless, the deep valleys between the stripes of ABS-made plate and thus the risk of fractures need to be kept in mind.

6 | CONCLUSIONS

We investigated the possibility of the usage of 3D printing materials for applications in generator of active particles, O_3 and UV radiation based on electrical discharges. As testing samples, we used plates from PLA or ABS materials, which were integrated into the generator's bodies. As a qualitative indicator of active particles, we used O_3 because of the wide range of its applications and UV because of its usage for sterilization purposes. After exposure of the plates to the O_3 and UV irradiation can be from the surface analysis by electron and optical microscopy, WCA measurement, Raman spectra, and Fourier-transform infrared spectroscopy concluded that from the macroscopic point of view both materials could be used for active particles, O_3 and UV radiation generators, at least on the scale of experimental usage. Nevertheless, we give preference to chambers made on PLA basis because of potentially higher mechanical and sealing stability and also due to ecological considerations. Investigated materials offer freedom flexibility and rapid discharge chamber manufacturing that can be operationally adjusted for prototyping of various types of the DBDs.

ORCID

Jan Mikeš http://orcid.org/0000-0003-2219-4320
Stanislav Pekárek http://orcid.org/0000-0002-7171-9341
Oleg Babčenko http://orcid.org/0000-0002-2228-1048
Ondřej Hanuš http://orcid.org/0000-0001-7869-5744
Jakub Kákona http://orcid.org/0000-0003-3666-205X
Pavla Štenclová http://orcid.org/0000-0003-3720-910X

REFERENCES

[1] J.-Y. Park, I.-H. Lee, *J. Polym. Res.* **2010**, *18*, 1287.

[2] H. Lee, N. H. Nguyen, S. I. Hwang, H. J. Lee, S. K. Hong, S.-S. Byun, *Int. Braz. J. Urol.* **2018**, *44*, 952.

[3] A. J. Capel, R. P. Rimington, M. P. Lewis, S. D. R. Christie, *Nat. Rev. Chem.* **2018**, *2*, 422.

[4] O. Avinc, A. Khoddami, *Fibre Chem.* **2009**, *41*, 391.

[5] E. Macdonald, R. Salas, D. Espalin, M. Perez, E. Aguilera, D. Muse, R. B. Wicker, *IEEE Access* **2014**, *2*, 234.

[6] S. J. Trenfield, A. Awad, A. Goyanes, S. Gaisford, A. W. Basit, *Trends Pharmacol. Sci.* **2018**, *39*, 440.

[7] J. C. Middleton, A. J. Tipton, *Biomaterials* **2000**, *21*, 2335.

[8] M. Wang, P. Favi, X. Cheng, N. H. Golshan, K. S. Ziemer, M. Keidar, T. J. Webster, *Acta Biomaterialia* **2016**, *46*, 256.

[9] M. Neumüller, A. Reichinger, F. Rist, C. Kern, *3D Research Challenges in Cultural Heritage*, LNCS 8355, Springer-Verlag, Berlin-Heidelberg, Germany **2014**, p. 119.

[10] G. Ryder, B. Ion, G. Green, D. Harrison, B. Wood, *Automat. Construct.* **2002**, *11*, 279.

[11] V. G. Gokhare, D. N. Raut, D. Shinde, *Int. J. Eng. Res. Technol.* **2017**, *6*.

[12] F. Fattahi, H. Izadan, A. Khoddami, *Prog. Color. Color. Coat.* **2012**, *5*, 15.

[13] S. Kanazawa, W. Eto, W. Imagawa, S. Akamine, R. Ichiki, *3rd Korea–Japan Conf. Plasma Electrostat. Technol.*, Tokyo, Japan, 103-106, **2014**.

[14] S. Kanazawa, W. Imagawa, S. Matsunari, S. Akamine, R. Ichiki, K. Kanazawa, *J. Plasma Environ. Sci. Technol.* **2017**, *11*, 38.

[15] S. K. Selvamani, M. Samykano, S. R. Subramaniam, W. K. Ngui, K. Kadirgama, G. Kanagaraj, M. S. Idris, *AIP Conf. Proc.*, Kuantan, Malaysia, *2059*, **2019**.

[16] H. Tsuji, *Macromol. Biosci.* **2005**, *5*, 569.

[17] W. J. Groot, T. Borén, *Int. J. Life Cycle Assess.* **2010**, *15*, 970.

[18] X. Qi, Y. Ren, X. Wang, *Int. Biodeterior. Biodegrad.* **2017**, *117*, 215.

[19] G. Wypych *Handbook of Polymers* (Ed: G. Wypych), Elsevier, Oxford, UK **2012**, pp. 436–440.

[20] G. Wypych *Handbook of Polymers* (Ed: G. Wypych), Elsevier, Oxford, UK **2012**, pp. 3–10.

[21] R. Lee, M. L. Coote, *Phys. Chem. Chem. Phys.* **2016**, *18*, 24663.

[22] R. Ramani, C. Ranganathaiah, *Polym. Degrad. Stab.* **2000**, *69*, 347.

[23] G.-H. Koo, J. Jang, *Fibers Polymers* **2008**, *9*, 674.

[24] H. Eren, O. Avinc, P. Uysal, M. Wilding, *Tex. Res. J.* **2011**, *81*, 1091.

[25] D. Qin, R. T. Kean, *Appl. Spectrosc.* **1998**, *52*, 488.

[26] T. Suzuki, A. Ei, Y. Takada, H. Uehara, T. Yamanobe, K. Takahashi, *Beilstein J. Org. Chem.* **2014**, *10*, 2997.

[27] K. Vano-Herrera, A. Misiun, C. Vogt, *J. Raman Spectrosc.* **2015**, *46*, 273.

[28] K. Yuniarto, Y. A. Purwanto, S. Purwanto, B. Welt, H. Purwadaria, T. Sunarti, *AIP Conf. Proc.*, Semarang, Indonesia, *1725*. 2016.

[29] G. Socrates, *Infrared and Raman characteristic group frequencies: Tables and charts*, Wiley, **2004**.

[30] G. Bikulčius, I. Ignatjev, A. Ručinskienė, *Transact. IMF* **2013**, *92*, 47.

[31] R. Lenz, K. Enders, C. A. Stedmon, D. M. Mackenzie, T. G. Nielsen, *Mar. Pollut. Bull.* **2015**, *100*, 82.

[32] J. Mofokeng, A. Luyt, T. Tábi, J. Kovacs, *J. Thermoplast. Compos. Mater.* **2012**, *25*, 927.

[33] E. Meaurio, N. López-Rodríguez, J. R. Sarasua, *Macromolecules* **2006**, *39*, 9291.

[34] M. A. Cuiffo, J. Snyder, A. M. Elliott, N. Romero, S. Kannan, G. P. Halada, *Appl. Sci.* **2017**, *7*, 579.

[35] W. Urbaniak-Domagala *Advanced aspects of spectroscopy* (Ed: M. A. Farrukh), IntechOpen, Rijeka, Croatia **2012**, pp. 82–104.

[36] S.-U. Zhang, *Appl. Sci.* **2018**, *8*, 1224.

[37] P. A. Steeman, R. J. Meier, A. Simon, J. Gast, *Polymer* **1997**, *38*, 5455.

[38] C. Desrousseaux, R. Cueff, C. Aumeran, G. Garrait, B. Mailhot-Jensen, O. Traoré, V. Sautou, *PLOS One* **2015**, *10*, 1.

[39] R. J. Meier, *Macromol. Symp.* **1997**, *119*, 25.

A.2 Driving voltage frequency and active electrode setup effects on ozone and UV generation of dielectric barrier discharge in air

**THE EUROPEAN
PHYSICAL JOURNAL D**

Regular Article

Driving voltage frequency and active electrode setup effects on ozone and UV generation of dielectric barrier discharge in air

Stanislav Pekárek[a] and Jan Mikeš

Czech Technical University in Prague, Faculty of Electrical Engineering, Technická 2, 166 27 Prague 6, Czech Republic

Abstract. We studied the effect of the driving voltage of frequencies 4, 7, and 10 kHz and two different active electrode setups on electrical properties, ozone production, and UV radiation of wavelengths $320-420$ nm of the dielectric barrier discharge in air. The first active electrode setup comprised the strip electrode made from the copper foil. The second setup comprised the stainless steel wire mesh electrode with square cells. The ozone concentration, as well as the ozone production yield, is higher for the discharge with the strip active electrode setup than for the discharge with the mesh active electrode set up. The increased frequency decreases the voltage required to obtain maximum ozone concentration. The intensity of UV radiation is higher for the discharge with the mesh active electrode setup than for the discharge with the strip active electrode setup for all investigated frequencies. The intensity of UV radiation at a particular voltage depending on the frequency and active electrode setup sharply increases. The high concentrations of ozone produced by the discharge with the strip active electrode setup are accompanied by lower intensities of generated UV radiation. For the discharge with the mesh active electrode setup, the situation is reversed.

1 Introduction

The chemically reactive species, together with the ultraviolet radiation (UV) generated by electrical discharges, are responsible for high non-thermal plasma reactivity, which can be used for a variety of applications [1,2]. In our study, we focused on ozone production and UV radiation of dielectric barrier discharge (DBD) in the air. We used ozone because it has a wide range of various usages such as water treatment, medicine, sterilization, food storage time increase, or in agriculture [3–5]. UV radiation can be used for inactivation of bacteria and viruses, sterilization, disinfection and surface treatment [6–9]. Except for it, the UV radiation can also be used for the photocatalyst activation [10,11].

Ozone generation in a DBD in the air at atmospheric pressure is a complex process involving a number of ozone generation as well as ozone decomposition reactions [12–15]. In DBD, the current flow is brought about by a large number of statistically distributed microdischarges [16]. Since ozone, formed in the microdischarge channels, diffuses immediately after its generation into the discharge volume [12,17] its production is affected by the number and distribution of microdischarge channels as well as their properties. These properties can be influenced by the electrical parameters of the discharge, the gap spacing, or properties of the dielectrics and the metal active

electrode. The discharge ozone production is consequently a result of a combination of all these factors.

The DBDs can exist in three basic configurations: volume (VDBD); surface (SDBD) and coplanar (CDBD) [18]. According to this paper, in the case of the SDBD, the development of the microdischarges along the dielectric surface depends on the electric field distribution. This field distribution, which is, first of all, determined by the active (powered) electrode setup, affects not only the existence of microdischarges but also their mutual influence. There exist numerous planar active electrode setups of SDBD that have been tested, such a set of parallel wires, strips, circles, squares, hexagonal or honeycomb structures, meshes, etc. [19–29]. Our attention in this study was focused on SDBD and VDBD.

An important quantity affecting the properties of SDBD is the frequency of the driving voltage. This frequency influences discharge properties through the interaction of microdischarges with residual charges left on the dielectric surface during the whole discharge cycle, as well as the influence of excited species generated in one microdischarge on the formation of another microdischarge [30]. Thus, for example, if this frequency is too low to keep the microdischarge remnants from dissipation (low frequency means that the period is longer than the typical lifetime of the microdischarge remnant), microdischarge repulsion effects are not observed [16].

Another output of SDBD is the emission of electromagnetic radiation of various wavelengths, also involving UV radiation. Efficient and cheap sources of UV

[a] e-mail: pekarek@fel.cvut.cz

radiation are important for various applications. At present, most frequent commercial sources of UV radiation are high-pressure mercury lamps with the emission of the 253.65 nm. Though there exist the attempts of development of planar UV excilamps excited by a surface barrier discharge as well as the studies of UV spectrum emitted by filamentary nanosecond surface dielectric barrier discharge [31–33], our research is not oriented in this direction. However, the synergy between active species and UV radiation generated by the discharge is interesting for the surface treatment applications because simultaneous ozone and UV application are generally effective for removing organic contaminants from the surfaces. In this case, the organic compounds are converted into volatile substances (e.g., water, carbon dioxide, nitrogen) by decomposition by ultraviolet rays and by strong oxidation during the formation and decomposition of O_3 and are removed from the contaminated surface [34].

In the air, the important contribution to the UV emission is caused by molecular bands of nitrogen [35,36]. From the wide band of the discharge electromagnetic radiation emitted by the discharge, we focused on the radiation within the range of wavelengths $320-420$ nm. One of the reasons why we choose this range of wavelengths is that this radiation can be used for surface treatment, for activation of various photocatalysts, e.g., for ozone production enhancement or decomposition of volatile organic compounds. Thus for activation of TiO_2 in the anatase phase is required the wavelength of 388 nm, TiO_2 in the rutile phase requires 413 nm, the photocatalyst ZnO requires 376 nm, $BaTiO_3$ needs 376 nm and finally for $SrTiO_3$ activation is required the radiation of wavelength 388 nm. Another reason for this choice of wavelengths is microorganism inactivation, which can be achieved at the UV wavelengths ranging from 100 to 400 nm, although a wavelength of 254 nm is the most effective [3].

In this study, we tested two active electrode setups, taking into account the characteristic dimensions of microdischarges [16,18]. In the first case, we used the active electrode setup for which the microdischarges could fully develop (strips). Secondly we used the active electrode setup for which the existence of microdischarges is substantially suppressed (stainless steel wire mesh with small dimensions of square cells). Our attention was focused on the study of discharge voltage and its frequency effects on discharge power, ozone production, and UV radiation for the DBD in the air with these two different active electrode setups.

The obtained results could be useful for the proper choice of the electrical parameters and the active electrode setup of the dielectric barrier discharge so that it can be used as a simultaneous source of balanced doses of ozone and UV radiation, e.g., for surface treatment of materials, biomedical applications, sterilization or activation of photocatalysts.

2 Experimental apparatus

The experimental apparatus used in this study is shown in Figure 1. It consists of a flat discharge chamber with the electrode system, a high voltage power supply system with electrical parameters diagnostics, an ozone monitor, a UV sensor and monitor, and an air supply system.

Our experiments were performed with the DBD of two different active electrode sets ups situated in two identical flat discharge chambers. These discharge chambers of dimensions $122 \times 122 \times 18$ mm were made by 3D printing from the polylactic acid-based material.

On the upper side of the discharge chamber was the opening for the plexiglass window of dimensions 80×70 mm. The space between the upper side of the dielectric plate and this window defined the height of the discharge volume, which was 6.5 mm. On the lower side of the chamber was a rectangular opening for the water cooler. On the left side of the chamber was the slit into which was inserted the dielectric alumina plate of dimensions $108 \times 108 \times 0.635$ mm, carrying the electrode setups. This alumina plate had a content of Al_2O_3 of 96%, a dielectric constant for 1 MHz of 9.6, electric strength of 14 kV/mm, and the heat conductivity for the temperature of 25°C was 24 W/mK.

The input of air into the discharge chamber was from the left side through three tubes of outer diameter 2.5 mm. Similarly, the output of air with the gas discharge products was from the right side of the discharge chamber. To measure the temperature of the output gas near the output of the discharge chamber was the optical fiber of the Neoptix thermometer (T).

We tested two active electrode setups created on the upper side of the alumina plate. The first one, the strip active electrode was formed by 14 strips of the length 59 mm, and width 1 mm, was made from a copper foil of thickness 0.035 mm. The distance between adjacent strips was 3 mm. This electrode was glued to the alumina plate. The capacitance of the electrode system with this active electrode was 202 pF. The second active electrode setup consisted of a stainless steel wire mesh with square cells of inner dimensions 1×1 mm. The diameter of the wire used for the mesh was 0.4 mm. Due to the structure of the mesh, the wires touched the alumina plate surface at points of intersections of orthogonal wires. The capacitance of the electrode system with the mesh active electrode was 103 pF.

The square ground electrode, on the lower side of the alumina plate, was the same for both types of the active electrode. It was made from the copper foil of dimensions $80 \times 90 \times 0.035$ mm. This electrode was through the thermal pad in contact with a copper water cooler.

The active electrode was connected to an AC high voltage power supply system. This system consisted of function/arbitrary waveform generator DG 1022, wideband AC power amplifier AL-600-HF-A (output power 600 W, frequency response 20 Hz to 800 kHz) and a high-frequency high voltage transformer AL-T1000.5 (peak voltage 10 kV, output power 1000 W and frequency response 4 to 12 kHz). The discharge was driven by sinusoidal voltage.

The average discharge power was calculated on the basis of the following equation:

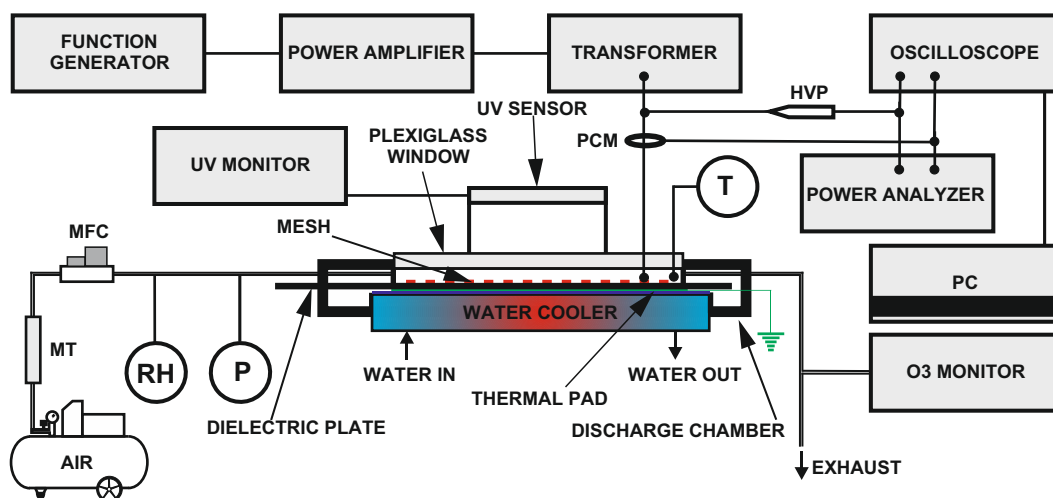$$P_{av} = \frac{1}{T} \int_0^T V(t)I(t)dt. \tag{1}$$

Fig. 1. The experimental apparatus.

In this equation, T is the period, $V(t)$, and $I(t)$ are voltage and current signals, respectively. The voltage and current waveforms were monitored by four channels digital oscilloscope DS 1204 B (200 MHz; 2 GSa/s). The discharge voltage signal was sampled and recorded on the first channel of this oscilloscope with a high voltage probe (HVP-28HF, Pintek, division ratio 1000/1, frequency up to 200 MHz). To determine the discharge current, we used a signal obtained from a Pearson current monitor (PCM, model 2877) with a bandwidth of up to 200 MHz. For instantaneous orientation power measurements, we simultaneously used the Rohde & Schwarz 8015 power analyzer. The power used for the calculation of the ozone production yield was determined from voltage and current monitor probes.

The concentration of ozone at the output of the discharge chamber was measured by the absorption of the 254 nm UV spectral line with an API 450 ozone monitor. The accuracy of ozone concentration measurements was ±0.5%.

We measured discharge UV emission for the wavelengths 320 to 420 nm using the AccuMAX UV monitor. We used an XS-365 sensor of the diameter of 21.6 mm for a range of intensities of $0-100$ mW/cm². For UV intensities measurements, the upper plexiglass window of the discharge chamber was removed and substituted by the window with the opening in which was inserted the tube of the inner diameter of 36.5 mm. The center of this tube coincided with the center of the active electrode. The UV sensor was situated at the end of this tube at a distance of 63.5 mm from the upper side of the alumina plate so that the UV peak intensities were obtained by registering the radiation emitted directly by the discharge.

The air for the discharge was supplied from an oil-free compressor through the moisture trap (MT) and the mass flow controller (MFC). The relative humidity of input air was measured by a sensor (RH), and the pressure in the discharge chamber was measured with a digital manometer (P).

3 Experimental results and discussion

The experiments were performed with the discharges in the air at constant flowrate through the discharge chamber 3 slm. At this flowrate, the pressure in the discharge chamber exceeded the atmospheric pressure by 10 hPa. The relative humidity of the input air was 20%. Due to the method of UV intensities measurements, the measurements of ozone concentrations and UV intensities were not performed simultaneously, but first of all, we determined ozone concentrations and at the next step were measured UV radiation intensities.

We used the sinusoidal driving voltage of frequencies 4, 7 or 10 kHz. The measurements of ozone concentrations were recorded for a given applied voltage and frequency after 1.10 min from the discharge ignition when the discharge steady-state ozone levels were recorded by the ozone monitor. Simultaneously with the ozone concentration, the temperature of the gas in the discharge chamber was recorded. Depending on the frequency and applied voltage, this temperature varied between 20.3 till 32.1°C. This temperature is low to cause thermal decomposition or to play a crucial role in the reaction rates of ozone decomposition reactions.

The photographs of the discharge with the strips or the mesh active electrode for the same discharge voltage, frequency, and airflow are shown in Figures 2a and 2b respectively. The photographs were taken with Nikon 850 camera, objective Micro-Nikkor 55 mm, $f = 5.6$, ISO = 1000 and exposition time 1/2 s.

In the case of the discharge with the strip active electrode setup, the electrode was made from a copper foil; consequently, the true surface dielectric barrier discharge could develop. On the photograph of this discharge, see Figure 2a could be seen that due to the distance between the strips, the microdischarges originating at strips can freely develop and terminate between the strips. This situation is reflected by the existence of the dark region in the middle between adjacent strips. However, at the corners when the strips meet with the connecting part of
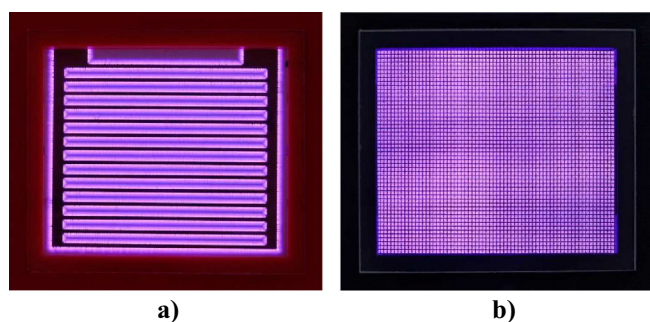
Fig. 2. Discharge with the strip active electrode setup (a) and the mesh active electrode setup (b). $V_{\max} = 3120\,\text{V}$, $f = 10\,\text{kHz}$ and $Q_{\text{air}} = 3\,\text{slm}$.

this active electrode, the partial suppression of microdischarges originating from the strips and the perpendicular part of the electrode connecting the strips (on the left and right side of Fig. 2a) can be observed. This suppression is reflected by the darker regions in the form of triangles at these corners. These triangles and darker regions between two adjacent strips could be seen in the zoom image of the discharge from Figure 2a, in Figure 3.

In the case of the discharge with the mesh active electrode setup, the electrode was made from stainless steel wire. Due to the structure of the mesh, the wires touched alumina plate surface at points of intersections of orthogonal wires, which resulted in the production of plasma produced not only by the surface but also by the volume dielectric barrier discharge. The detailed analysis of the physics of various configurations of the dielectric barrier discharges configurations is given in [18]. Following this review, all configurations of DBD exist in the pre-breakdown, streamer, and the decay phases. As long as we used different active electrode setups, we affected the distribution of the electric field and, consequently, the pre-breakdown phase. Apart from it, due to the small dimensions of the mesh cells, the development of microdischarges from each side of the square cell was suppressed. It could be therefore said that when the geometry of the active electrode does not allow full development of the microdischarges and there exist volume and surface discharge simultaneously, the visual appearance of the discharge is changed in comparison with the discharge with the geometry of active electrode with fully developed microdischarges.

3.1 Electrical parameters of the discharge

The DBDs are normally characterized by a large number of microdischarges per unit of electrode area and per period of the driving voltage. Their existence is accompanied by the current pulses. Under certain conditions, the microdischarges increase their cross-section, merge, and the discharge appears to be homogeneous. The occurrence of microdischarges and their pattern are determined not only by the amplitude and frequency of the driving voltage, type of the gas, its humidity, and presence of admixtures in the gas but also by the surface properties and

the geometry of the electrode arrangement. According to [37], the duration of microdischarges in air at atmospheric pressure and 1 mm discharge gap is of about $10-100\,\text{ns}$.

Since ozone formation is associated with these microdischarges, their number and distribution pattern plays for ozone generation important role. We, therefore, investigated the effect of the driving voltage and active electrode setup on the generation of these mirodischarges. The important information about the height and number of current pulses per unit of time brings the voltage-current (V–I) waveforms. To have an impression about these quantities in the following Figure 4 are, as an illustrative example, shown the V–I waveforms for the discharge from Figure 2a ($V_{\max} = 3120\,\text{V}$, $f = 10\,\text{kHz}$ and $Q_{\text{air}} = 3\,\text{slm}$) with the strip active electrode setup, for one-quarter of a period of the driving voltage.

To demonstrate the effect of the active electrode setup on the occurrence of microdischarges, the V–I waveforms for the discharge with the strips and mesh active electrode setups are shown in Figures 5 and 6, respectively. These figures are for the same driving voltage frequency 4 kHz and approximately the same discharge voltage. The waveforms correspond to the points, which are shown in Figure 9, showing the dependence of the discharge power as a function of the discharge voltage for the strip active electrode setup (point A) and the mesh electrode setup (point B).

From a comparison of these two figures can be seen the strong effect of the active electrode setup on the V–I waveforms. The difference in these waveforms is due to the different materials of active electrode (copper or stainless steel), the geometry of this electrode (strips or square mesh) as well as type of the electrode (foil or wire). Besides, in these two figures can also be seen the asymmetry in the number and height of current peaks that appear during the positive and negative discharge voltage half-periods for both active electrode setups. From Figure 5 can be concluded that for the discharge with the strip active electrode setup, the number and height of current peaks in positive discharge voltage half-periods are higher than in negative half-periods.

On the other hand, if the active electrode setup is changed from the strips to the mesh (Fig. 6), the V–I waveforms substantially change. In this case, the number and height of current peaks in negative discharge voltage half-periods are higher than in positive half-periods. Generally speaking, the polarity of the active electrode determines the discharge dynamics, which is rather different for the negative polarity from that with positive polarity (photoemission or emission of secondary electrons due to the impact of positive ions on the cathode) [18].

Another important quantity affecting voltage-current waveforms is the frequency of the driving voltage. The illustrative examples of the frequency effects on these waveforms for the mesh active electrode setup are shown in Figures 7 and 8. Figure 7 is for frequency 4 kHz, discharge voltage 2960 V and Figure 8 is for the frequency 10 kHz and voltage 3000 V.

From a comparison of these two figures can be seen that for the mesh active electrode for approximately the same discharge voltage, the current pulses are with
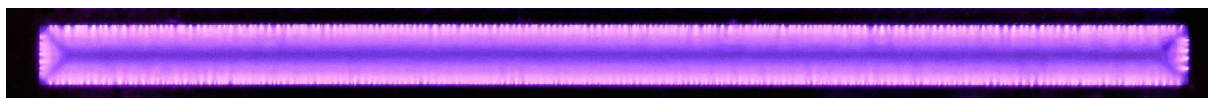
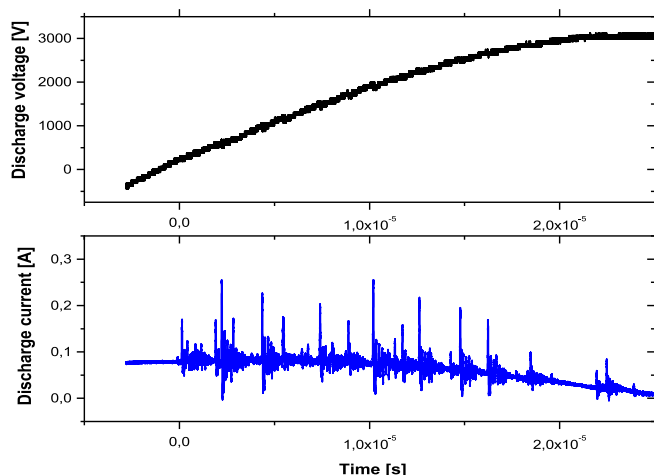**Fig. 3.** Zoomed image of the discharge between two adjacent strips.

Fig. 4. V–I waveforms for the discharge with the strip active electrode setup. $V_{\max} = 3120$ V, $f = 10$ kHz and $Q_{\mathrm{air}} = 3$ slm.

Fig. 6. V–I waveforms for the mesh active electrode setup. $V_{\max} = 4160$ V, $f = 4$ kHz and $Q_{\mathrm{air}} = 3$ slm. Point B in Figure 9.

Fig. 5. V–I waveforms for the strip active electrode setup. $V_{\max} = 4240$ V, $f = 4$ kHz and $Q_{\mathrm{air}} = 3$ slm. Point A in Figure 9.

an increasing frequency more numerous and have higher amplitude. Qualitatively the same effect was observed for the discharge with the strip active electrode. The explanation of the change in the number of current pulses per unit of time with the change of frequency [15] is mainly based on the accumulated charges of the microdisharges over the dielectric material from the preceding half cycle of the applied voltage, which enhances the electric field and subsequently the discharge in the next half cycle of the applied voltage. The results shown in Figures 5–8 agree and extend the results presented in [8,15,19,38,39] for the majority of active electrode configurations.

An important quantity for evaluation of the discharge efficiency from the standpoint of its ozone generation is the

discharge power. The dependencies of the discharge power as a function of the discharge voltage for the discharge with the strips or the mesh active electrode setups for frequencies 4, 7, and 10 kHz are shown in Figure 9.

From this figure, it is seen that the active electrode setup substantially influences the average discharge power. Generally speaking, for the particular voltage and frequency, the discharge with the mesh active electrode setup allows obtaining higher power than the discharge with the strip active electrode setup. Thus, for example, for the frequency 4 kHz and discharge voltage 4240 V, the average discharge power for the strip electrode setup is 16.5 W (point A), and for the mesh active electrode setup and the voltage 4160 V, the power is 38.3 W (point B). This result can be explained by plasma production not only by the surface but also by the volume dielectric barrier discharge.

The dependence of the discharge power on the frequency of the driving voltage for a particular active electrode setup corresponds to the already known results that is for a particular voltage, the increase in frequency increases average discharge power [15,40–42].

The change in electrical parameters of the discharge caused by the change in the frequency of the driving voltage, as well as by the change of the active electrode setup, is certainly reflected by the change of the discharge ozone production and UV radiation.

3.2 Discharge ozone production and intensity of UV radiation

The dependences of ozone concentrations produced by the discharge with the strips and the mesh active electrode setups and frequencies of the driving voltage 4, 7, and
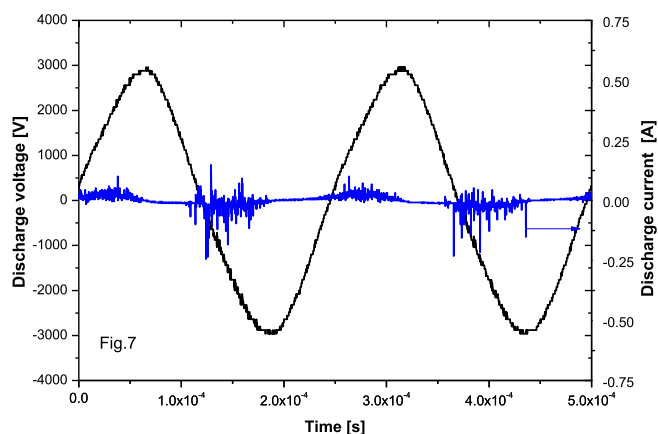
Fig. 7. V–I waveforms for the mesh active electrode setup. $V_{\max} = 2960$ V, $f = 4$ kHz and $Q_{\mathrm{air}} = 3$ slm. Point C in Figure 9.
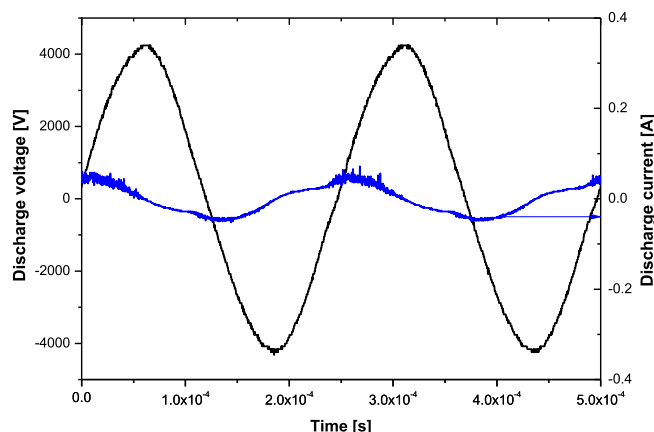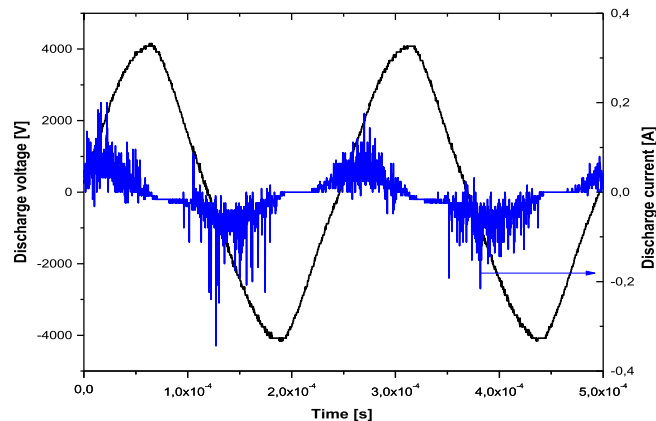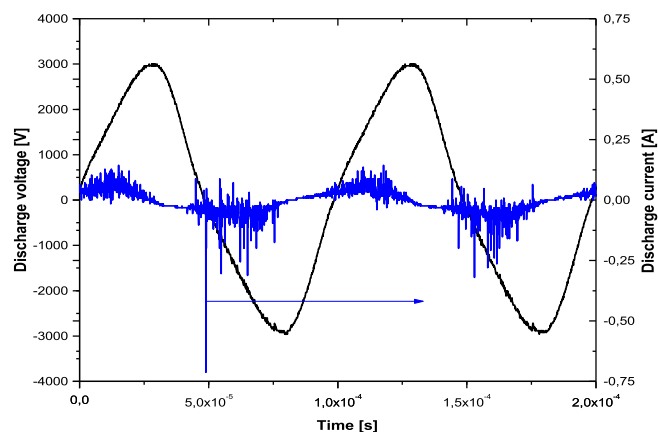

Fig. 8. V–I waveforms for the mesh active electrode setup. $V_{\max} = 3000$ V, $f = 10$ kHz and $Q_{\mathrm{air}} = 3$ slm. Point D in Figure 9.

Fig. 9. Average discharge power versus voltage for the discharge with the strips or the mesh active electrode and frequencies of the driving voltage 4, 7 and 10 kHz. Black squares – mesh active electrode; red circles – strip active electrode. Full symbols – frequency 4 kHz; horizontally crossed empty symbols – 7 kHz; half-empty symbols – frequency 10 kHz.

Fig. 10. Ozone concentration versus voltage for the discharge in the air with the strips or the mesh active electrode setups and frequencies of the driving voltage 4, 7 and 10 kHz. Black squares – mesh active electrode setup; red circles – strip active electrode setup. Full symbols – frequency 4 kHz; horizontally crossed empty symbols – frequency 7 kHz; half-empty symbols – frequency 10 kHz.

10 kHz as the functions of the discharge voltage are shown in Figure 10.

Each ozone concentration presented as a point in this figure represents an equilibrium between complex of processes leading to ozone generation and decomposition. This equilibrium concentration depends on various factors, such as the operating parameters of the discharge (voltage, current, frequency) as well as on the active electrode setup. From the comparison of the ozone concentration dependence on the discharge voltage for the strips or the mesh active electrode setups and frequencies of the driving voltage 4, 7, and 10 kHz can be concluded that except for the low voltage (<2100 V), the ozone concentration for the discharge with the strip active electrode set up is for all three frequencies higher than for the discharge with the mesh active electrode setup. From this figure, it is also seen that increased frequency decreases the voltage required to obtain maximum ozone concentration. This effect is more distinct for the strips than for the mesh active electrode setup. The results presented in this figure are in agreement and extend the results deal-

ing with the effect of frequency on ozone generation by the surface dielectric barrier discharge in dry air [40].

An important quantity from the standpoint of practical applications is the ozone production yield α, which is defined as the amount of energy required for the production of 1 g of ozone:

$$\alpha = \frac{0.385 \times \mathrm{O_3}\,[\mathrm{ppm}]}{P_{\mathrm{av}}\,[\mathrm{W}]} \ [\mathrm{g/kWh}]. \tag{2}$$

The numerical constant 0.385 in equation (2) involves the density of ozone as well as all conversion factors of the airflow rate and energy.

Fig. 11. Ozone production yield versus voltage for the discharge with the strips or the mesh active electrode and frequencies of the driving voltage 4, 7 and 10 kHz. Black squares – mesh active electrode setup; red circles – strip active electrode setup. Full symbols – frequency 4 kHz; horizontally crossed empty symbols – frequency 7 kHz; half-empty symbols – frequency 10 kHz.

Fig. 12. Peak intensity of UV radiation versus voltage for the discharge in the air with the strips or the mesh active electrode setups and frequencies of the driving voltage 4, 7 and 10 kHz. Black squares – mesh active electrode setup; red circles – strip active electrode setup. Full symbols – frequency 4 kHz; horizontally crossed empty symbols – frequency 7 kHz; half-empty symbols – frequency 10 kHz.

The dependences of ozone production yield versus discharge voltage for the discharge with the strips and the mesh active electrode setups and frequencies of the driving voltage 4, 7 and 10 kHz are shown in Figure 11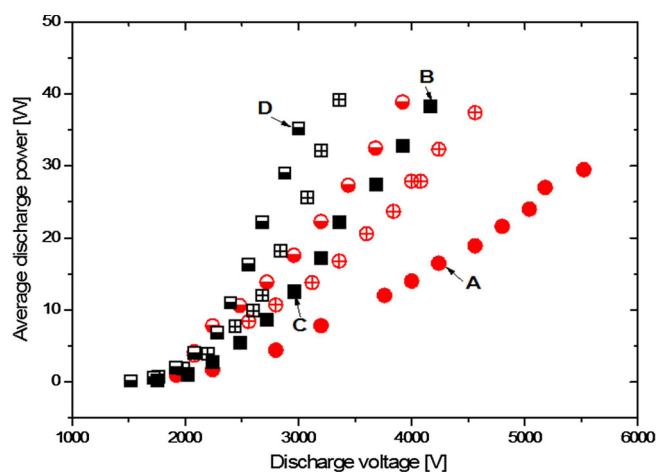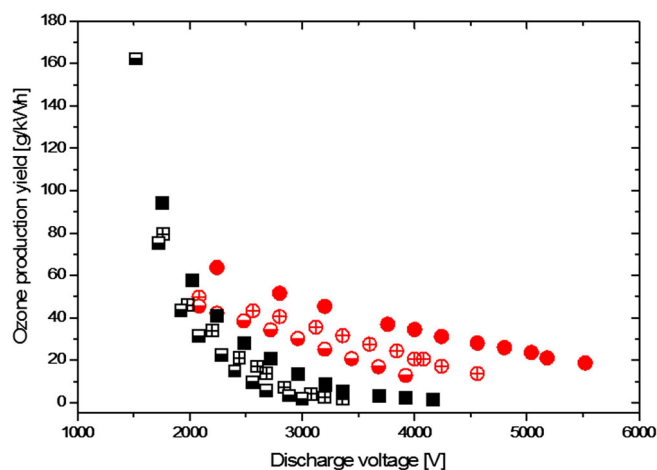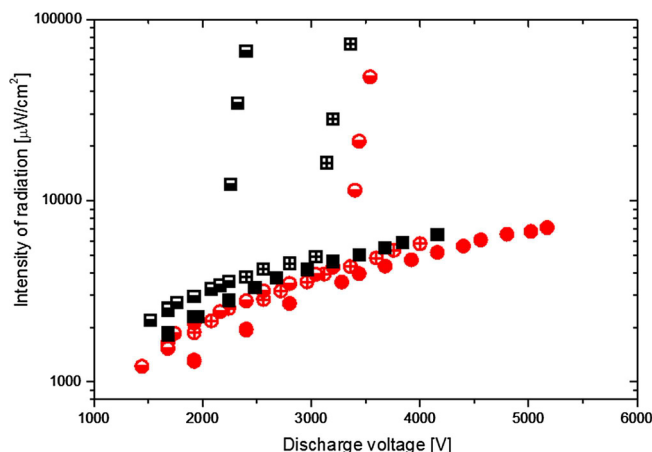. From this figure can be seen that the production yield for all three investigated frequencies is higher for the discharge with the strip active electrode setup than for the mesh active electrode setup. Except for it, for both active electrode setups and particular voltage, the production yield with the increasing frequency of the driving voltage decreases.

The obtained values of the ozone production yield ranging from 3 to 100 g/kWh for the investigated active electrode setups and the discharge in the air are comparable to the values reported in earlier literature. The values of the yield reported for the various types of DBD in air varied between 0 and 100 g/kWh [15,21,29]. It should be mentioned here that the examples quoted above represent the most frequently reported values of the ozone production yield.

The dependences of the peak intensity of UV radiation of the discharge versus discharge voltage for frequencies 4, 7, and 10 kHz, and both active electrode setups are shown in Figure 12.

The first conclusion from this figure is that for all investigated frequencies and both active electrode setups, with increasing driving voltage, the intensity of radiation increases. For all three investigated frequencies, for particular discharge voltage, the intensity of radiation is higher for the discharge with the mesh active electrode setup than for the discharge with the strip active electrode setup. The increasing frequency for a particular discharge voltage increases the intensity of UV radiation for both active electrode setups. We can also see that for a particular voltage, the lowest intensity of UV radiation is for driving voltage frequency 4 kHz and the strip active electrode setup.

An interesting effect, shown in this figure, is a sharp increase in the intensity of UV radiation at particular – onset – voltage. This increase in intensity is related to the driving voltage frequency as well as to the active electrode setup. Thus for the frequency 10 kHz, this effect was observed for both active electrode setups, though different voltages were required for its onset. Thus for the mesh or strip active electrode setup, the onset voltage of this sharp increase in intensity was 2200 V and 3200 V, respectively. From Figure 12 it is also seen that for particular active electrode setup the decrease in frequency increases the onset voltage of this effect. For the strip active electrode setup, this sharp increase in radiation intensity is observed only for 10 kHz because the discharge voltage was not sufficient to obtain this increase of radiation intensity at lower frequencies.

The observed results dealing with the intensity of UV radiation could be explained by a complex action of various factors. The intensity of radiation depends on the energy transmitted by this radiation per unit of time and per unit of area perpendicular to the energy flow. All variables which can affect these three quantities can influence the intensity of radiation. These variables involve, e.g., the discharge voltage, which affects the number of microdischarge channels per active phase of the discharge, frequency of a driving voltage or the duration of individual microdischarges. The duration of mirodischarges is influenced not only by the type of the gas but also by the electrode setup and surface properties of used materials.

From a comparison of Figures 10 and 12 can also be concluded that a high concentration of ozone produced by the discharge with the strip active electrode setup is accompanied by lower intensities of UV radiation of this discharge. On the other hand, high intensity of UV radiation of the discharge with the mesh active electrode setup is accompanied by a lower concentration of ozone produced by the discharge with this electrode setup.

For the sake of complexity, it should be however mentioned that high intensities of UV radiation for the

discharge with mesh active electrode setup can also contribute to ozone decomposition processes, which results in lower ozone production for the mesh active electrode setup in comparison with ozone generation by discharge with the strip active electrode setup.

4 Conclusions

We studied the effect of the driving voltage frequency and active electrode setup on electrical properties, ozone production, and UV radiation of wavelengths $320-420\,\mathrm{nm}$ of the dielectric barrier discharge in air at atmospheric pressure. The experiments were performed with frequencies of the driving voltage 4, 7, and $10\,\mathrm{kHz}$ and with two active electrode setups. The first setup comprised the strips electrode made from the copper foil. The second setup comprised the stainless steel wire mesh electrode with square cells. Our findings can be summarized as follows:

– For both active electrode setups and the same discharge voltage, the current pulses are with an increasing frequency more numerous and have higher amplitudes.
– For the same voltage and frequency for the mesh active electrode setup, the current pulses are for both polarities of the driving voltage higher and more numerous than for the strip active electrode setup.
– Ozone concentration, as well as the ozone production yield, is higher for the discharge with the strip active electrode setup than for the discharge with the mesh active electrode set up.
– The increased frequency decreases the voltage required to obtain maximum ozone concentration. This effect is more distinct for the discharge with the strips than for the mesh active electrode setup.
– The intensity of UV radiation for a particular voltage is higher for the discharge with the mesh active electrode setup than for the discharge with the strip active electrode setup for all investigated frequencies.
– The intensity of UV radiation at a particular voltage depending on the frequency and active electrode setup sharply increases. The increase in driving voltage frequency causes the shift of this onset voltage to lower values.

The general conclusion from our study is that high concentrations of ozone produced by the discharge with the strip active electrode setup are accompanied by lower intensities of generated UV radiation. For the discharge with the mesh active electrode setup, the situation is reversed. The obtained results could be useful for the design of the active electrode setups of the non-thermal plasma generators so that they can be used as sources of balanced doses of ozone and UV radiation for surface treatment of materials, biomedical applications, sterilization or activation of photocatalysts.

Author contribution statement

Both authors contributed equally to the paper.

References

1. I. Adamovich, et al., J. Phys. D: Appl. Phys. **50**, 323001 (2017)
2. K.D. Weltmann, et al., Plasma Process. Polym. **16**, e1800118 (2019)
3. S.T. Summerfelt, Aquac. Eng. **28**, 21 (2003)
4. W.Q. Ding, et al., Water Res. **160**, 339 (2019)
5. J. Ehlbeck, et al., J. Phys. D: Appl. Phys. **44**, 013002 (2011)
6. T. Bintsis, E. Litopoulou-Tzanetaki, R.K. Robinson, J. Sci. Food Agric. **80**, 637 (2000)
7. A. Gupta, P. Avci, T. Dai, Y.Y. Huang, M.R. Hamblin, Adv. Wound Care (New Rochelle) **8**, 422 (2013)
8. S. Rudakowski, *UV Light – A Powerful Tool for Surface Treatment* (OSRAM GmbH), http://www.circuitnet.com/news/uploads/1/Xeradex_VUV.pdf
9. E. Stoffels, A.J. Flikweert, W.W. Stoffels, G.M.W. Kroesen, Plasma Sources Sci. Technol. **11**, 383 (2002)
10. M. Kaneko, I. Okura, *Photocatalysis – Science and Technology* (Springer-Verlag, Berlin, Heidelberg, New York, 2002)
11. G. Magesh, B. Viswanathan, R.P. Viswanath, T.K. Varadarajan, Environ Energy Fuel **21**, 1 (2007)
12. U. Kogelschatz, Plasma Chem. Plasma Process. **23**, 1 (2003)
13. S. Yagi, M. Tanaka, J. Phys. D: Appl. Phys. **12**, 1509 (1979)
14. S. Pekárek, Eur. Phys. J. D **56**, 91 (2010)
15. A.A. Abdelaziz, T. Ishijima, T. Seto, N. Osawa, H. Wedaa, Y. Otani, Plasma Sources Sci. Technol. **25**, 035012 (2016)
16. A. Fridman, A. Chirokov, A. Gutsol, J. Phys. D: Appl. Phys. **38**, R1 (2005)
17. G. Vezzù, J.L. Lopez, A. Freilich, K.H. Becker, IEEE Trans. Plasma Sci. **37**, 890 (2009)
18. V.I. Gibalov, G.J. Pietsch, Plasma Sources Sci. Technol. **21** (2012)
19. Z. Xia, Y. Bi, Z. Qi, L. Ji, Y. Zhao, X. Chang, W. Wang, D. Liu, J. Appl. Phys. **123**, 083301 (2018)
20. M.A. Malik, Ch. Jiang, S.K. Dhali, R. Heller, K.H. Schoenbach, Plasma Chem. Plasma Process. **34**, 871 (2014)
21. M.A. Malik, K.H. Schoenbach, M. Tarek, A. Fattah, R. Heller, Ch. Jiang, Plasma Chem. Plasma Process. **37**, 59 (2016)
22. K. Takaki, Y. Hatanaka, K. Arima, S. Mukaigawa, T. Fujiwara, Vacuum **83**, 128 (2009)
23. E.G. Finantu-Dinu, D. Korzec, M. Teschke, J. Engemann, Surf. Coat. Technol. **174**–**175**, 524 (2003)
24. S. Pekárek, J. Phys. D: Appl. Phys. **45**, 075201 (2012)
25. S. Jodzis, Ozone Sci. Eng. **34**, 378 (2012)
26. L. Yang, H.J. Yan, X.H. Qi, S.X. Zhao, Ch.S. Ren, IEEE Trans. Plasma Sci. **43**, 3653 (2015)

27. R. Tirumala, N. Benard, E. Moreau, M. Fenot, G. Lalizel, E. Dorignac, J. Phys. D: Appl. Phys. **47**, 255203 (2014)
28. X. Wang, H. Luo, Z. Liang, T. Mao, R. Ma, Plasma Sources Sci. Technol. **15**, 845 (2006)
29. D. Yuan, Z. Wang, C. Ding, Y. He, R. Whiddon, K. Cen, J. Phys. D: Appl. Phys. **49**, 455203 (2016)
30. X.P. Xu, M.J. Kushner, J. Appl. Phys. **84**, 4153 (1998)
31. N.N. Guivan, J. Janča, A. Brablec, P. St'ahel, P. Slavíček, L.L. Shimon, J. Phys. D: Appl. Phys. **38**, 3188 (2005)
32. R. Prakash, A.M. Hossain, U.N. Pal, N. Kumar, K. Khairnar, M. Krishna Mohan, Sci. Rep. **7**, 17426 (2017)
33. S.A. Shcherbanev, A.Y. Khomenko, S.A. Stepanyan, N.A. Popov, S.M. Starikovskaia, Plasma Sources Sci. Technol. **26**, 02LT01 (2017)
34. J. Shao, J. Liu, C.M. Carr, Coloration Technol. **117**, 270 (2006)
35. N.N. Misra, D. Ziuzina, P.J. Cullen, K.M. Keener, Trans. ASABE **56**, 1011 (2013)
36. A.A. Garamoon, D.M. El-zeer, Plasma Sources Sci. Technol. **18**, 045006 (2009)
37. R. Brandenburg, Plasma Sources Sci. Technol. **26**, 053001 (2017)
38. J. Pons, E. Moreau, G. Touchard, J. Phys. D: Appl. Phys. **38**, 3635 (2005)
39. S. Pekárek, Eur. Phys. J. D **67**, 94 (2013)
40. S. Masuda, K. Akutsu, M. Kuroda, Y. Awatsu, Z. Shibuyaz, IEEE Trans. Ind. Appl. **24**, 223 (1988)
41. S. Portugal, S. Roy, J. Lin, Sci. Rep. **7**, 6388 (2017)
42. M. Šimek, S. Pekárek, V. Prukner, Plasma Chem. Plasma Process. **32**, 743 (2012)

A.3 Temperature-and airflow-related effects of ozone production by surface dielectric barrier discharge in air

S. Pekárek and J. Mikeš, 'Temperature-and airflow-related effects of ozone production by surface dielectric barrier discharge in air,' *The European Physical Journal D*, vol. 68, no. 10, Oct. 2014. DOI: 10.1140/epjd/e2014-50393-x.

**THE EUROPEAN
PHYSICAL JOURNAL D**

Temperature-and airflow-related effects of ozone production by surface dielectric barrier discharge in air

Stanislav Pekárek[a] and Jan Mikeš

Czech Technical University in Prague, FEE, Technická 2, 16627 Prague 6, Czech Republic

Abstract. Discharge ozone production depends on different quantities and the effect of one quantity on this process cannot be separated from the effects of other quantities. Thus the temperature influences the reaction rates of individual reactions involved in ozone generation and destruction, the thermodynamic properties, and the density of the feeding gas. The density of the feeding gas influences the reduced electric field, which affects ionization of the gas, production of electrons and consequently the electrical parameters of the discharge. Taking into account these considerations we investigated the effect of temperature and various arrangements of the input and output of the feeding gas to and from the discharge chamber together with related changes of electrical parameters of the surface dielectric barrier discharge on its ozone production for the temperatures in which commercial ozone generators function. We found that if the temperature of air at the output from the discharge chamber is increased from 15.0 ± 0.5 to 25.0 ± 0.5 °C, the discharge ozone production and peak discharge voltage decrease. Both the discharge ozone production and the peak discharge voltage are also affected by the way in which the feeding air is supplied to and leaves the discharge chamber. We also showed that for all ways in which the feeding air is supplied to and leaves the discharge chamber the discharge nitrogen dioxide production follows the same trends as discharge ozone production.

1 Introduction

Due to its high relative speed of reactions with chemical and biological species, ozone has found widespread applications in many areas including wastewater and drinking water treatment, oxidation, sterilization, deodorization, bacterial deactivation, food treatment, and so on. For all these applications efficient and stable sources of ozone are required.

Most of the ozone for the above-mentioned applications is produced by dielectric barrier discharges or corona discharges from oxygen or air. In spite of the fact that ozone production from air is burdened by existence of nitrogen oxides in many types of commercial ozonizers as a feeding gas is used air. In this case additional ionic species (N^+, N_2^+) together with excitation and dissociation of nitrogen molecules causes appearance of new species e.g. nitrogen oxides and provide additional reaction paths for both ozone formation as well as its destruction [1–3].

Generation of ozone from air by electrical discharge is a complex process [4–8], which, apart from electrical parameters of the discharge, pressure, humidity, and so on, depends mainly on the temperature of air and flow of air in the discharge chamber. The temperature of air in the discharge chamber can be associated with the balance of the discharge heat generation and the heat removal. The heat generation in the discharge chamber depends on discharge power. The heat removal from the discharge chamber can be affected by varying airflow patterns in the discharge chamber as well as by the cooling.

The temperature of air determines not only its thermodynamic properties but also the reaction coefficients of reactions leading to both ozone generation as well as its destruction. The most important reaction leading to ozone generation from air at atmospheric pressure is, according to reference [2], the reaction

$$O + O_2 + M \rightarrow O_3 + M, \qquad (1)$$
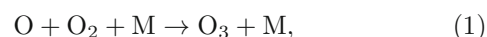
where M represents the third collision partner, which, for air, is molecular oxygen or nitrogen. For molecular nitrogen, the dependence of the reaction rate coefficient k_{gen} of this reaction on the temperature of the gas T_{gas} in the volume where this reaction takes place is given by the following expression [9]:

$$k_{gen} = 6.2 \times 10^{-34} \exp\left(300|T_{gas}\right)^2 \ [\text{cm}^6 \ \text{s}^{-1}; \text{K}]. \qquad (2)$$

From this expression it is seen that with increasing gas temperature the reaction rate coefficient k_{gen} decreases. The most important reaction leading to ozone destruction in air is the reaction

$$NO + O_3 \rightarrow NO_2 + O_2. \qquad (3)$$
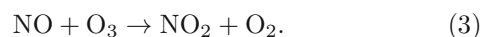
[a] e-mail: pekarek@fel.cvut.cz

According to [10], the reaction rate coefficient k_{destr} of this reaction depends on the temperature of a gas in the following way

$$k_{destr} = 4.3 \times 10^{-12} \exp\left(-1560|T_{gas}\right) [\text{cm}^3 \text{ s}^{-1}; \text{K}]. \quad (4)$$

This expression shows that with increasing temperature, ozone destruction increases. In the context of the dominant reactions leading to ozone generation and destruction, it should be pointed out, however, that the role of particular reactions leading to ozone generation and destruction varies with the temperature of a gas. Thus according to [4], for a temperature of air gas lower than 350 K, the dominant reaction for ozone loss is the reaction

$$\text{e} + \text{O}_3 \rightarrow \text{O} + \text{O}_2 + \text{e}, \quad (5)$$
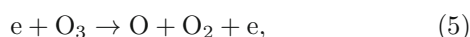
for which the reaction rate coefficient is $5.88 \times 10^{-9} [\text{cm}^3 \text{ s}^{-1}]$ [10].

The temperature of air in the discharge chamber certainly also depends on the heat removal from the discharge chamber through cooling of the chamber as well as on the flow of air through the chamber. Ozone generation depends on the time during which the particles used for this generation stay in the volume in which they are affected by the discharge. As can be seen from equation (1), ozone is formed mainly from oxygen atoms in a process, which takes about 100 μs in air [3]. The time during which the particles used for ozone generation stay in the volume in which they are affected by the discharge can be influenced by changing the air flow rate through the discharge chamber or by varying the airflow patterns in the discharge chamber. The airflow patterns in the discharge chamber could be changed by using different combinations of inputs and outputs of air to and from the discharge chamber.

Most of the papers on the study of ozone generation and its dependence on temperature and processes, which are affected by temperature are devoted to the effect of higher temperature on these processes, for example, temperatures up to 500 K [4,5]. However, commercial ozonizers most frequently function at ambient temperature. We have therefore investigated ozone production of the surface dielectric barrier discharge (SDBD) in air for temperatures of air at the output from the discharge chamber of 15.0 ± 0.5 °C and 25.0 ± 0.5 °C and for various arrangements of inputs and outputs of air to and from the discharge chamber.

As long as the generation of ozone from air by an electrical discharge could not be separated from production of nitrogen oxides [1,2,11,12], we also investigated effect of various combinations of inputs/outputs of air to or from the discharge chamber on discharge production of nitrogen monoxide NO and nitrogen dioxide NO_2.

In context of discharge ozone generation it should be however pointed out, that the influence of individual quantities such as temperature on this process could not be separated from the effects of other quantities involved in discharge ozone production. Thus, for example, temperature influences the reaction rates of individual reactions involved in ozone generation and destruction, the thermodynamic properties of the feeding gas, and of course
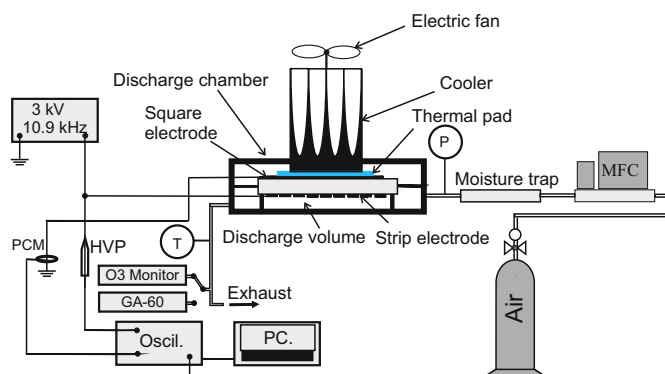
Fig. 1. Experimental arrangement.

the density of the feeding gas. The density of the feeding gas influences the reduced electric field, which affects ionization of the gas, the production of electrons and consequently the electrical parameters of the discharge. Taking into account these considerations we also investigated the effect of temperature and various arrangements of the input and output of the feeding gas to and from the discharge chamber on the electrical parameters of the discharge.

2 Experimental arrangement

The experimental arrangement used for the study of SDBD is shown in Figure 1. It consists of a flat ozone generator made from polymethyl-methacrylate plexiglass. The generator comprises an electrode system which was screen-printed on a 50×50 mm high-purity alumina Al_2O_3 dielectric plate of 0.635 mm thickness. This alumina plate, produced by the company Elceram, was of white color, with a content of Al_2O_3 of 96%, mass density of 3.7 g/cm^3, roughness 0.25–0.7 μm, a dielectric constant for 1 MHz of 9.6, electric strength of 14 kV/mm and the heat conductivity for temperature of 25 °C of 24 W/m K. The alumina plate divided the ozone generator into two parts. In the lower part there was a discharge chamber, which was opened to nine interconnected strips active electrode on the alumina plate. The width of each strip was 1 mm. The dimensions of the discharge chamber were $40 \times 40 \times 4.8$ mm. Through the thermal pad, the upper surface of the dielectric plate, which was carrying a square electrode, was in contact with a cooler, cooled by an electric fan.

The discharge chamber was flushed by air from a cylinder, which was delivered through the moisture trap and the mass flow controller (MFC). The input of air into the discharge chamber was through three tubes, P1, P2, and P3. Each of these tubes could be closed by a valve. Similarly the output of air was through three tubes, V1, V2, and V3, and each of these tubes could be closed by valve. By closing valves on individual tubes it was possible to affect the airflow patterns and consequently the residence time of air molecules in the discharge chamber. The layout of the electrode system, together with input and output
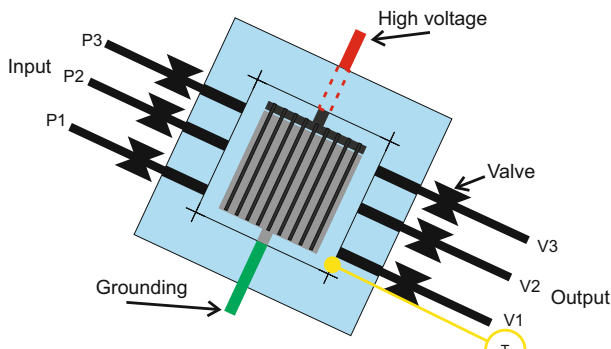
Fig. 2. Electrode system with air inputs P1, P2, and P3 and outputs V1, V2, and V3.

Fig. 3. Ozone concentration versus average discharge power for two air temperatures at the output of the discharge chamber and various inputs and outputs of air. Full symbols indicate the temperature of 15.0 ± 0.5 °C; empty symbols indicate the temperature of 25.0 ± 0.5 °C.

Fig. 4. Ozone production yield versus average discharge power for two air temperatures at the output of the discharge chamber and various inputs and outputs of air. Full symbols indicate the temperature of 15.0 ± 0.5 °C; empty symbols indicate the temperature of 25.0 ± 0.5 °C.

tubes and the position of the thermocouple T to measure the temperature of the output air, is shown in Figure 2.

The experiments were performed with the sinusoidal driving voltage. We used a high voltage power supply HVPS working at a frequency of 10.9 kHz. To determine the average discharge power, on the first channel of an ADS 1102CM digital storage oscilloscope (150 MHz) we sampled and recorded the discharge voltage through the high voltage probe (HVP-28HF, Pintek; division ratio: 1000/1; frequency: up to 200 MHz). To determine the discharge current we used a signal obtained from a Pearson current monitor (PCM, model 2877).

The ozone concentration was measured by absorption of the 254 nm UV spectral line using an API 450 ozone monitor. The concentrations of nitrogen monoxide NO and nitrogen dioxide NO_2 were measured by the flue gas analyzer GA-60. This analyzer is equipped with electro-chemical cells for measuring concentrations of nitrogen monoxide, nitrogen dioxide, oxygen and carbon monoxide. To make these measurements with the same airflow through the discharge chamber as in the case of ozone production measurements we could use either ozone monitor or flue gas analyzer.

The temperature field in the discharge chamber was recorded with a Fluke TiS thermocamera. Pressure at the input of the discharge chamber was measured with a digital manometer P.

3 Experimental results and discussion

To evaluate the efficiency of discharge ozone production from the standpoint of energy requirements, we used the so-called ozone production yield α, which is defined in the following way:

$$\alpha = \frac{21.44 \times (Ozone\ concentration) \times Air\ flow \times 6 \times 10^{-3}}{P_{av}}\ [\text{g/kWh}],$$

(6)

where the concentration of ozone produced by the discharge is substituted in parts per million, the airflow in
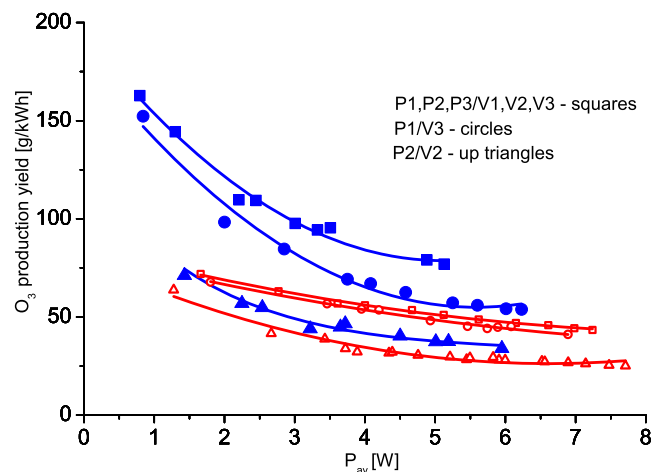
standard litres per minute (slm), and the mean discharge power in watts. The airflow through the discharge chamber was fixed to 1.8 slm in our experiments.

3.1 Concentration of ozone and ozone production yield

The dependence of ozone concentration on average discharge power for air temperatures of 15.0 ± 0.5 °C and 25.0 ± 0.5 °C at the output from the discharge chamber as measured by the thermocouple T, for various arrangements of inputs and outputs of air to and from the discharge chamber is shown in Figure 3. The analogical dependence for the ozone production yield is shown in Figure 4.

From Figure 3 it can be seen that even a small increase of the output air temperature from 15.0 ± 0.5 °C to 25.0 ± 0.5 °C for a particular power and for the same arrangement of inputs and outputs of air to and from the discharge chamber substantially decreases the ozone concentration, and the concentration of produced ozone depends strongly on the way in which the feeding air is supplied to the discharge chamber and how its output is organized. Similar conclusions can also be drawn for the ozone production yield. From these two figures it is also seen that both ozone concentration and ozone production yield are highest if the inputs/outputs of air to/from the discharge chamber are through the tubes P1, P2, P3/V1, V2, V3, which are at equal distances along the side of the discharge chamber parallel to the active electrode strips. On the other hand, if the input and output of air to the discharge chamber are only through one tube situated at the centre of the side parallel to the strips of the active electrode, that is P2/V2, the concentration of ozone and the ozone production yield are the lowest.

These results can be at least partially understood by taking into account the combination of non-uniform temperature field distribution inside the discharge chamber and different airflow patterns in the discharge chamber when varying inputs/outputs of air to/from the discharge chamber together with associated changes of electrical parameters of the discharge. The changes of electrical parameters of the discharge are discussed in Section 3.3.

In the case of the arrangement of inputs/outputs of air to/from the discharge chamber P1, P2, P3/V1, V2, V3 the airflow pattern immediately after entering the chamber and during all of its path through the discharge chamber is the most uniform in comparison with the two other arrangements of air inputs/outputs, which allows maximum interaction of the discharge with the feeding air. When varying the inputs/outputs of air to or from the discharge chamber, we can affect the airflow patterns in the discharge chamber. In case of P1/V3 and P2/V2 combination the flow will probably be more turbulent than in case of P1P2P3/V1V2V3 combination. A characteristic feature of turbulent flows is the occurrence of eddies of different length scales. These eddies affect mixing of particular reagents and therefore could affect their chemistry.

Another effect which could be responsible for different values of discharge ozone production in the case when we use different arrangements of air input and output to and from the discharge chamber could be associated with the fact that the properties of microdischarges are affected by the various airflow patterns in the discharge chamber. Indeed, remaining active species produced by the preceding upstream microdischarges could modify the physical processes such as ionization and attachment for the formation of a new downstream microdischarge. A similar effect exists in the case of plasma displays or plasma bar-graphs, where preionization of the volume in which the discharge occurs due to the previous discharge decreases the onset voltage of the following discharge.

From Figures 3 and 4, it can be seen that the ozone concentration depends on temperature. To gain a deeper
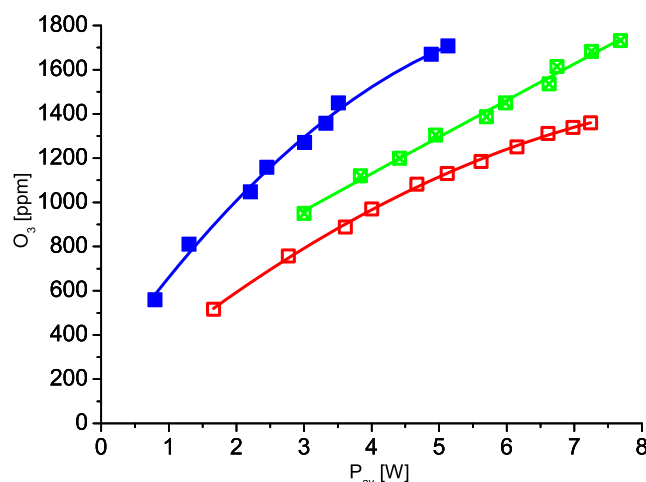
Fig. 5. Temperature dependence of ozone concentration versus average discharge power for the air inputs/outputs P1, P2, P3/V1, V2, V3. Full squares indicate the temperature of 15.0 ± 0.5 °C; crossed squares indicate the temperature of 20.0 ± 0.5 °C; empty squares indicate the temperature of 25.0 ± 0.5 °C.
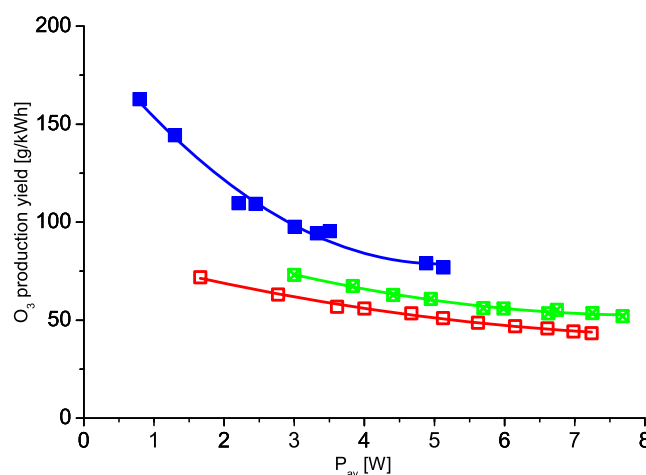
Fig. 6. Temperature dependence of ozone production yield versus average discharge power for air inputs/outputs P1, P2, P3/V1, V2, V3. Full squares indicate the temperature of 15.0 ± 0.5 °C; crossed squares indicate the temperature of 20.0 ± 0.5 °C; empty squares indicate the temperature of 25.0 ± 0.5 °C.

insight into this dependence, we performed additional experiments dealing with this dependence for the arrangements of inputs and outputs giving the highest ozone production, that is, P1, P2, P3/V1, V2, V3, but for three air temperatures at the output from the discharge chamber. The results of these experiments are shown in Figures 5 and 6.

From Figures 5 and 6, it can be seen that even a small change of temperature strongly affects both the concentration of ozone produced by the discharge and the ozone production yield. This conclusion should be considered as a result of not only the effect of temperature on the reaction rates of processes leading to the ozone production and
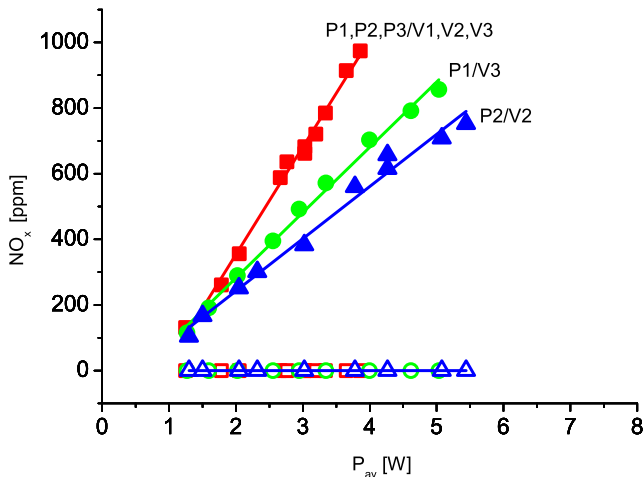
Fig. 7. Concentration of nitrogen monoxide (empty symbols) and nitrogen dioxide (full symbols) versus average discharge power for air inputs/outputs P1, P2, P3/V1, V2, V3 (red squares); P1/V3 (green circles) and P2/V2 (blue up-triangles) for the temperature of air at the output of the discharge chamber of 25.0 ± 0.5 °C.

decomposition but also the associated effect of the temperature on the density of feeding air. The density of the feeding gas influences the reduced electric fields, which affects the ionization of the gas, the production of electrons, and consequently the discharge ozone production.

Besides these effects it should also be mentioned that according to reference [13] the changes in temperature-related gas density also modify the distribution of ion space charge so that the propagation of the microdischarges is affected, which could modify the surface conductivity and consequently the surface charge distribution on the dielectric surface together with the related electric field profile, and finally, the dielectric surface temperature controls the secondary emission.

To demonstrate how combination of inputs/outputs of air to or from the discharge chamber affects discharge production of nitrogen monoxide NO and nitrogen dioxide NO_2 for all three combinations of inputs/outputs of air P1/V3; P2/V2 and P1, P2, P3/V1, V2, V3 in following Figure 7 are shown concentrations of nitrogen monoxide NO and nitrogen dioxide NO_2 for all three combinations of inputs/output of air for temperature of air at the output from the discharge chamber of 25.0 ± 0.5 °C.

From this figure can be taken following conclusions. First of all for investigated range of average power as well as for all combinations of inputs/outputs of air to the discharge chamber the concentration of nitrogen monoxide NO is negligible. The fact that concentration of nitrogen monoxide is negligible for the discharge before the discharge poisoning occurs is in agreement with results for the dielectric barrier discharge published in reference [1] or for corona discharge published in references [11,12]. The second conclusion deals with production of nitrogen dioxide NO_2. Concentration of NO_2 increases with the average power and it depends on combination of inputs/outputs of air from the discharge chamber. The highest concentration

of NO_2 was obtained for combination of inputs/outputs P1, P2, P3/V1, V2, V3; lower concentration of NO_2 was obtained for combination of inputs/outputs P1/V3 and finally the smallest concentration was obtained for inputs/outputs P2/V2. From the comparison of O_3 concentrations (Fig. 3) and NO_2 concentrations (Fig. 7) for various combinations of inputs/outputs of air into/out of the discharge chamber can be seen, that the highest O_3 as well as NO_2 concentrations were obtained for the same combination P1, P2, P3/V1, V2, V3. On the other hand the smallest O_3 as well NO_2 concentrations were obtained for the same combination P2/V2. Finally for the combination P1/V3 both O_3 as well as NO_2 concentrations are between corresponding concentrations for combinations P1, P2, P3/V1, V2, V3 and P2/V2.

From comparison of these two figures could be also seen that there are similar trends between O_3 and NO_2 concentrations. Both O_3 and NO_2 concentrations increase with specific energy. This result is in agreement with the results published in reference [1]. Besides of it the highest "slope" to the dependence of NO_2 or O_3 is for combination of inputs/outputs P1, P2, P3/V1, V2, V3; smaller "slope" was obtained for combination of inputs/outputs P1/V3 and finally the smallest "slope" was obtained for inputs/outputs P2/V2.

3.2 Temperature field distribution in the discharge chamber

From the results presented in Figures 3–6, the important role of temperature in ozone generation can be seen. The increase in temperature of the discharge volume is due to the fact that only a minor part of the energy delivered to the discharge is used for ozone production and most of this energy is converted into heat [14]. The result of the dynamical balance between the heat sources and sinks is then represented by temperature field distribution in the discharge chamber.

The heat sources are the consequence of the energy transfer from the electric field to the gas particles in the discharge. The surface dielectric barrier discharge consists of a set of parallel microdischarge channels, which originate at the conductive electrode and propagate perpendicular to this electrode on the dielectric surface [15]. The temperature in the microdischarge channels is much higher than that of the gas around them [14,15]. Moreover the temperature in these channels also changes in time. The gas expanding effect [14] causes mixing of the locally heated gas with the cold one, so that the temperature in the discharge volume averages.

The heat sinks are represented by cooling of the discharge chamber walls by the fan, by air flowing through the discharge chamber etc. The feeding air stream drags the volume of the heated air toward the output from the discharge chamber. In our case the situation is even more complicated by various combinations of inputs/outputs of air into/out of the discharge chamber. Resultant temperature field distribution in the chamber then reflects all above mentioned processes.
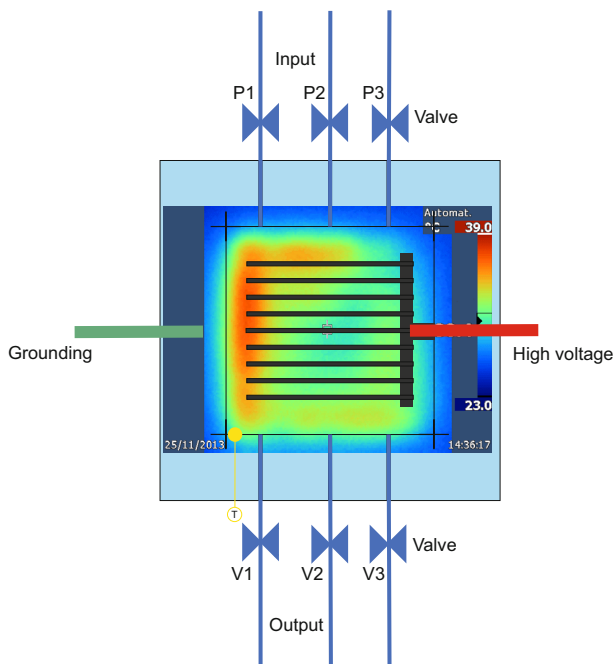
Fig. 8. Thermocamera image of the discharge chamber for air inputs/outputs of air P1, P2, P3/V1, V2, V3.

Fig. 9. Thermocamera image of the discharge chamber for air input/output P1/V3.

As long as the ozone concentration is the highest if the inputs/outputs of air to/from the discharge chamber are through the tubes P1, P2, P3/V1, V2, V3, in Figure 7 we show the temperature field distribution in the discharge chamber when the discharge is on obtained with the thermocamera. From this figure it is seen that the temperature field is strongly non-uniform and the maximum temperature in the discharge chamber is at the left part of the discharge chamber, that is, at the end of the active electrode strips. The region along the interconnecting part of the active electrode on the right side of this figure is colder.

In order to demonstrate the change in the temperature field distribution when the inputs/outputs of air to/from the discharge chamber were changed from P1, P2, P3/V1, V2, V3 to P1/V3 in Figure 8 is shown the thermocamera image giving the temperature field distribution in the discharge chamber for this situation.

From comparison of Figures 8 and 9 it is seen that when the input/output of feeding air was changed from P1, P2, P3/V1, V2, V3 to P1/V3, the temperature field was substantially changed. This effect was caused by the different airflow patterns in the discharge chamber and consequent changes in the mixing of locally heated air in microdischarges, with the cold air entering the discharge chamber.

3.3 Electrical parameters of the discharge

Our experiments with ozone generation by surface dielectric barrier discharge were performed with the sinusoidal driving voltage of frequency 10.9 kHz. As an illustrative example Figure 10 shows discharge voltage and current

Fig. 10. Discharge voltage and current waveforms for combination of air inputs/outputs P1, P2, P3/V1, V2, V3.

waveforms for combination of air inputs/outputs P1, P2, P3/V1, V2, V3. The temperature field for this air inputs/outputs combination is shown in Figure 8.

As already mentioned, the discharge ozone production depends on different quantities and the effect of one quantity on this process cannot be separated from the effects of other quantities. Thus the temperature not only influences the reaction rates of reactions involved in ozone generation, but also, through its effect on density, influences the reduced electric field and consequently the electrical parameters of the discharge. Taking into account these considerations, we investigated the effect of temperature and various arrangements of the input/output of the feeding
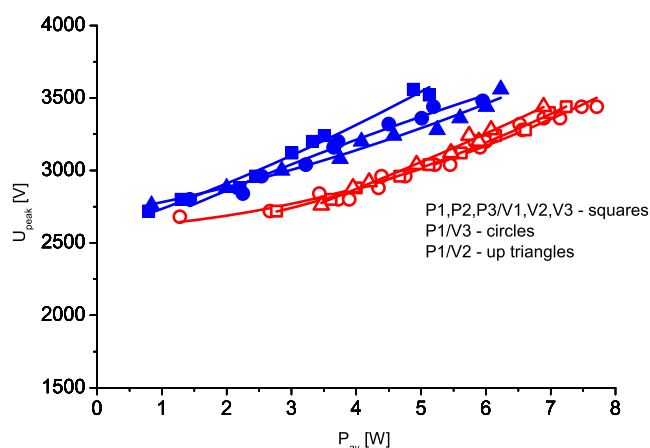
Fig. 11. Effect of temperature on the peak discharge voltage for various inputs/outputs of air to/from the discharge chamber. Full symbols indicate the temperature of 15.0 ± 0.5 °C; empty symbols indicate the temperature of 25.0 ± 0.5 °C.

gas to/from the discharge chamber on the peak discharge voltage for a particular discharge power.

The peak discharge voltage was determined from the digitalized data for each experimental point.

In order to demonstrate the fact that the discharge voltage is affected by temperature and partly also by the various arrangements of input/output of air to/from the discharge chamber, Figure 11 shows the effect of temperature and various arrangements of inputs/outputs of air to/from the discharge chamber on the peak discharge voltage.

From Figure 11 can be seen that at a particular power for all arrangements of input/outputs of air to/from the discharge chamber, the peak discharge voltage decreases with increasing temperature. This result is in agreement with the results presented in reference [16], where a linear reduction in applied onset voltage is shown for filament initiation with an increase in temperature. For temperature of output air from the discharge chamber 25.0 ± 0.5 °C the peak discharge voltage does not substantially depends on the arrangement of the input/output of air to/from the discharge chamber. For temperature of output air from the discharge chamber 15.0 ± 0.5 °C the peak discharge voltage depends on the arrangement of input/output air from the discharge chamber for higher power.

Another conclusion which can be drawn from Figure 11 is that, for a particular power, the peak discharge voltage is the highest for the inputs/outputs of air P1, P2, P3/V1, V2, V3 and for the output air temperature of 15.0 ± 0.5 °C. This result implies that the reduced electric field E/n (where E is the electric field strength, and n is the density of the feeding gas) will also be highest for this arrangement of inputs and outputs and for this temperature. Ionization will therefore be more effective and the electron density will be greater, and consequently there will be higher oxygen atom density and therefore higher ozone production. This conclusion is in agreement with the results presented in Figure 3.

4 Conclusions

For the surface dielectric barrier discharge in air we investigated the effect of temperature and various arrangements of the input and output of the feeding gas of the discharge chamber together with related changes of electrical parameters on the discharge ozone production for the temperatures in which commercial ozone generators function. We also showed that the effect of one quantity on discharge ozone production could not be separated from the effects of other quantities.

We found that if the temperature of air at the output from the discharge chamber is increased from 15.0 ± 0.5 °C to 25.0 ± 0.5 °C the discharge ozone production and the peak discharge voltage are decreased. Both the discharge ozone production and, partially, the peak discharge voltage are affected by the way in which the feeding air is supplied to and leaves the discharge chamber. The highest values of ozone concentration for a particular temperature of output air were obtained when the arrangement of inputs and outputs of air into and from the discharge chamber allowed a more or less uniform distribution of airflow immediately after entering the chamber and during the whole of its path through the discharge chamber, that is, for inputs/outputs P1, P2, P3/V1, V2, V3. We also showed that for all ways in which the feeding air is supplied to and leaves the discharge chamber the discharge nitrogen dioxide production follows the same trends as discharge ozone production. Besides of it it was found that the arrangement of air inputs/outputs P1, P2, P3/V1, V2, V3 for the output air temperature of 15.0 ± 0.5 °C gave the highest peak discharge voltage for a particular power.

The obtained results are useful for the construction of commercial ozone generators because they show the importance of temperature as well as airflow patterns in the discharge chamber on the electrical parameters of the discharge and on its ozone production.

References

1. U. Kogelschatz, B. Eliason, M. Hirth, Ozone Sci. Eng. **10**, 367 (1998)
2. S. Yagi, M. Tanaka, J. Phys. D **12**, 1509 (1979)
3. U. Kogelschatz, B. Eliason, W. Egli, J. Phys. IV France **07**, C4–47 (1997)
4. H.Y. Kim, S.K. Kang, H.C. Kwon, H.W. Lee, J.K. Lee, Plasma Process. Polym. **10**, 686 (2013)
5. J. Chen, J.H. Davidson, Plasma Chem. Plasma Process. **22**, 495 (2002)
6. V.I. Gibalov, G.J. Pietsch, J. Phys. D **33**, 2618 (2000)
7. Y. Nakai, A. Takashi, N. Osawa, Y. Yoshioka, R. Hanaoka, J. Chem. Chem. Eng. **5**, 1107 (2011)

8. M. Takayama, K. Ebihara, H. Stryczewska, T. Ikegami, Y. Gyoutoku, K. Kubo, M. Tachibana, Thin Solid Films **506**, 396 (2006)
9. A. Kossyi, A.Y. Kostinsky, A.A. Matvejev, V.P. Silakov, Plasma Sources Sci. Technol. **1**, 207 (1992)
10. F.J. Gordillo-Vazques, J. Phys. D **41**, 234016 (2008)
11. S. Pekárek, J. Rosenkranz, Ozone Sci. Eng. **24**, 221 (2002)
12. S. Pekźrek, Eur. Phys. J. D **61**, 657 (2011)
13. N. Jidenko, E. Bourgeois, J.P. Borra, J. Phys. D **43**, 295203 (2010)
14. S. Jodzis, Eur. Phys. J. Appl. Phys. **61**, 24319 (2013)
15. V.I. Gibalov, G.J. Pietsch, Plasma Sources Sci. Technol. **21**, 024010 (2012)
16. E. Bourgeois, N. Jidenko, M. Alonso, J.-P. Borra, J. Phys. D **42**, 205202 (2009)

A.4 Effect of a diamond layer on the active electrode on the ozone generation of the dielectric barrier discharge in air

S. Pekárek, O. Babchenko, J. Mikeš *et al.*, 'Effect of a diamond layer on the active electrode on the ozone generation of the dielectric barrier discharge in air,' *Journal of Physics D: Applied Physics*, vol. 53, p. 275 203, Mar. 2020. DOI: 10.1088/1361-6463/ab831f.

PAPER

Effect of a diamond layer on the active electrode on the ozone generation of the dielectric barrier discharge in air

To cite this article: Stanislav Pekárek *et al* 2020 *J. Phys. D: Appl. Phys.* **53** 275203

View the article online for updates and enhancements.

Erratum: Effect of a diamond layer on the active electrode on the ozone generation of the dielectric barrier discharge in air (2020 *J. Phys. D: Appl. Phys.* 53 275203)

Stanislav Pekárek[1],*, **Oleg Babchenko**[1], **Jan Mikeš**[1] and **Alexander Kromka**[2]

[1] Czech Technical University in Prague, Faculty of Electrical Engineering, Technická 2, 166 27 Prague 6, Czech Republic
[2] Institute of Physics of the Czech Academy of Sciences, Division of Solid State Physics, Cukrovarnická 10/112, 162 00 Prague 6, Czech Republic

E-mail: pekarek@fel.cvut.cz

CrossMark

(Some figures may appear in color only in the online journal)

Due to a mistake during the production of this article, figure 6 was mistakenly repeated in place of figure 5. The correct figure is reproduced below.
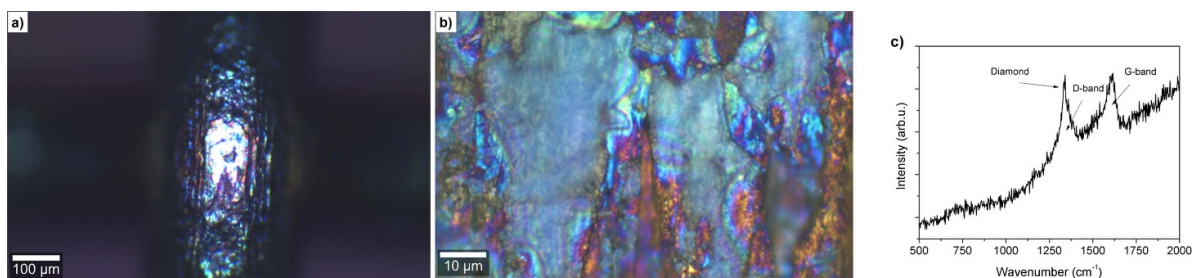
Figure 5. The optical images of stainless-steel mesh after the diamond deposition captured with the objective of $10\times$ (a) and $100\times$ (b) magnification and collected scattered Raman signal (c).

ORCID iDs

Stanislav Pekárek https://orcid.org/0000-0002-7171-9341
Oleg Babchenko https://orcid.org/0000-0002-2228-1048
Jan Mikeš https://orcid.org/0000-0003-2219-4320
Alexander Kromka https://orcid.org/0000-0002-3531-6748

* Author to whom any correspondence should be addressed.

Effect of a diamond layer on the active electrode on the ozone generation of the dielectric barrier discharge in air

Stanislav Pekárek[1,3] ⓘ**, Oleg Babchenko**[1] ⓘ**, Jan Mikeš**[1] ⓘ **and Alexander Kromka**[2] ⓘ

[1] Czech Technical University in Prague, Faculty of Electrical Engineering, Technická 2,166 27 Prague 6, Czech Republic
[2] Institute of Physics of the Czech Academy of Sciences, Division of Solid State Physics, Cukrovarnická 10/112, 162 00 Prague 6, Czech Republic

E-mail: pekarek@fel.cvut.cz

CrossMark

Abstract
We investigated the effect of a non-doped diamond layer deposition on the active electrode of the dielectric barrier discharge in the air on its electrical characteristics and ozone generation. We found that this new non-traditional application of diamond layers affects electrical parameters of the discharge and increases not only the concentration of ozone produced by the discharge but also ozone production yield by ~70%. Considering obtained results together with the high corrosion resistivity and chemical inertness of the diamond layers, the application of these layers on the dielectric barrier discharge electrode can be an interesting alternative to the usage of photocatalysts for the enhancement of ozone generation by electrical discharges.

Keywords: diamond layer, ozone, dielectric barrier discharge, electrodes

(Some figures may appear in colour only in the online journal)

1. Introduction

Due to its chemical reactivity, ozone is used in a wide range of applications such as the treatment of drinking and wastewater, medicine, food fruit and vegetable processing, restoration of buildings after fire and floods, etc. Ozone is usually generated in three different ways:

- Electrochemical generation.
- Generation by ultraviolet rays.
- Generation by electrical discharges.

Most of the ozone for practical applications is generated by electrical discharges in air or oxygen [1–6]. Ozone generation by electrical discharge in air occurs mainly in the discharge volume. The main ozone-generating reaction dominant at atmospheric pressure [7], is

$$O + O_2 + M \rightarrow O_3^* + M \rightarrow O_3 + M, \qquad (1)$$
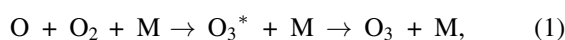
where M is a third-body collision partner, which in the air is the molecular O_2 or N_2, or a solid metallic/dielectric surface [8].

The first ozone generation by the silent discharge was performed in 1857 by Siemens, and the first ozone generator for plant treatment was built in 1860 in Monaco. Even though the ozone generation for practical application is used for more than 150 years, there exist continuous efforts to increase the efficiency of its production. These efforts are stimulated not only by the new emerging ozone applications but also by innovative ideas concerning optimization of ozone generators, applications of various photocatalysts [9–12], and at the last time usage of materials with unique properties such as enamel or diamond layers [13–16].

The most efficient discharge for ozone generation is the dielectric barrier discharge (DBD). The electrode system of this discharge consists of the active and grounded electrodes, which are separated by the layer of a dielectric material. According to the arrangement of the dielectric barrier and conductive electrodes, the DBDs exist in three forms: volume, surface, and coplanar. The volume dielectric barrier discharge

---

[3] Author to whom any correspondence should be addressed.
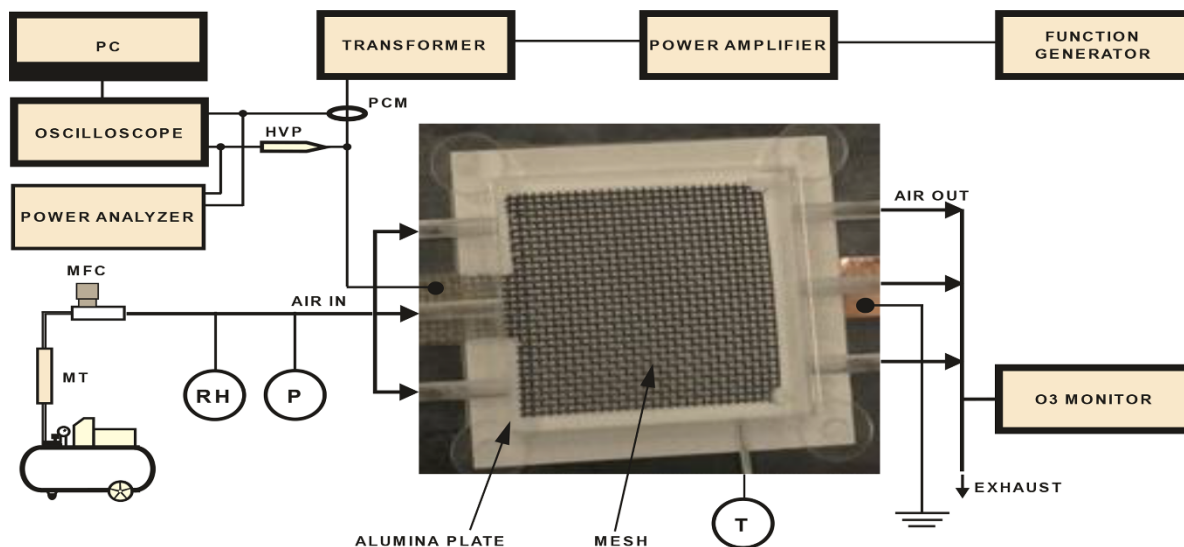
Figure 1. The experimental setup.
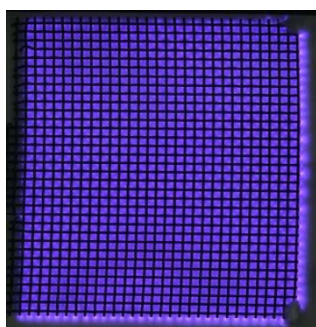
Figure 2. Photo of the discharge with the active stainless-steel mesh electrode covered by a diamond layer. $V_{max} = 2480$ V, $f = 10$ kHz, $Q_{air} = 1.8$ slm.

(VDBD) occurs in a gas gap between two conductive electrodes separated by a dielectric layer. In the case of the surface dielectric barrier discharge (SDBD) the active conductive electrode of various geometries (e.g. strips, honeycombs, mesh) is formed on one side of the plate or the cylinder made from the dielectric material. On the other side of the plate or cylinder is formed the grounded electrode. The coplanar dielectric barrier discharge (CDBD) consists of one or several pairs of parallel electrodes embedded in a dielectric material near a surface with the discharge on the surface of the dielectric.

The electrical properties of the discharge are strongly affected by the properties of both dielectrics as well as conductive electrodes materials. These materials are constantly exposed to the effect of charged particles, neutral radicals, excited species, UV radiation as well as an aggressive function of ozone when it comes into contact with the electrodes and other materials in the ozone generator. These aspects result in the aging of the electrode materials, sputtering of electrodes, and consequently, in the decrease of the electrode system lifetime.

One of the ways to suppress the role of these effects is the deposition of various passivation coatings on the electrode. Our research was also inspired by the approaches which were used to protect the electrodes by a diamond layer in electrochemical ozone generation [17].

We, therefore, investigated new non-traditional diamond films application that is their deposition on the active electrode of the DBD in the air at atmospheric pressure for ozone generation. Diamond films have outstanding mechanical, electrochemical, electronic, thermal, and biological properties. Due to these properties, they have a wide range of applications, e.g. in photovoltaic, computer technology, optics, biomaterials, medicine, etc. From the standpoint of ozone generation, important diamond properties involve chemical inertness and resistance against corrosion. In the context of ozone generation by electrical discharge, the important role is also played by the electrical properties of a diamond. The non-doped diamond is a dielectric material with a dielectric constant $\varepsilon_r = 5.7$, the bandgap 5.45 eV, and the electrical breakdown field 10^7 V cm^{-1} [13].

In this work, our attention was therefore focused on the DBD, in which the active electrode made from the stainless-steel mesh was covered by a layer of a non-doped diamond. In contrast with papers dealing with the preparation of diamond layers using various types of plasma we studied the impact of the diamond layer on the active electrode of the DBD on discharge ozone production and its electrical parameters

2. Experimental setup

The experimental setup used in this study is shown in figure 1. It consists of a discharge chamber, an air supply system, a high voltage power supply system with electrical parameters diagnostics, and an ozone monitor.

The discharge chamber, the photograph of which is shown at the center of figure 1, was made from the polymethylmethacrylate Plexiglas. The active electrode is a stainless-steel

wire mesh with square cells of inner dimensions 1×1 mm^2. The diameter of the wire used for the mesh was 0.4 mm. The experiments were also performed with the same active electrode, however, covered by a layer of a diamond. The active electrode was placed on one side of the high-purity alumina plate of dimensions $50.8 \times 50.8 \times 0.635$ mm. This alumina plate had a content of Al_2O_3 of 96%, a dielectric constant for 1 MHz of 9.6, and an electric strength of 14 kV mm^{-1}. The square ground electrode, on the other side of the alumina plate, was the same for both types of active electrodes. It was made by the screen printing from the air firing nickel conductor 2554-N-3. This electrode was cooled by a fan.

The active electrode was connected to an AC high voltage power supply system. This system consisted of function waveform generator DG 1022, wideband AC power amplifier AL-600-HF-A (output power 600 W, frequency response 20 Hz–800 kHz) and a high-frequency high voltage transformer AL-T1000.5 (peak voltage 10 kV, output power 1000 W and frequency response 4–12 kHz).

The electrical parameters of the discharge were monitored by four channels digital oscilloscope DS 1204 B (200 MHz; 2 GSa/s). The discharge voltage signal was sampled and recorded on the first channel of this oscilloscope with a high voltage probe (HVP-28HF, Pintek, division ratio 1000/1, frequency up to 200 MHz). To determine the discharge current, we used a signal obtained from a Pearson current monitor (PCM, model 2877) with a bandwidth of up to 200 MHz. Average discharge power was calculated based on the following equation:

$$P_{av} = \frac{1}{T} \int_0^T V(t)\,I(t)\,dt. \qquad (2)$$

In this expression, T is the period, $V(t)$ and $I(t)$ are voltage and current signals respectively. For orientation power measurements, we simultaneously used the Rohde and Schwarz 8015 power analyzer. The results in the following figures are presented as functions of the power determined from equation (2). The photograph of the discharge with the active stainless-steel electrode covered by a diamond layer, taken with Nikon 850 camera, is shown in figure 2.

The concentration of ozone at the output of the discharge chamber was measured by dual-beam UV ozone monitor BMT 964 BT, with the range up to 2300 ppm.

The air to the discharge chamber was supplied from an oil-free compressor through the moisture trap MT, and the mass flow controller MFC. On the left and right sides of the discharge chamber (figure 1) can be seen three openings for input and output air tubes.

The relative humidity of input air was measured by a sensor RH, and the pressure in the discharge chamber was measured with a digital manometer P. The temperature of the air at the output from the discharge chamber was measured by a thermocouple T.

3. Experimental results

3.1. Deposition of a diamond layer on the active electrode and layer characteristics

Diamond layer on the mesh active electrode was grown by the chemical vapor deposition (CVD) process in the large area pulsed microwave plasma system equipped with linear antennas [18]. Before diamond deposition, the stainless-steel mesh electrode was cleaned in the ultrasound bath and seeded (nucleated) by diamond nanoparticles by the following procedure. This procedure includes ultrasound wash in acetone for 10 min, rinse by the flow of deionized water, then, ultrasound wash in the isopropylalcohol for 10 min, again rinse by the deionized water and drying by the nitrogen blowing.

Following step is the exposition of the mesh to the low-pressure oxygen discharge to ensure hydrophilic surface and seeding with diamond nanoparticles by the ultrasound bath treatment in the water-based diamond powder (nominal particles size 5 nm, New Metals and Chemicals Corp. Ltd., Kyobashi) suspension for 40 min. Flat, one-side polished Si pieces, treated by the same cleaning and diamond nanoparticles seeding procedure, were used as the reference samples. To prevent the possible reactions of stainless-steel mesh with the graphite table (20×30 cm^2) of the deposition system during the 20 h CVD process, the all samples were placed on the Si/SiO$_2$ holder. The diamond deposition was realized from the gas mixture of hydrogen—0,2 slm, carbon dioxide—0,03 slm, and methane—0,01 slm at total gas pressure 0,1 mbar. The microwave power delivered from both antennas sides was 2×1500 W while the average process temperature measured on Si/SiO$_2$ holder was 300°C.

The diamond layers characterization was realized by optical microscopy, Raman shift measurements, and scanning electron microscopy (SEM). Optical microscopy images and Raman spectra were collected using a WITec alpha 300RAS system. The optical microscopy was done using objectives with magnification $10\times$, $20\times$, $50\times$, $100\times$ (not all shown). All Raman spectra were measured by 532 nm laser at power 2 mW, microscope objective with magnification $100\times$ and grating 600 gr mm^{-1}. The SEM and samples morphology investigation were realized using low voltages scanning electron microscope (MAIA3, TESCAN).

The surface of the stainless-steel mesh electrode was analyzed before and after the exposure to the diamond CVD process, while the Si samples were taken as the reference to confirm the diamond film growth.

The optical images and collected Raman signal on stainless steel mesh before diamond deposition are shown in figure 3. The optical images (figures 3(a) and (b)) demonstrate macroscopically not uniform morphology of the steel wire surface. The Raman shift measurement (figure 3(c)) shows only the noise signal (i.e. no bond vibration is detectable) of scattered light that can be observed on the clean metal surface.

The SEM images of the stainless-steel wire with different magnification (see the scale bar) are shown in figure 4. The surface micro-roughness and deep voids in the wire can be seen
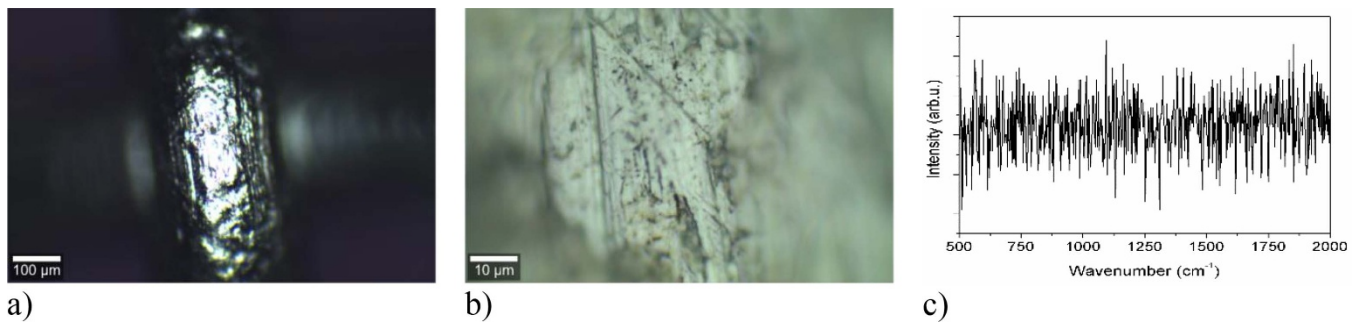
Figure 3. The optical images of stainless-steel mesh captured with the objective of $10\times$ (a) and $100\times$ (b) magnification and collected scattered Raman signal (c).
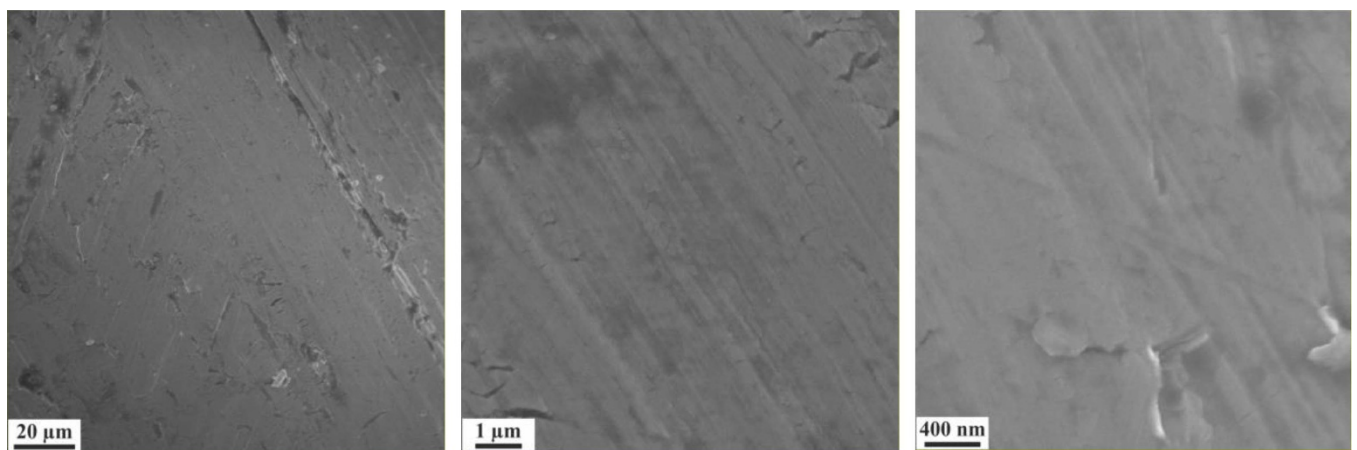
Figure 4. The SEM images of stainless-steel mesh with different magnification.
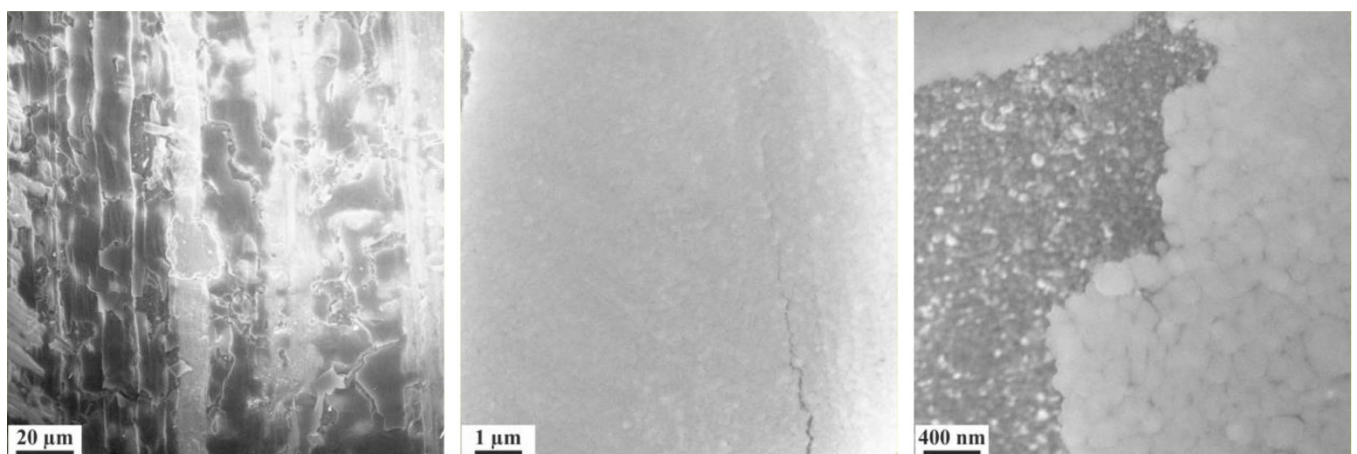
Figure 5. The optical images of stainless-steel mesh after the diamond deposition captured with the objective of $10\times$ (a) and $100\times$ (b) magnification and collected scattered Raman signal (c).

on these images, i.e. the wire surface cannot be assumed as flat even for micro-size areas.

The optical images of stainless-steel mesh and Raman signal after the diamond deposition are shown in figure 5. These images (figures 5(a) and (b)) show change of stainless-steel color related to processing by the CVD while the color variations within the captured surface can be of the different reason (e.g. light interference via diamond layer,

total surface roughness or layer delamination). The Raman shift measurements demonstrate the signal intensity variation within the scanned area (not shown here) as well. The as-measured Raman shift spectrum, a representative for the deposited layer, is shown in figure 5(c). The bands observed in the spectrum reflect characteristic fuaters of diamond layers [19]. In this case, the diamond peak (centered at 1335 cm^{-1}) is significantly affected by the strong disordered carbon band

J. Phys. D: Appl. Phys. **53** (2020) 275203

S Pekárek *et al*
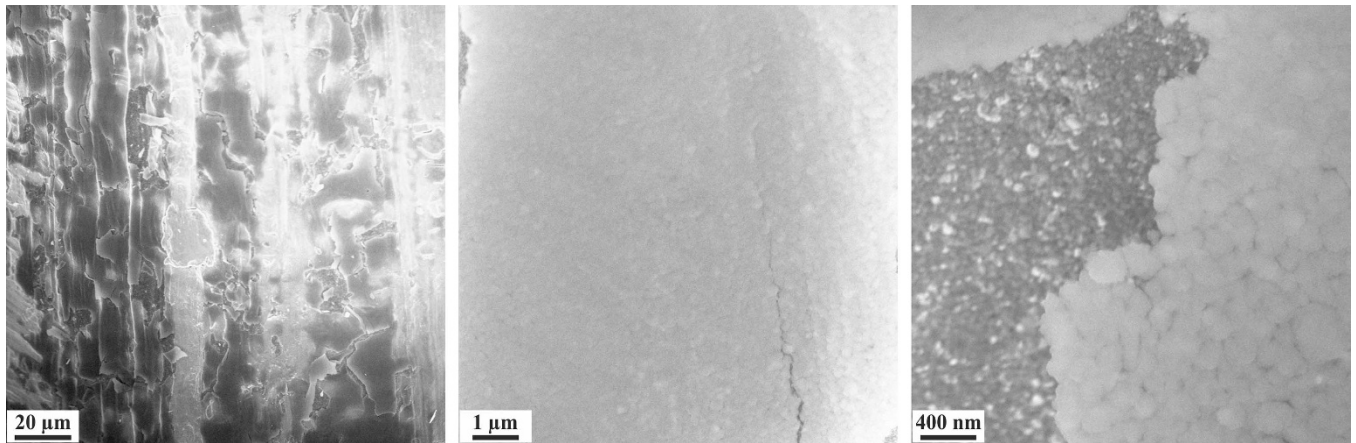
Figure 6. The SEM images of stainless-steel mesh after the diamond deposition, with different magnification.

(centered at 1350 cm^{-1}). The band related to graphitic phase is centered at the 1604 cm^{-1}. In general, the measured spectrum confirms the deposition of the diamond layer onto the stainless-steel mesh surface.

The SEM images of stainless-steel mesh after the diamond deposition are shown in figure 6. The SEM images show cracking and delamination of the deposited layer on the large areas (see large scale image), while the remained diamond layers demonstrate cauliflower-like structures consisting of ultra-small clustered grains typical for diamond films deposited in the linear antenna system [18]. Although the diamond layers delaminated from the mesh (see small scale image) the mesh surface in these places seems to be remained covered by nano-structured features. The partial delamination of a diamond is in agreement with a variation of Raman signal intensity and assumed to be caused by not homogeneous mesh surface and not optimal diamond adhesion. Here it needs to point out that the Raman shift signal measured on the mesh area exposed to plasma discharge during the CVD process varied in the intensity but never dropped to the level of noise signal of the clean mesh (figure 3(c)).

3.2. Discharge ozone production

The experiments concerning the discharge ozone production and its electrical characteristics were performed with the ambient air and the flowrate 1.8 slm. The relative humidity of air in the input of the discharge chamber was 20%. The discharge was driven by sinusoidal voltage.

The present ozone generators work in a wide range of frequencies, starting from the frequencies from the mains supply of 50 Hz, medium frequencies to 10 kHz, up to the high frequencies about approximately 25 kHz. Considering this range of driving voltage frequencies, our experiments were performed with frequencies 7 and 10 kHz.

The quantity which determines the concentration of ozone produced by the discharge is the amount of energy applied to the discharge. This energy depends on the combination of the discharge voltage and frequency. Generally speaking, high discharge voltages increase the stress on the dielectric

resulting in more frequent failures of the device. By using higher frequencies and lower discharge voltages, the dielectric stress is minimized. There is, therefore, a space to vary the discharge voltage or frequency to optimize electrical parameters of the discharge and requirements applied to properties of materials used for the electrode systems.

The discharge voltage, in case of the surface dielectric barrier discharges, affects the area covered by the microdischarges. When the voltage is increased, the number of microdischarge channels grows; consequently the area covered by the microdischarges also increases [20].

The frequency of the driving voltage influences discharge properties through the interaction of microdischarges with residual charges left on the dielectric surface during the whole discharge cycle, as well as the influence of excited species generated in one microdischarge on the formation of another microdischarge [21] Thus, for example, if this frequency is too low to keep the microdischarge remnants from dissipation (low frequency means that the period is longer than the typical lifetime of the microdischarge remnant), microdischarge repulsion effects are not observed [22].

In our paper, our attention is focused on the effect of the diamond layer on the active electrode of the dielectric barrier discharge on its ozone production. This is a reason why we present our results as a function of a quantity that involves both discharge voltage as well as the frequency of the driving voltage simultaneously, that is on the discharge power. In this context, it should also be mentioned that for the constant airflow rate through the discharge chamber, the discharge power is directly proportional to the specific input energy, which is sometimes also used for the presentation of obtained results.

The measurements were performed in cycles. In each cycle was, first of all, recorded the initial air temperature at the output from the discharge chamber, then the discharge was switched on. After adjusting the discharge voltage, the concentration of ozone increased and reached a certain maximum. The value of this maximum concentration was recorded together with the temperature of output air and electrical signals. After each concentration measurement, the discharge was
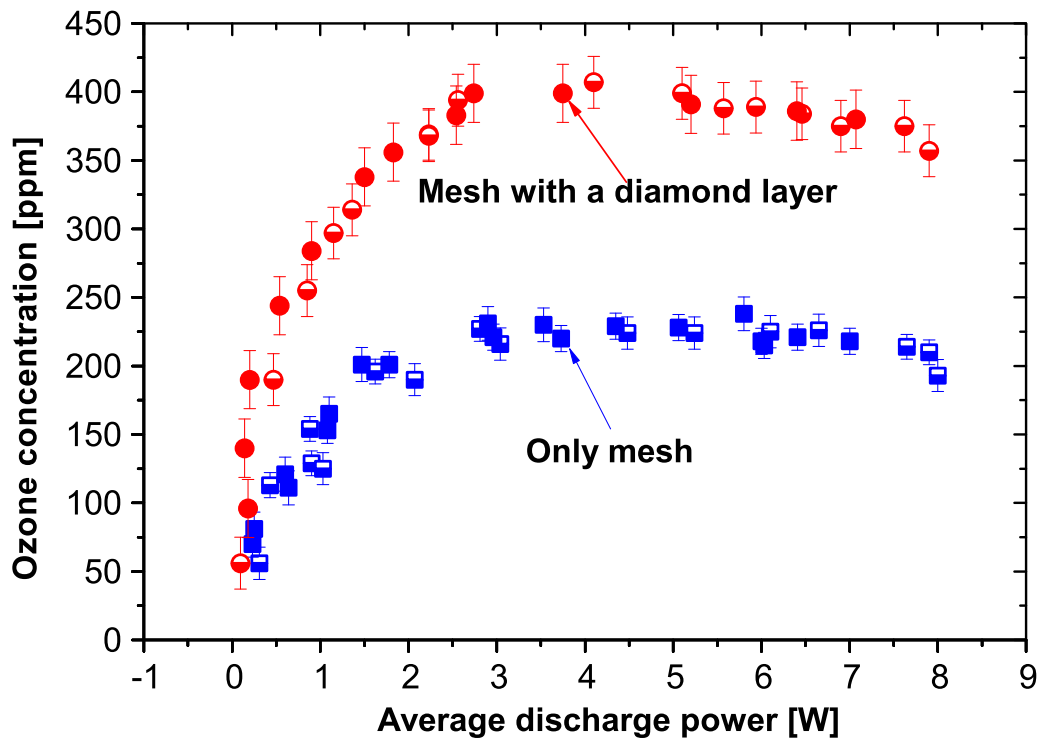
Figure 7. Ozone concentration versus average power for the discharge in the air with the mesh or the mesh covered by the layer of a diamond electrode and frequencies of the driving voltage 7, and 10 kHz. Full symbols—frequency 7 kHz; half-empty symbols—frequency 10 kHz.

switched off, and the next measurement cycle was performed when the temperature of output air reached the initial value. Depending on the applied voltage, the maximum increase of air temperature at the output from the discharge chamber during one measurement cycle was about 5°C for the discharge with the diamond layer.

The dependence of ozone concentration produced by the discharge versus average discharge power for the discharge with the mesh active electrode and the mesh with the diamond layer active electrode is shown in figure 7. As a source for calculation of error bars, we used the standard deviation of data.

From figure 7, it can be seen that the deposition of the diamond layer on the mesh electrode for particular discharge power increases the concentration of ozone generated by the discharge by more than 70%. This result was obtained for both frequencies of the driving voltage.

To evaluate the mass of ozone produced by 1 kWh of energy, the ozone production yield α is used [4, 5]. This quantity is defined by the following equation:

$$\propto = \frac{2.144 \times \text{Ozone concentration} \times \text{Airflow}}{\text{Power}} \qquad (3)$$

In this equation, 2.144 kg m^{-3} is the density of ozone at STP. For our experimental conditions, that is airflow rate of 1.8 slm, we for the ozone production yield obtain:

$$\propto = \frac{0.231 \times O_3\,[ppm]}{P_{av}\,[W]} \cdot \left[\text{g kWh}^{-1}\right] \qquad (4)$$

The numerical constant 0.231 involves the density of ozone (2.144 kg m^{-3}) as well as all conversion factors of the airflow rate and energy.

The dependence of the ozone production yield on average discharge power for the discharge with the stainless-steel active electrode, and this active electrode covered by a layer of a diamond is shown in figure 8. Similarly, as in the case of figure 7, as a source for calculation of error bars, we used the standard deviation of data.

From this figure, it can be seen that the deposition of the diamond layer on the active electrode of the discharge increases ozone production yield within all range of investigated powers by ~70%. Another conclusion that can be taken is that the ozone production yield, when presented as a function of the discharge power, does not depend on the frequency of the driving voltage.

The interesting conclusions can be made based on a comparison of the results presented in figures 7 and 8 with the results of the ozone generation enhanced by the presence of photocatalysts in the discharge region.

The review of the history and development of plasma-assisted catalysis, focusing mainly on the use of atmospheric pressure, non-thermal plasma is given in [9]. There also exist numerous works dealing with the effects of various photocatalysts placed as layers or three-dimensional objects in different regions of DBD ozone generators. Thus, in our previous paper [10], we showed that the placement of a layer of the TiO$_2$ photocatalyst on the plane opposite to the active electrode of the dielectric barrier discharge increases the maximum concentration of ozone generated by the discharge by ~20%.
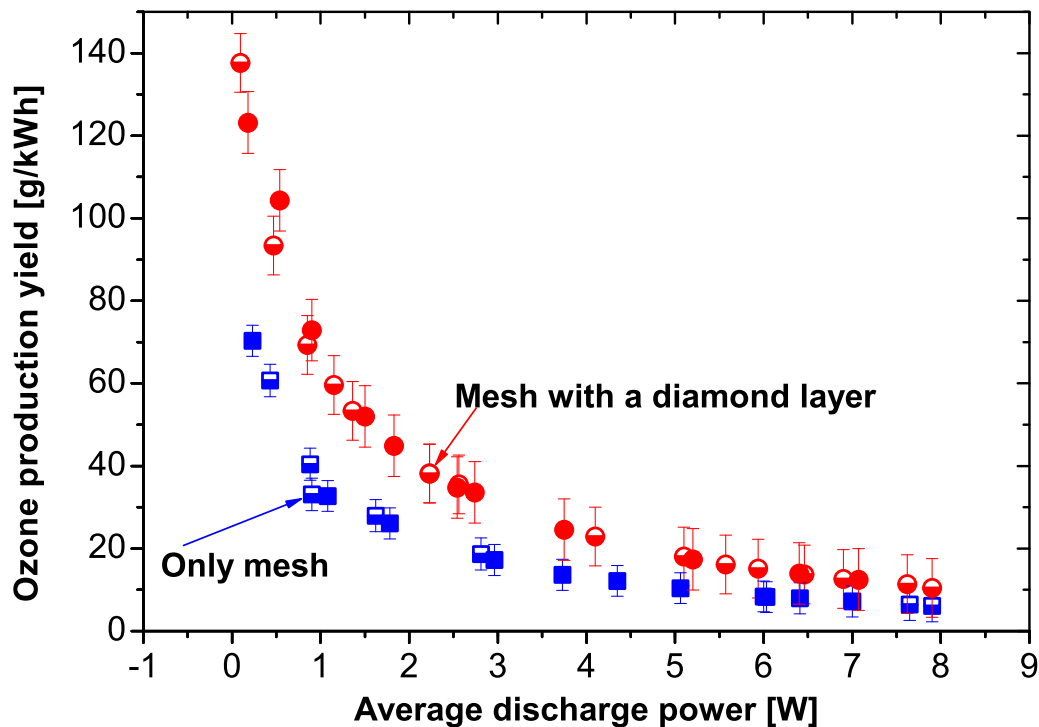
Figure 8. Ozone production yield versus average power for the discharge in the air with the mesh or the mesh covered by the layer of a diamond electrode and frequencies of the driving voltage 7 and 10 kHz. Full symbols—frequency 7 kHz; half-empty symbols—frequency 10 kHz.

It should be pointed out that activation of the photocatalyst was by UV radiation generated by the discharge. The TiO_2 deposited on various regions of the dielectric plate carrying the active electrode differently affects SDBD ozone production. The best results from the standpoint of ozone production were obtained when the TiO_2 layer was deposited only on the surface of the active electrode. The increase in the concentration of ozone produced by the discharge reached ~10% [11]. The energy efficiency of generating ozone in the DBD/TiO_2 system has been approximately raised by 38% compared to the pure DBD [12].

From this comparison, it can be concluded that for ozone generation by DBD is the deposition of the diamond layer on the active electrode more efficient than the application of the TiO_2 photocatalyst.

4. Discussion

Our results showing the increase of ozone concentration and ozone production yield when the diamond layer is deposited on the active electrode of the discharge could be at least qualitatively understood based on the change in the DBD mechanism and associated changes in the plasma-chemical processes leading to the ozone production.

First of all, it should be mentioned that the conductive mesh electrode is in our experiments in contact with the dielectric plate at the point of intersections of orthogonal wires creating the mesh and in between these points the wires are at a small distance from the alumina plate. This is a reason

why the discharge with the stainless-steel mesh active electrode (conductor) on the dielectric alumina plate (dielectric, $\varepsilon_r = 9.5$) could be considered as a certain combination of the volume and the surface discharge. On the other hand, when the stainless-steel mesh electrode covered by a layer of the diamond (the conductor is embedded in the dielectric of $\varepsilon_r = 5.7$) is placed on the alumina plate (dielectric), the discharge could be considered as a certain combination of the volume and the coplanar discharge.

According to the comprehensive review of the DBD mechanism [20], all types of DBDs (volume, surface, and coplanar) exist in pre-breakdown, streamer and decay phases. The importance of discrete phenomena in each of these three phases and for various types of streamers varies, and differently affects the discharge performance. From the standpoint of reactive particle generation, the most important of these phases is the streamer phase. Thus, for this phase and the cathode directed streamer, the main source of electrons is photoemission from surfaces. Other sources, such as the emission of secondary electrons due to the impact of positive ions on the cathode, do not play a comparable role. In the case of SDBD, the distinct microdischarge channels develop along the conductive electrode on the dielectric surface. The performance of the discharge is therefore, except the type of the gas or electrode geometry affected by the properties both of the dielectric material (alumina, quartz, macor, ceramic, PTFE) as well as by the properties of the conductive electrode (copper, aluminum, nickel, stainless-steel). Another aspect that is associated with the fact that diamond is a dielectric material is that its layer on the active conductive electrode causes the appearance of
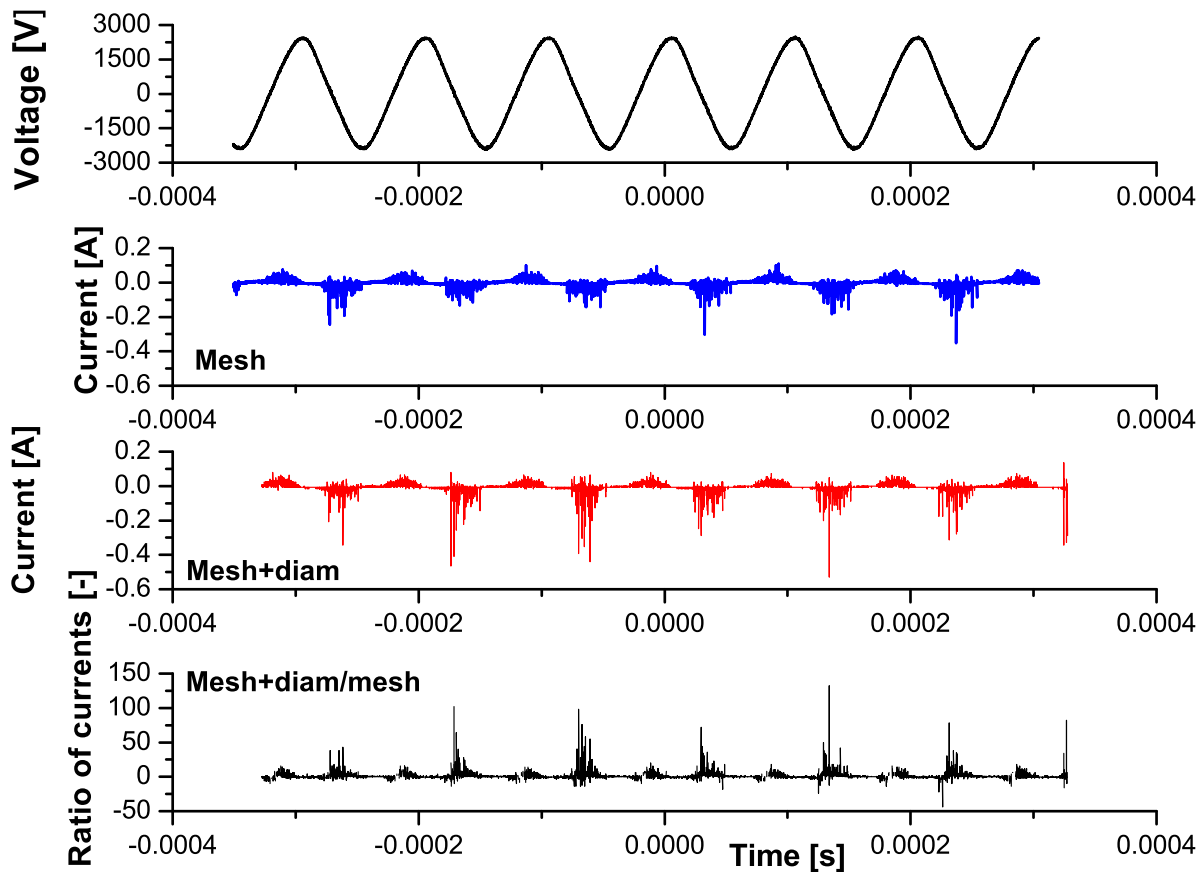
Figure 9. Electrical parameters of the discharge in air. $V_{max} = 2440$ V, $f = 10$ kHz, $Q_{air} = 1.8$ slm.

surface charges. These surface charges affect the ion-induced secondary emission [23]. It, therefore, is seen that both photoemission as well as the ion emission current, and consequently, the discharge current is influenced by the type of solid surfaces.

To demonstrate the effect of a diamond layer on the active electrode on the discharge current, we measured the discharge current for particular voltage first of all for the discharge with the stainless-steel active electrode and secondly for this electrode covered by a diamond layer. The illustrative results for the frequency of the driving voltage 10 kHz and the voltage amplitude 2440 V are shown in figure 9.

The first row of this figure shows the driving voltage waveform. In the second row (Mesh) is shown the discharge current for the discharge with the stainless-steel mesh electrode. The third row (Mesh + diam) shows discharge current for this electrode covered with the diamond layer. Finally, the fourth row (Mesh + diam/mesh) gives the ratio of the discharge current for the discharge with the mesh electrode covered with the diamond layer and the current of the discharge with the clean mesh electrode. From this comparison, it is seen that in case of the discharge with the active electrode covered with a layer of a diamond (Mesh + diam), for the negative polarity of the driving voltage, there appear current peaks which are up to 100

times higher than the current peaks for the discharge with the clean mesh electrode (Mesh).

This observation is similar to the effect described in [24], which was devoted to the influence of photocatalytic material TiO_2 on the dynamic of the plasma current amplitude in a barrier discharge. According to this paper, the high current peaks begin probably because of the local electric field enhancement due to the high dielectric constant of TiO_2 nanoparticles. Even, the diamond dielectric constant is much lower, cold emission from the diamond surface can significantly contribute to current peaks. However, the exact cause of this effect still needs to be investigated.

5. Conclusions

We studied the effect of a non-doped diamond layer deposited on the active electrode of the dielectric barrier discharge in the air at atmospheric pressure on its electrical characteristics and ozone generation. We showed that this new non-traditional application of diamond layers substantially increases not only ozone concentration produced by the discharge but also ozone production yield. Our conclusions, for both investigated frequencies of the driving voltage 7 kHz and 10 kHz, can be summarized as follow:

- In comparison with the discharge with the stainless-steel active electrode, in case of the discharge with this active electrode covered by the diamond layer, there appear high current peaks for the negative polarity of the driving voltage.
- The deposition of the diamond layer on the active electrode of the discharge increases maximum ozone concentration by ~70% in comparison with the ozone concentration generated by the discharge with the active electrode without a diamond layer.
- The deposition of the diamond layer on the active electrode of the discharge increases ozone production yield by ~70%.

Considering the obtained results together with the high corrosion resistivity and chemical inertness of the diamond layers, the application of these layers on the dielectric barrier discharge active electrode can be an interesting alternative to the application of photocatalysts for ozone generation. It should be, however, mentioned that to assess from all standpoints the specific effect and possible benefits of diamond layer on the active electrode of the surface dielectric barrier discharge for ozone generation, further comparative studies with other dielectric coatings are needed.

ORCID iDs

Stanislav Pekárek https://orcid.org/0000-0002-7171-9341
Oleg Babchenko https://orcid.org/0000-0002-2228-1048
Jan Mikeš https://orcid.org/0000-0003-2219-4320
Alexander Kromka https://orcid.org/0000-0002-3531-6748

References

[1] Kogelschatz U, Eliasson B and Hirth M 1998 *Ozone Sci. Eng.* **10** 367
[2] Malik M A and Hughes D 2016 *J. Phys. D: Appl. Phys.* **49** 135202
[3] Jodzis S 2012 *Ozone Sci. Eng.* **34** 378
[4] Abdelaziz A A, Ishijima T, Seto T, Osawa N, Wedaa H and Otani Y 2016 *Plasma Sources Sci. Technol.* **25** 035012
[5] Yuan D, Ding C, He Y, Wang Z, Kumar S, Zhu Y and Cen K 2017 *Plasma Chem. Plasma Process.* **37** 1165
[6] Pekárek S 2017 *Plasma Chem. Plasma Process.* **37** 1313
[7] Yagi S and Tanaka M 1979 *J. Phys. D: Appl. Phys.* **12** 1509
[8] Schmidt-Szalowski K 1996 *Ozone Sci. Eng.* **18** 41
[9] Whitehead J C 2016 *J. Phys. D: Appl. Phys.* **49** 243001
[10] Pekárek S 2012 *J. Phys. D: Appl. Phys.* **45** 075201
[11] Pekárek S, Mikeš J and Krýsa J 2015 *Appl. Catal.* A **502** 122
[12] Lu N, Hui Y, Shang K, Jiang N, Li J and Wu Y 2018 *Plasma Chem. Plasma Process.* **38** 1239
[13] Vezzù G, Lopez J L, Freilich A and Becker K H 2009 *IEEE Trans. Plasma Sci.* **37** 6
[14] Arnault J C 2017 *Nanodiamonds, Advanced Material Analysis, Properties and Applications* (Amsterdam: Elsevier)
[15] May P W 2000 *Phil. Trans. R. Soc. Lond.* A **358** 473
[16] Kalish R 2007 *J. Phys. D: Appl. Phys.* **40** 6467
[17] Gorokhovsky V *et al* 2015 Diamond coated electrodes for electrochemical processing and applications thereof *US Patent* US 2015/0376804 A1
[18] Kromka A, Babchenko O, Izak T, Hruska K and Rezek B 2012 *Vacuum* **86** 776
[19] Davis R F 1993 *Diamond Films and Coatings: Development, Properties, and Applications* (Park Ridge, NJ: Noyes)
[20] Gibalov V I and Pietsch G J 2012 *Plasma Sources Sci. Technol.* **21** 024010
[21] Xu X P and Kushner M J 1998 *J. Appl. Phys.* **84** 4153
[22] Fridman A, Chirokov A and Gutsol A 2005 *J. Phys. D: Appl. Phys.* **38** R1
[23] Yao C, Chen S, Chang Z, Mu H B and Zhang G J 2019 *J. Phys. D: Appl. Phys.* **52** 455202R1
[24] Guaitella O, Thevenet F, Guillard C and Rousseau A 2006 *J. Phys. D: Appl. Phys.* **39** 2964

A.5 Experimental and modelling study of the effect of airflow orientation with respect to strip electrode on ozone production of surface dielectric barrier discharge

Experimental and modelling study of the effect of airflow orientation with respect to strip electrode on ozone production of surface dielectric barrier discharge ⊘

J. Mikeš; S. Pekárek; I. Soukup

Check for updates

CrossMark

View Online   Export Citation

Experimental and modelling study of the effect of airflow orientation with respect to strip electrode on ozone production of surface dielectric barrier discharge

J. Mikeš,[1,a)] S. Pekárek,[1] and I. Soukup[1,2]

[1]*Czech Technical University in Prague, Faculty of Electrical Engineering, Technická 2, 166 27 Prague 6, Czech Republic*
[2]*Charles University in Prague, Faculty of Mathematics and Physics, Sokolovská 49/83, 186 75 Prague 8, Czech Republic*

This study examines the effect of airflow orientation with respect to the strip active electrode on concentration of ozone and nitrogen dioxide produced in a planar generator based on the surface dielectric barrier discharge. The orientation of the airflow was tested in parallel and perpendicular with respect to the strips. It was found that in the investigated range of average discharge power, the ozone concentration increases approximately by 25% when airflow was oriented in parallel with respect to the strips in comparison with perpendicular orientation of the airflow. Similarly the increase of nitrogen dioxide concentration was observed for parallel orientation of the airflow with respect to the strips in comparison with the perpendicular orientation of the airflow. Within the range of wavelengths from 250 to 1100 nm, the changes of intensities of spectral lines associated with airflow orientation have been observed. A 3D numerical model describing ion trajectories and airflow patterns have also been developed. *Published by AIP Publishing.*
[http://dx.doi.org/10.1063/1.4966603]

I. INTRODUCTION

Ozone is a powerful oxidizing agent with very good disinfecting and reacting properties. It is used, for instance, in the treatment of drinking water, in the papermaking industry, in odour removal products, in medicine, in sterilization, in stomatology, in decontamination of biologically polluted environments, etc. A wide spectrum of ozone applications, coupled with the fact that ozone is an unstable gas that is generated at the site of its use or consumption, has led us to construct an ozone generator in a way that maximizes its efficiency and ozone yield production, and reduces production costs.

The ozone generators based on the dielectric barrier discharge (DBD) date back to 1857 and to the discovery ascribed to the German electrical engineer Werner von Siemens.[1] Studies[2–4] describe the application of the surface dielectric barrier discharge (SDBD) not only for ozone generation, but also for numerous industrial applications (such as plasma displays, CO_2 lasers, planar excimer ultraviolet lamps and air control), in medicine and for surface treatment of materials including the application of thin layers.

Generation of ozone from air by electrical discharge is a complex process,[5–12] which, apart from the type of the working gas (air, oxygen), electrical parameters of the discharge, pressure, temperature, humidity, etc., depends also on the flow of the working gas in the discharge chamber.

There exist various papers describing the effect of airflow on the discharge performance and on discharge ozone generation.[7–16] Important paper describing the effect of air

flows on repetitive nanosecond pulse discharges with a plate-plate electrode configuration is Ref. 14. Presented results show that the volume discharge in the gap strongly depends on the airflows, and the corresponding images show that the discharge modes vary from filament to diffuse modes when the airflow is applied. The effect of the flow rate on silent discharge ozonizer performance has been investigated in Ref. 15. It was shown that the flow rate of the working gas is a more effective parameter on ozone concentration than for example, gas pressure. The effect of the air flow rate on ozone generation by pulsed streamer discharge in air was studied in Ref. 16. The results indicate that ozone concentration is increasing with the voltage but decreasing with the flow rate. The relationship between residence time and concentration of produced ozone is also discussed. The effect of oxygen flow in two opposite directions on ozone synthesis for concentric actuator has been investigated in Ref. 17. It was shown that the gas flow direction practically does not influence concentration of ozone produced by the discharge.

In our paper we present our results of the systematic study of surface dielectric barrier discharge ozone generation in dependence on two different airflow orientations that is parallel or perpendicular with respect to the strips of the active electrode. As long as the generation of ozone from air by electrical discharge could not be separated from the production of nitrogen oxides, we also examined the effect of airflow orientation on the production of nitrogen oxides. Plasma chemistry of this process is rather complicated.[10–12] Production of nitrogen oxides from the standpoint of ozone generation represents certain drawbacks, however, on the other side, nitrogen oxides exhibit important antimicrobial effects.[11]

a)Author to whom correspondence should be addressed. Electronic mail: mikes.jan@fel.cvut.cz.

In order to have a deeper insight into the effect of air-flow orientation with respect to the strip electrode on the discharge performance we also studied the emission spectra of the discharge.

Apart from it, a 3D numerical model describing ion trajectories and airflow patterns in the discharge chamber has also been developed. Even though numerical experiments appeared in studies examining the effect of airflow on SDBD[18–29] it was not possible to completely transfer the methods presented in these papers to the solution of our problem. In most cases, the reasons are an inadequate description of the parameters choice (both physical and discretization ones), vague elimination of the model's singularities, and finally insufficient specification of initial and/or boundary conditions. The key points of our own numerical method together with presentation of all the parameters will be described in the section devoted to the numerical model. The mathematical analysis of the numerical solution will be the subject of our future paper.

II. EXPERIMENTAL ARRANGEMENT

The experimental arrangement, which is shown in Figure 1, consists of surface dielectric barrier discharge ozone generator with a cooling system, an electrical supply unit with diagnostics, an air supply system, instruments for analysis of output products and spectrometers.

An ozone generator in the shape of a box, is made from polymethyl-methacrylate plexiglass. The bottom side of the box is formed by a dielectric alumina plate carrying the electrode system. Active electrode of the system in the form of nine interconnected strips on the upper side of the plate is opened to the discharge chamber. The grounded square electrode on the lower side of the plate is placed on a cooler so that there is both thermal as well as electric contact between this electrode and a cooler.

The alumina plate has a content of Al_2O_3 of 96%, a dielectric constant for 1 MHz of 9.6, electric strength of 14 kV/mm and the heat conductivity for a temperature of 25 °C of 24 W/m K. The dimensions of this plate were $50 \times 50 \times 0.635$ mm.

Both active strip electrode, as well as grounded square electrode, were screen printed on the dielectric plate using conductive DuPont 9538 nickel paste. The geometry of the active strip electrode and the grounded electrode is shown in Figures 2 and 3, respectively.
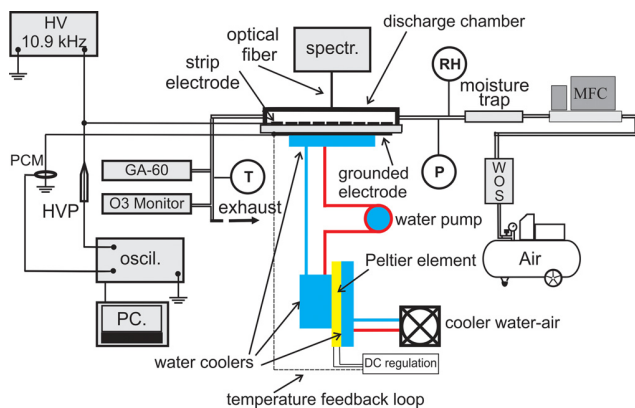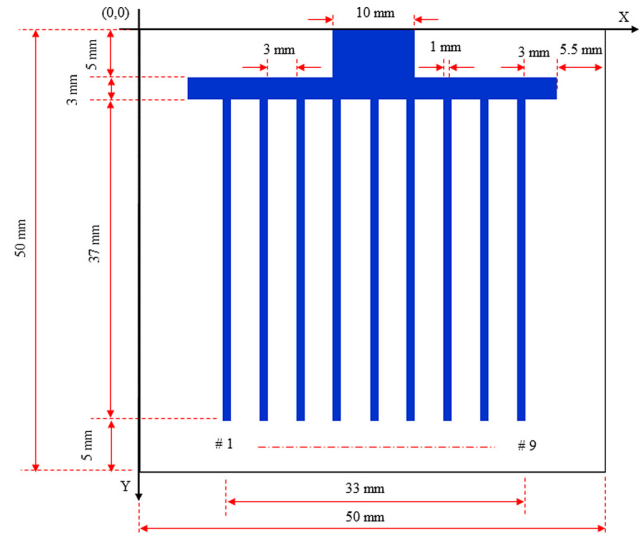
FIG. 2. Geometry of the strip active electrode.

To control the stability of output air temperature, a discharge chamber water cooling system was used. The cooling element Alphacool GPU HF 14 was in contact with the side of dielectric plate carrying the grounded electrode. This cooling element was connected via an identical cooler through polyvinyl chloride (PVC) tubes with a water pump (150 m^3/h) and a 2 l water reservoir. The second Alphacool GPU HF 14 element was in contact with the Peltier element TEC1–12703, which was cooled by a Cooler Master Seidon 120 V compact cooler. The temperature was controlled by a Peltier controller QC-PC-C01C. Dimensions of the Peltier element were $40 \times 40 \times 4.7$ mm. The parameters of the Peltier element were adjusted in such a way that the temperature of air at the output of the discharge chamber was kept constant at 25 °C.

To study the effect of airflow orientation with respect to the strip electrode on ozone and nitrogen oxides concentrations and on emission spectra of the discharge, on each side the discharge chamber were three openings to which were connected tubes for input and output of air. We used three inputs and

FIG. 1. Experimental arrangement.
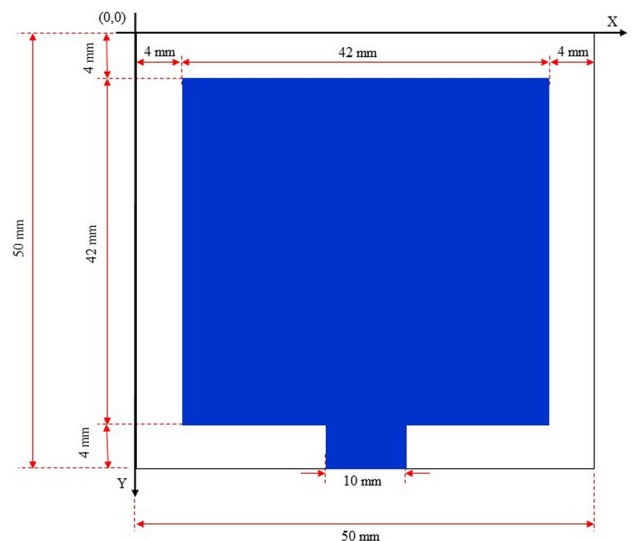
FIG. 3. Geometry of the grounded electrode.
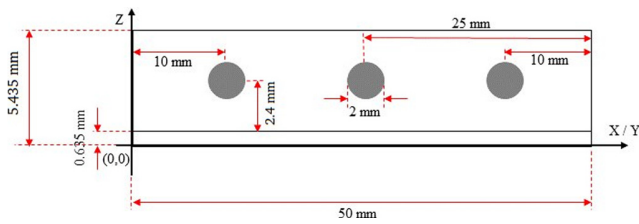
FIG. 4. Geometry of the inputs and outputs of air from one side of the discharge chamber.

outputs in order to have airflow patterns in the discharge chamber more laminar than in case of only one input and output. The geometry of air inputs and outputs, which is shown in Figure 4, is on each side of the discharge chamber identical. On each of the tubes there was a valve, so that it was possible to close any input or input tube. Our experiments were performed with airflow parallel or perpendicular to the strip electrode. Thus for example, for perpendicular airflow, the valves on 3 tubes allowing input of air and 3 tubes allowing output of air along the strips were closed. This situation could be seen in Figure 5.

The geometry of inputs and outputs of air from one side of the discharge chamber is shown in Figure 4.

The experiments were performed with a sinusoidal driving voltage of 10.9 kHz. On the first channel of an ADS 1102 CM digital storage oscilloscope (150 MHz) we sampled and recorded the discharge voltage through the high voltage probe (HVP-28HF, Pintek; division ratio: 1000/1; frequency: up to 200 MHz) to determine the average discharge power. To determine the discharge current we used a signal obtained from a Pearson current monitor (PCM, model 2877). For the purpose of this paper, the amplitude of the discharge voltage is referred to as a discharge voltage. The average discharge P_{AV} power was calculated on basis of the following equation:

$$P_{AV} = \frac{1}{T} \int_0^T U(t) \cdot I(t) \cdot dt, \quad (1)$$

FIG. 5. Photograph of the discharge in ozone generator (Perpendicular airflow orientation with respect to the strip electrode).
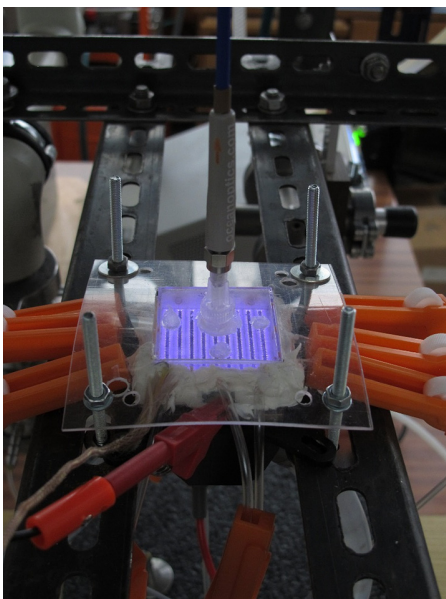
where T is the period, and $U(t)$ and $I(t)$ are voltage and current signals, respectively.

The air supply system consisted from a compressor, a mass flow controller and a moisture trap. The air from a compressor, was through a mass flow controller and a moisture trap supplied to the discharge chamber. The pressure **P** in the discharge chamber was measured using Lutron VC-9200 vacuum meter. The relative humidity **RH** of input air was measured with GMH 3330 device, which was placed between the moisture trap and input to the discharge chamber. The temperature **T** of the output air was measured using thermocouple thermometer.

The ozone concentration was measured by absorption of the 254 nm UV spectral line using an API 450 monitor with the upper limit of ozone concentration of 5000 ppm. To measure concentrations of nitrogen dioxide and nitrogen oxide, a GA-60 gas analyzer equipped with various electrochemical cells has been used. The upper limit of nitrogen dioxide concentration was 1000 ppm.

To study the effect of airflow orientation with respect to the strip electrode on discharge emission spectra we used two HR2000+ spectrometers, the first one for the range of wavelengths from 250 to 700 nm and the second one for wavelengths from 680 to 1100 nm. As it is seen in Figures 1 and 5, the emission spectra were collected by optical fiber through an opening in the upper side of the discharge chamber.

A photograph of the discharge in ozone generator with perpendicular airflow orientation with respect to the strip electrode is shown in Figure 5.

III. EXPERIMENTAL RESULTS AND DISCUSSION

All experiments were performed with constant airflow through the discharge chamber of 1.8 slm and relative humidity of air ∼4%. Due to the constant mass flow of air there was a small overpressure of about 4 Torr in the discharge chamber with respect to the atmospheric pressure. The temperature of input air was equal to the ambient temperature of the laboratory; the temperature of air at the output of the discharge chamber 25 °C was kept constant using the cooling system.

A dependence of ozone concentrations as a function of average discharge power for parallel and perpendicular airflow orientations with respect to the strip electrode is shown in Figure 6.

It can be seen in Figure 6 that the concentration of ozone produced by the discharge with parallel airflow orientation with respect to the strip electrode is higher for the same average power than for the configuration with perpendicular airflow orientation with respect to the strip electrode.

Important quantity from the standpoint of practical applications is the ozone production yield, which expresses the amount of energy required for production of 1 g of ozone. Ozone production yield α is defined in the following way:

$$\alpha = \frac{21.44 \times (ozone\, concentration) \times airflow \times 6 \times 10^{-3}}{P_{AV}} \left[\frac{g}{kWh}\right], \quad (2)$$

FIG. 6. Ozone concentration versus average discharge power for two airflow orientations with respect to the strip electrode.
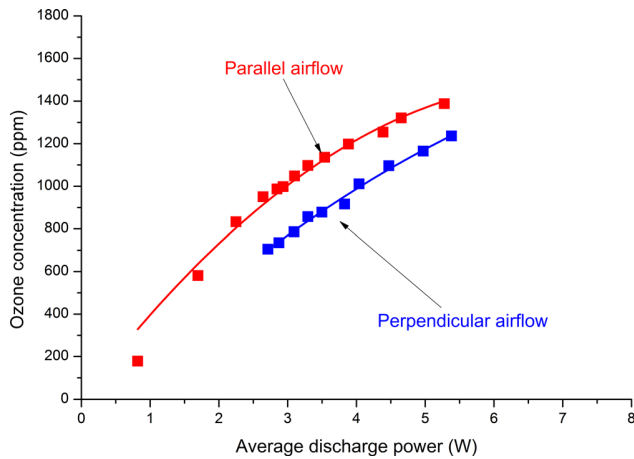
FIG. 8. Nitrogen dioxide concentration versus average discharge power for two airflow orientations with respect to the strip electrode.

where the concentration of ozone produced by the discharge is substituted in parts per million, the airflow in standard litres per minute, and the average discharge power in watts.

Ozone production yield for parallel and perpendicular airflow orientations with respect to the strip electrode is shown in Figure 7. From this graph, it could be seen that ozone production yield for parallel airflow orientation with respect to the strip electrode is higher than for the perpendicular airflow orientation, therefore this type of airflow is more favorable for practical applications.

As long as the generation of ozone from air by electrical discharge could not be separated from the production of nitrogen oxides we also examined the effect of airflow orientation on the production of nitrogen dioxide. The nitrogen dioxide concentrations for parallel and perpendicular airflow orientations with respect to the strip electrode are shown in Figure 8.

From this figure, it can be seen that for particular discharge, power concentration of nitrogen dioxide is higher for parallel orientation of airflow with respect to the strip
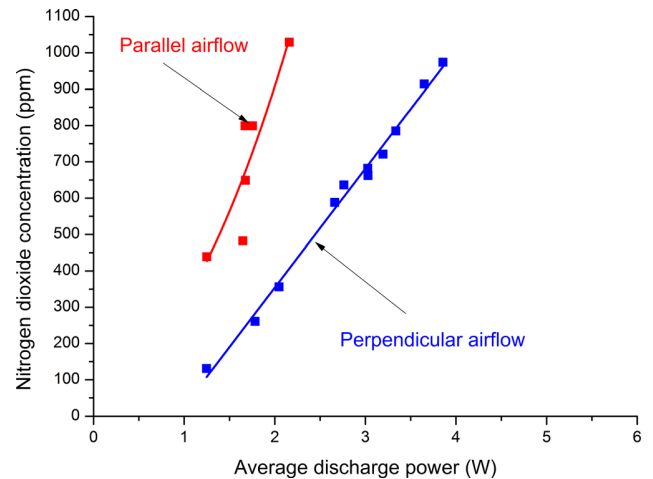
electrode than for perpendicular orientation. Apart from it, concentration of NO_2 increases steeply with the average power.

Besides nitrogen dioxide concentration dependence versus average discharge power we also measured the concentration of nitrogen monoxide within the same range of average discharge power from 0 to 6 W. We found that for all this, the range concentration of nitrogen monoxide was below the detectable limit of our instrument. This result coincides with the facts mentioned and explained in Refs. 11 and 30.

In order to have a deeper insight on the effect airflow orientation with respect to strip electrode on the discharge performance and its ozone and nitrogen oxides production we also investigated the change in emission spectra of the discharge for these two flow orientations. In the following Figures 9 and 10 are shown emission spectra of the discharge for the range of wavelength 250–700 nm and 680–1100 nm respectively. These spectra, which were taken for the same discharge voltage 4300 V, are given for both airflow orientations with respect to the strip electrode.

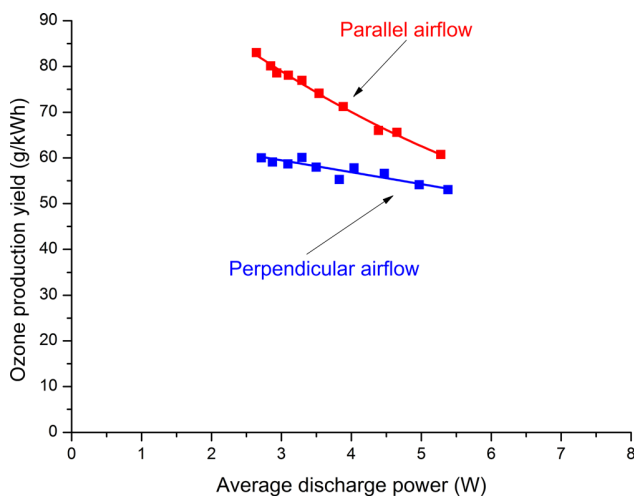FIG. 7. Ozone production yield versus average discharge power for two airflow orientations with respect to the strip electrode.


FIG. 9. Emission spectra intensity for the range of wavelength 250–700 nm for two airflow orientations with respect to the strip electrode and for the discharge voltage 4300 V.
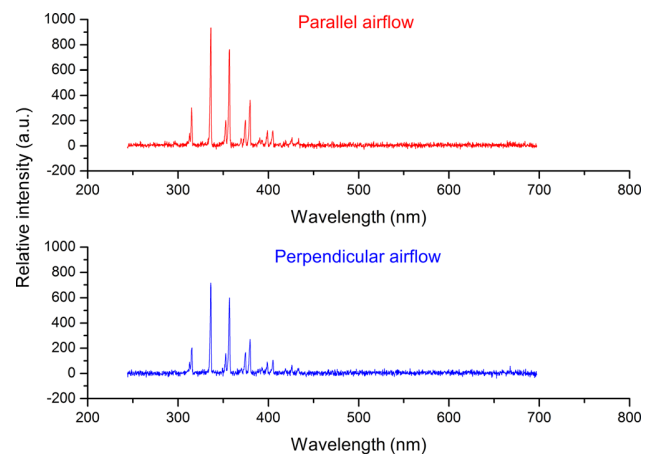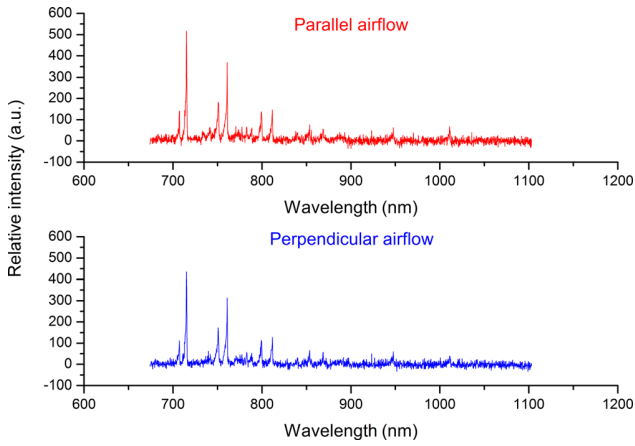
FIG. 10. Emission spectra intensity for the range of wavelength 680–1100 nm for two airflow orientations with respect to the strip electrode and for the discharge voltage 4300 V.

FIG. 11. Dependence of the discharge voltage versus average discharge power for two airflow orientations with respect to the strip electrode.

From Figures 9 and 10 could be concluded that for both ranges of wavelengths the intensities of spectral lines for the same discharge voltage are higher in case of parallel airflow compared to that in the perpendicular airflow.

The results presented in Figures 6–10 show that ozone concentration, ozone production yield, nitrogen dioxide concentration, and discharge emission spectra depend on orientation of airflow with respect to the strip active electrode. This result could be at least qualitatively explained by combination of several effects.

The first effect is based on the change of electric field associated with flow orientation. The higher electric field in case of parallel airflow could be caused by faster removal of residual charged (ionic) species left behind by the discharge event that otherwise, lowers the electric field necessary for the next discharge event for the same input energy condition. The species important for ozone formation are among others nitrogen ions involved, e.g., in the second positive system of nitrogen $C^3\Pi_u \rightarrow B^3\Pi_b$ and the first positive system of nitrogen $B^3\Pi_b \rightarrow A^3\Sigma_u^+$. The lifetime of $A^3\Sigma_u^+$ is of the order of around 10^{-2} s (Ref. 31) and is much longer than the half-period of the discharge voltage. The metastable state of ions $A^3\Sigma_u^+$ forms a reservoir of energy at the time of forming the discharge.[32,33] If the airflow orientation is parallel with respect to the strip electrode (i.e., perpendicular to the microdischarge channels), the ions in this metastable state are removed from the area of discharge and consequently a higher voltage is needed to maintain the discharge. Therefore, ozone concentration is also higher due to the increased voltage. If the airflow is oriented perpendicularly with respect to the strip electrode, the ions in these metastable states are transferred within individual microdischarges (particles move in a parallel direction along the microdischarge length), they are not removed, and hence there is no increase in the discharge voltage and ozone concentration (Fig. 11).

The second effect could be associated with the influence of airflow orientation on microdischarge dimensions and consequently on the residence time. The longer the residence time, the probability of dissociation of oxygen molecules
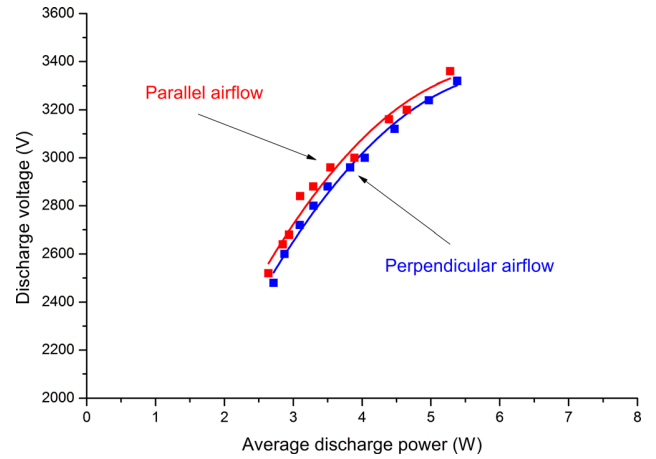
into atomic oxygen increases and hence the ozone generation also increases. The residence time can be taken as a ratio of the dimensions of the region in which the ozone generation occurs and the air velocity. According to Ref. 15 the ozone generation in dielectric barrier discharge takes place mainly in microdischarges. The microdischarge radius is according to approximately 100–200 μm and its length (depending on the polarity of the surface electrode) is of the order of a millimeter.[4] As long as the magnitude of air velocity at a particular point of the discharge chamber is the same for both orientations of airflow, the residence time is influenced only by the dimensions of the microdischarge channels. The dimensions of the microdischarge channels could be changed due to the fact that the particles are dragged by the airflow. Thus the relative change of radius of the microdischarge for the case of parallel airflow with respect to strip electrode is greater than the relative change of the length of the microdischarge channel for the case of perpendicular airflow with respect to the strip electrode.

IV. NUMERICAL MODELLING

In order to have a deeper insight into the observed effects, a mathematical model has been proposed accompanied by a numerical solution using our original numerical method. The list of used symbols is given in the Appendix.

A. Mathematical model

We assume $\Omega \subset R^3$ to be a bounded domain and $T > 0$ a given time. We set $Q_T = \Omega \times [0, T]$ and by $\partial\Omega$ we denote the boundary of Ω. Furthermore, we assume Ω to be a composition of two disjoint domains, $\Omega = \Omega_{Die} \cup \Omega_{Air}$, and $\partial\Omega$ to consist of several disjoint parts, $\partial\Omega = \Gamma_{Grnd} \cup \Gamma_{Walls}$, where $\Gamma_{Walls} = \Gamma_{BottomWalls} \cup \Gamma_{TopWalls} \cup \Gamma_{In} \cup \Gamma_{Out}$ (see Figure 2). Furthermore, the interface between Ω_{Die} and Ω_{Air} consists of two disjoint parts, $\partial\Omega_{Die} \cap \partial\Omega_{Air} = \Gamma_{AirToDie} \cup \Gamma_{Strip}$.

In the definition of the model describing the SDBD we follow the models from Refs. 20, 25, and 27. Hence, we start with the relation between the electric field $\vec{E} : Q_T \rightarrow R^3$ and the electric potential $\Phi : Q_T \rightarrow R$

$$\vec{E} = -\nabla\Phi \text{ in } Q_T, \tag{3}$$

where ∇ denotes the gradient with respect to the space variable. Following the reasoning introduced in Ref. 20, we model the electric field by means of the Poisson equation, where we assume the potential to be decomposed into two parts: one being a potential induced by the external electric field, $\phi : Q_T \to R$, and the other being a potential induced by the net charge density in the plasma, $\varphi : \Omega_{Air} \times (0, T) \to R$, i.e., $\Phi = \phi + \varphi$ and

$$\nabla \cdot (\varepsilon_{Air}\varepsilon_0 \nabla\varphi) = -e(n_e - n_i) \quad \text{in } \Omega_{Air} \times (0, T), \tag{4}$$

$$\nabla \cdot (\varepsilon_r \varepsilon_0 \nabla\phi) = 0 \quad \text{in } Q_T, \tag{5}$$

where $\nabla\cdot$ represents the divergence operator, $n_e : \Omega_{Air} \times (0, T) \to R$ denotes the electron density, $n_i : \Omega_{Air} \times (0, T) \to R$ denotes the ion density, $\varepsilon_0 = 8.85 \times 10^{-12} \frac{F}{m}$ is the vacuum permittivity and the piecewise constant function ε_r is the relative permittivity of air ($\varepsilon_r|_{\Omega_{Air}} = \varepsilon_{Air} = 1.0006$) and dielectric material ($\varepsilon_r|_{\Omega_{Die}} = \varepsilon_{Die} = 9.6$), and $e = 1.6022 \times 10^{-19}$ C is the elementary charge. The time evolution of electron and ion densities is determined by the continuity equation where the ionization rate is expressed as a function of the electron flux and the Townsend coefficient, i.e., the time evolution equations are described as follows:

$$\frac{\partial n_i}{\partial t} + \nabla \cdot (n_i \vec{V}_i) = A \cdot p \cdot \exp\left\{-\frac{B \cdot p}{\|\vec{E}\|}\right\} \|n_e \vec{V}_e\|$$
$$- rn_i n_e \quad \text{in } \Omega_{Air} \times (0, T) \tag{6}$$

$$\frac{\partial n_e}{\partial t} + \nabla \cdot (n_e \vec{V}_e) = A \cdot p \cdot \exp\left\{-\frac{B \cdot p}{\|\vec{E}\|}\right\} \|n_e \vec{V}_e\|$$
$$- rn_i n_e \quad \text{in } \Omega_{Air} \times (0, T) \tag{7}$$

where $\exp\{\}$ stands for the classical exponential function, $\vec{V}_i : \Omega_{Air} \times (0, T) \to R^3$ is the ion velocity field, $\vec{V}_e : \Omega_{Air} \times (0, T) \to R^3$ is the electron velocity field, $p = 760$ Torr is the constant air pressure, $r = 2 \times 10^{-12}$ m^{3}s^{-1} denotes the electron-ion recombination rate and $A = 1.5 \times 10^3$ m^{-1} Torr^{-1} and $B = 3.56 \times 10^4$ Vm^{-1} Torr^{-1} are pre-exponential and exponential constants, respectively. For the sake of completeness, it should be noted that $\|\cdot\|$ represents the usual Euclidean norm in R^3. Further, using the so-called Drift-Diffusive model we rewrite electron and ion fluxes as

$$n_i \vec{V}_i = n_i \mu_i \vec{E} - D_i \nabla n_i \quad \text{in } \Omega_{Air} \times (0, T), \tag{8}$$

$$n_e \vec{V}_e = -n_e \mu_e \vec{E} - D_e \nabla n_e \quad \text{in } \Omega_{Air} \times (0, T), \tag{9}$$

where $\mu_e = \frac{4.4 \times 10^1}{p}$ [m^2 V^{-1} s^{-1}] and $\mu_i = \frac{1.45 \times 10^{-1}}{p}$ [m^2 V^{-1} s^{-1}] are the electron and ion mobility coefficients, respectively, and $D_e = \frac{k_B}{e}\mu_e T_e$ [m^{2}s^{-1}] and $D_i = \frac{k_B}{e}\mu_i T_i$ [m^2 s^{-1}] are the electron and ion diffusion coefficients, respectively, where $k_B = 1.3806488 \times 10^{-23}$ m^{2}kgs^{-2}K^{-1} is Boltzmann's constant, $T_e = 60000$ K is the electron temperature, and $T_i = 300$ K is the ion temperature. All the constants were taken from the literature.[34]

The numerical solution of equation (5) can be computed independently of the remaining equations. Then, by substituting (3), (8), and (9) into (6) and (7) and using the results of (5) we can reduce the problem to three scalar equations for three scalar unknown quantities (φ, n_i, n_e) and compute the remaining entities afterwards.

It remains to formulate the initial and boundary conditions for (ϕ) and (φ, n_i, n_e). We assume the following:

$$\phi(x, 0) = 0 \quad \text{in } \Omega, \tag{10}$$

$$\phi(x, t) = U_{amp} \sin(\omega t) \quad \text{on } \Gamma_{Strip} \times (0, T),$$
$$\phi(x, t) = 0 \quad \text{on } \Gamma_{Grnd} \times (0, T), \tag{11}$$

$$\nabla\phi \cdot \vec{n} = 0 \quad \text{on } \Gamma_{Walls} \times (0, T), \tag{12}$$

$$\varphi(x, 0) = 0, \quad n_i(x, 0) = n_0, \quad n_e(x, 0) = n_0 \quad \text{in } \Omega_{Air}, \tag{13}$$

$$\varphi(x, t) = 0, \quad n_i(x, t) = 0 \quad \text{on } \Gamma_{Strip} \times (0, T), \tag{14}$$

$$\nabla\varphi(x, t) \cdot \vec{n} = 0 \quad \text{on } \Gamma_{TopWalls} \cup \Gamma_{In} \cup \Gamma_{Out} \cup \Gamma_{AirToDie} \times (0, T), \tag{15}$$

$$\nabla n_i(x, t) \cdot \vec{n} = 0 \quad \text{on } \Gamma_{TopWalls} \cup \Gamma_{In} \cup \Gamma_{Out} \cup \Gamma_{AirToDie} \times (0, T), \tag{16}$$

$$\nabla n_e(x, t) \cdot \vec{n} = 0 \quad \text{on } \partial\Omega_{Air} \times (0, T), \tag{17}$$

where $\vec{n}$ denotes the outer unit normal vector to Γ, $n_0 = 2 \times 10^{15}$ m^{-3} is the reference density,[22] $U_{amp} = 3.1$ kV is the discharge voltage, $\omega = 2\pi f$ is the angular velocity, and $f = 10.9$ kHz is the frequency.

Moreover, we study the airflow in the ozone generator. We consider air to behave as an incompressible Newtonian fluid, i.e., its flow is governed by the following Navier-Stokes (N-S) equations:

$$\nabla\vec{V} = 0, \tag{18}$$

$$\rho\frac{\partial\vec{V}}{\partial t} + \rho\vec{V} \cdot \nabla\vec{V} - \mu_{air}\nabla^2\vec{V} = -\nabla P, \tag{19}$$

where $\vec{V} : \Omega_{Air} \times (0, T) \to R^3$ denotes the air velocity field, $P : \Omega_{Air} \times (0, T) \to R$ denotes the air pressure, $\rho = 1.225$ kgm^{-3} stands for the constant air density, and $\mu_{Air} = 1.8860763 \times 10^{-5}$ kgm^{-1} s^{-1} denotes the constant air viscosity. The initial and boundary conditions are assumed to be as follows:

$$\vec{V}(x, 0) = 0 \quad \text{in } \Omega_{Air}, \tag{20}$$

$$\vec{V}(x, t) = 0 \quad \text{on } \Gamma_{Strip} \cup \Gamma_{AirToDie} \cup \Gamma_{TopWalls} \times (0, T), \tag{21}$$

$$\vec{V}(x, t) = \vec{V}_{in}(x, t) \quad \text{on } \Gamma_{in} \times (0, T), \tag{22}$$

$$\frac{\partial\vec{V}}{\partial n}(x, t) = 0 \quad \text{on } \Gamma_{out} \times (0, T), \tag{23}$$

where $\vec{V}_{in}(x, t) = 3.1831$ ms^{-1} in $\Gamma_{in} \times (0, T)$ is the constant inlet velocity of air.

It should be noted that we neglect here the effect of the SDBD on the airflow since our aim is only to illustrate the

airflow patterns for different cases of inflow orientations with respect to the strip electrode. Even though we are able to compute the effect of the SDBD on stationary air, we are not able to solve a similar problem for low-speed airflow. It is a fact[21] that the characteristic timescale in the system describing the SDBD is of an order of magnitude of $O(10^{-6})$ s for electron flux and for low-speed airflow it is of an order of magnitude of $O(10^{-1})$ s, i.e., the computational cost is unbearable.

B. Numerical method

The solution of the presented models starts with the process of non-dimensionalization. Motivated by the non-dimensionalization scheme presented in Ref. 24, we introduce new variables and new dimensionless quantities as follows:

$$t = \frac{\tau}{\omega}, \quad x_j = Lz_j \, (j = 1, 2, 3), \quad x_i = Lz_i, \quad n_e = n_0 N_e,$$

$$n_i = n_0 N_i, \quad \Phi = \frac{k_B T_e}{e_c} \Phi_{nd}, \quad \vec{V} = \vec{v} V_0, \quad P = p P_0,$$

where $L = 0.05$ m is the so-called characteristic length, $V_0 = 1\,\text{ms}^{-1}$ is the so-called characteristic velocity, and $P_0 = \rho V_0^2$ is the so-called characteristic pressure.

Further, we define the Galerkin weak formulation for the SDBD model and use a standard finite element method (FEM) method with Lagrangian elements of the first order for the discretization in space variable. The time discretization for the SDBD is based on the Backward difference formula of the second order (BDF-2) scheme.

In particular, we introduce an approximation of the obtained discrete problem where we replace the ionization rate $\exp\left\{-\frac{B \cdot p}{\|\nabla\Phi\|}\right\} \|n_e \mu_e \nabla\Phi - D_e \nabla n_e\|$ by its linear approximation using the solutions from the previous time step. More precisely, the linear approximation is performed using the Taylor series and by taking extra care of cases where the approximation is not defined, i.e., everywhere $\|\nabla\Phi\|$ and $\|n_e\mu_e\nabla\Phi - D_e\nabla n_e\|$ are zero or close to zero. The problem here is not only a correct definition of linear approximation of the ionization rate term but also careful handling of the machine's precision in the process of linearization. Absolutely identical problems have to be overcome even if we skip the linearization process and use directly the Newton method.

Now, since the system we obtain after linearization of the ionization rate term is still non-linear, we use the Newton iteration method where the formed linear system is solved by the GMRES (Generalized Minimal RESidual) iteration method with an Incomplete Lower-Upper (ILU) preconditioner. The absolute convergence criterion (for residuum norm) for GMRES and Newton is set to 10^{-10}.

Afterwards, we reconstruct the entities $\vec{E}$, $\vec{V}_i$, and $\vec{V}_e$, which is quite straightforward. We only have to be more cautious about the reconstruction of $\vec{V}_i$ and $\vec{V}_e$, since there might be no particles to track in some parts of the domain. In particular, we employ a simple heuristic, "where there are only a few particles there is no movement," i.e., we define a minimal amount of particles, $N_{min} = 10\,\text{m}^{-3}$, and whenever the
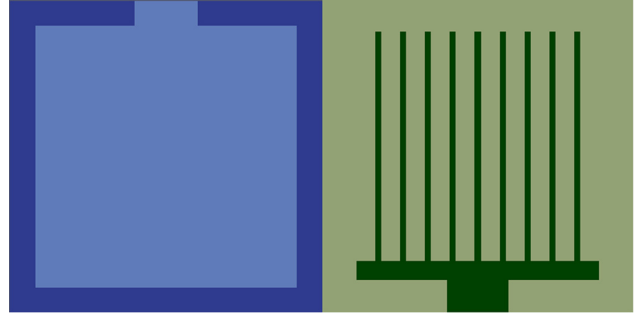
FIG. 12. The marking of the domain boundary, Γ_{Strip}, $\Gamma_{AirToDie}$, Γ_{Grnd}, and $\Gamma_{BottomWalls}$.

ion or electron density drops below N_{min}, we set the corresponding particle velocity to zero.

Finally, we solve the problem of airflow using the FEM discretization in space with the Lagrangian elements of the second order for velocity and of the first order for pressure (i.e., Taylor-Hood elements). The time discretization is based on the explicit Euler scheme. The convective term is linearized using the velocity from the previous time step. Thus, we get a linear system of saddle-point structure. We construct an ILU preconditioner for the convection-diffusion part of the saddle-point matrix and an Algebraic Multigrid inverse of the Schur complement approximation. The solution is then found using the GMRES iteration method.

C. Numerical experiment

Let us start with the definition of the domain Ω and its mesh. We use metre as a unit of distance in the following definitions. The domain Ω is defined as a simple cuboid C. In particular, $C = \{\vec{x} \in R : x \in (0, 0.05), \, y \in (0, 0.05), z \in (0, 0.005435)\}$, i.e., C is an open cuboid of the size $50 \times 50 \times 5.435$ mm. Further, $\Gamma_{Strip} = \{\vec{x} \in R^3 : (x, y) \in S_{xy}, z = 0.000635\}$, where $S_{xy} \subset R^2$ is a closed set defined in Figure 2 as the blue area. Next, $\Gamma_{Grnd} = \{\vec{x} \in R^3 : (x, y) \in G_{xy}, z = 0.0\}$, where $G_{xy} \subset R^2$ is a closed set defined in Figure 3 as the blue area. The inlet and outlet parts of the domain (in the perpendicular as well as in the parallel case) are set in a similar manner (see Figure 4, where all the details are described).

Now, we label the boundary of the domains Ω, Ω_{Air}, Ω_{Die}. For reasons of simplicity, let us introduce the definition of the boundary parts with the help of Figures 12 and 13, i.e., Γ_{Strip} is defined as the part of $\partial\Omega_{Air}$ coloured in dark green, $\Gamma_{AirToDie}$ is coloured in light green, Γ_{Grnd} is coloured in light blue, and $\Gamma_{BottomWalls}$ is coloured in dark blue.
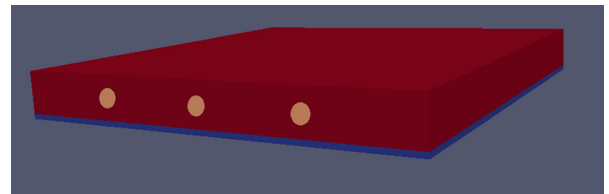

FIG. 13. The marking of the domain boundary, $\Gamma_{TopWalls}$, Γ_{In}, and $\Gamma_{BottomWalls}$.

$\Gamma_{TopWalls}$ is coloured in red, Γ_{In} is coloured in light brown, and Γ_{Out} is defined analogously as Γ_{In}.

Further, the mesh consists of approximately 600 000 tetrahedrons. It was generated in tetgen (see [tetgen.org]) using a predefined set of vertices. The predefined set of vertices divides the domain into cubes refined near electrodes, inlet, and outlet parts of the domain. There are four levels of refinement and the smallest cube is of the size $0.00025 \times 0.00025 \times 0.0003175$ m.

We solved the numerical problem by $T = T_{SDBD} = \frac{1}{2f}$ s ≈ 0.0000459 s, i.e., $T \approx 46 \, \mu$s, with a time step of size $\Delta T_{SDBD} = 10^{-7}$s $= 0.1 \, \mu$s and the airflow is simulated by $T = T_{Air} = 1$ s with a time step of size $\Delta T_{Air} = 0.01$ s.

Figures 14 and 15 show the computed trajectories of ions, Figure 16 shows the ion density while Figures 17 and 18 present the computed airflow patterns for parallel and perpendicular airflow cases, respectively.
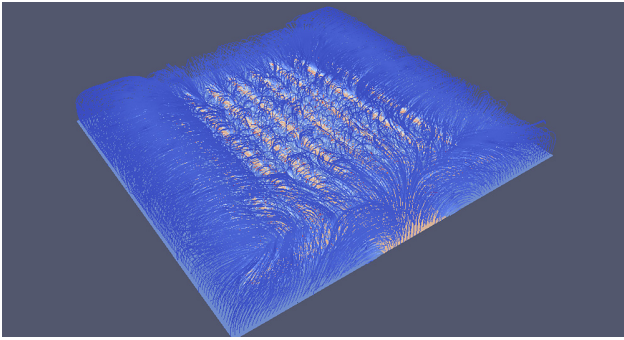
FIG. 14. The ion trajectories above the strip electrode at the time $\frac{T_{SDBD}}{2}$.
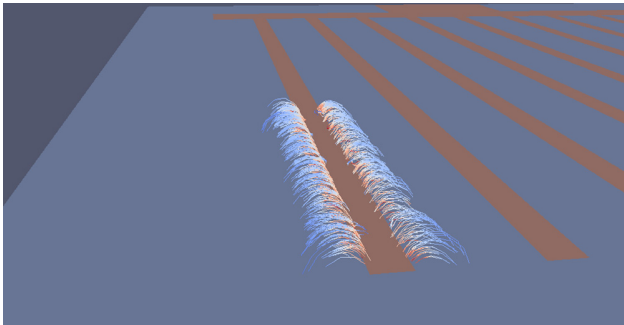
FIG. 15. Close-up look at ion trajectories at the time $\frac{T_{SDBD}}{2}$.
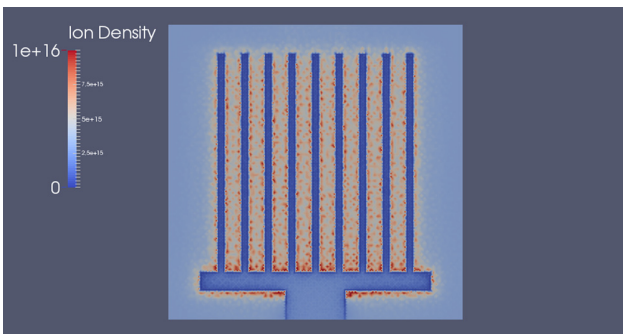
FIG. 16. The ion density near the strip electrode ($z = 0.636$ mm) at the time $\frac{T_{SDBD}}{2}$.
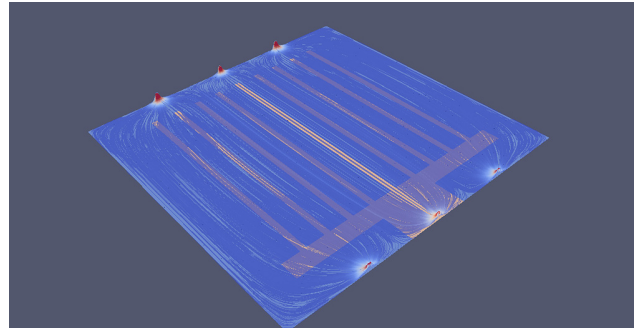
FIG. 17. The airflow patterns near the strip electrode at the time T_{Air} (parallel airflow).
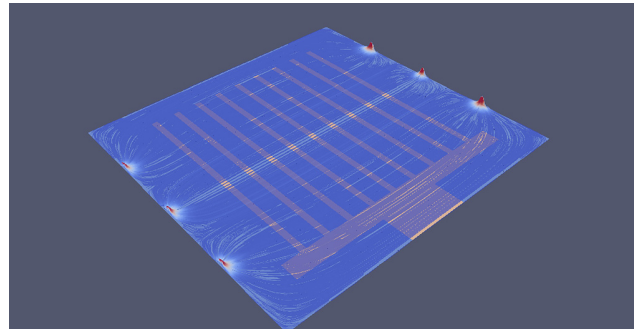
FIG. 18. The airflow patterns near the strip electrode at the time T_{Air} (perpendicular airflow).

The ion trajectories above the strip electrode at the time $\frac{T_{SDBD}}{2}$ are solved in Figure 14. The occasional "disorderliness" of these trajectories far away from strip electrode is mainly caused by machine precision error.

The ion density, which is shown in Figure 16 corresponds well with the image of plasma, shown in Figure 5.

CONCLUSIONS

For the surface dielectric barrier discharge in air energized by the ac voltage of frequency 10.9 kHz we studied the effect of parallel or perpendicular airflow orientation with respect to the strip active electrode on concentration of ozone and nitrogen dioxide produced by the discharge, on discharge emission spectra and on electrical parameters of the discharge. The mathematical model has been proposed accompanied by a numerical solution using our original numerical method. Presented experimental results were obtained for the discharge in air at atmospheric pressure, temperature 25 °C and relative humidity of 4%.

Our findings can be summarized as follows:

- For the same average discharge power, the ozone concentration increases approximately by 25% when the airflow was oriented in parallel with respect to the strips in comparison with perpendicular orientation of the airflow.
- For the same average discharge power, the ozone production yield is higher when the airflow was oriented in parallel with respect to the strips in comparison with perpendicular orientation of the airflow.
- For the same average discharge power, the nitrogen dioxide concentration is higher when the airflow was oriented

in parallel with respect to the strips in comparison with perpendicular orientation of the airflow.

- For the same discharge voltage, the intensities of spectral lines are higher in case of parallel airflow with respect to the strips compared to that in the perpendicular flow.
- For the same average discharge power, the discharge voltage is higher when the airflow was oriented in parallel with respect to the strips in comparison with perpendicular orientation of the airflow.
- A 3D numerical model describing trajectories of ions in a stationary air have been developed.
- A 3D airflow patterns for parallel and perpendicular flow in the discharge chamber have been developed.

Obtained results could be used for the design of more efficient ozone generators or generators producing nitrogen oxides.

ACKNOWLEDGMENTS

APPENDIX: TABLE OF SYMBOLS

$\partial\Omega = \Gamma_{Grnd} \cup \Gamma_{Walls}$	Domain boundary
$\Gamma_{Walls} = \Gamma_{BottomWalls} \cup$ $\Gamma_{TopWalls} \cup \Gamma_{In} \cup \Gamma_{Out}$	Division of walls boundary
$\Omega = \Omega_{Die} \cup \Omega_{Air}$	Division of domain
$\partial\Omega_{Die} \cap \partial\Omega_{Air} = \Gamma_{AirToDie} \cup \Gamma_{Strip}$	Division of inner boundary between domains
$\Gamma_{Strip} = \{\vec{x} \in R^3 : (x, y)$ $\in S_{xy}, z = 0.000635\}$	Definition of strip electrode
$\Gamma_{Grnd} = \{\vec{x} \in R^3 : (x, y)$ $\in G_{xy}, z = 0.0\}$	Definition of grounded electrode
$\Gamma_{AirToDie}$	Boundary between air and dielectric domains without strip electrode
$\Gamma_{BottomWalls}$	Boundary of dielectric domain without boundary of air domain and grounded electrode
$T_{SDBD} \approx 46 \times 10^{-6}$ s	Total time of SDBD simulation
$T_{Air} = 1$ s	Total time of N-S simulation
$\Delta T_{SDBD} = 0.1 \times 10^{-6}$ s	Time step for SDBD computation
$\Delta T_{Air} = 0.01$ s	Time step for N-S computation
$\vec{E} : Q_T \to R^3$	Electric field
$\Phi : Q_T \to R$	Electric potential
$\phi : Q_T \to R$	Potential induced by the external electric field
$\varphi : \Omega_{Air} \times (0, T) \to R$	Potential induced by the net charge density in the plasma
$\varepsilon_0 = 8.85 \times 10^{-12} \frac{F}{m}$	Vacuum permittivity
$\varepsilon_r|_{\Omega_{Air}} = \varepsilon_{Air} = 1.0006$	Relative permittivity of air
$\varepsilon_r|_{\Omega_{Die}} = \varepsilon_{Die} = 9.6$	Relative permittivity of dielectric material
$e = 1.6022 \times 10^{-19}$ C	Elementary charge
$n_e : \Omega_{Air} \times (0, T) \to R$	Electron density
$n_i : \Omega_{Air} \times (0, T) \to R$	Ion density
$\vec{V}_e : \Omega_{Air} \times (0, T) \to R^3$	Electron velocity field
$\vec{V}_i : \Omega_{Air} \times (0, T) \to R^3$	Ion velocity field

(Continued.)

$A = 1.5 \times 10^3$ m^{-1}Torr^{-1}	Townsend pre-exponential constant
$B = 3.56 \times 10^4$ Vm^{-1}Torr^{-1}	Townsend exponential constants
$p = 760$ Torr	Atmospheric pressure
$r = 2 \times 10^{-12}$ m^{3}s^{-1}	Electron-ion recombination rate
$\mu_i = \frac{1.45 \times 10^{-1}}{p}$ [m^{2}V^{-1}s^{-1}]	Ion mobility coefficient
$D_i = \frac{k_B}{e}$ [$\mu_i T_i$m^{2}s^{-1}]	Ion diffusion coefficients
$\mu_e = \frac{4.4 \times 10^1}{p}$ [m^{2}V^{-1}s^{-1}]	Electron mobility coefficient
$D_e = \frac{k_B}{e}$ [$\mu_e T_e$m^{2}s^{-1}]	Electron diffusion coefficients
$k_B = 1.3806488 \times 10^{-23}$ [m^{2}kgs^{-2}K^{-1}]	Boltzmann's constant
$T_e = 60000$ K	Electron temperature
$T_i = 300$ K	Ion temperature
$\vec{n}$	Outer unit normal vector to Γ
$U_{amp} = 3.1$ kV	Discharge voltage
$\omega = 2\pi f$	Angular velocity
$f = 10.9$ kHz	Frequency of the driving voltage
$n_0 = 2 \times 10^{15}$ m^{-3}	Reference particle density
$\vec{V} : \Omega_{Air} \times (0, T) \to R^3$	Air velocity field
$P : \Omega_{Air} \times (0, T) \to R$	Air pressure
$\rho = 1.225$ kgm^{-3}	Air density
$\mu_{air} = 1.8860763$ $\times 10^{-5}$ kgm^{-1}s^{-1}	Air viscosity
$\vec{V}_{in}(x, t) = 3.1831$ ms^{-1} in $\Gamma_{in} \times (0, T)$	Inlet velocity of air
$\tau = \omega t$	Dimensionless time
$L = 0.05$ m	Characteristic length
$z_j = \frac{x_j}{L}, j = 1, 2, 3$	Dimensionless space variable components
$N_e = n_e/n_0$	Dimensionless electron density
$N_i = n_i/n_0$	Dimensionless ion density
$\Phi_{nd} : Q_T \to R$	Dimensionless electric potential
$V_0 = 1$ ms^{-1}	Characteristic velocity
$\vec{v} = \vec{V}/V_0$	Dimensionless air velocity field
$P_0 = \rho V_0^2$	Characteristic pressure
$p = P/P_0$	Dimensionless air pressure
$N_{min} = 10$ m^{-3}	Minimal amount of particles

[1] W. V. Siemens, Annalen der Chemie und Physik **102**, 66 (1857).
[2] U. Kogelschatz, B. Eliasson, and W. Egli, Pure Appl. Chem. **71**, 1819 (1999).
[3] U. Kogelschatz, Plasma Chem. Plasma Process. **23**, 1 (2003).
[4] V. I. Gibalov and G. J. Pietsch, Plasma Sources Sci. Technol. **21**, 024010 (2012).
[5] H. Y. Kim, S. K. Kang, H. C. Kwon, H. W. Lee, and J. K. Lee, Plasma Processes Polym. **10**, 686 (2013).
[6] V. I. Gibalov and G. J. Pietsch, J. Phys. D: Appl. Phys. **33**, 2618 (2000).
[7] S. Jodzis, Ozone: Sci. Eng. **34**, 378 (2012).
[8] S. Pekárek and J. Mikeš, Eur. Phys. J. D **68**, 10 (2014).
[9] S. Pekárek, J. Mikeš, and J. Krýsa, Appl. Catal. A: General **502**, 122 (2015).
[10] U. Kogelschatz, B. Eiasson, and M. Hirth, Ozone: Sci. Eng. **10**, 367 (1988).
[11] M. A. Malik, C. Jiang, R. Heller, J. Lane, D. Hughes, and K. H. Schoenbach, Chem. Eng. J. **283**, 631 (2016).
[12] A. Abdelaziz, T. Ishijima, T. Seto, N. Osawa, H. Wedaa, and Y. Otani, Plasma Sources Sci. Technol. **25**, 035012 (2016).
[13] S. Pavon, J.-L. Dorier, Ch. Hollenstein, P. Ott, and P. Leyland, J. Phys. D: Appl. Phys. **40**, 1733 (2007).
[14] J. Tang, L. Wei, Y. Huo, J. Song, D. Yu, and Ch. Zhang, Plasma Sci. Technol. **18**, 273 (2016).
[15] A. A. Garamoon, F. F. Elakshar, A. M. Nossair, and E. F. Kotp, Plasma Sources Sci. Technol. **11**, 254 (2002).
[16] Z. Buntat, I. R. Smith, and N. A. M. Razali, Appl. Phys. Res. **42**, 1 (2009).
[17] S. Jodzis, T. Smoliński, and P. Sówka, IEEE Trans. Plasma Sci. **39**, 4 (2011).

[18]D. Braun, V. Gibalov, and G. Pietsch, Plasma Sources Sci. Technol. **1**, 166 (1992).

[19]S. Roy, Appl. Phys. Lett. **86**, 101502 (2005).

[20]Y. B. Suzen, P. G. Huang, J. D. Jacob, and D. E. Ashpis, "Numerical simulations of plasma based flow control applications," AIAA Paper 2005–4633, 2005.

[21]B. Jayaraman, S. Thakur, and W. Shyy, "Modeling of dielectric barrier discharge and resulting fluid dynamics," AIAA Paper 2006–686, 2006.

[22]B. Jayaraman, Y. C. Cho, and W. Shyy, "Modeling of dielectric barrier discharge plasma actuator," AIAA Paper 2007–4531, 2007.

[23]K. P. Singh and S. Roy, J. Appl. Phys. **103**, 013305 (2008).

[24]H. Kumar and S. Roy, Phys. Plasmas **12**, 093508 (2005).

[25]C. C. Wang and S. Roy, "Geometry effects of dielectric barrier discharge on a flat surface," AIAA Paper 2011–732, 2011.

[26]S. Pavón, Ph.D. thesis, École polytechnique fédérale de Lausanne, Lausanne, 2008.

[27]F. Roveda, Ph.D. thesis, Università degli Studi di Bologna, Bologna, 2012.

[28]M. Abdollahzadeh, J. C. Pascoa, and P. J. Oliveira, Comput. Fluids **128**, 77 (2016).

[29]G. Dufour and F. Rogier, Aerospace Lab J. **10**, 1 (2015).

[30]S. Pekárek, Eur. Phys. J. D **61**, 657 (2011).

[31]T. Makabe, H. Awai, and T. Mori, J. Phys. D: Appl. Phys. **17**, 2367 (1984).

[32]F. Massines, P. Ségur, N. Gherardi, C. Khamphan, and A. Ricard, Surf. Coat. Technol. **174–175**, 8 (2003).

[33]N. Naudé, J.-P. Cambronne, N. Gherardi, and F. Massines, J. Phys. D: Appl. Phys. **38**, 530 (2005).

[34]Y. P. Raizer, *Gas Discharge Physics* (Springer, Berlin, 2001).

A.6 A 3D Numerical Study of the Surface Dielectric Barrier Discharge Initial Phase

J. Mikeš, I. Soukup and S. Pekárek, 'A 3d numerical study of the surface dielectric barrier discharge initial phase,' *Mathematics*, vol. 11, no. 4, 2023, ISSN: 2227-7390. DOI: 10.3390/ math11041025.

Article

A 3D Numerical Study of the Surface Dielectric Barrier Discharge Initial Phase

Jan Mikeš * [ID]**, Ivan Soukup** [ID] **and Stanislav Pekárek** [ID]

Faculty of Electrical Engineering, Czech Technical University in Prague, Technická 2,
166 27 Prague, Czech Republic
* Correspondence: mikes.jan@fel.cvut.cz; Tel.: +420-224355148

Abstract: This study presents the results of the numerical modeling of surface dielectric barrier discharge in planar configuration with the strips active electrode. A positive half-period of the sinusoidal driving voltage and the two-species case is assumed in this study. Currently, many numerical models of surface dielectric barrier discharge deal with different electrode geometries, longer timescales, or discharge energizations. However, the main innovation presented in this study is developing a three-dimensional numerical model for the initial phase of the discharge phenomenon and a deeper focus on the numerical theory behind it. Based on the fluid model, this study presents a detailed mathematical and numerical formulation of the problem, stable numerical reconstruction of ion and electron velocity fields and an explanation of the need for linear approximation of ionization rate. Finally, it computes the potential and electric field distributions, electron and ion densities, and their velocities. The obtained results of a numerical simulation showing trajectories and velocities of electrons and ions reflect the active region of the discharge. A numerical simulation demonstrates the method in a three-dimensional domain inspired by a real-life experiment. The model can be used to optimize the electrode geometry of the discharge.

Keywords: plasma physics; numerical modeling; 3D fluid model; surface dielectric barrier discharge; sinusoidal driving voltage; discharge initial phase; voltage positive half-period; two-species model

MSC: 65Z05; 76X05

1. Introduction

The usage of surface dielectric barrier discharge (SDBD) [1] is on the rise in many applications, such as active particles, ozone, and ultraviolet generation [2], pollution control [3], surface treatment [4,5], plasma-chemical vapor deposition [6], in biological and chemical applications [7], and air-flow control [8,9]. Surface discharges are generated on the surface of a dielectric. Regarding the configuration of electrodes, two types of discharges are distinguished—surface barrier discharges and coplanar barrier discharges. Our attention was focused on surface dielectric barrier discharges. SDBD has been frequently studied within a planar experimental configuration [10], where an active electrode, cut out of a thin foil made of an electrically conductive material (copper, aluminum, stainless steel, special steel), connected to an alternating high voltage power supply system and serving as a high-voltage (active) electrode, is applied to one side of a planar dielectric plate (barrier) by means of screen printing, steaming, and dusting or, eventually, is glued by conductive glue. A grounded electrode, often made of the same material in an oblong or square shape and overlapping the active electrode surface by several mm, is located on the lower (opposite) side. The actual shape of the active electrode is usually selected in keeping with the purpose to be served by the designed generator of active particles and ozone (it can also be a source of ultraviolet irradiation). The configuration frequently features thin parallel strips, circles, and segments in the shape of a honeycomb, but it can

also take the form of a mesh [11–13]. The recent articles offer a predominance of studies describing the origin and behavior of dielectric barrier discharge from an experimental point of view [14–18], while phenomena characterized by physical-mathematical models are treated less frequently [19–24]. The past few decades have seen the development of mathematical models describing—with a certain, smaller, or greater precision and success rate—the specific configuration of the phenomenon being modeled [25–29]. The authors of Refs. [14,17,30,31] classify such models into simplified (phenomenological) ones and first-principles ones that employ mathematical approaches to solving the given task. The category of simplified models comprises, for instance, Electrostatic models, Linearized force models, or Potential flow models. For their part, first-principles-based models include Kinetics models and Fluid models [21,32,33]. The latter ones, in particular, are the subject of our studies.

Our main goal is to expose the numerical theory to the community focused on the SDBD studies in much more detail than usual. In alignment with this particular chief objective, we will focus heavily on the proper formulation of the problem, the description of the critical issues, and the complications.

The presented mathematical model deals with the surface dielectric barrier discharge. Therefore, it should reflect the physics of the discharge. As long as our research is oriented toward the discharge generation of various active species such as ozone [34], the critical quantity which determines the efficiency of this generation is the dimension of the active volume in which the processes of species generation occur. In the case of SDBD, the discharge develops along the dielectric surface. At critical field strength, a set of microdischarges appears on the dielectric surface, which is accompanied by the luminosity of the discharge near the strip electrodes. This luminosity area and, consequently, the active discharge volume, do not cover the whole area of the dielectric. The physics of the discharge, leading to the formation of the active volume, is rather complex; therefore, we had to make essential simplifications. Thus, we restricted ourselves to the positive half-period of the driving voltage only, used only one type of positive ions-electrons model, and restricted ourselves to a time interval of $T = 46$ ns. This assumption is associated with the processes of electron production from the electrodes. In the case of the strip electrode's positive polarity, the photoemission current plays a decisive role. The ion emission current plays a minor role [35]. According to this paper, the photoemission starts after more than $T = 15$ ns. In fact, for the negative polarity of the strip electrode, the photoemission current reaches a maximum at about $T = 6$ ns. Thus, the photoemission and the ion emission from electrodes in the chosen simulation time interval can be neglected. Besides, this time interval limitation allows us to neglect the heating of electrodes, gas heating, and heat-related effects on electrodes and gas properties.

For the assumptions mentioned above, we present a numerical method based on the Finite Elements Method (FEM) and our results from the respective numerical experiment [34]. The experiment is implemented in a FEniCS environment (see fenicsproject.org, accessed on 15 January 2023), its mesh consisting of approximately 600,000 tetrahedrons generated in tetgen (see tetgen.org, accessed on 15 January 2023), using a predefined set of vertices [34].

Presently, a variety of models of the SDBD deal with complex chemistry, electrode geometries, and longer timescales. However, the main innovation presented in our paper is developing a 3D numerical model for the initial phase of the SDBD.

2. Introducing the Models

Let us start with the definition of mathematical models describing the physical entities that appear in the SDBD phenomena.

Since we present numerical results of an experiment motivated by a real-life experiment [34], we will restrict ourselves to a small extent and formulate the problem on a specific domain. Otherwise, we will try to keep the problem on a general level.

Thus, let $\Omega \subset \mathbb{R}^3$ be a bounded domain and $T > 0$ a given time. We set $Q_T = \Omega \times [0, T]$ and by $\partial\Omega$, we denote the boundary of Ω. Further, let Ω be a composition of two disjoint domains, $\Omega = \Omega_{Die} \cup \Omega_{Gas}$, and $\partial\Omega$ consist of several disjoint parts, $\partial\Omega = \Gamma_{Grnd} \cup \Gamma_{Walls}$, where $\Gamma_{Walls} = \Gamma_{BottomWalls} \cup \Gamma_{TopWalls}$ (see Figures 1 and 2 in Section 2). Next, let the interface between Ω_{Die} and Ω_{Gas} consist of two disjoint parts, $\partial\Omega_{Die} \cap \partial\Omega_{Gas} = \Gamma_{GasToDie} \cup \Gamma_{Strip}$.
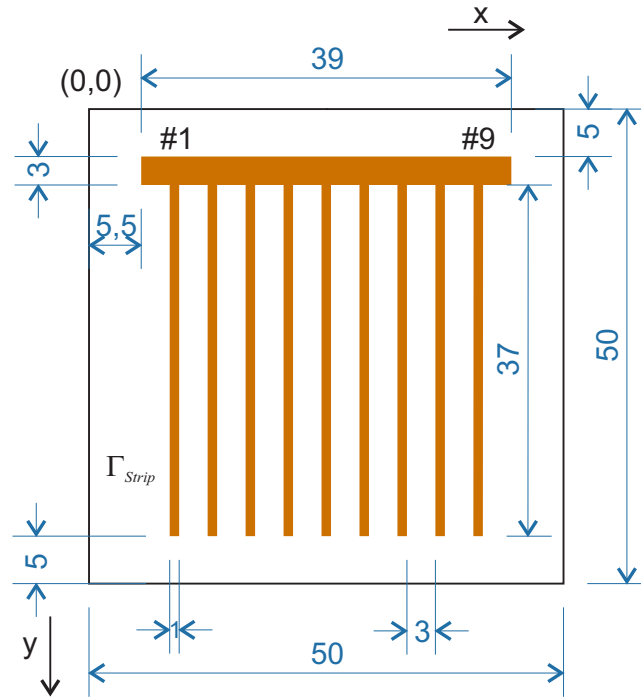

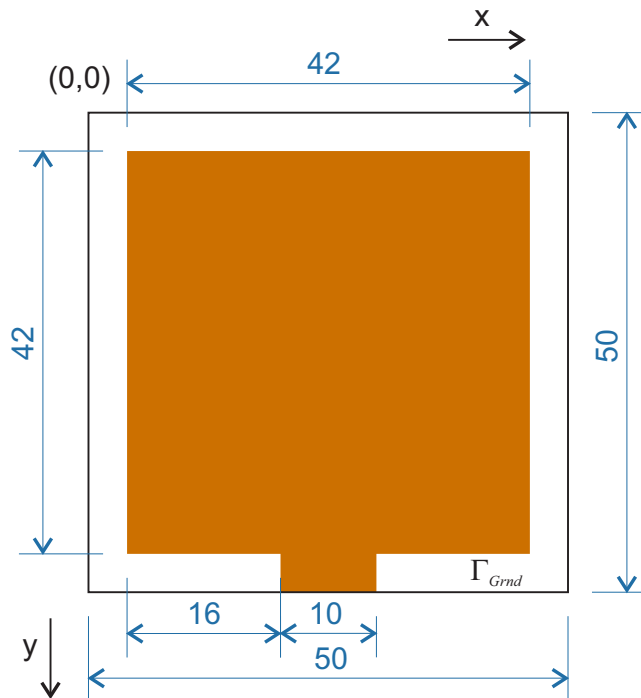**Figure 1.** 2D geometry of the active strip electrode.

Figure 2. 2D geometry of the grounded electrode.

The SDBD Phenomena

The presented article uses a two-species model with electrons and one type of ions, notably for positive ions. Moreover, we restrict ourselves to the initial phase of the positive half-period of the applied voltage and neglect different ionic reactions.

Therefore, the definition of the model follows from Refs. [24,29,34,36–38]. Hence, we first model the relation between the electric field $\mathbf{E} : Q_T \to \mathbb{R}^3$ and the electric potential $\Phi : Q_T \to \mathbb{R}$ by means of the Poisson equation as follows

$$\mathbf{E} = -\nabla\Phi \quad \text{in } Q_T, \tag{1}$$

where ∇ represents the gradient with respect to the space variable. Further, we assume the electric potential to be decomposed into two parts: $\phi : Q_T \to \mathbb{R}$ being induced by the external electric field and $\varphi : \Omega_{Air} \times (0, T) \to \mathbb{R}$ being induced by the net charge density in the plasma, i.e., $\Phi = \phi + \varphi$ and

$$\nabla \cdot (\varepsilon_{Air}\varepsilon_0 \nabla\varphi) = -e_c(n_e - n_i) \quad \text{in } \Omega_{Air} \times (0, T), \tag{2}$$

$$\nabla \cdot (\varepsilon_r \varepsilon_0 \nabla\phi) = 0 \quad \text{in } Q_T, \tag{3}$$

where ∇ represents the divergence operator, $n_e : \Omega_{Air} \times (0, T) \to \mathbb{R}$ denotes the electron density, $n_i : \Omega_{Air} \times (0, T) \to \mathbb{R}$ denotes the ion density, ε_0 is the vacuum permittivity, ε_r is a piecewise constant function denoting the relative permittivity of air ($\varepsilon_r = \varepsilon_{Air}$ on Ω_{Air}) and dielectric material ($\varepsilon_r = \varepsilon_{Die}$ on Ω_{Die}) and e_c is the elementary charge.

Further, the time evolution of electrons and ions concentrations are determined by the continuity equations where the ionic reactions are defined using the Townsend coefficients [39], i.e., the time evolution equations are described as follows

$$\frac{\partial n_i}{\partial t} + \nabla \cdot (n_i \mathbf{V}_i) = A p_c \exp\left\{-\frac{B p_c}{\|\mathbf{E}\|}\right\} \|n_e \mathbf{V}_e\| - r_{i\leftrightarrow e} n_i n_e \tag{4}$$

in $\Omega_{Air} \times (0, T)$.

Summing up, the used assumptions, including chosen simulation time interval, allowed us to write a continuity equation for electrons in the form of (5),

$$\frac{\partial n_e}{\partial t} + \nabla \cdot (n_e \mathbf{V}_e) = A p_c \exp\left\{-\frac{B p_c}{\|\mathbf{E}\|}\right\} \|n_e \mathbf{V}_e\| - r_{i\leftrightarrow e} n_i n_e, \tag{5}$$

in $\Omega_{Air} \times (0, T)$, where $\mathbf{V}_i : \Omega_{Air} \times (0, T) \to \mathbb{R}^3$ is the ion velocity field, $\mathbf{V}_e : \Omega_{Air} \times (0, T) \to \mathbb{R}^3$ is the electron velocity field, p_c is the constant air pressure, $r_{i\leftrightarrow e}$ denotes the electron-ion recombination rate, A and B are pre-exponential and exponential constants, respectively. For the sake of completeness, let us note that $\|\cdot\|$ represents the usual Euclidean norm.

Remark: Let us comment on the assumption of constant air pressure. Since we will work within a very small time range ($\approx$ns), it seems reasonable to assume the air pressure to be constant. Although it is still by no means obvious that this simplification is insignificant, we are also not able to compute the approximate solution without this assumption as of yet.

Further, using the so-called Drift-Diffusive model (see Refs. [39,40]), we can rewrite the electronic and ionic fluxes as

$$n_i \mathbf{V}_i = n_i \mu_i \mathbf{E} - D_i \nabla n_i \quad \text{in } \Omega_{Air} \times (0, T), \tag{6}$$

$$n_e \mathbf{V}_e = -n_e \mu_e \mathbf{E} - D_e \nabla n_e \quad \text{in } \Omega_{Air} \times (0, T), \tag{7}$$

where μ_e and μ_i are the electron and ion mobility coefficients, respectively, and D_e and D_i are the electron and ion diffusion coefficients, respectively.

Now we observe that the numerical solution of Equation (3) can be computed independently of the remaining equations. Therefore, by substituting (1), (6), and (7) into (4) and (5) and using the results of (3), we can reduce the remaining equations to three scalar equations

for three scalar unknowns (φ, n_i, n_e) and compute the remaining entities afterward. In total, we therefore, focus on finding a solution (ϕ) of Equation (3) in Q_T and solution (φ, n_i, n_e) for Equation (2) coupled with the following equations

$$
\begin{aligned}
\frac{\partial n_i}{\partial t} &+ \nabla \cdot (-n_i \mu_i \nabla(\phi + \varphi) - D_i \nabla n_i) \\
&= A p_c \exp\{-\frac{B p_c}{\|\nabla(\phi + \varphi)\|}\} \|n_e \mu_e \nabla(\phi + \varphi) - D_e \nabla n_e\| \\
&\quad - r_{i \leftrightarrow e} n_i n_e
\end{aligned}
\tag{8}
$$

$$
\begin{aligned}
\frac{\partial n_e}{\partial t} &+ \nabla \cdot (n_e \mu_e \nabla(\phi + \varphi) - D_e \nabla n_e) \\
&= A p_c \exp\{-\frac{B p_c}{\|\nabla(\phi + \varphi)\|}\} \|n_e \mu_e \nabla(\phi + \varphi) - D_e \nabla n_e\| \\
&\quad - r_{i \leftrightarrow e} n_i n_e,
\end{aligned}
\tag{9}
$$

in $\Omega_{Air} \times (0, T)$.

Thus, formulating the initial and boundary conditions for (ϕ) and (φ, n_i, n_e) remains. We assume the following setting [34]

$$\phi(x, 0) = 0 \quad \text{in } \Omega, \tag{10}$$

$$\phi(x, t) = 0 \quad \text{on } \Gamma_{Grnd} \times (0, T), \tag{11}$$

$$\phi(x, t) = U_{amp} \sin(\omega t) =: \phi_{Strip}(x, t) \quad \text{on } \Gamma_{Strip} \times (0, T) \tag{12}$$

$$\frac{\partial \phi}{\partial \boldsymbol{n}}(x, t) = 0 \quad \text{on } \Gamma_{Walls} \times (0, T) \tag{13}$$

$$\varphi(x, 0) = 0, \quad \text{in } \Omega_{Air}, \tag{14}$$

$$\varphi(x, t) = 0 \quad \text{on } \Gamma_{Strip} \times (0, T), \tag{15}$$

$$\frac{\partial \varphi}{\partial \boldsymbol{n}}(x, t) = 0 \quad \text{on } \Gamma_{TopWalls} \cup \Gamma_{AirToDie} \times (0, T), \tag{16}$$

$$n_i(x, 0) = n_i^0(x) \quad \text{in } \Omega_{Air}, \tag{17}$$

$$n_i(x, t) = 0, \quad \text{on } \Gamma_{Strip} \times (0, T), \tag{18}$$

$$\frac{\partial n_i}{\partial \boldsymbol{n}}(x, t) = 0 \quad \text{on } \Gamma_{TopWalls} \cup \Gamma_{AirToDie} \times (0, T), \tag{19}$$

$$n_e(x, 0) = n_e^0(x) \quad \text{in } \Omega_{Air}, \tag{20}$$

$$\frac{\partial n_e}{\partial \boldsymbol{n}}(x, t) = 0 \quad \text{on } \partial \Omega_{Air} \times (0, T), \tag{21}$$

where $\phi_{Strip} : \Gamma_{Strip} \times (0, T) \to \mathbb{R}$ is an electric potential boundary function, $\boldsymbol{n}$ denotes the outer unit normal vector to $\partial \Omega$, $n_i^0 : \Omega_{Air} \to \mathbb{R}$ and $n_e^0 : \Omega_{Air} \to \mathbb{R}$ is the initial ion density and electron density, respectively, U_{Amp} is the discharge voltage, $\omega = 2\pi f$ is the angular velocity, and f is the frequency.

Remark 1. *Let us comment on the boundary conditions for ions and electrons. Although there are several theories regarding a proper setting of boundary conditions for them [21,41], we prefer to assume the homogeneous Neumann condition on the whole boundary. An exception will be for the Γ_{Strip} for ions, where it is clear and physically reasonable to assume a homogeneous Dirichlet condition for the positive half-period of the discharge. Since there is uncertainty in the proper setting of those boundary conditions, we instead implement the general condition even though, numerically, it brings worse stability to the computations.*

3. Problem Formulation

In this section, we start with the process of partial non-dimensionalization and then introduce the weak formulations of the studied problems. The partial non-dimensionalization

is motivated by better numerical stability due to the appropriate rescaling of the quantities we are simulating.

Non-Dimensionalization and Weak Formulations

Inspired by the non-dimensionalization scheme presented in Ref. [26], we introduce new variables and new dimensionless quantities as follows

$$\tau = \frac{t}{t_0}, \quad z_i = \frac{x_i}{L}, \, i = 1, 2, 3,$$

$$N_e = \frac{n_e}{n_0}, \quad N_i = \frac{n_i}{n_0}, \quad \Phi_{nd} = \frac{e_c}{k_B T_e} \Phi, \tag{22}$$

where t_0 is the reference time, L is the characteristic length, n_0 is the reference particle density, k_B is the Boltzmann's constant, and T_e is the electron temperature.

Let us now define

$$\mathcal{D}^G = \{ \tilde{\phi} \in H^1(\Omega) : \tilde{\phi} = 0 \text{ on } \Gamma_{Grnd} \}$$

$$\mathcal{D}^{SG} = \{ \tilde{\phi} \in H^1(\Omega) : \tilde{\phi} = 0 \text{ on } \Gamma_{Strip} \cup \Gamma_{Grnd} \}$$

$$\mathcal{D}^S_{Air} = \{ \tilde{\varphi} \in H^1(\Omega_{Air}) : \tilde{\phi} = 0 \text{ on } \Gamma_{Strip} \}$$

and assume there exists $\phi^*_{Strip} \in \mathcal{C}(0, T; \mathcal{D}^G)$ such that ϕ_{Strip} is its trace on $\Gamma_{Strip} \times (0, T)$. Now we are ready to introduce the weak formulation of the problem governed by Equation (3) and boundary conditions (10)–(13). Let us denote this weak formulation as (*SDBD-0*): Find $\phi \in L^2(0, T; \mathcal{D}^G)$ so that it holds:

$$\phi - \frac{e_c}{k_B T_e} \phi^*_{Strip} \in L^2(0, T; \mathcal{D}^{SG}),$$

$$a(\phi, \tilde{\phi}) = 0 \text{ for a.e. } t \in (0, T), \forall \tilde{\phi} \in \mathcal{D}^{SG},$$

$$\lim_{t \to 0} \| \phi(\cdot, t) \|_{L^2(\Omega)} = 0, \tag{23}$$

where

$$a(\phi, \tilde{\phi}) = \varepsilon_{Air} \int_{\Omega_{Air}} \nabla \phi \nabla \tilde{\phi} dx + \varepsilon_{Die} \int_{\Omega_{Die}} \nabla \phi \nabla \tilde{\phi} dx. \tag{24}$$

Further, let us also introduce the weak formulation to a problem governed by Equations (2), (8) and (9) and conditions (14)–(21). Let $\phi \in L^2(0, T; \mathcal{D}^G)$ be a weak solution of problem (*SDBD-0*). We denote the weak formulation as (*SDBD-1*): Find $\varphi \in L^2(0, T; \mathcal{D}^S_{Air})$, $N_i \in L^2(0, T; \mathcal{D}^S_{Air})$ and $N_e \in L^2(0, T; H^1(\Omega_{Air}))$ such that for a.e. $t \in (0, T)$, $\forall \tilde{\varphi} \in \mathcal{D}^S_{Air}$, $\forall \tilde{N}_i \in \mathcal{D}^S_{Air}$ and $\forall \tilde{N}_e \in \mathcal{H}^1(\Omega_{Air})$

$$a_{Air}(\varphi, \tilde{\varphi}) = L(N_i, N_e, \tilde{\varphi}),$$

$$\int_{\Omega_{Air}} \frac{\partial N_i}{\partial \tau} \tilde{N}_i dx + \mu_i c(N_i, \varphi, \phi, \tilde{N}_i) + D_i d(N_i, \tilde{N}_i)$$

$$- f_e(N_e, \varphi, \phi, \tilde{N}_i) = R(N_i, N_e, \tilde{N}_i),$$

$$\int_{\Omega_{Air}} \frac{\partial N_e}{\partial \tau} \tilde{N}_e dx - \mu_e c(N_e, \varphi, \phi, \tilde{N}_e) + D_e d(N_e, \tilde{N}_e)$$

$$- f_e(N_e, \varphi, \phi, \tilde{N}_e) = R(N_i, N_e, \tilde{N}_e), \tag{25}$$

and

$$\lim_{t \to 0} \|\varphi(\cdot, t)\|_{L^2(\Omega_{Air})} = 0,$$

$$\lim_{t \to 0} \|N_i(\cdot, t) - \frac{1}{n_0} n_i^0(\cdot)\|_{L^2(\Omega_{Air})} = 0,$$

$$\lim_{t \to 0} \|N_e(\cdot, t) - \frac{1}{n_0} n_e^0(\cdot)\|_{L^2(\Omega_{Air})} = 0,$$

where (for $N, \tilde{N} \in \mathcal{H}^1(\Omega_{Air})$)

$$a_{Air}(\varphi, \tilde{\varphi}) = \int_{\Omega_{Air}} \nabla \varphi \nabla \tilde{\varphi} dx,$$

$$c(N, \varphi, \phi, \tilde{N}) = \frac{k_B T_e t_0}{e_c L} \int_{\Omega_{Air}} N(\nabla \varphi + \nabla \phi) \nabla \tilde{N} dx,$$

$$d(N, \tilde{N}) = \frac{t_0}{L} \int_{\Omega_{Air}} \nabla N \nabla \tilde{N} dx,$$

$$\cdot \|\frac{\mu_i k_B T_e t_0}{e_c L} N(\nabla \varphi + \nabla \phi) + \frac{D_i t_0}{L} \nabla N\| \cdot \tilde{N} dx,$$

$$f_e(N, \varphi, \phi, q) = A p_c \int_{\Omega_{Air}} \exp\{-\frac{B p_c e_c L}{k_B T_e \|\nabla \varphi + \nabla \phi\|}\}$$

$$\cdot \|\frac{\mu_e k_B T_e t_0}{e_c L} N(\nabla \varphi + \nabla \phi) - \frac{D_e t_0}{L} \nabla N\| \cdot \tilde{N} dx,$$

$$L(N_i, N_e, \tilde{\varphi}) = \frac{e_c^2 L^2 n_0}{\varepsilon_{Die} k_B T_e} \int_{\Omega_{Air}} \tilde{\varphi}(N_i - N_e) dx,$$

$$R(N_i, N_e, \tilde{N}) = -r_{i \leftrightarrow e} n_0 t_0 \int_{\Omega_{Air}} \tilde{N} N_i N_e dx.$$

4. Discretization

We suppose that the domain Ω is polyhedral with the Lipschitz boundary. By $\mathcal{T}_h$, we denote a regular partition of the domain Ω, and by $\mathcal{T}_h^{Air} \subset \mathcal{T}_h$, we denote a regular partition of the domain Ω_{Air}. Let us define

$$\mathcal{D}_h^G = \{\tilde{\phi}_h \in \mathcal{D}^G : \tilde{\phi}_h|_K \in P_r(K), K \in \mathcal{T}_h\},$$

$$\mathcal{D}_h^{SG} = \{\tilde{\phi}_h \in \mathcal{D}^{SG} : \tilde{\phi}_h|_K \in P_r(K), K \in \mathcal{T}_h\},$$

$$\mathcal{D}_{Air,h}^S = \{\tilde{N}_h \in \mathcal{D}_{Air}^S : \tilde{N}_h|_K \in P_r(K), K \in \mathcal{T}_h^{Air}\},$$

$$\mathcal{D}_{Air,h} = \{\tilde{N}_h \in H^1(\Omega_{Air}) : \tilde{N}_h|_K \in P_r(K), K \in \mathcal{T}_h^{Air}\},$$

$$\boldsymbol{L}_h = \{\mathbf{E}_h \in L^2(\Omega)^3 : \mathbf{E}_h|_K \in P_{r-1}(K)^3, K \in \mathcal{T}_h\},$$

$$\boldsymbol{L}_h^{Air} = \{\mathbf{V}_h \in L^2(\Omega_{Air})^3 : \mathbf{V}_h|_K \in P_{r-1}(K)^3, K \in \mathcal{T}_h^{Air}\},$$

where $P_r(K)$, $P_s(K)$ and $P_q(K)$ denote the space of all polynomials on K of a degree less or equal to r, s and q, respectively. Moreover, we assume $r \geq 2$, $s \geq 1$ and $q \geq 1$.

For the time discretization of (*SDBD-0*) and (*SDBD-1*) we consider a uniform partition of the time interval $[0, T]$ formed by the time instants $t_j = j\Delta t$, $j = 0, 1, \dots, j_{max}$, with a time step $\Delta t = T/j_{max}$.

4.1. Approximate Solution for (SDBD-0)

Let $g_h^j \in \mathcal{D}_h^G \approx U_{amp} \sin(\omega t_j)$ on Γ_{Strip}, $j = 0, \dots, j_{max}$. We define the approximate solution of (SDBD-0) problem obtained by the Finite Elements Method as a set of functions $\phi_h^j \in \mathcal{D}_h^G$, $j = 0, \dots, j_{max}$, satisfying

$$
\begin{aligned}
&\phi_h^j - g_h^j \in \mathcal{D}_h^{SG} \quad \forall j = 0, \dots, j_{max}, \\
&a(\phi_h^j, \tilde{\phi}_h) = 0 \quad \forall j = 0, \dots, j_{max}, \forall \tilde{\phi}_h \in \mathcal{D}_h^{SG} \\
&\|\phi_h^0\|_{L^2(\Omega)} = 0.
\end{aligned}
\tag{26}
$$

4.2. Approximate Solution for (SDBD-1)

Let $\{\phi_h^j\}_{j=0}^{j_{max}}$ be an approximate solution of (SDBD-0). We define the approximate solution of the (SDBD-1) problem obtained by the BDF-2 method (BDF stands for Backward differentiation formula) and the Finite Elements Method as functions $(\varphi_h^j, N_{i_h}^j, N_{e_h}^j) \in \mathcal{D}_{Air,h}^S \times \mathcal{D}_{Air,h}^S \times \mathcal{D}_{Air,h}$, $j = 0, \dots, j_{max}$, satisfying for all $j = 1, \dots, j_{max}$

$$
\begin{aligned}
&a_{Air}(\varphi_h^j, \tilde{\varphi}_h) = L(N_{e_h}^j, N_{i_h}^j, \tilde{\varphi}_h) \quad \forall \tilde{\varphi}_h \in \mathcal{D}_{Air,h}^S \\
&\frac{1}{\Delta \tau} \int_{\Omega_{Air}} (N_{i_h}^j - \frac{4}{3} N_{i_h}^{j-1} + \frac{1}{3} N_{i_h}^{j-2}) \tilde{N}_{i,h} dx \\
&\qquad = \frac{2}{3} \mathbf{F}_i(N_{i_h}^j, N_{e_h}^j, \varphi_h^j, \phi_h^j, N_{i_h}^{j-1}, \varphi_h^{j-1}, \phi_h^{j-1}, \tilde{N}_{i,h}) \\
&\qquad\quad \forall \tilde{N}_{i,h} \in \mathcal{D}_{Air,h}^S, \\
&\frac{1}{\Delta \tau} \int_{\Omega_{Air}} (N_{e_h}^j - \frac{4}{3} N_{e_h}^{j-1} + \frac{1}{3} N_{e_h}^{j-2}) \tilde{N}_{e,h} dx \\
&\qquad = \frac{2}{3} \mathbf{F}_e(N_{i_h}^j, N_{e_h}^j, \varphi_h^j, \phi_h^j, N_{e_h}^{j-1}, \varphi_h^{j-1}, \phi_h^{j-1}, \tilde{N}_{e,h}) \\
&\qquad\quad \forall \tilde{N}_{e,h} \in \mathcal{D}_{Air,h},
\end{aligned}
\tag{27}
$$

where $\Delta \tau = \frac{\Delta t}{t_0}$, $(\varphi_h^0, N_{i_h}^0, N_{e_h}^0)$ and $(\varphi_h^{-1}, N_{i_h}^{-1}, N_{e_h}^{-1})$ are defined as the $L^2(\Omega)$ projections of the initial data $(0, \frac{n_i^0}{n_0}, \frac{n_e^0}{n_0})$ and $(0, 0, 0)$, respectively, on $\mathcal{D}_{Air,h}^S \times \mathcal{D}_{Air,h}^S \times \mathcal{D}_{Air,h}$ and

$$
\begin{aligned}
&\mathbf{F}_i(N_{i_h}^j, N_{e_h}^j, \varphi_h^j, \phi_h^j, N_{i_h}^{j-1}, \varphi_h^{j-1}, \phi_h^{j-1}, \tilde{N}_{i,h}) \\
&\quad = \mu_i c(N_{i_h}^j, \varphi_h^j, \phi_h^j, \tilde{N}_{i,h}) - D_i d(N_{i_h}^j, \tilde{N}_{i,h}) \\
&\qquad + \tilde{f}_e(N_{e_h}^j, \varphi_h^j, \phi_h^j, N_{e_h}^{j-1}, \varphi_h^{j-1}, \phi_h^{j-1}, \tilde{N}_{i,h}) \\
&\qquad + R(N_{i_h}^j, N_{e_h}^j, \tilde{N}_{i,h}) \\
&\mathbf{F}_e(N_{i_h}^j, N_{e_h}^j, \varphi_h^j, \phi_h^j, N_{e_h}^{j-1}, \varphi_h^{j-1}, \phi_h^{j-1}, \tilde{N}_{e,h}) \\
&\quad = -\mu_e c(N_{e_h}^j, \varphi_h^j, \phi_h^j, \tilde{N}_{e,h}) - D_e d(N_{e_h}^j, \tilde{N}_{e,h}) \\
&\qquad + \tilde{f}_e(N_{e_h}^j, \varphi_h^j, \phi_h^j, N_{e_h}^{j-1}, \varphi_h^{j-1}, \phi_h^{j-1}, \tilde{N}_{e,h}) \\
&\qquad + R(N_{i_h}^j, N_{e_h}^j, \tilde{N}_{e,h})
\end{aligned}
$$

where $\tilde{f}_e$ is the linear approximation of f_e, defined in the following Section 4.2.

Linear Approximation of Ionization Rate

Even though it might seem that we should directly use the Newton method to solve the presented non-linear problem, we would rather introduce a linear approximation of ionization rate separately and with extra care. As we will show below, it is necessary to carefully treat the possibility of division by zero and problems with finite machine precision. Most importantly, identical problems have to be overcome even if we skip the linearization

process and directly use the Newton method since the derivatives performed in the Newton method will introduce similar "controversial" terms.

Let us define the following operator f acting on $\mathcal{D}_{Air,h} \times \mathcal{D}_{Air,h}$

$$f(\varphi_h, N_h) = \alpha \exp\{-\frac{\beta}{\|\nabla\varphi_h\|}\}\|\gamma N_h \nabla\varphi_h - \delta\nabla N_h\| : \Omega \to \mathbb{R}, \tag{28}$$

where $\alpha, \beta, \gamma, \delta$ are generic constants. It is obvious that $f(\varphi_h, N_h)$ is not defined on set $\Theta = \{x \in \Omega_{Air} : \|\nabla\varphi_h(x)\| = 0\}$ for given $\varphi_h \in \mathcal{D}_{Air,h}$. Nevertheless, we can set $f(\varphi_h, N_h) \equiv 0$ on Θ and then for such $f(\varphi_h, N_h)$ holds that $f(\varphi_h, N_h) \in \mathcal{C}(\Omega_{Air})$.

Now, we present the linearization of the operator (28) for any $(\varphi_h, N_h) \in \mathcal{D}_{Air,h} \times \mathcal{D}_{Air,h}$ from which one can easily deduce the linear approximation of ionization rate.

Let $\vec{\psi}_h = \{\psi_h^i\}_{i=1}^{m_d}$ be the basis of space $\mathcal{D}_{Air,h}$, $m_d = dim(\mathcal{D}_{Air,h})$. Now, any $\varphi_h \in \mathcal{D}_{Air,h}$ can be uniquely represented as $\varphi_h = \vec{\Psi} \cdot \vec{\psi}_h = \sum_{i=1}^{m_d} \Psi_i \psi_h^i$, where $\vec{\Psi} \in \mathbb{R}^{m_d}$.

Consequently, operator f can be understood as an operator acting on $\mathbb{R}^{m_d} \times \mathbb{R}^{m_d}$, i.e.,

$$\begin{aligned}
f(\varphi_h, N_h) &= f(\vec{\Psi}_\varphi, \vec{\Psi}_N) \\
&= \alpha \exp\{-\frac{\beta}{\|\vec{\Psi}_\varphi \cdot \nabla\vec{\psi}_h\|}\}\|\gamma\vec{\Psi}_N \cdot \vec{\psi}_h \vec{\Psi}_\varphi \cdot \nabla\vec{\psi}_h - \delta\vec{\Psi}_N \cdot \nabla\vec{\psi}_h\|
\end{aligned}$$

Using the Taylor series, we introduce a linear approximation of $f(\vec{\Psi}_\varphi, \vec{\Psi}_N)$ near point $(\vec{\Psi}_\varphi^0, \vec{\Psi}_N^0) \in (\mathbb{R}^{m_d} \times \mathbb{R}^{m_d})$ as follows

$$\begin{aligned}
f(\vec{\Psi}_\varphi, \vec{\Psi}_N) &\approx f(\vec{\Psi}_\varphi^0, \vec{\Psi}_N^0) + \frac{\partial f}{\partial\vec{\Psi}_\varphi}(\vec{\Psi}_\varphi^0, \vec{\Psi}_N^0) \cdot (\vec{\Psi}_\varphi - \vec{\Psi}_\varphi^0) \\
&\quad + \frac{\partial f}{\partial\vec{\Psi}_N}(\vec{\Psi}_\varphi^0, \vec{\Psi}_N^0) \cdot (\vec{\Psi}_N - \vec{\Psi}_N^0),
\end{aligned}$$

where using marking $\mathbb{J} = \gamma\vec{\Psi}_N^0\vec{\psi}_h\vec{\Psi}_\varphi^0\nabla\vec{\psi}_h - \delta\vec{\Psi}_N^0\nabla\vec{\psi}_h$

$$\begin{aligned}
\frac{\partial f}{\partial\vec{\Psi}_\varphi}(\vec{\Psi}_\varphi^0, \vec{\Psi}_N^0) &= \nabla\vec{\psi}_h\Big[\alpha\exp\{-\frac{\beta}{\|\vec{\Psi}_\varphi^0\nabla\vec{\psi}_h\|}\}\gamma\vec{\Psi}_N^0\vec{\psi}_h\frac{\mathbb{J}}{2\|\mathbb{J}\|} \\
&\quad + \|\mathbb{J}\|\beta\exp\{-\frac{\beta}{\|\vec{\Psi}_\varphi^0\nabla\vec{\psi}_h\|}\}\frac{\vec{\Psi}_\varphi^0\nabla\vec{\psi}_h}{2\|\vec{\Psi}_\varphi^0\nabla\vec{\psi}_h\|^3}\Big] \\
\frac{\partial f}{\partial\vec{\Psi}_N}(\vec{\Psi}_\varphi^0, \vec{\Psi}_N^0) &= \Big[\alpha\exp\{-\frac{\beta}{\|\vec{\Psi}_\varphi^0\nabla\vec{\psi}_h\|}\}\frac{\mathbb{J}}{2\|\mathbb{J}\|}\Big] \\
&\quad \cdot \Big(\gamma\vec{\Psi}_\varphi^0\nabla\vec{\psi}_h \cdot \vec{\psi}_h - \delta\nabla\vec{\psi}_h\Big),
\end{aligned}$$

under the assumption that every term on the right-hand side makes sense.

Here, we can observe that we should take care of possible divisions by zero and potential problems introduced by the machine precision limitations, as mentioned earlier.

Let us now switch back to the equivalent representation of operator f by (28). We finally present the approximation of f at the point $(\varphi_h, N_h) \in \mathcal{D}_{Air,h} \times \mathcal{D}_{Air,h}$ near point $(\varphi_h^0, N_h^0) \in \mathcal{D}_{Air,h} \times \mathcal{D}_{Air,h}$

$$f(\varphi_h, N_h) \approx \tilde{f}(\varphi_h, N_h, \varphi_h^0, N_h^0) \tag{29}$$

$$= \tilde{f}_{00}(\varphi_h^0, N_h^0) + \tilde{f}_{10}(\varphi_h^0, N_h^0) \cdot \nabla(\varphi_h - \varphi_h^0) \tag{30}$$

$$+ \tilde{f}_{01}(\varphi_h^0, N_h^0) \cdot \Big[\gamma\nabla\varphi_h^0(N_h - N_h^0) - \delta\nabla(N_h - N_h^0)\Big],$$

where using marking $\mathbb{K} = \gamma N_h^0 \nabla \varphi_h^0 - \delta \nabla N_h^0$

$$\tilde{f}_{00}(\varphi_h^0, N_h^0) = 0, \qquad\qquad \text{if } \|\nabla \varphi_h^0\| < \frac{10^{-2}}{\beta},$$

$$= \alpha \exp\{-\frac{\beta}{\|\nabla \varphi_h^0\|}\}\|\mathbb{K}\|, \quad \text{else}$$

$$\tilde{f}_{10}(\varphi_h^0, N_h^0) = 0, \qquad\qquad \text{if } \|\nabla \varphi_h^0\| < \frac{10^{-2}}{\beta},$$

$$= \|\mathbb{K}\|\beta \exp\{-\frac{\beta}{\|\nabla \varphi_h^0\|}\}\frac{\nabla \varphi_h^0}{2\|\nabla \varphi_h^0\|^3},$$

$$\text{if } \|\nabla \varphi_h^0\| \geq \frac{10^{-2}}{\beta}, \|\mathbb{K}\| < \frac{1}{2}\alpha\gamma \exp\{-\frac{\beta}{\|\nabla \varphi_h^0\|}\}$$

$$= \alpha \exp\{-\frac{\beta}{\|\nabla \varphi_h^0\|}\}\gamma N_h^0 \frac{\mathbb{K}}{2\|\mathbb{K}\|}$$

$$+ \|\mathbb{K}\|\beta \exp\{-\frac{\beta}{\|\nabla \varphi_h^0\|}\}\frac{\nabla \varphi_h^0}{2\|\nabla \varphi_h^0\|^3}, \quad \text{else}$$

$$\tilde{f}_{01}(\varphi_h^0, N_h^0) = 0,$$

$$\text{if } \|\nabla \varphi_h^0\| < \frac{10^{-2}}{\beta} \text{ or } \|\mathbb{K}\| < \frac{1}{2}\alpha \exp\{-\frac{\beta}{\|\nabla \varphi_h^0\|}\}$$

$$= \alpha \exp\{-\frac{\beta}{\|\nabla \varphi_h^0\|}\}\frac{\gamma N_h^0 \nabla \varphi_h^0 - \delta \nabla N_h^0}{2\|\gamma N_h^0 \nabla \varphi_h^0 - \delta \nabla N_h^0\|}, \text{ else.}$$

It is clear that $\tilde{f}$ is linear. Taking here $\varphi_h^j + \phi_h^j$ instead of φ_h, $N_{e_h}^j$ instead of N_h, $\varphi_h^{j-1} + \phi_h^{j-1}$ instead of φ_h^0, $N_{e_h}^{j-1}$ instead of N_h^0 and by proper choice of α, β, γ and δ, one easily gets the linear approximation of the ionization rate.

4.3. The Reconstruction of **E**, **V**$_i$ *and* **V**$_e$

In order to reconstruct the entities **E**, **V**$_i$ and **V**$_e$, we use Equations (1), (6) and (7), respectively. First, we define the approximate solution to (1) as a projection of $(\nabla(\phi_h^j + \varphi_h^j))$ on L_h, i.e., as a function $\mathbf{E}_h^j \in L_h$, $j = 0, \ldots, j_{max}$, satisfying for all $\tilde{\mathbf{E}}_h \in L_h$

$$\int_\Omega \mathbf{E}_h^j \tilde{\mathbf{E}}_h dx = -\frac{k_B T_e}{e_c L}(\int_\Omega \nabla \phi_h^j \tilde{\mathbf{E}}_h dx + \int_{\Omega_{Air}} \nabla \varphi_h^j \tilde{\mathbf{E}}_h dx),$$

where ϕ_h^j is the approximate solution of (*SDBD-0*) and φ_h^j is the first component of the approximate solution of (*SDBD-1*).

Now, the reconstruction of **V**$_i$ and **V**$_e$ has to be more cautious. Since the precomputed particle densities $N_{i_h}^j$ and $N_{e_h}^j$ may be of zero value, Equations (6) and (7) become meaningless at some parts of the domain (there might be no particles to track). To make the method worse, since we work within computer arithmetic, the values might not be equal to zero but just close to the machine epsilon. This may lead to absurd values of particle velocities.

Therefore, we employ a simple heuristic: "where there are a few particles, there is no movement". We define a minimal amount of particle coefficient N_{min}. Further, we define the approximate solution to (6) as a function $\mathbf{V}_i^{hj} \in L_h^{Air}$, $j = 0, \ldots, j_{max}$, satisfying for all $\tilde{\mathbf{E}}_h \in L_h^{Air}$ and for all $K \in \mathcal{T}_h^{Air}$

$$\int_K \mathbf{V}_i^{hj} \tilde{\mathbf{E}}_h dx = \int_K \left(\mu_i \mathbf{E}_h^j - \frac{D_i}{L} (\nabla N_{i_h}^j / N_{i_h}^j) \right) \tilde{\mathbf{E}}_h dx,$$

$$\text{if } \int_K N_{i_h}^j dx > N_{min}$$

$$= 0,$$

$$\text{if } \int_K N_{i_h}^j dx <= N_{min}.$$

Analogously, we define the approximate solution to (7) as the function $\mathbf{V}_e^{hj} \in L_h^{Air}$, $j = 0, \ldots, j_{max}$.

5. Numerical Scheme

As stated in the introduction, we carried out the implementation in FEniCS environment, and we will describe the numerical scheme using pseudocode based on FEniCS libraries.

We start by describing the numerical solution (*SDBD-0*) and (*SDBD-1*). First, let us note that all the presented discrete problems are equivalent to a system of linear algebraic equations.

SDBD-0

We use the FEniCS in-built GMRES (Generalized Minimal RESidual) iteration method with ILU preconditioner to solve the system of linear algebraic equations. The absolute convergence criterion (based on the norm of residuum) for GMRES is set to 10^{-9} with a maximum of 200 iterations [34].

SDBD-1

We use a similar setting as for (*SDBD-0*), i.e., we use the FEniCS in-built GMRES iteration method with ILU preconditioner with the same criterion settings.

Reconstructions

Using the FEniCS method *project* (from *dolfin.fem.projection*), we implement the reconstruction algorithms and obtain approximative solutions.

Pseudocode of the Main Scheme

Now the main algorithm scheme is as follows:

timestamp$_{\text{SDBD}}$ = $\Delta\tau$
while timestamp$_{\text{SDBD}}$ $\leq$ T:
    Solve (*SDBD-0*) at timestamp$_{\text{SDBD}}$
    Compute coefficients for $\tilde{f}_e$
    Solve (*SDBD-1*) at timestamp$_{\text{SDBD}}$
    Compute reconstructions at timestamp$_{\text{SDBD}}$
    timestamp$_{\text{SDBD}}$ += $\Delta\tau$

6. Numerical Experiment Simulation

Let us start with the definition of the domain Ω and its mesh. Note that we use the meter as a unit for distance in the following definitions.

The domain Ω is defined as a cuboid. In particular, $\Omega = \{ \mathbf{x} \in \mathbb{R}^3 : x_1 \in (0, 0.05), x_2 \in (0, 0.05), x_3 \in (0, 0.005715) \}$, i.e., Ω is an open cuboid of the size $50 \times 50 \times 5.715$mm. Next, $\Omega_{Air} = \{ \mathbf{x} \in \mathbb{R}^3 : x_1 \in (0, 0.05), x_2 \in (0, 0.05), x_3 \in (0.000635, 0.005715) \}$ and $\Omega_{Die} = \{ \mathbf{x} \in \mathbb{R}^3 : x_1 \in (0, 0.05), x_2 \in (0, 0.05), x_3 \in (0, 0.000635) \}$. Further, $\Gamma_{Strip} = \{ \mathbf{x} \in \mathbb{R}^3 : (x_1, x_2) \in \mathbf{S}_{xy}, x_3 = 0.000635 \}$, where $\mathbf{S}_{xy} \subset \mathbb{R}^2$ is a closed set, defined in Figure 1 as the orange area.

Furthermore, $\Gamma_{Grnd} = \{\boldsymbol{x} \in \mathbb{R}^3 : (x_1, x_2) \in \mathbf{G}_{xy}, x_3 = 0\}$, where $\mathbf{G}_{xy} \subset \mathbb{R}^2$ is a closed set, defined in Figure 2 as the orange area.

Finally, with the help of Figures 3 and 4, we define the remaining parts of boundaries as $\Gamma_{AirToDie} = (\partial\Omega_{Air} \cap \Omega_{Die}) \setminus \Gamma_{Strip}$ (light grey color), $\Gamma_{BottomWalls} = \partial\Omega_{Die} \setminus (\partial\Omega_{Air} \cup \Gamma_{Grnd})$ (dark purple color,) and $\Gamma_{TopWalls} = \partial\Omega_{Air} \setminus (\partial\Omega_{Die})$ (green color).
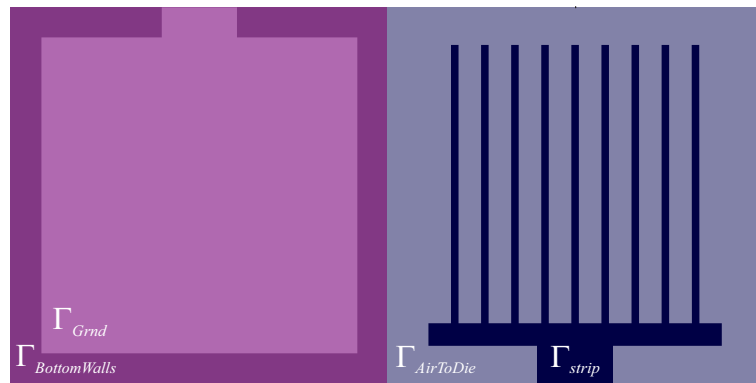

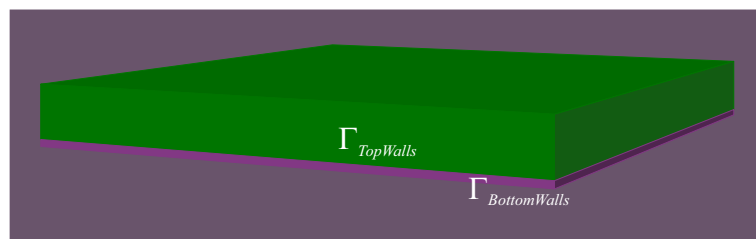**Figure 3.** The marking of the domain boundary parts around electrodes.

Figure 4. The marking of the outer domain boundary parts.

Further, the mesh consists of approximately 600,000 tetrahedrons [34]. It was generated in tetgen (see tetgen.org) using a predefined set of vertices. The predefined set of vertices divides the domain into cubes adaptively refined near electrodes (Γ_{Strip} and Γ_{Grnd}). There are four levels of refinement, and the smallest cube is of the size $0.00025 \times 0.00025 \times 0.0003175$ m, i.e., $0.25 \times 0.25 \times 0.3175$ mm.

Now we proceed to the parameters settings. We first specify the physical coefficients. Hence, we set the vacuum permittivity $\varepsilon_0 = 8.85 \times 10^{-12}$ Fm^{-1}, the air permittivity coefficient $\varepsilon_{Air} = 1.0006$, the dielectric permittivity coefficient $\varepsilon_{Die} = 9.6$, the elementary charge $e_c = 1.6022 \times 10^{-19}$ C, and the exponential and pre-exponential coefficients are set to $A = 1.5 \times 10^3$ m^{-1}torr^{-1} and $B = 3.56 \times 10^4$ V m^{-1}torr^{-1}, respectively.

Furthermore, we set the ion and electron mobility coefficients $\mu_i = 0.145/\pi$ m^{2}s^{-1}V^{-1} and $\mu_e = 44/\pi$ m^{2}s^{-1}V^{-1}, respectively, the ion and electron diffusion coefficients $D_i = (k_B/e_c)T_i\mu_i$ m^{2}s^{-1} and $D_e = (k_B/e_c)T_e\mu_e$ m^{2}s^{-1}, respectively, Boltzmann's constant is $k_B = 1.3806488 \times 10^{-23}$ m^{2}kgs^{-2}K^{-1}, the ion and electron temperature $T_i = 300$ K and $T_e = 60{,}000$ K, respectively, the reference particle density $n_0 = 2 \times 10^{15}$ m^{-3}. Further, we define the initial ion/electron particle densities $n_i^0(x) = n_e^0(x) = n_0$ and set $U_{amp} = 3000$ V, $\omega = 2\pi f$ and $f = 10.9 \times 10^3$ Hz. Moreover, we choose the reference time $t_0 = 1/\omega$ s, the characteristic length $L = 0.05$ m, and the characteristic velocity $V_0 = 1 \times 10^{-6}$ ms^{-1}.

Finally, the degrees of polynomial approximations are set to $r = 2$, $s = 2$ and $q = 1$, respectively. The problem is solved for $T = \frac{1}{2f} \times 10^{-3}$ s, i.e., $T \approx 46$ ns, with time step $\Delta\tau = 0.1$ ns, i.e., $j_{max} = 460$. The minimal amount of particles coefficient is set to $N_{min} = 10$.

The Results

The presented experiment took about a day on a standard personal computer. In the following, we present the visualization of several key numerical simulation results

using the open-source software ParaView (see https://www.paraview.org/, accessed on 15 January 2023).

Firstly, we show the top view of the difference in ions and electrons densities $n_i - n_e$ at various instants of time close to the tip of the strips; see Figures 5–8. These figures show that close to the strip electrode, the density of electrons exceeds the density of positive ions. On the other hand, the situation is the opposite, farther from the strip electrode. This conclusion agrees with the results presented in Ref. [24], and our analysis is for the positive half-period of the driving voltage.

Depending on the discharge conditions, the lifetime of the microdischarges ranges to several tens of nanoseconds, which is why we used for our numerical experiment the time scale $T = 46$ ns [35]. The distribution of electron density is narrower than that of the positive ions. This outcome agrees with the results presented in Figures 5–8.
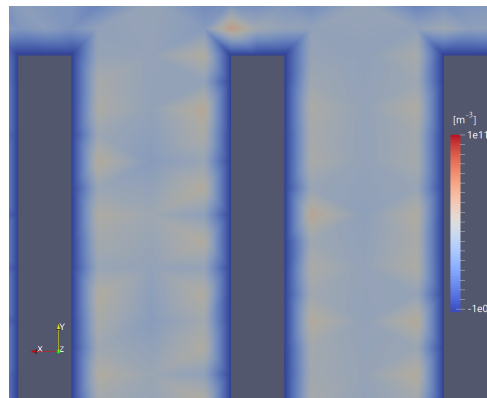

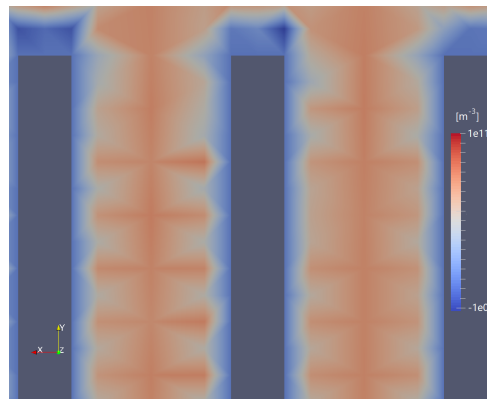**Figure 5.** Species densities difference $n_i - n_e$ at time 6 ns.

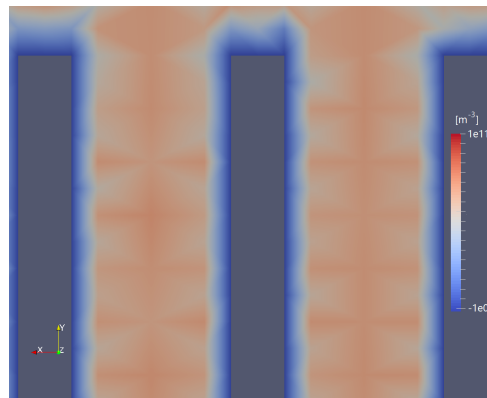**Figure 6.** Species densities difference $n_i - n_e$ at time 18 ns.
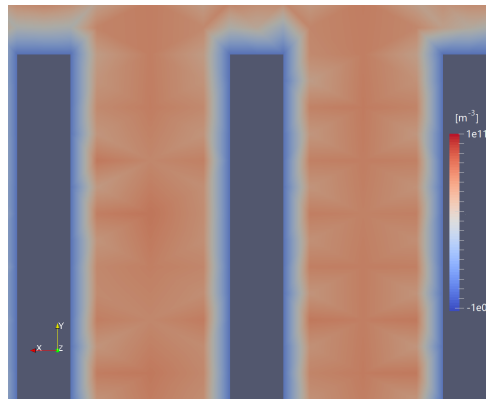

Figure 7. Species densities difference $n_i - n_e$ at time 30 ns.

Figure 8. Species densities difference $n_i - n_e$ at time 46 ns.

Secondly, in Figures 9–12, we show the trajectories of electrons and ions at two instants of time, $T = 18$ ns and $T = 46$ ns, with the corresponding V_i and V_e velocities. The color of the individual parts of the trajectories expresses the magnitude of the velocity. For better readability, only trajectories between two neighboring strips are shown close to their tips. It should be pointed out that these trajectories represent the situation in the initial phase of the positive half-period of the driving voltage only. From the comparison of the trajectories of electrons and ions, it can be concluded that the electrons do not extend as much from the edge of the strips as the ions.

This trajectory of these particles could be associated with the luminous region around the strip electrode, which represents the active volume of the discharge. Therefore, this result could be used to optimize the distance among neighboring strips. This would have a strong impact on the design of the electrode system.
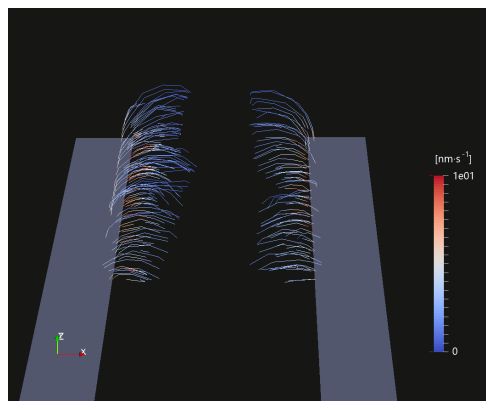
Figure 9. Trajectories and velocities of ions V_i at time 18 ns.
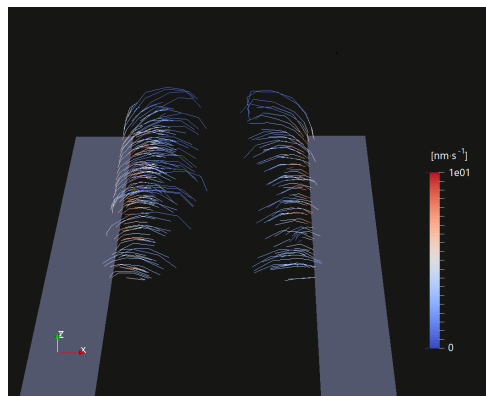
Figure 10. Trajectories and velocities of ions V_i at time 46 ns.
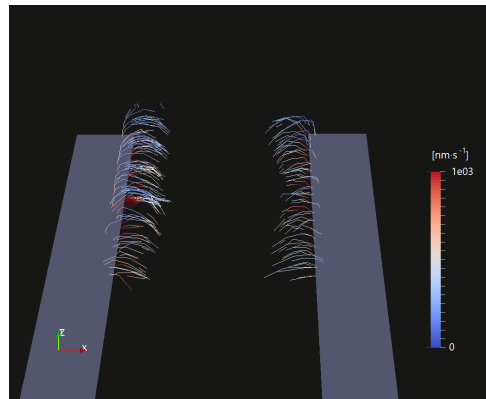
Figure 11. Trajectories and velocities of electrons V_e at time 18 ns.
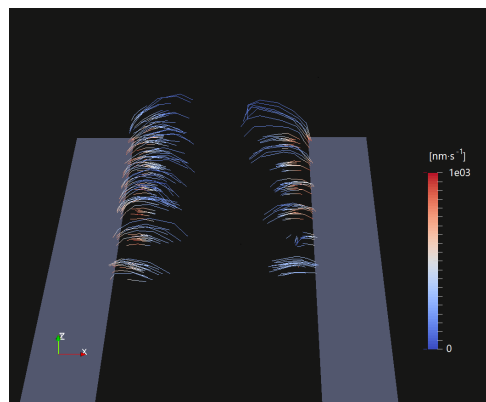
Figure 12. Trajectories and velocities of electrons V_e at time 46 ns.

7. Conclusions

We developed a 3D numerical model for the initial phase of the surface dielectric barrier discharge in planar configuration with the strips active electrode. We assume a positive half-period of the sinusoidal driving voltage and the two-species model. Based on the fluid model, we present the following

- Mathematical formulation of the problem;
- Detailed formulation of the numerical model;
- Linear approximation of the ionization rate;
- Stable reconstruction of ion and electron velocity fields;
- Simulations showing trajectories and velocities of electrons and ions.

In contrast with the preceding models mentioned in existing literature, the main innovation presented in our paper is developing a 3D numerical model of the initial phase of the surface dielectric barrier discharge. We have paid particular attention to the proper formulation of the problem, description of the key issues, and possible numerical complications. Overall, we exposed the numerical theory in much more detail and laid down a good theoretical foundation for further research of the SDBD.

For future development of the model, we consider involving additional ionic effects on the electrodes so that it could be used for negative half-periods of the driving voltage. For simulations of extended periods, other techniques for stabilization need to be adopted.

Our model can be used to optimize the electrode geometry of the discharge. We believe the presented deeper mathematical insight into the problems will help predict and understand the experimental results in a better way.

References

1. Gibalov, V.I.; Pietsch, G.J. The development of dielectric barrier discharges in gas gaps and on surfaces. *J. Phys. D Appl. Phys.* **2000**, *33*, 2618–2636. [CrossRef]
2. Mikeš, J.; Pekárek, S.; Babčenko, O.; Hanuš, O.; Kákona, J.; Štenclová, P. 3D printing materials for generators of active particles based on electrical discharges. *Plasma Process. Polym.* **2020**, *17*, 1900150.
3. Kogelschatz, U. UV Production in Dielectric Barrier Discharges for Pollution Control. In *Non-Thermal Plasma Techniques for Pollution Control*; Springer: Berlin/Heidelberg, Germany, 1993; pp. 339–354. [CrossRef]
4. Borcia, G.; Anderson, C.A.; Brown, N.M.D. Dielectric barrier discharge for surface treatment: Application to selected polymers in film and fibre form. *Plasma Sources Sci. Technol.* **2003**, *12*, 335–344. [CrossRef]
5. Bednar, N.; Matović, J.; Stojanović, G. Properties of surface dielectric barrier discharge plasma generator for fabrication of nanomaterials. *J. Electrost.* **2013**, *71*, 1068–1075. [CrossRef]
6. Boscher, N.D.; Hilt, F.; Duday, D.; Frache, G.; Fouquet, T.; Choquet, P. Atmospheric Pressure Plasma Initiated Chemical Vapor Deposition Using Ultra-Short Square Pulse Dielectric Barrier Discharge. *Plasma Process. Polym.* **2014**, *12*, 66–74. [CrossRef]
7. Ambrico, P.F.; Šimek, M.; Rotolo, C.; Morano, M.; Minafra, A.; Ambrico, M.; Pollastro, S.; Gerin, D.; Faretra, F.; Angelini, R.M.D.M.; et al. Surface Dielectric Barrier Discharge plasma: A suitable measure against fungal plant pathogens. *Sci. Rep.* **2020**, *10*, 3673. [CrossRef]
8. Pavon, S.; Dorier, J.L.; Hollenstein, C.; Ott, P.; Leyland, P. Effects of high-speed airflows on a surface dielectric barrier discharge. *J. Phys. D Appl. Phys.* **2007**, *40*, 1733–1741. [CrossRef]
9. Pavón, S. Interaction between a Surface Dielectric Barrier Discharge and Transonic Airflows. Ph.D. Thesis, École Polytechnique Fédérale de Lausanne, École polytechnique fédérale de Lausanne, Lausanne, Switzerland, 2008. [CrossRef]
10. Yuan, D.; Ding, C.; He, Y.; Wang, Z.; Kumar, S.; Zhu, Y.; Cen, K. Characteristics of Dielectric Barrier Discharge Ozone Synthesis for Different Pulse Modes. *Plasma Chem. Plasma Process.* **2017**, 37, 1165–1173. [CrossRef]
11. Pekárek, S. Asymmetric properties and ozone production of surface dielectric barrier discharge with different electrode configurations. *Eur. Phys. J. D* **2013**, *67*, 94. [CrossRef]
12. Pekárek, S.; Babčenko, O.; Mikeš, J.; Kromka, A. Effect of a diamond layer on the active electrode on the ozone generation of the dielectric barrier discharge in air. *J. Phys. D Appl. Phys.* **2020**, *53*, 275203. [CrossRef]
13. Ye, Q.; Wu, Y.; Li, X.; Chen, T.; Shao, G. Uniformity of dielectric barrier discharges using mesh electrodes. *Plasma Sources Sci. Technol.* **2012**, *21*, 065008. [CrossRef]
14. Pekárek, S.; Mikeš, J. Temperature-and airflow-related effects of ozone production by surface dielectric barrier discharge in air. *Eur. Phys. J. D* **2014**, *68, 310*. [CrossRef]
15. Shimizu, K.; Blajan, M. Dielectric Barrier Discharge Microplasma Actuator for Flow Control. In *Actuators*; InTech: Vienna, Austria, 2018. [CrossRef]
16. Wei, L.S.; Yuan, D.K.; Zhang, Y.F.; Hu, Z.J.; Dong, G.P. Experimental and theoretical study of ozone generation in pulsed positive dielectric barrier discharge. *Vacuum* **2014**, *104*, 61–64. [CrossRef]
17. Xie, S.; He, Y.; Yuan, D.; Wang, Z.; Kumar, S.; Zhu, Y.; Cen, K. The effects of gas flow pattern on the generation of ozone in surface dielectric barrier discharge. *Plasma Sci. Technol.* **2019**, *21*, 055505. [CrossRef]
18. Wei, L.; Yuan, D.; Zhang, Y.; Hu, Z.; Tan, Z.; Dong, G.; Tao, S. An analysis of the effect of inert gases on ozone generation using dielectric barrier discharge in oxygen. *Eur. Phys. J. D* **2014**, *68*, 17. [CrossRef]
19. Ahmadi, A.; Labadin, J.; Piau, P.; Rigit, A.R. Numerical Modeling of the Dielectric Barrier Discharges Plasma Flow. In Proceedings of the 2010 Fourth Asia International Conference on Mathematical/Analytical Modelling and Computer Simulation, Kota Kinabalu, Malaysia, 26–28 May 2010. [CrossRef]
20. Jayaraman, B.; Cho, Y.C.; Shyy, W. Modeling of dielectric barrier discharge plasma actuator. *J. Appl. Phys.* **2008**, *103*, 053304. [CrossRef]
21. Jayaraman, B.; Shyy, W. Modeling of dielectric barrier discharge-induced fluid dynamics and heat transfer. *Prog. Aerosp. Sci.* **2008**, *44*, 139–191. [CrossRef]

22. Jayaraman, B.; Shyy, W.; Thakur, S. Modeling of dielectric barrier discharge and resulting fluid dynamics. In Proceedings of the 44th AIAA Aerospace Sciences Meeting and Exhibit, Reno, NV, USA, 9–12 January 2006; American Institute of Aeronautics and Astronautics: Reston, VA, USA, 2006. [CrossRef]

23. Jayaraman, B.; Thakur, S.; Shyy, W. Modeling of Fluid Dynamics and Heat Transfer Induced by Dielectric Barrier Plasma Actuator. *J. Heat Transf.* **2007**, *129*, 517. [CrossRef]

24. Shang, J.S.; Huang, G.P. Modeling of ac dielectric barrier discharge. *J. Appl. Phys.* **2010**, *107*, 113302. [CrossRef]

25. Abdollahzadeh, M.; Pascoa, J.C.; Oliveira, P.J. Implementation of the classical plasma–fluid model for simulation of dielectric barrier discharge (DBD) actuators in OpenFOAM. *Comput. Fluids* **2016**, *128*, 77–90. [CrossRef]

26. Kumar, H.; Roy, S. Multidimensional hydrodynamic plasma-wall model for collisional plasma discharges with and without magnetic-field effects. *Phys. Plasmas* **2005**, *12*, 093508. [CrossRef]

27. Roy, S. Flow actuation using radio frequency in partially ionized collisional plasmas. *Appl. Phys. Lett.* **2005**, *86*, 101502. [CrossRef]

28. Singh, K.P.; Roy, S. Force approximation for a plasma actuator operating in atmospheric air. *J. Appl. Phys.* **2008**, *103*, 013305. [CrossRef]

29. Wang, C.C.; Roy, S. Geometry Effects of Dielectric Barrier Discharge on a Flat Surface. In Proceedings of the 49th AIAA Aerospace Sciences Meeting including the New Horizons Forum and Aerospace Exposition, Orlando, FL, USA, 4–7 January 2011. [CrossRef]

30. Abdelaziz, A.A.; Ishijima, T.; Seto, T.; Osawa, N.; Wedaa, H.; Otani, Y. Characterization of surface dielectric barrier discharge influenced by intermediate frequency for ozone production. *Plasma Sources Sci. Technol.* **2016**, *25*, 035012. [CrossRef]

31. Yuan, D.; Wang, Z.; Ding, C.; He, Y.; Whiddon, R.; Cen, K. Ozone production in parallel multichannel dielectric barrier discharge from oxygen and air: The influence of gas pressure. *J. Phys. D Appl. Phys.* **2016**, *49*, 455203. [CrossRef]

32. Bouchmal, A. Modeling of Dielectric-Barrier Discharge Actuator: Implementation, Validation and Generalization of an Electrostatic Model. Master's Thesis, Delft University of Technology, Delft, The Netherlands, 2011.

33. Liu, C.; Dobrynin, D.; Fridman, A. Uniform and non-uniform modes of nanosecond-pulsed dielectric barrier discharge in atmospheric air: Fast imaging and spectroscopic measurements of electric fields. *J. Phys. D Appl. Phys.* **2014**, *47*, 252003. [CrossRef] [PubMed]

34. Mikeš, J.; Pekárek, S.; Soukup, I. Experimental and modelling study of the effect of airflow orientation with respect to strip electrode on ozone production of surface dielectric barrier discharge. *J. Appl. Phys.* **2016**, *120*, 173301. [CrossRef]

35. Gibalov, V.; Pietsch, G. Dynamics of dielectric barrier discharges in different arrangements. *Plasma Sources Sci. Technol.* **2012**, *21*, 024010. [CrossRef]

36. Roveda, F. Numerical analysis of Dielectric Barrier Discharge. Ph.D. Thesis, Università degli Studi di Bologna, Bologna, Italy, 2012.

37. Bogdanov, E.; Kudryavtsev, A.; Kuranov, A.; Kozlov, I.; Tkachenko, T. 2D Simulation and Scaling of DBD Plasma Actuator in Air. *Am. Inst. Aeronaut. Astronaut.* **2008**. [CrossRef]

38. Luo, H.; Liu, K.; Junxia, R.; Yue, Y.; Wang, X.; Ling, Y.; Wong, C. Study of Dielectric Barrier Townsend Discharge in 3-mm Air Gap at Atmospheric Pressure. *Plasma Sci. IEEE Trans.* **2014**, *42*, 1211–1215. [CrossRef]

39. Raizer, Y.P. *Gas Discharge Physics*, 2nd ed.; Springer: Berlin/Heidelberg, Germany, 1997; ISBN 978-354-019-462-0.

40. Surzhikov, S.T. *Computational Physics of Electric Discharges in Gas Flows*; De Gruyter: Vienna, Austria, 2013.

41. Yu, J.; Chen, F.; Liu, H.; Song, Y. Numerical Study of Fluid Dynamics and Heat Transfer Induced by Plasma Discharges. *Plasma Sci. Technol.* **2015**, *17*, 41–49. [CrossRef]

A.7 Air Supply Mode Effects on Ozone Production of Surface Dielectric Barrier Discharge in a Cylindrical Configuration

S. Pekárek, J. Mikeš, M. Červenka *et al.*, 'Air supply mode effects on ozone production of surface dielectric barrier discharge in a cylindrical configuration,' *Plasma Chemistry and Plasma Processing*, vol. 41, no. 3, pp. 779–792, Jan. 2021. DOI: 10.1007/s11090-021-10154-x.

ORIGINAL PAPER

Air Supply Mode Effects on Ozone Production of Surface Dielectric Barrier Discharge in a Cylindrical Configuration

Stanislav Pekárek[1] · Jan Mikeš[1] · Milan Červenka[1] · Ondřej Hanuš[1]

Abstract

We investigated the air supply mode effects on ozone production of the surface dielectric barrier discharge in the cylindrical configuration. The air into the discharge volume between two coaxial cylinders was supplied through four nozzles axially or tangentially. Using tangential air supply, the vortex flow in the part of the discharge chamber was created. Because the active electrode was in the form of interconnected rings on the outer surface of the glass tube, we changed the airflow orientation concerning this electrode. The existence of vortex airflow affects the plasmachemical processes taking part in the discharge, and therefore, it affects discharge ozone production. We also paid attention to ozone concentration and temperature of output air measurements as a function of the duration of the experiment for both tangential and axial air supply modes. We found that the time required for the stabilization of generated ozone concentration depends on the discharge power, and for our experimental conditions, it smaller than approximately 70 s. Besides, in the case of tangential air supply into the discharge chamber, the concentration of ozone produced by the discharge is for higher discharge power increased in comparison with the concentration for the axial air supply mode.

Keywords Surface dielectric barrier discharge · Ozone · Airflow · Vortex

Introduction

Because ozone is one of the strongest oxidizing agents with important antibacterial properties, its generation by electrical discharges and, namely by dielectric barrier discharges from the air, is at the center of interest of many researchers for more than a hundred years. To improve the efficiency of ozone generation, various approaches are tested. Among them it should be mentioned proper choice of the discharge type [1, 2], optimization of the electrode layout [3, 4] the discharge energization [5, 6] including variations of the duty cycle and optimization of electrical parameters of the discharge [7–10], adjustment of working gas parameters [11–13], application of the catalysts usually in the discharge chamber [14, 15] application of external agents (magnetic field, ultrasound, UV radiation) on the

---

✉ Stanislav Pekárek
pekarek@fel.cvut.cz

1 Czech Technical University in Prague, FEE, Technická 2, 166 27 Prague 6, Czech Republic

discharge [16, 17], or "stretching" the microdischarge channels using a rotating electrode [18, 19].

The important quantity which strongly affects discharge properties, as well as its ozone generation, is the flow rate of the working gas through the discharge chamber. There exist numerous works dealing with this topic [20–22]. Generally speaking, changing the flow rate through the discharge chamber affects the residence time of charge carriers in the discharge region, the mixing of the gas, temperature, heat exchange, etc. It should be, however, pointed out that in these papers, the direction of the working gas flow with respect to the discharge electrodes was fixed, and the systematic study of the effect of working gas flow orientation concerning the electrodes is missing.

The effects of the magnitude and direction of airflow rate on the characteristics of the corona discharge generated in a wire-duct reactor were studied in [23]. Two airflow directions were attempted: one parallel to, and the other normal to the discharge wire in the reactor. The ozone concentration generated by either dc, ac, or pulsed coronas with the parallel flow is higher than that produced with the normal flow with the same discharge conditions. The effect of airflow orientation with respect to the strip active electrode on ozone production of surface dielectric barrier discharge (SDBD) was investigated in [23]. It was found that ozone concentration increased when airflow was oriented in parallel concerning the strips electrode in comparison with the perpendicular orientation of the airflow. The impact of flow patterns on the uniformity and turbulence of gas flow and, consequently, on the ozone production yield was studied in [25]. It was shown that the type of flow patterns—transversal or lateral concerning the active electrode, or different lateral flow inputs positions have a remarkable impact on ozone production. The effect of the gas flow direction on ozone generation by concentric actuator has been investigated in [26]. It has been shown that the concentration of ozone generated from oxygen by concentric actuator slightly depends on the oxygen flow direction. The effect of the flow orientation concerning the electrode symmetry on the diameter of the discharge channel for the pulsed dielectric barrier discharges was investigated in [27]. It was found that this diameter changes because of the change of charge density owing to the convective transport under the action of airflow. The fact that the velocity of the space charges in the nanosecond pulsed dielectric barrier discharge in atmospheric airflow for different electrode structures depends on airflow velocities was also observed in [28].

In our study, attention is focused on air supply modes effects on the ozone generation of the SDBD in a cylindrical configuration. The air into the discharge volume between two coaxial cylinders was supplied through four nozzles axially or tangentially. The output of air from the chamber was, in both cases axial, the same as the axial input. We also paid attention to the correlation between ozone concentration, discharge power, and temperature of the gas at the output of the discharge chamber as a function of the duration of the experiment for both tangential and axial air supply modes.

Experimental Arrangement

The experimental set-up used for our studies is shown in Fig. 1. It consists of a cylindrical discharge chamber with an electrode system, a high voltage power supply with electrical parameters diagnostics, an ozone monitor, and an air supply system. To suppress the effect of temperature on ozone concentration measurements, we used water cooling of the central electrode, and we placed the discharge chamber in the thermobox Pol-Eko-Aparatura,
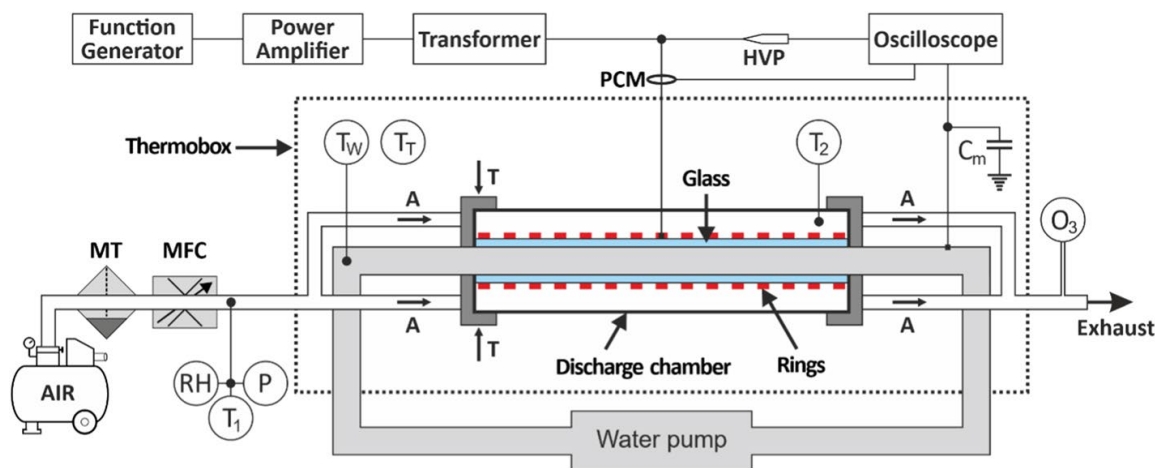
Fig. 1 Experimental arrangement

which provides a stable, controllable temperature between 3 and 70 °C regardless of ambient conditions.

The cylindrical discharge chamber of total length 172 mm consisted of the polymethyl-methacrylate-plexiglass tube of outer diameter 30 mm, inner diameter 24 mm, and with 3D printed caps for input/output of air on its sides. The experiments were performed with two types of air input caps. In the first case, there were four nozzles in the cap (Fig. 2—left) axially oriented with respect to the axis of the cylindrical discharge tube. The centers of these nozzles were in the middle of the gap between outer radius of the Simax glass tube and the inner radius of the plexiglass tube of the discharge chamber. This is a situation of axial air input, which is shown in Fig. 1 by letter A. In the second case, there were also four nozzles in the input cap, oriented clockwise tangentially to the discharge tube (Fig. 2—right). The positions of these tangential inputs are in Fig. 1 shown by letter T. For both types of inputs, the output of air from the discharge chamber was through the cap with four axial openings A of the same dimensions as those in the cup for axial air input. The diameters of the input and output nozzles were 2 mm. The caps had an outer diameter of 38 mm and a length of 31 mm.

Inside the discharge chamber was situated the electrode system, which consisted of active and grounded electrode on a Simax glass tube. The inner diameter of this glass

Fig. 2 Left: axial air input/output cap. Right: tangential air input

tube was 17.4 mm, the outer diameter was 20.0 mm, and the length of the tube was 150 mm. The Simax glass relative permittivity and the loss angle at temperature 20 °C and frequency 1 MHz are 4.6 and 4.9×10^{-3}, respectively. On the outer side of this glass tube, there was an active electrode in the form of 30 circular interconnected rings of widths 1 mm separated by the distances 2.5 mm. This electrode was made from the copper foil of thickness 0.06 mm. The length of the active electrode was 117 mm. The brass tube, which served as the grounded electrode, was inserted into the Simax glass tube. The capacitance of the electrode system was 1.05×10^{-10} F.

For the cooling of grounded electrode, we used the closed water circuit with the water pump. Water was supplied to the tube from the opposite side to which was supplied air inside the discharge tube.

The active electrode was connected to an AC high voltage power supply system. This system consisted from function/arbitrary waveform generator DG 1022, wideband AC power amplifier AL-600-HF-A (output power 600 W, frequency response 20 Hz to 800 kHz) and a high-frequency high voltage transformer AL-T1000.5 (peak voltage 10 kV, output power 1000 W and frequency response 4 to 12 kHz). The discharge was driven by sinusoidal voltage.

The electrical parameters of the discharge were monitored by the digital oscilloscope Tektronix MDO 4054B-3 (3 GHz; 2.5 GSa/s). The discharge voltage signal $V(t)$ was sampled and recorded on the first channel of this oscilloscope with a high voltage probe (HVP-28HF, Pintek, division ratio 1000/1, frequency up to 200 MHz). To determine discharge power, we used two methods. In the first case, the discharge power was calculated based on the following equation:

$$P_{av} = \frac{1}{T} \int_0^T V(t) I(t) dt, \tag{1}$$

The discharge current $I(t)$ was determined from a signal from a Pearson current monitor (PCM, model 2877, bandwidth up to 200 MHz) that was recorded on the second channel of the oscilloscope.

In the second case, the third channel of the oscilloscope was used to detect the voltage drop V_m on the measuring capacitor $C_m = 1.0 \times 10^{-7}$ F, inserted between the grounded electrode and grounding lead. The discharge power was calculated from the following equation:

$$P = f . \oint V(t) . \frac{dQ}{dt} dt = f . C_m \oint V(t) dV_m, \tag{2}$$

where f is the frequency of the driving voltage.

The air into the discharge chamber was supplied through the moisture trap (MT) and the mass flow controller Bronkhorst F-201C (MFC) from an oil-free compressor. We also measured the pressure in the input of the discharge chamber (P) and the relative humidity (RH) of air. The optical fiber thermometer Neoptix was used to monitor the temperature of the air at the input (T_1) and output (T_2) of the discharge chamber, the temperature of the cooling water T_W and the temperature in the thermobox T_T. The ozone concentration (O_3) was measured by the dual-beam UV photometer (254 nm) BMT 964. For illustrative purposes is shown in Fig. 3 the photograph of the discharge with tangential air supply into the discharge chamber. This photo was taken with Canon PowerShot G12 and exposition time 2 s. The dark regions on this photograph are the interconnected rings, which constitute the active electrode.
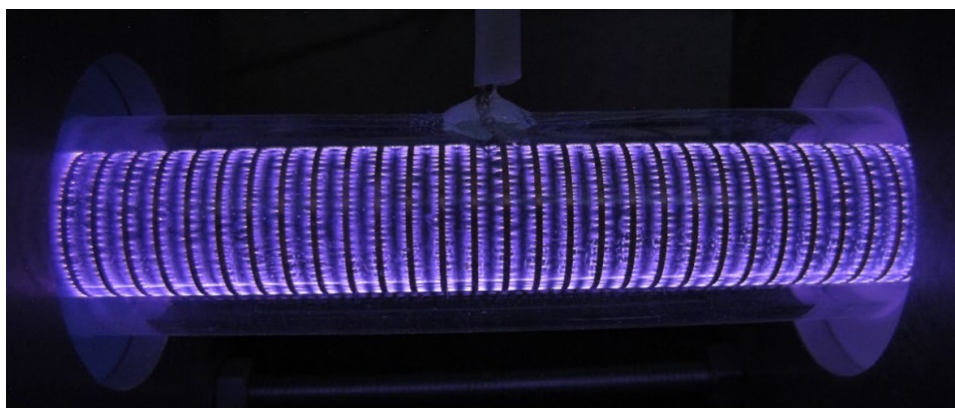
Fig. 3 Photograph of the discharge with tangential air supply. $V_{ampl} = 5430$ V, $Q_{air} = 6$ slm

Experimental Results and Discussion

All experiments described below were performed with an air of fixed flow rate 6 slm through the discharge chamber. In the case of both, tangential or axial air supply modes, the pressure in the discharge chamber exceeded the atmospheric pressure of about 36 Torr. The relative humidity of air was below 3%. The temperature of the input air into the discharge chamber as well as the temperature of cooling water and the temperature in the thermobox were adjusted to 20 °C. The discharge was driven by the sinusoidal voltage of frequency 10 kHz.

Discharge Power, Ozone Concentration, and Temperature of Output Air: Time Dependence

The discharge voltage and current signals, ozone concentration, and the temperature of the air at the output of the discharge chamber were recorded when the discharge was switched on. These measurements were performed in 10 periods; each period lasted 5 min. After each measurement period, the discharge was for 5 min switched off, and then another value of the discharge voltage was adjusted.

The ozone concentration, together with the air temperature at the output from the discharge chamber, was recorded each 2 s, which means that we have 150 values of these quantities for each measuring period. Because of the time 20 s required to save electrical signals on the oscilloscope, we have for each of these measuring periods 15 data sets of electrical quantities based on which was calculated the discharge power.

The average discharge power from 15 measurements of each measuring period obtained through the Pearson current monitor or the measuring capacitor as a function of discharge voltage amplitude for axial or tangential air supply mode, is shown in Fig. 4. The error bars represent $\pm 7\%$ of the discharge power. From this figure, it is seen that the way of air supply into the discharge chamber does not substantially affect the discharge power.

The time sequence of the instantaneous values of the discharge power obtained through the measuring capacitor or a current monitor for the first to the tenth measuring period for both tangential and axial air supply modes is shown in Fig. 5.

From this graph it is seen, that for the 1st measuring period the values of instantaneous discharge power are very much spread. This 1st period corresponds to the onset on
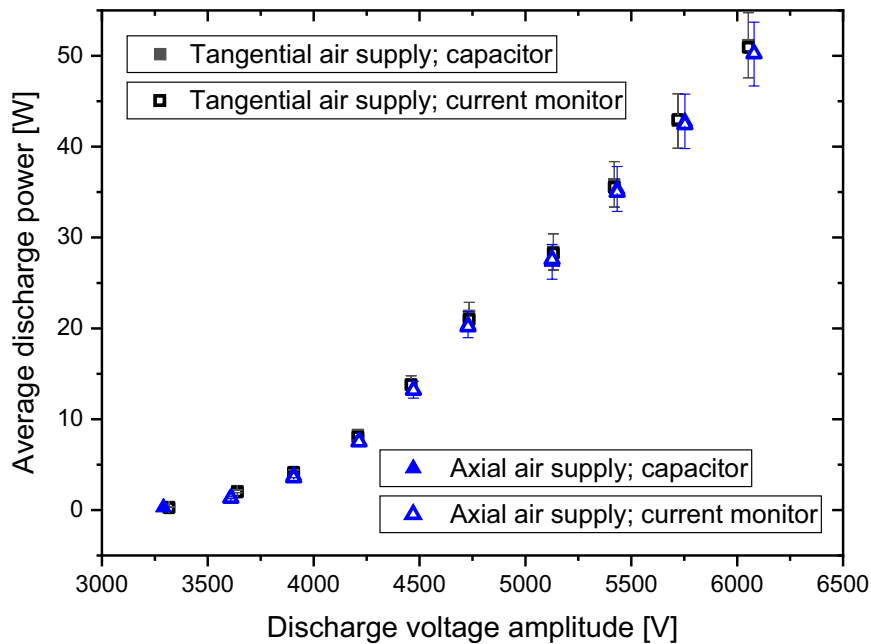
Fig. 4 The average discharge power over each measuring period obtained through the measuring capacitor or a current monitor as a function of discharge voltage amplitude for tangential or axial air supply mode
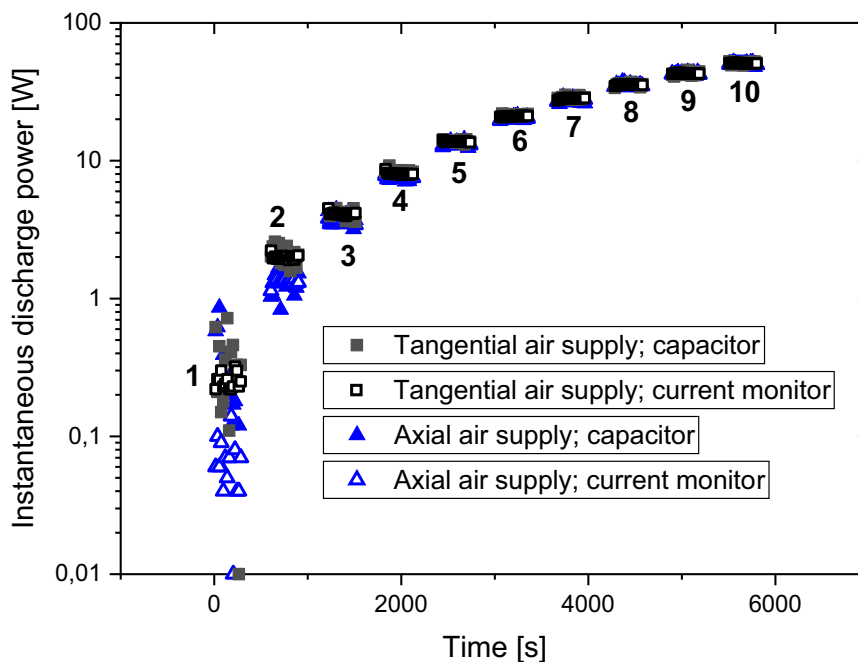
Fig. 5 The time sequence of the instantaneous values of the discharge power obtained through the measuring capacitor or a current monitor for the first to the tenth measuring periods for both tangential and axial air supply modes

the discharge which occurs at the discharge voltage ∼ 3310 V. At this voltage appear first current peaks on the displacement current signal, recorded by the current monitor. The spread of the discharge power values is smaller for the 2nd measuring period (discharge voltage ∼ 3630 V) and with increasing voltage it decreases.

The time dependence of ozone concentration for the same measuring periods as for the discharge power measurement is shown in the following Fig. 6. The ozone concentration
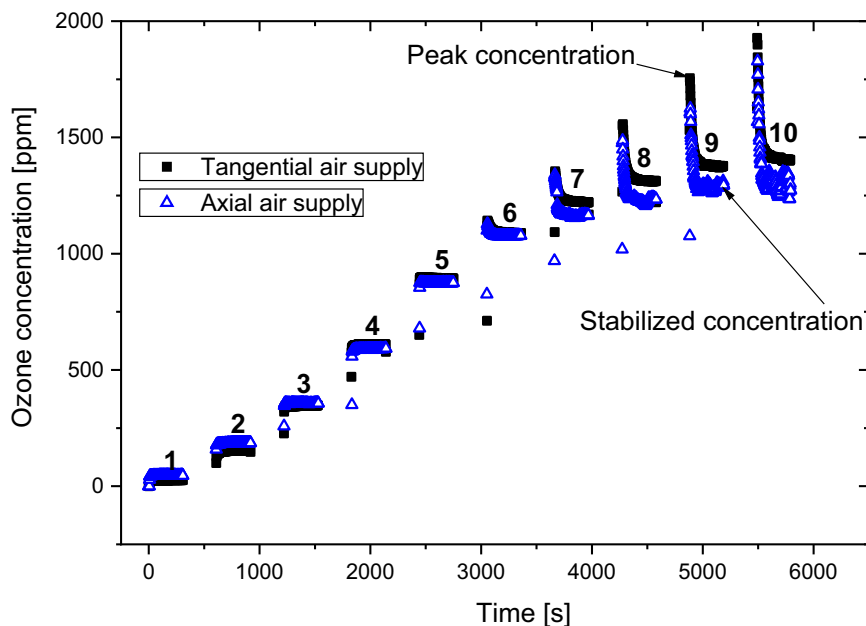
Fig. 6 The concentration of ozone generated by the discharge as a function of time for tangential or axial air supply mode

between measuring periods, when the discharge was switched off, decreased to zero. From this figure it is also seen, that the concentrations of ozone produced by the discharge for measuring periods 4 till 10 (discharge power higher than 8 W) are higher for the discharge with tangential air supply than for the discharge with axial supply mode. Finally, for measuring periods 1–5 (small discharge powers), the ozone concentration is stable almost immediately after the discharge ignition. When the discharge power is increased (measuring periods 6–10) the ozone concentration after the discharge ignition is, first, sharply increased, reaches the peak value, then it is decreased, and after a certain time, it becomes stabilized. Thus for the highest discharge power (10th measuring period), the ozone concentration is stabilized approximately 70 s after the discharge ignition.

Because ozone generation and destruction depend on the temperature, we also measured the temperature (T_2) of the air at the output from the discharge chamber. These measurements were performed for the same periods as for results presented in Figs. 5 and 6. This dependence is shown in Fig. 7. From this figure, it is seen that, depending on the discharge power, the air is in the discharge heated. This heating is more important for higher discharge powers. An interesting conclusion from this figure is that in the case of tangential air supply, the temperature of the air at the output from the discharge chamber is higher than for axial air supply mode. Thus, for example, for tangential air supply mode at the end of the 10th measuring period, the temperature of output air is 37.1 °C, and for axial air supply, it is 36.0 °C.

Ozone Concentration and Ozone Production Yield: Discharge Power Dependence

The effect of the tangential/axial air supply into the cylindrical discharge chamber on the concentration of ozone produced by the discharge is shown in Fig. 8. This figure has been constructed based on stabilized values of ozone concentrations from Fig. 6 and average values of power for corresponding measuring periods. The error bars represent $\pm 6\%$ of ozone concentration.

Fig. 7 The temperature of the air at the output from the discharge chamber as a function of time for tangential or axial air supply mode
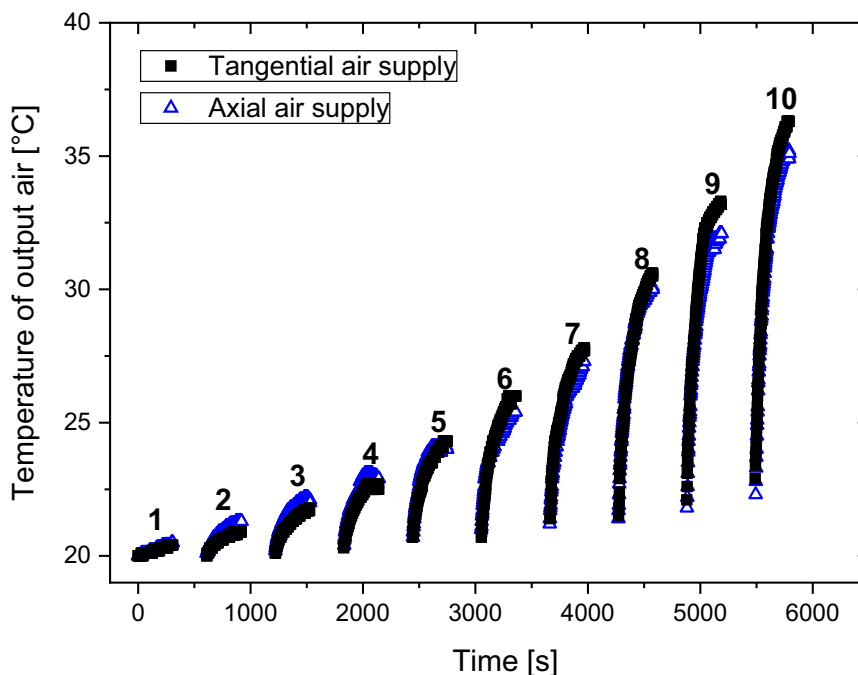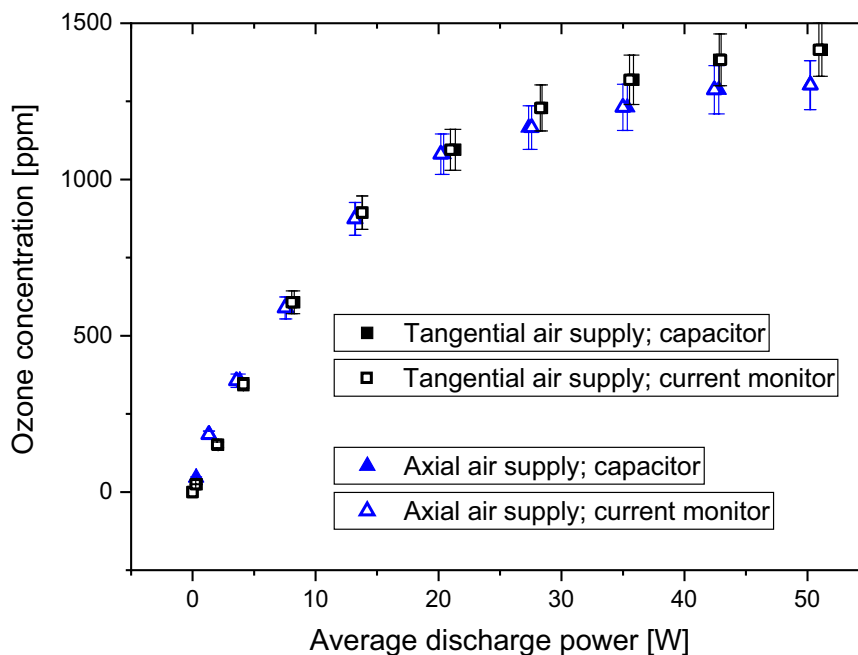

Fig. 8 Ozone concentration as a function of the average discharge power obtained through the measuring capacitor or a current monitor for both tangential or axial air supply modes

From Fig. 8 could be seen that for higher discharge power, the ozone concentration for the discharge with tangential air supply is higher than for axial supply. In the case of small discharge powers, the way of air supply into the discharge chamber does not affect ozone concentration. The increase in ozone concentration is for the discharge power of 50 W, approximately 9%.

An important quantity from the standpoint of practical applications is the ozone production yield α, which is defined as a mass of ozone produced by 1 kWh of energy. This quantity is for our experimental conditions calculated from the following equation:

$$\alpha = \frac{0.771 \times O_3\,[\text{ppm}]}{P_{av}[\text{W}]} \quad [\text{g/kWh}] \tag{3}$$

The numerical constant 0.771 involves the density of ozone as well as all conversion factors of the airflow rate, power, and energy.
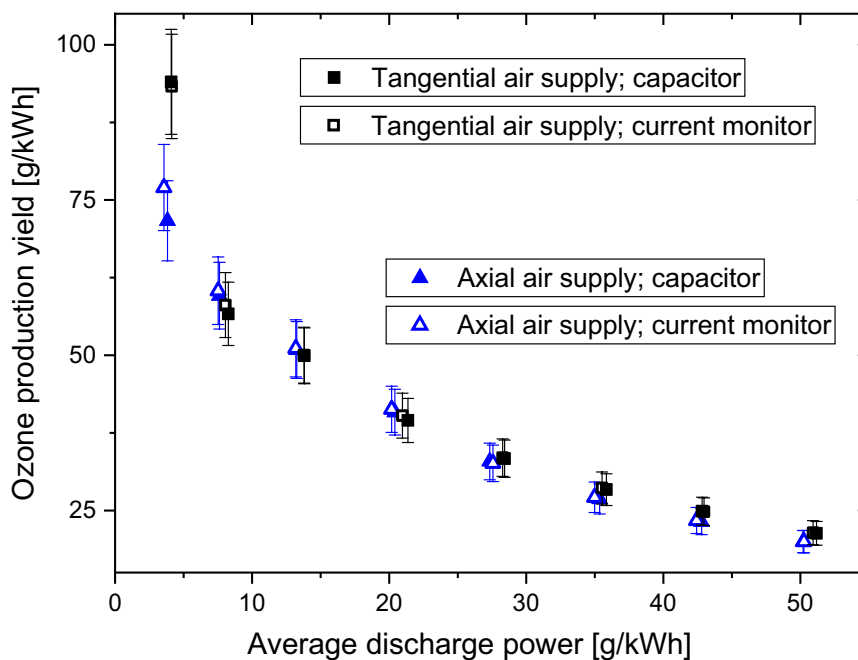
A dependence of ozone production yield as a function of average discharge power calculated from the current monitor signal or voltage drop on the measuring capacitor for the discharge with tangential or axial air supply to the discharge chamber is shown in Fig. 9. To have reliable values of the yield and to eliminate the spread of the discharge power values just after the onset of the discharge, we present the graph of the ozone production yield based on the relatively stable values of the discharge power from the 3rd to the 10th measuring periods shown in Fig. 5, only. The relative uncertainty of the yield, based on the uncertainties of ozone concentration and power measurements, was evaluated as ~9%.

From this figure can be concluded that the ozone production yield calculated from data obtained by the Pearson current monitor or measuring capacitor for tangential air supply and the smallest discharge power is ~93 g/kWh and the highest investigated power is ~21 g/kWh. The corresponding values of the yield for axial air supply mode are ~75 g/kWh and ~19 g/kWh, respectively.

Fig. 9 Ozone production yield as a function of the average discharge power obtained through the measuring capacitor or a current monitor for both tangential or axial air supply modes

Discussion

The change in the production of ozone generated by the SDBD in the cylindrical configuration for axial and tangential air supply mode could be at least qualitatively explained by the combination of different effects. Among them, it should be, first of all, mentioned the change of the streamlines orientation with respect to the microdischarges. Speaking generally, the SDBD consists of a set of parallel microdischarge channels, which propagate perpendicular to the active electrode [29]. According to [30], the ozone generation in dielectric barrier discharge takes place mainly in microdischarges. The properties of microdischarges depend on many factors, e.g., on the pressure, gap spacing, dielectric barrier, or on the flow of the gas.

The typical microdischarge length (depending on the polarity surface electrode) is of the order of a millimeter, and its radius is approximately 50–200 μm [29, 31].

The residence time is taken as a ratio of the dimensions of the region in which the ozone generation occurs and air velocity. The longer the residence time, the probability of dissociation of oxygen molecules into atomic oxygen increases, and consequently, the ozone generation also increases. In electronegative gases such as air, the main charge carrying species in the discharge are the negative ions. The mass of negative ions is approximately the same as the mass of neutral particles, the motion of which we affect via different modes of air supply into the discharge volume. Thus, through the collisions of neutral particles, mostly with the negative ions, the properties of the microdischarges are affected. We, therefore, have a reverse situation to the surface nonthermal plasma actuators in which the electric wind is induced by collisions between ions and neutral particles and due to the streamer propagation [32].

We investigated the SDBD in a cylindrical configuration with the active electrode in the form of interconnected rings (dark regions in the Fig. 3) on the outer surface of the inner glass tube. As it is seen from this figure, the microdischarge channels, perpendicular to the ring electrode, were oriented axially. To affect the discharge ozone production, we attempted to change microdischarge properties by varying orientation the airflow streamlines concerning to the microdischarges using axial or tangential air supply into the discharge chamber. Consequently, the relative change of radius of the microdicharge channels for the case of axial airflow supply should be different than for tangential airflow supply, which results in different discharge ozone production.

To support these assumptions, we performed the modeling of airflow streamlines in the discharge volume for tangential or axial air supply into the discharge volume. The modeling was performed using a commercial software COMSOL. The streamline patterns for the axial air supply into the discharge chamber are shown in Fig. 10. In this case, the nozzles in input and output caps were situated along the same lines. From this figure, it is seen that the streamlines are axial; they are therefore aligned along the microdischarge channels.

The streamline patterns for tangential air supply into the discharge chamber are shown in Fig. 11. From this figure it is seen that in the side of the discharge chamber in which the air is supplied, there is induced vortex flow. Therefore, the streamlines are inclined concerning the length of the microdischarges. It can be therefore said that in this region, air velocity has a component, which is perpendicular to the microdischarge channels; therefore, their properties are affected. These changes of the microdischarges properties influence the plasmachemical processes and consequently discharge ozone production.

Another quantity that affects ozone concentration generated by the discharge is the temperature of the air in the discharge chamber [11, 33]. As is seen in Fig. 7 in the
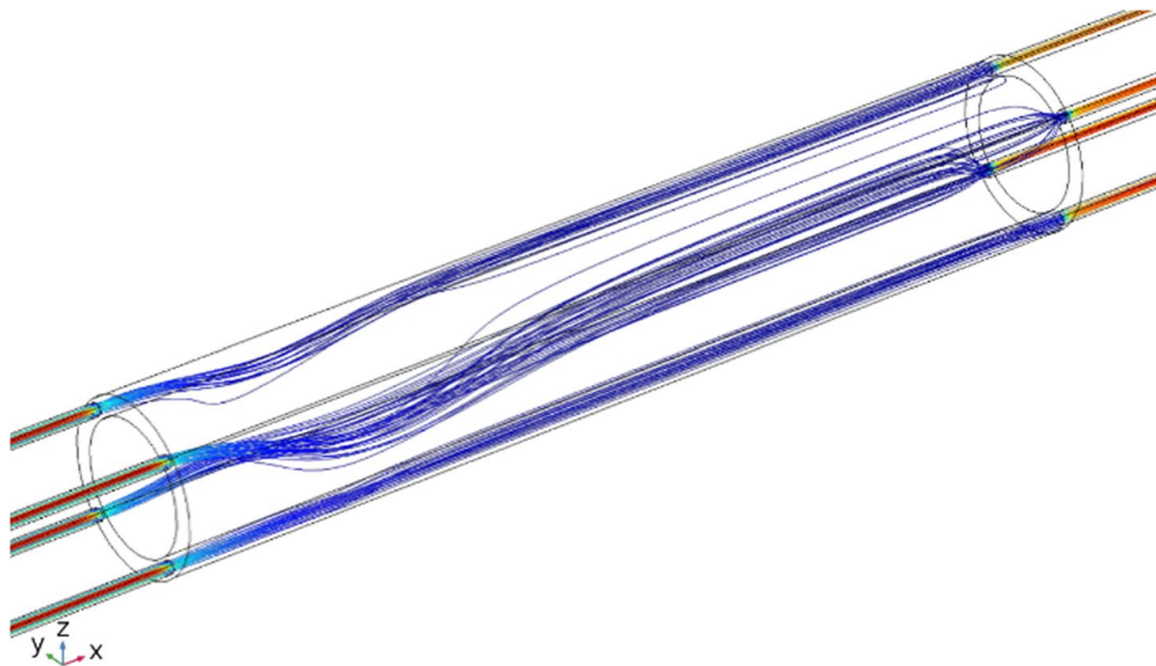
Fig. 10 The streamlines patterns for the axial air supply into the discharge chamber. $Q_{air} = 6$ slm
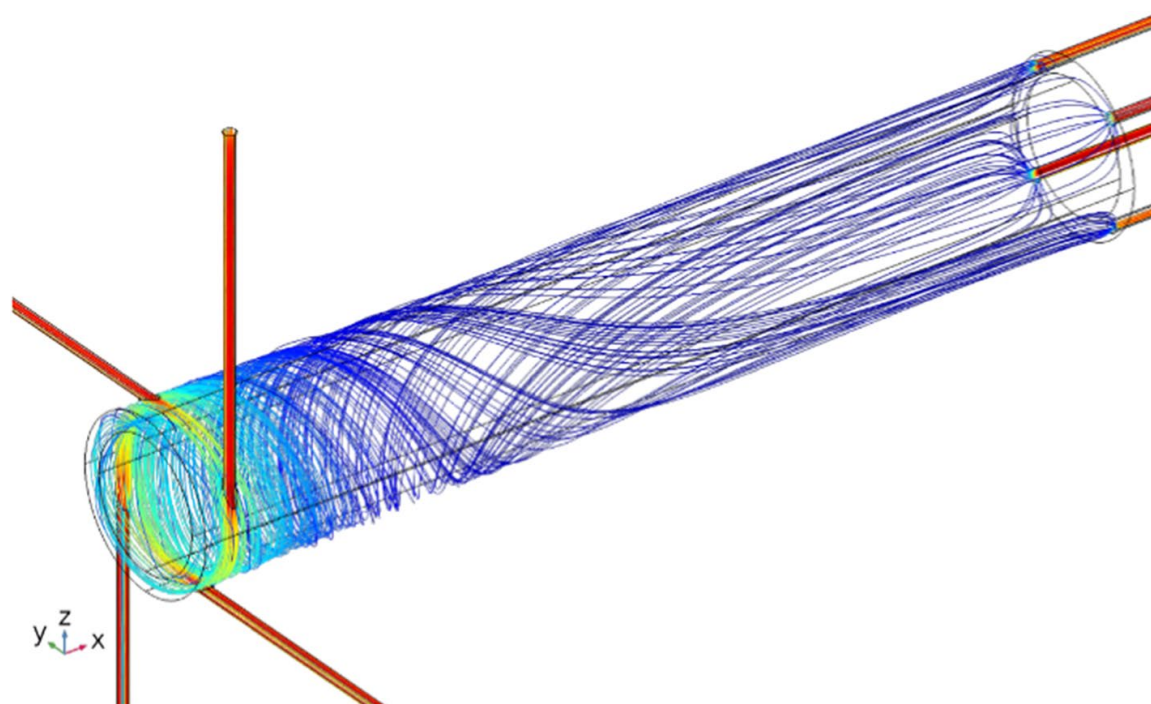
Fig. 11 The streamlines patterns for tangential air supply into the discharge chamber. $Q_{air} = 6$ slm

case of tangential air supply, the temperature of the air at the output from the discharge chamber is slightly higher than for axial air supply. This result can be attributed to the fact that in the case of tangential air supply the path and consequently the time in which the air is heated in the discharge volume is increased due to the vortex airflow. However, this small difference in temperature of the air at the output from the discharge chamber (about 1 °C for the highest discharge power) could not be considered as responsible for

the difference in ozone concentration produced by the discharge with the tangential or axial air supply mode. The outcomes from this study, therefore, justify and extend our results presented in [24] for the planar SDBD with parallel or perpendicular airflow orientation with respect to the strip electrode. They are also consistent with the observations presented in [27, 28].

Both concentrations of ozone produced by the DBD, as well as the ozone production yield, were investigated for various experimental conditions by many authors. The absolute values of these two quantities vary within a broad range because they depend on the way of discharge energizing (sinusoidal, pulse, duty cycle), electrode geometry, the usage of catalysts, UV irradiation, or external fields. In the following Table 1 are shown examples of the ozone production yield from the discharge in air obtained by different authors before and after the variation of selected quantities.

Conclusions

We investigated air supply mode effects on ozone production of surface dielectric barrier discharge in a cylindrical configuration. As long as the active electrode was in the form of interconnected rings, by varying air supply from tangential to axial, we changed the orientation of the airflow with respect to the microdischarges, which affected ozone generation. We also paid attention to the correlation between ozone concentration, discharge power, and temperature of the air at the output of the discharge chamber as a function of the duration of the experiment for both tangential and axial air supply modes.

Our findings can be summarized as follow:

- When the discharge is ignited, the ozone concentration is, depending on the power, at first, sharply increased, reaches the peak value, it is decreased, and after a certain time, it becomes stabilized. Thus, for the highest investigated discharge power, the ozone concentration is stabilized approximately 70 s after the discharge ignition
- The ozone concentration depends on the discharge power, and for higher power for the discharge with tangential air supply into the discharge chamber is higher than for axial air supply. This increase in concentration for the highest investigated discharge power reaches ∼9%.
- The ozone production yield for tangential air supply is slightly higher than for axial air supply mode at high discharge powers.

Finally, it should be mentioned, that for SDBD in cylindrical geometry with the ring active electrode, the tangential air supply into the discharge chamber can be combined with other approaches, e.g., a variation of the duty cycle, pulse energizing, optimization of electrode systems, usage of various catalysts or UV irradiation. This combination can contribute to the improvement of the ozone generator's performance. The obtained results, therefore, have a significant application potential, which implies the necessity of further research in this direction.

Table 1 Ozone production yields before and after the variation of selected quantity or application of an agent

Type of the discharge	Working gas	Ozone production yield (g/kWh)	Variated quantity/application of an agent	Yield after application (g/kWh)	References
Surface DBD, planar configuration	Air	90–20	Frequency 1, 5, 10 kHz	No effect	[8]
Multi-hollow SDBD	Synthetic	168	Duty cycle 10–40%	205	[9]
	Air	205	40–100%	200	
Multichannel DBD	Air	66–49	Increase of pressure from 0.10 to 0.14 MPa	77–66	[12]
Surface DBD, planar configuration	Air	52–10	Photocatalyst TiO$_2$	75–10	[15]
Surface DBD, planar configuration	Air	60–53	Airflow perpendicular or parallel to strips	86–61	[24]
Surface DBD, planar configuration	Air	52–32	Frequency 10–5 kHz	Increase by 10%	[33]
Coupled SBD, planar configuration	Air	90–50	Multiple interconnected electrodes	90–80	[34]
Surface DBD, cylindrical configuration	Air	75–19	Change from axial to tangential air input	93–21	Present manuscript

The values of ozone production yield before and after the variation of selected quantity or application of an agent are given for approximately the same specific input energy or discharge power
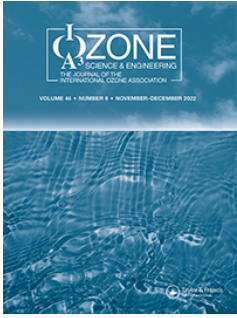
References

1. Brandenburg R (2017) Plasma Sources Sci Technol 26:053001
2. Nassour K, Brahami M, Nemmich S, Hammadi N, Zouzou N, Tilmatine A (2016) Ozone Sci Eng 38:70–76
3. Finan-tu-Dinu EG, Korzec D, Teschke M, Engemann J (2003) Surf Coat Technol 174–175:524–529
4. Xia Y, Bi Z, Qi Z, Ji L, Zhao Y, Chang X, Wang W, Liu D (2018) J Appl Phys 123:083301
5. Williamson JM, Trump DD, Bletzinger P, Ganguly BN (2006) J Phys D Appl Phys 39:4400–4406
6. Yuan D, Ding C, He Y, Wang Z, Kumar S, Zhu Y, Cen K (2017) Plasma Chem Plasma Process 37:1165–1173
7. Wei LS, Pongrac B, Zhang YF, Liang X, Prukner V, Šimek M (2018) Plasma Chem Plasma Process 38:355–364
8. Šimek M, Pekárek S, Prukner V (2012). Plasma Chem Plasma Process. https://doi.org/10.1007/s11090-012-9382-z
9. Homola T, Prukner V, Hoffer P, Simek M (2020) Plasma Sources Sci Technol 29:095014
10. Zhang YF, Wei LS, Liang X, Deng HZ, Šimek M (2018) Plasma Chem Plasma Process 38:1199–1208
11. Kim HY, Kang SK, Kwon HC, Lee HW, Lee JK (2013) Plasma Process Polym 10:686–697
12. Yuan D, Wang Z, Ding C, He Y, Whiddon R, Cen K (2016) J Phys D Appl Phys 49:455203
13. Zhang X, Bok Lee BJ, Im HG, Cha MS (2016) IEEE Trans Plasma Sci 44:2288–2296
14. Kim HH, Teramoto Y, Ogata A, Takagi H, Nanba T (2016) Plasma Chem Plasma Process 36:45–72
15. Pekárek S (2012) J Phys D Appl Phys 45:075201
16. Pekárek S (2018) Plasma Chem Plasma Process 38:1081
17. Lu X, Laroussi M (2005) J Appl Phys 98:023301
18. Yu D, Ye Q, Yang F, Zeng X, Zhao L, Tan D (2013) Plasma Process Polym 10:880–887
19. Cieplak T, Yamabe CH, Ihara S, Satoh S, Pawlat J, Cieplak J, Pollo I (2000) Ozone Sci Eng 22:563–573
20. Masuda S, Akutsu K, Kuroda M, Awatsu Y, Shibuya Y (1988) IEEE Trans Ind Appl 24:223–231
21. Jodzis S (2012) Ozone Sci Eng 34:378–386
22. Peschke P, Goekce S, Leyland P, Ott P (2016) J Phys D Appl Phys 49:025204
23. Yehia A, Mizuno A, Takashima K (2000) J Phys D Appl Phys 33:2807
24. Mikeš J, Pekárek S, Soukup I (2016) J Appl Phys 120:173301
25. Xie S, He Y, Yuan D, Wang Z, Kumar S, Zhu Y, Cen K (2019) Plasma Sci Technol 21:055505
26. Jodzis S, Smolinski T, Sówka P (2011) IEEE Trans Plasma Sci 39:1055–1060
27. Höft H, Becker MM, Kettlitz M (2016) Phys Plasmas 23:033504
28. Xu Y, Guo H, Wang Y, Fan Z, Ren Ch (2020) Plasma Sci Technol 22:055403
29. Gibalov VI, Pietsch GJ (2012) Plasma Sources Sci. Technol. https://doi.org/10.1088/0963-0252/21/2/024010
30. Kogelschatz U (2003) Plasma Chem Plasma Process 23:1–46
31. Fridman A, Chirokov A, Gutsol A (2005) J Phys D Appl Phys 38:R1–R24
32. Moreau E (2000) J Phys D Appl Phys 40:605–636
33. Abdelaziz AA, Ishijima T, Seto T, Osawa N, Wedaa H, Otani Y (2016) Plasma Sources Sci Technol. https://doi.org/10.1088/0963-0252/25/3/035012
34. Malik MA, Schoenbach KH, Richard Heller R (2014) Chem Eng J 256:222–229

A.8 Surface Dielectric Barrier Discharge in a Cylindrical Configuration – Effect of Airflow Orientation to the Microdischarges

Surface Dielectric Barrier Discharge in a Cylindrical Configuration – Effect of Airflow Orientation to the Microdischarges

J. Mikeš, S. Pekárek & O. Hanuš

Surface Dielectric Barrier Discharge in a Cylindrical Configuration – Effect of Airflow Orientation to the Microdischarges

J. Mikeš 📵, S. Pekárek 📵, and O. Hanuš 📵

Faculty of Electrical Engineering, Czech Technical University in Prague, Prague, Czech Republic

ABSTRACT

This paper is devoted to studying the effect of airflow orientation on the microdischarges of the surface dielectric barrier discharge in cylindrical configuration through varying air input into the discharge chamber, the number of input nozzles, and the geometry of the active electrode. The air is supplied into the discharge chamber tangentially, radially, or axially through one or four input nozzles. Air input into the discharge chamber and the number of input nozzles determine the airflow regime. We used two active electrode geometries that are the axial strips or azimuthal rings. The change of active electrode geometry from rings to strips affects the orientation of microdischarges with respect to the airflow. For the discharge, the variation of air inputs and the number of input nozzles influences the flow regime in the discharge chamber, which, together with the active electrode geometry, affects the temperature field distribution in the chamber. These factors play an important role in plasmachemical processes leading to the discharge generation of various species, such as ozone. It is found that, for the maximum effect of airflow on discharge ozone generation, the streamlines should be uniformly distributed in the discharge chamber and predominantly oriented perpendicular to the majority of microdischarges.

Introduction

The surface dielectric barrier discharge in cylindrical configuration is an efficient tool for ozone and other active particles generated from air for sanitary and disinfecting purposes, in medicine, the food-processing industry or for surface-treatment (Choudhury et al. 2020; Draou et al. 2018; Machala, Hensel, and Akishev 2012; Volkoff et al. 2020; Yousfi et al. 2011). The ozone generators based on this type of the discharge are operating in the range of powers from watts to several dozens of kilowatts. To obtain high efficiency of ozone generation it is necessary to have a deep knowledge of not only the discharge physics but also to understand a complex of technological aspects of ozone generator devices associated with the properties of the materials used, geometry of the discharge chamber, type, and properties of the feeding gas, flow of the working gas in the discharge volume, discharge energizing etc.

There exist numerous studies devoted to the physics of the dielectric barrier discharge as well as the effects of the above-mentioned quantities on the discharge performance (Brandenburg 2017; Fridman 2008; Gibalov and Pietsch 2000, 2012; Kogelschatz 2003; Wei, Liang, and Zhang 2018a). For a wide range of these quantities, we focused in this study on the role of airflow and its orientation with respect to the microdischarges on ozone generation and

electrical parameters of the surface dielectric barrier discharge in cylindrical configuration with two different geometries of the active electrode. The effect of the gas flow direction on ozone generation by concentric actuator has been investigated in (Jodzis, Smolinski, and Sowka 2011). It has been shown that the concentration of ozone generated from oxygen by concentric actuator slightly depends on the oxygen flow direction.

A detailed study of the interaction between high-speed gas flows and surface dielectric barrier discharges is presented in (Pavón et al. 2007). It is demonstrated that the airflow has a significant influence on the plasma characteristics: the glow component is reduced, the discharge becomes more filamentary and most importantly, the light emission duration from individual microdischarges is reduced by more than a factor of 10 at high-flow velocities. Besides in Pavón (2008) is shown, for this discharge, the voltage at which the plasma ignites uniformly over the whole electrode surface depends on the orientation of the flow with respect to the conducting strips electrode. When the flow is parallel to the strips, this voltage at 1 kHz driving voltage frequency and Mach number M = 0.7 doubles in comparison with the discharge without airflow, whereas it is only multiplied by 1.4 if the flow is perpendicular to the strips.

CONTACT J. Mikeš ✉ mikes.jan@fel.cvut.cz 🖳 Faculty of Electrical Engineering, Czech Technical University in Prague, Technická 2, 166 27 Prague 6, Prague, Czech Republic

The effect of the flow orientation concerning the electrode symmetry on the diameter of the discharge channel for the pulsed dielectric barrier discharges was investigated in (Höft, Becker, and Kettlitz 2016). It is found that this diameter changes due to the change of charge density owing to the convective transport under the action of airflow.

The flow stabilization of the discharges is discussed in (Bruggeman, Iza, and Brandenburg 2017). It is stated that varying the gas flow rate does not only control heat removal but also affect mixing of gases and residence time of species, which affects the overall performance of the plasma source. The investigation of airflow effects on the dielectric barrier discharge with single/double discharge channel arrangement was performed in (Fan et al. 2018). The transition from a filamentary discharge to a diffuse discharge is observed under certain airflow conditions, and the discharge channels move with the airflow with a movement velocity less than the corresponding airflow velocity.

Ozone production utilizing surface dielectric barrier discharge in planar configuration was experimentally studied for different flow patterns considering the influences of transversal flow, lateral flow, and different lateral flow positions in (Xie et al. 2019). The attention was devoted to the effects of gas flow pattern on the generation of ozone in surface dielectric barrier discharge. The results show that the flow patterns have a remarkable impact on the ozone yield by affecting the uniformity and turbulence of gas flow.

The effect of gas flow design on the performance of a dielectric barrier discharge reactor for dry reforming of methane was investigated in (Uytdenhouwen et al. 2021). A new multi-inlet/outlet parallel plate DBD reactor was designed that allows to quickly change the geometry of the reaction volume, in order to accommodate a multitude of different flow and mixing patterns. It was shown that, besides the choice of the main gas, the direction of gas flow largely affects the conversion and energy cost, while the gas inlet position during separate addition only influences the product distribution.

An important role in surface DBD ozone generation is played by the number of the microdischarges generated in the discharge volume. The effect of the number density of plasma channels and lower voltage for the same specific input energy on ozone synthesis from air and oxygen was explored in (Malik and Hughes 2016). It was found that the number of plasma channels and energy per pulse increased in direct proportion to the increase in the effective length of the high voltage electrode.

An integral part of almost each paper dealing with the dielectric barrier discharge is a section dealing with the electrical parameters of the discharge. Thus, the equivalent circuit approach for the electrical diagnostics of dielectric barrier discharges is presented in (Pipa and Brandenburg 2019). This contribution presents the main stages of the development of electrical diagnostics of DBDs, which are based on lumped electrical elements.

The effect of airflow orientation with respect to the strips active electrode on the concentration of ozone and nitrogen dioxide produced by the planar surface dielectric barrier discharge was investigated in (Mikeš, Pekárek, and Soukup 2016). It was found that in the investigated range of discharge power, the ozone, as well nitrogen oxide, concentrations increase when airflow is oriented in parallel with respect to the strips active electrode. A 3D numerical model describing ion trajectories and airflow patterns has also been developed.

The air supply mode effects on ozone production from surface dielectric barrier discharge in a cylindrical configuration with the active electrode in the form of interconnected rings with tangential or axial input of air into the discharge chamber were studied in (Pekárek et al. 2021). The attention was paid to the correlation between ozone concentration, discharge power, and temperature of the air at the output of the discharge chamber as a function of the duration of the experiment for both tangential and axial air supply modes. It was found that the ozone production yield for tangential air supply is slightly higher than for axial air supply mode at high discharge powers.

However, many commercial ozonizers use only one air input – radial or axial. We, therefore, performed a detailed investigation of various air input effects on ozone synthesis in surface dielectric barrier discharge in a cylindrical configuration. We used three different air inputs – radial, axial, or tangential. We also investigated the role of changing the number of air input nozzles in the discharge volume from 1 to 4. Besides, we also altered the geometry of the active electrode of the discharge from the rings to the strips, and finally, the experiments were performed with two different temperatures of cooling water and in the thermobox, 10 °C, and 20 °C. Therefore, the results obtained in this study substantially extend our previous research and fully justify already received results (Mikeš, Pekárek, and Soukup 2016; Pekárek et al. 2021).

Experimental arrangement

The experimental arrangement used in this study is shown in Figure 1. It consists of a cylindrical discharge chamber, the air source accompanied with the measurement of air's temperature, pressure, and humidity, power supply system with the equipment of electrical parameters of the discharge measurements, ozone
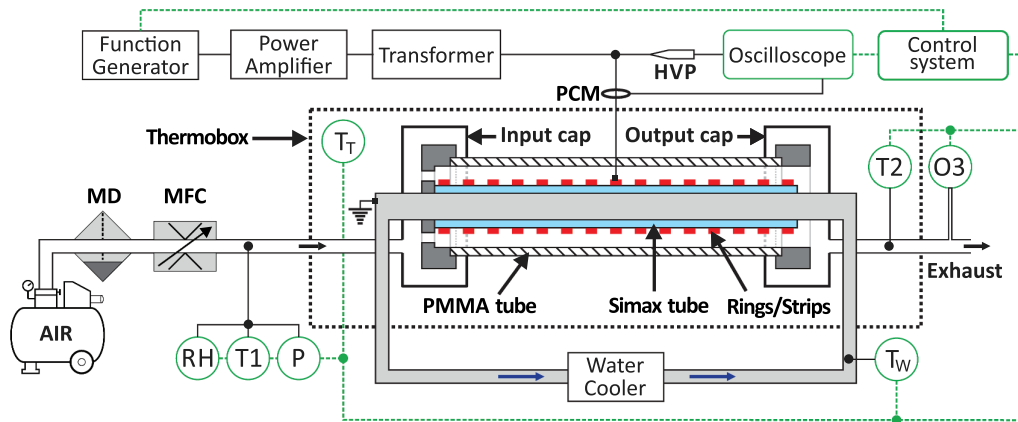
Figure 1. Experimental arrangement.

analyzer, cooling system with the temperature stabilization box, and a control system. This figure shows the arrangement with the rings active electrode and the inner part of the input cap with four axial nozzles. This experimental arrangement is a modification of the system, which is described in our previous paper (Pekárek et al. 2021).

The cylindrical discharge chamber consists of three coaxial tubes. The outer tube of an outer/inner diameter 30/24 mm, respectively, and 172 mm was made from polymethyl methacrylate – PMMA. The Simax glass inner tube with an outer diameter of 20 mm and an inner diameter of 17.4 mm, had a length of 150 mm. The discharge is produced in the annular space between these two tubes. Finally, a brass tube of an inner diameter of 13.8 mm was closely inserted into the Simax tube.

The input of air into the discharge volume is through the input cap situated on the discharge chamber's left side. The output of air with ozone and other discharge products is through an output cap on the other side of the chamber.

The input cap consisted of the outer and inner parts. The outer part of this cap encloses the inner part so that there is a space between these two parts from which the air is supplied to the individual nozzles. In this way, the pressure of air in this region is constant. The inner parts, which were inserted into the cap's outer part, were different to vary the airflow orientation concerning the active electrode. The second difference consisted in the number of nozzles to the discharge volume. We used one or four nozzles, each with a diameter of 2 mm. The

nozzles were oriented so that the radial, axial, or tangential flow in the discharge chamber was created. The experiments were therefore performed with six different inner parts of the input cap.

Throughout this paper, for the strips and the rings, active electrode following system is used to describe the number of input nozzles and way of air input through the inner parts of the input cap to the discharge chamber. The number (1 or 4) at the beginning of the acronym expresses the number of nozzles, and capital letters A, R, or T are used for the way of air input. Thus, the letter A is for axial air input, letter T expresses tangential air input, and finally, letter R is used for radial input, W means without airflow. As an example, the acronym 4 T is used for four input nozzles oriented tangentially. As an illustration, the inner parts of the input cap with four nozzles (a, b, c) and the inner part of the output cap (d) are shown in Figure 2. These components were printed from the polylactic acid on – PLA a 3D printer, and their geometry was designed in the OpenSCAD program.

The output cap also consisted of two parts. The outer part of this cap was the same as the outer part of the input cap. However, the output of air from the discharge space is directed to the annular volume and finally to the exhaust. The outer parts of both caps were made from polyamide. The outer parts of the input and the output cap can be seen on the discharge chamber's general view, shown in Figure 3.

The electrode system of the surface dielectric barrier discharge consists of the active and grounded electrodes separated by the Simax glass tube. The active electrode,
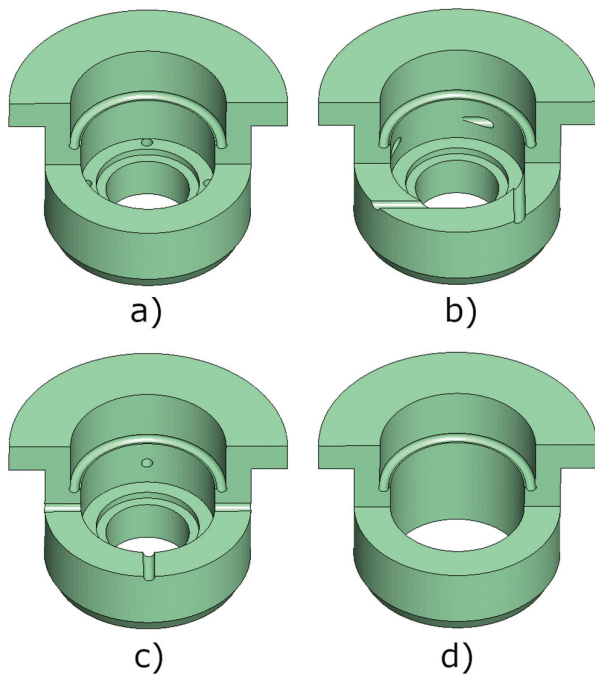
Figure 2. The inner parts of input/output caps. a) Inputs – 4A; b) Inputs – 4 T; c) Inputs – 4 R; d) Air output.

made from 0.06 mm thick copper foil, was glued on this Simax tube's outer side. As a grounded electrode, which was simultaneously used for cooling, a brass tube was used. The experiments were performed with two geometries of the active electrode.

- The electrode was made from 30 rings of 1 mm width and 3 mm gap between the rings. The rings were connected in parallel (Figure 4(a)).
- The electrode consisted of 16 strips connected on both ends by a ring of the same dimensions as in the preceding case (Figure 4(b)).

In Figure 1, it is shown that the discharge chamber has an active electrode in the form of rings. Considering the Simax glass's relative permittivity, at temperature
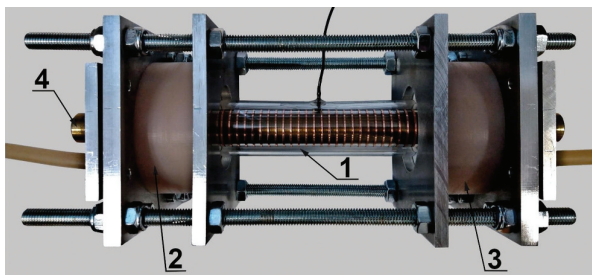
Figure 3. General view of the discharge chamber. 1 – Discharge chamber; 2 – Air input cap; 3 – Air output cap; 4 – Brass tube.
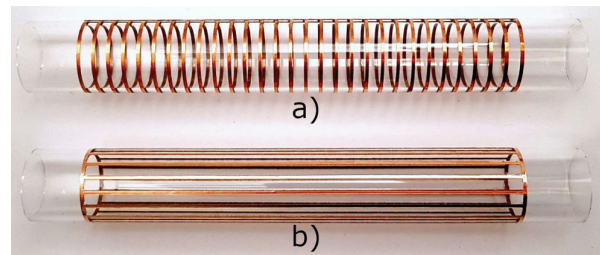
Figure 4. Geometries of the active electrode. a) Rings; b) Strips.

20 °C and frequency 1 MHz of 4.6, the electrode system's capacitance for the frequency 10 kHz was 104.8 pF for the rings active electrode and 151.1 pF for the strips active electrode.

To keep the temperature of the discharge chamber constant, we used two methods. Firstly, the cooling water flowing through the central brass tube was supplied to the thermostat WCR P12. The temperature of the water (TW) was in this way controlled. Secondly, the discharge chamber was placed into the cooled thermo-box POL-EKO-APARATURA, offering the possibility of regulating the temperature from +3 to +70 °C with accuracy ±0.1 °C. The experiments were performed with the cooling water TW temperature, and the temperature in the thermobox TT adjusted to 10 °C or 20 °C.

This air is supplied from an oil-free compressor through a membrane dryer (MD) and mass flow controller (MFC). The relative humidity RH, temperature T1, and pressure P of air before the discharge chamber input (see Figure 1) were monitored. We also measured the temperature T2 of air at the output from the discharge chamber. To monitor the relative humidity, we used a TH3 sensor. A digital manometer detected the pressure Siemens Sitrans P. Finally, the air temperature was measured by the optical fiber thermometer Neoptix. A BMT 964 ozone analyzer measured the concentration of generated ozone at the output from the discharge chamber.

The power supply system consisted of the function generator KEYSIGHT 33500B, a wideband AC power amplifier AL-1400-HF-A (1000 W, frequency response 5 Hz to 800 kHz), and a high-frequency high-voltage transformer AL-T1000.7 (1000 W, frequency response 3.5 to 11 kHz).

The discharge's electrical parameters were recorded by a digital four-channel oscilloscope Tektronix MDO4054B-3 (3 GHz, 2.5 GS/s). The discharge voltage signal $V_j(t)$, measured by a high-voltage probe Pintek HVP-28HF (division ratio 1000/1, frequency up to 200 MHz), was sampled and recorded on the first channel of this oscilloscope. The discharge current,

monitored by a Pearson current monitor (PCM – model 2877, bandwidth up to 200 MHz), was recorded on this oscilloscope's second channel. The discharge power was calculated from the following equation:

$$P = \frac{1}{N} \cdot \sum_{j=1}^{N} V_j(t) \cdot I_j(t) \cdot dt \qquad [1]$$

In this equation N denotes the number of samples per period, and $V_j(t)$ and $I_j(t)$ are voltage and current signals, respectively.

To perform the experiments, we developed a control system. The measuring instruments were connected using their voltage outputs (0–10 V) or through current loops (0/4–20 mA). Individual measurements consisted of predefined autonomous steps. The first step was to check the system's integrity and the setup of all the measuring chain elements. The following step consisted in the initiation of measurements by activating the output of the function generator, corresponding to the amplitude of the discharge voltage of 3320 V. This voltage was kept constant for 22 minutes during which non-electric quantities (temperature, pressure, and humidity of air together with ozone concentration) were recorded in two seconds intervals, while electric signals $V_j(t)$, and $I_j(t)$, were saved each 2 minutes. For one minute the function generator was switched off in the following step so that ozone from the ozone monitor and the discharge chamber was removed. In the next step, the discharge voltage was increased so that the voltage interval between initial voltage 3320 and maximum voltage 6240 V was divided into ten equal steps. For this voltage, the measurements of all the quantities mentioned above were repeated. This procedure continued until the discharge voltage reached the maximum value of 6240 V. The time interval of 22 minutes was chosen to record both ozone concentration during the transition process after switching on the discharge and its stable value.

The photos of the discharge with and without airflow and with the strips and rings active electrode are shown in Figure 5.

The fundamental conclusion taken from these photos is that depending on the active electrode's geometry, the orientation of the microdischarges concerning the axis of the cylindrical discharge tube changes. As long as the active electrode in the first case is in the form of axial strips (a), the microdischarges are oriented azimuthally. In the second case (b), the active electrode is in the form of rings so that the microdischarges are oriented axially.
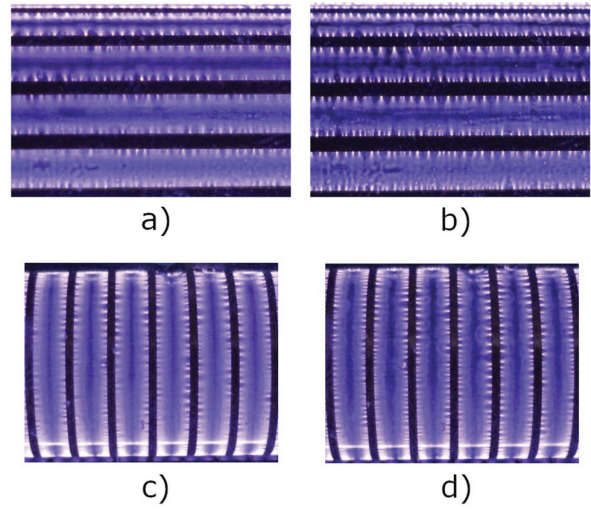
Figure 5. The discharge – a) with the strips electrode without airflow, b) with the strips electrode with airflow, c) with the rings active electrode with airflow, d) with the rings active electrode without airflow. The airflow through the discharge chamber 6 slm and effective voltage 3860 V.

Results

In this paper, we studied the effect of airflow orientation concerning the microdischarges, the impact of air input nozzle number into the discharge chamber, and the effect of the active electrode geometry on ozone production and electrical parameters of the surface dielectric barrier discharge in a cylindrical configuration. We tested radial, axial, or tangential air inputs through one or four nozzles into the discharge chamber. We used the active electrode in the form of strips or rings. Both numerical modeling and the experiments were performed with a constant airflow of 6 slm through the discharge chamber.

Numerical modeling of the flow

To have a deeper insight into the streamlines patterns, we performed numerical modeling of the flow in the discharge chamber for radial, axial, and tangential air inputs through one or four nozzles. It should be pointed out that the output from the discharge chamber was the same for all these cases. The models were built in the COMSOL environment. We considered air to behave as an incompressible Newtonian fluid, i.e., its flow being governed by the following Navier–Stokes equations:

$$\overrightarrow{V} = 0 \qquad [2]$$

$$\rho \frac{\partial \overrightarrow{V}}{\partial t} + \rho \overrightarrow{V} - \mu_{air} \ \overrightarrow{V} = - \ P \qquad [3]$$

In this equation $\overrightarrow{V} : \Omega_{air} \times (0, T) \to R^3$ denotes air velocity field, $P : \Omega_{air} \times (0, T) \to R$ denotes air pressure, $\rho = 1.225 \ kgm^{-3}$ stands for air density, and $\mu_{air} = 1.886 \times 10^{-5} \ kgm^{-1}s^{-1}$ expresses air viscosity. The initial and boundary conditions are assumed to be as follows:

$$\overrightarrow{V}(x, 0) = 0 \ in \ \Omega_{air} \qquad [4]$$

$$\overrightarrow{V}(x, t) = 0 \ on \ \Gamma_{walls} \times (0, T) \qquad [5]$$

$$\overrightarrow{V}(x, t) = \overrightarrow{V}_{in}(x, t) \ on \ \Gamma_{in} \times (0, T) \qquad [6]$$

$$\frac{\partial \overrightarrow{V}}{\partial n}(x, t) = 0 \ on \ \Gamma_{out} \times (0, T) \qquad [7]$$

where $\overrightarrow{V}_{in}(x, t) = 31.831 \ ms^{-1} \ in \ \Gamma_{in} \times (0, T)$ is the input velocity of air. For demonstration purposes, we present in each of the following figures 50 streamlines.

One air input nozzle

The streamline patterns for one air input nozzle oriented axially, radially, and tangentially are shown in Figure 6. Besides, the streamlines the bar-graphs of the airflow velocities are also presented.

Figure 6(a) shows that for axial air supply into the discharge chamber, the flow looks like a "beam" filling a relatively small part of the discharge chamber volume. Figure 6(b) shows the streamlines for radial air input. In this case, we can see that the streamlines occupy a more important part of the discharge chamber, and in more than half of its length, they are oriented axially. This type of air input is the most frequently used in commercial ozone generators. Finally, Figure 6(c) is for tangential input of air. This figure shows that approximately in the first third of the discharge chamber length, the vortex flow is created. This vortex along the discharge chamber's length gradually extinguishes so that in the right part of the discharge chamber, the axial airflow is prevailing.
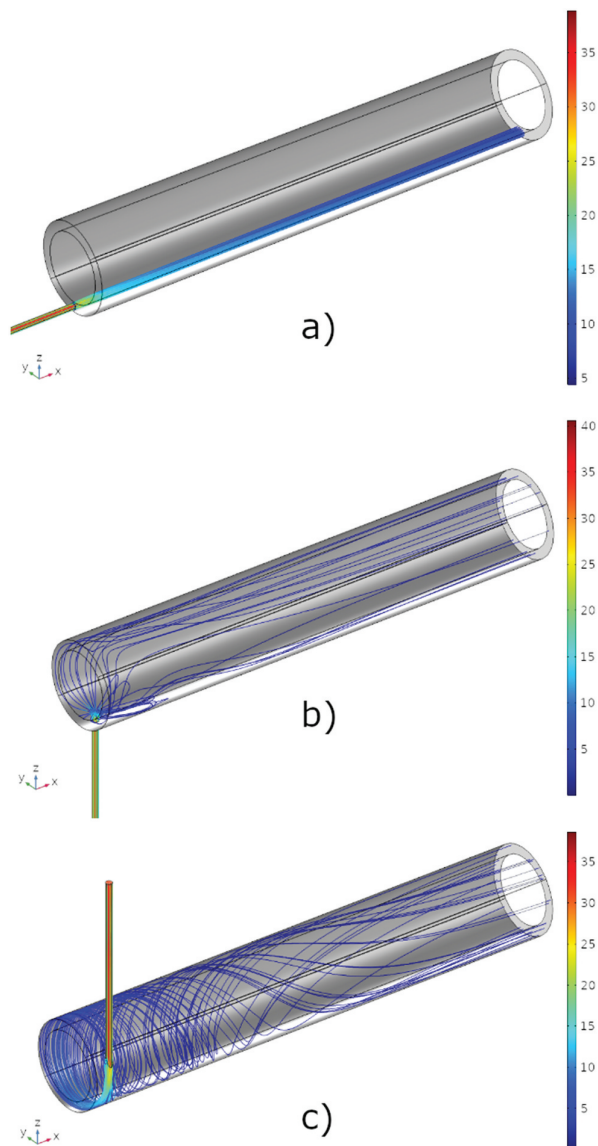
Four air input nozzles

In Figure 7, the results of numerical modeling for four air input nozzles oriented axially, radially, and tangentially are shown. As long as the airflow through the discharge chamber for one and four nozzles is the same, the input air velocity for four nozzles is substantially lower than in the case of one air input nozzle.

The first general conclusion from the comparison of the results for one and four input nozzles is that there is a more uniform distribution of the streamlines within the whole discharge chamber than in the case of one input nozzle. The streamlines patterns for axially oriented four input nozzles are shown in Figure 7(a). Due to the interaction of the flows from the neighboring nozzles in the initial part of the discharge chamber, there appears turbulent airflow that gradually changes into a uniform flow, mainly in the second part of the discharge chamber. The results for the radial input of air are shown in Figure 7(b). It is seen that the streamlines are almost uniformly distributed azimuthally as well along the length of the discharge chamber. Finally, Figure 7(c) shows the situation for tangential air input. Similarly, as in the case of one input nozzle, a vortex flow develops approximately in the same part of the discharge chamber length. This can be caused by the fact that the number of nozzles was increased from 1 to 4; however, air input velocity was decreased by the same ratio. From Figures 6 and 7 can be concluded that by the proper choice of air input into the discharge chamber and the suitable choice of input nozzle number, it is possible to distribute working gas in the chamber more uniformly. Simultaneously, it is possible to change the orientation of streamlines from axial to tangential. The streamlines' orientation plays an important role because it influences the properties of microdischarges.

Experiments

During the experiments, the airflow of 6 slm through the discharge chamber was kept constant. The relative humidity of the air was circa 3%. The air temperature at the input into the discharge chamber and the temperature of cooling water, and the temperature in the thermobox were adjusted to 10 °C or 20 °C. The discharge was driven by the sinusoidal voltage of frequency 10 kHz. Our experiments with both geometries of the active electrode and all air inputs were performed with the same discharge chamber. For both active electrode geometries, the condition to keep constant the width of the active electrode and the distance between neighboring strips/rings resulted in the different lengths of the strips and rings active electrode. The number of microdischarge originating from the active electrode increases with the discharge voltage, but it also depends on the active electrode's length (Malik and Hughes 2016). The production of ozone and the electrical parameters of the discharge depend on the number of microdischarges. As long as the lengths of the rings and strips active electrode were different, it is not possible to compare ozone concentration and the electrical parameters of the discharge for the strips and rings active electrodes quantitatively. On the other hand, it is justified to compare
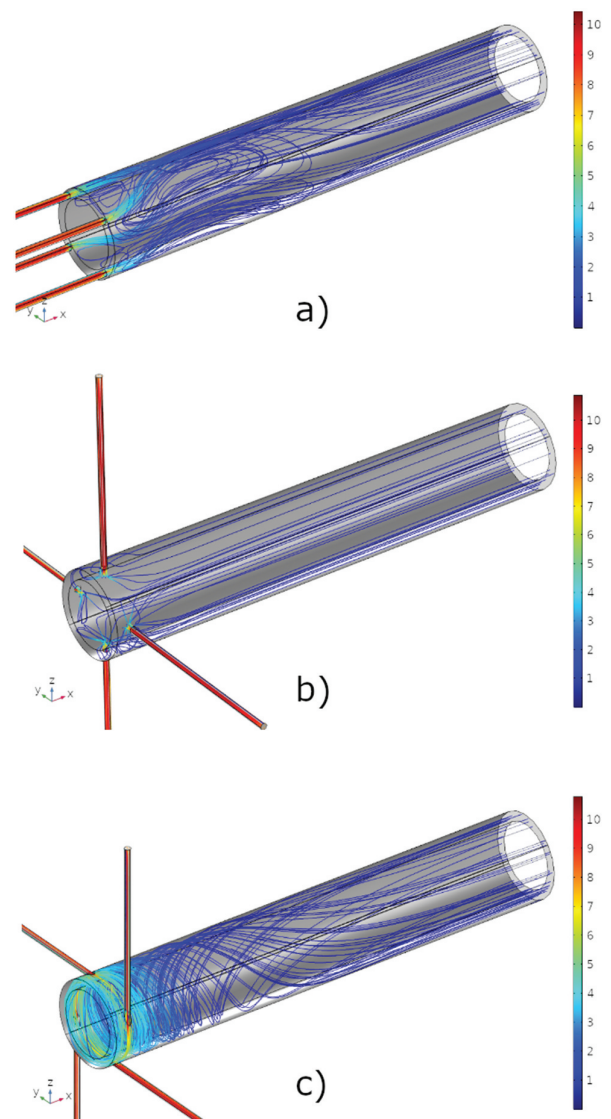
Figure 6. Airflow streamlines in the discharge chamber for one input nozzle. a) Nozzle axial – 1A; b) Nozzle radial – 1 R; c) Nozzle tangential – 1 T.


Figure 7. Airflow streamlines in the discharge chamber for four air inputs nozzles. a) Nozzles axial – 4A; b) Nozzles radial – 4 R; c) Nozzles tangential – 4 T.

quantitatively the effect of the way of air input (tangential, radial, or axial) through one or four nozzles for the strips or rings active electrode separately.

The strips active electrode
This section summarizes the results dealing with the concentration of ozone and electrical parameters of the discharge with the strips active electrode for one or four air input nozzles oriented radially, axially, or tangentially.

One input nozzle. The dependences of ozone concentration as a function of the discharge power for the strips active electrode and one air input nozzle oriented radially, axially, or tangentially are shown in Figure 8. The electrical parameters of the discharge are given in Figures 9–11.

From Figure 8 can be seen that the effect of the way of air supply into the discharge on the concentration of ozone produced by the discharge can be observed for higher discharge powers. The highest ozone concentration of circa 1900 ppm is obtained for radial air input
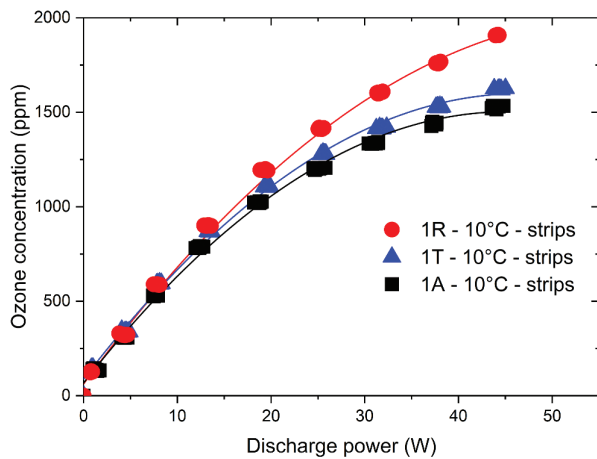
Figure 8. Ozone concentration versus instantaneous discharge power for the strips active electrode and one air input nozzle oriented radially, axially, and tangentially.

Figure 9. Effective values of the current versus discharge voltage for the strips active electrode and one air input nozzle oriented radially, axially, or tangentially.

and discharge power 44.6 W. In this case, the microdischarges are oriented azimuthally. As seen from the streamline patterns in Figure 6(b), most of them are oriented axially; therefore, they are perpendicular to the microdischarges. In this case, the flow strongly affects the microdischarges, which results in the highest ozone concentration. Therefore, these considerations justify our assumption that the airflow orientation plays an important role in discharge ozone production.

Based on the measured instantaneous current signals we calculated effective values of the discharge current, which are shown, as a function of the effective voltage, in Figure 9.

From the dependencies of the effective current versus discharge voltage, see Figure 9, it appears that for a particular voltage, the way of air input has a minimal effect on effective values of current. The dependences of the phase shift and the discharge power on the effective voltage are shown in Figures 10 and 11, respectively.

The measured current $I(t)$ contains the current associated with charge transfer and the displacement current in the gas gap. At the low amplitude of the applied voltage $V(t)$, the discharge is not ignited, and there is no charge transfer. In this situation, the ozone generator behaves like an ideal capacitor. The phase shift between the effective voltage and current signals is 90 degrees (see the first point in Figure 10).

To calculate the phase shift between the voltage and current signals, we used a numerical code implemented as a Matlab function. The measurement is based on Discrete Fourier Transform and Maximum Likelihood estimation of the signals' initial phases (Sedláček 2003; Sedláček and Krumpholc 2005). The method is highly noise resistive. From Figure 10 can be seen that for the low voltage, the phase shift is 90
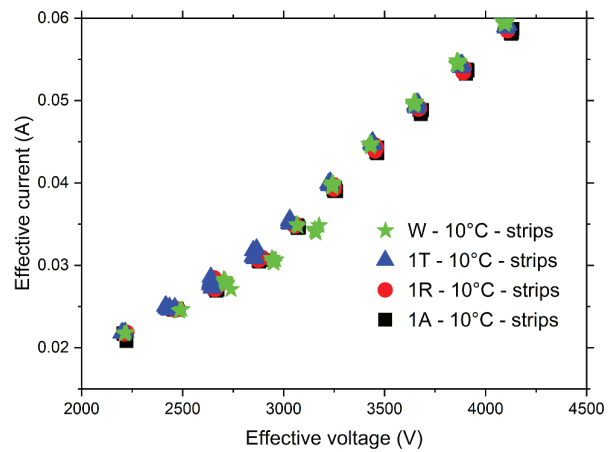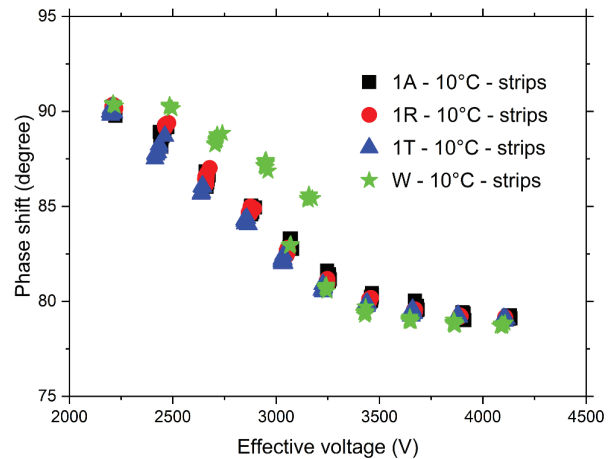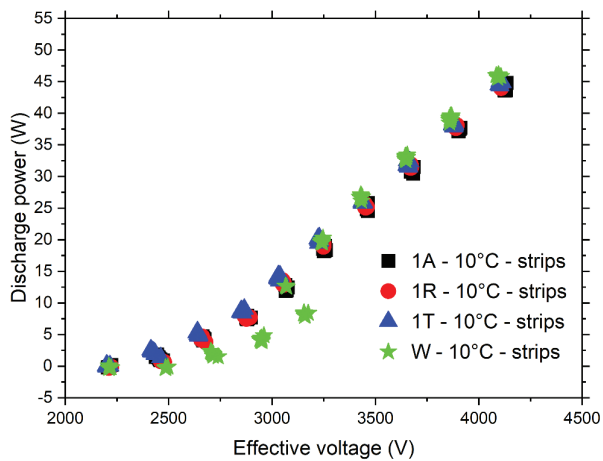

Figure 10. Phase shift versus effective discharge voltage for the strips active electrode and one air input nozzle oriented radially, axially, or tangentially.

degree, which corresponds to the displacement current. With increasing voltage, the phase shift decreases, and for these higher voltages, the way of air supply does not affect it.

The electrical behavior depicted in Figures 9, 10, and 11 has been observed in all configurations of electrodes and input nozzles described below. All conducted experiments show that the way of air supply does not substantially affect the electrical parameters of the discharge, including instantaneous power.

Four input nozzles. The dependence of ozone concentration as a function of discharge power for the strips active electrode and four air input nozzles oriented radially, axially, or tangentially are shown in Figure 12.

Figure 11. Instantaneous discharge power versus effective voltage for the strips active electrode and one air input nozzle oriented radially, axially, or tangentially.

The results dealing with the dependence of ozone concentration on the discharge power presented in this figure can be explained based on the same considerations used to justify the results obtained for one input nozzle (Figure 8). However, to show that the explanation also works for the smallest ozone concentration, we show that, in this figure, the lowest ozone concentrations is also obtained, that is, for tangential air input 4 T. For this input for the discharge power 44.6 W, the concentration of generated ozone is circa 1663 ppm. From the streamlines patterns in Figure 7(c), it can be seen that the vortex flow is created in the left part of the discharge chamber. For the strips active electrode, the microdischarges are oriented azimuthally. Thus, in the discharge chamber volume with vortex flow, the airflow
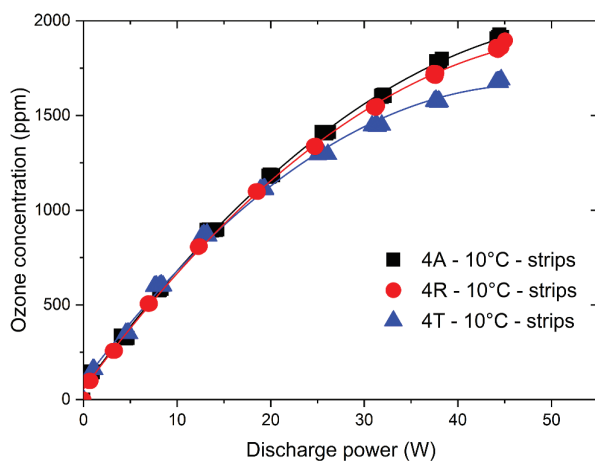
Figure 12. Ozone concentration versus instantaneous discharge power for the strips active electrode and four air input nozzles oriented radially, axially, or tangentially.

streamlines are parallel to the microdischarges. Due to this, the airflow in this region has no substantial effect on the microdischarge channels, which results in a lower concentration of generated ozone.

Increasing the amplitude of the applied voltage $V(t)$ increases the amplitude of the current peaks and the amplitude of the displacement current as well. The current peaks appear in a larger range, and they start earlier regarding the voltage phase. The number of microdischarges slightly increases with the applied voltage but its frequency stays constant (regardless with/without airflow).

Figure 13 shows that due to the airflow there is only a small effect on the shape of the current waveform. For the highest voltage (3870 V) of both variants 4A and 4 T with airflow, microdischarges decrease in the negative half-period.
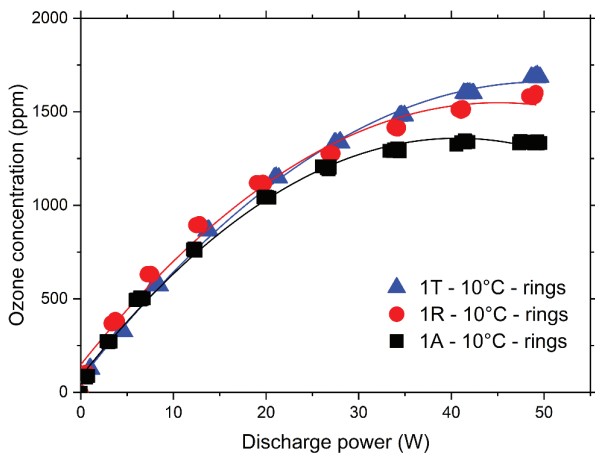
The rings active electrode

This section summarizes the results dealing with the concentration of ozone and electrical parameters of the discharge with the rings active electrode for one or four air input nozzles oriented radially, axially, or tangentially.

One input nozzle. The dependence of ozone concentration versus discharge power for the rings active electrode and one air input nozzle oriented radially, axially, or tangentially is shown in the following Figure 14.

From Figure 14 can be seen that for the discharge with the rings active electrode and one input nozzle, the highest ozone concentration of circa 1670 ppm and discharge power 49 W is obtained for the discharge with tangential air input 1 T. From Figure 5(c,d) it is seen that the microdischarges are oriented axially. Because in the case of 1A air input, the streamlines are oriented axially and do not uniformly fill the whole volume of the discharge chamber (see Figure 6(a)), the effect of this flow on microdischarges on ozone concentration will be minimal. In the case of 1 R air input (see Figure 6(b)), there appear the streamlines with azimuthal components, so that it is reasonable to expect a higher ozone concentration. Finally, for 1 T air input in the left part of the discharge chamber, the vortex flow is created. Consequently, there appear the streamlines, which are perpendicular to the microdischarges. Due to this, there is a maximum effect of the flow on the microdischarges, which results in high ozone concentration. Thus, the maximum concentration of ozone produced by the discharge with the rings active electrode depending on the orientation of the input nozzles, for the discharge power of 49 W, follows this order: 1 T > 1 R > 1A.
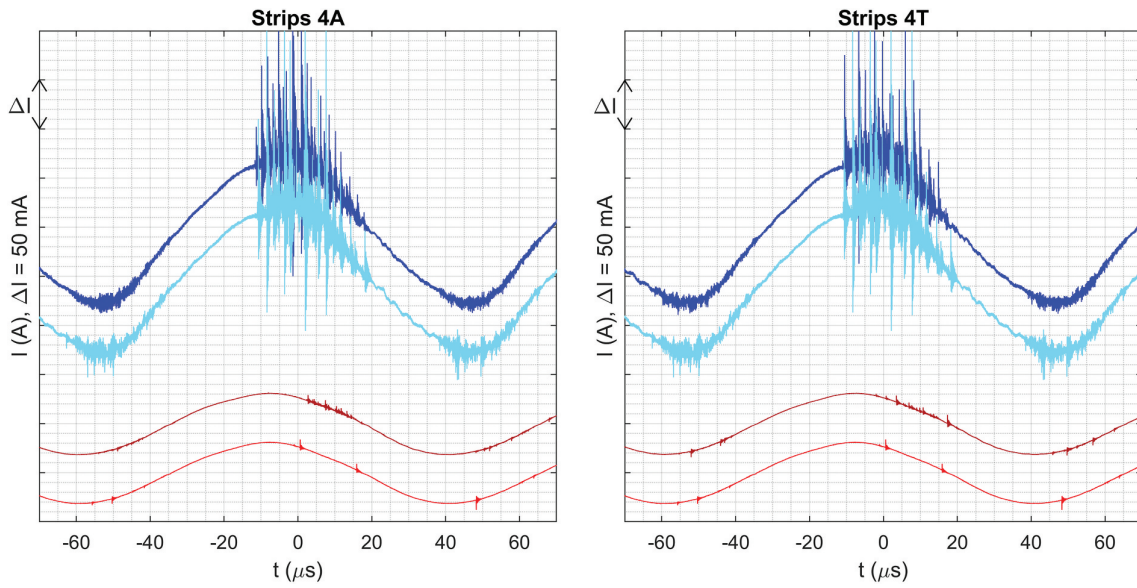
Figure 13. Instantaneous discharge current versus time for variants for the strips electrode a) 4A (highest ozone concentration) and b) 4 T (lowest ozone concentration); red curves for effective voltage 2200 V and blue curves for effective voltage 3870 V; for each pair, the bottom curve is without airflow.

Figure 14. Ozone concentration versus instantaneous discharge power for the rings active electrode and one air input nozzle oriented radially, axially, or tangentially.

Four input nozzles. The dependence of ozone concentration versus instantaneous discharge power for the rings active electrode and four air input nozzles oriented radially, axially, or tangentially is shown in Figure 15.

Similarly, as in the case of four input nozzles for the discharge with the strips active electrode, we show that our explanation also works for the smallest ozone concentration for the discharge with the rings active electrode. From Figure 15 can be seen that for the discharge power of 49 W, the smallest ozone concentration of 1492 ppm was obtained for 4 R air input. From the

comparison of streamlines and microdischarges orientations, the streamlines are primarily parallel to the microdischarges; therefore, the effect of the flow on their properties will be the smallest.

Figure 16 confirms the same results as in Figure 13 that the airflow has only a small effect on the shape of the current waveform. In the case of both variants 4 T and 4 R with airflow there is a decrease in the number of microdischarges in the negative half-period.

Figure 15. Ozone concentration versus instantaneous discharge power for the rings active electrode and four air input nozzles oriented radially, axially, or tangentially.

Figure 16. Instantaneous discharge current versus time for variants for rings electrode a) 4 T (highest ozone concentration) and b) 4 R (lowest ozone concentration); red curves for effective voltage 2200 V and blue curves for effective voltage 3870 V; for each pair, the bottom curve is without airflow.
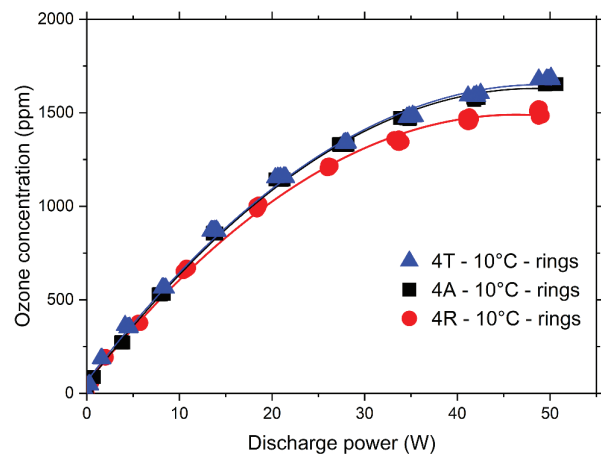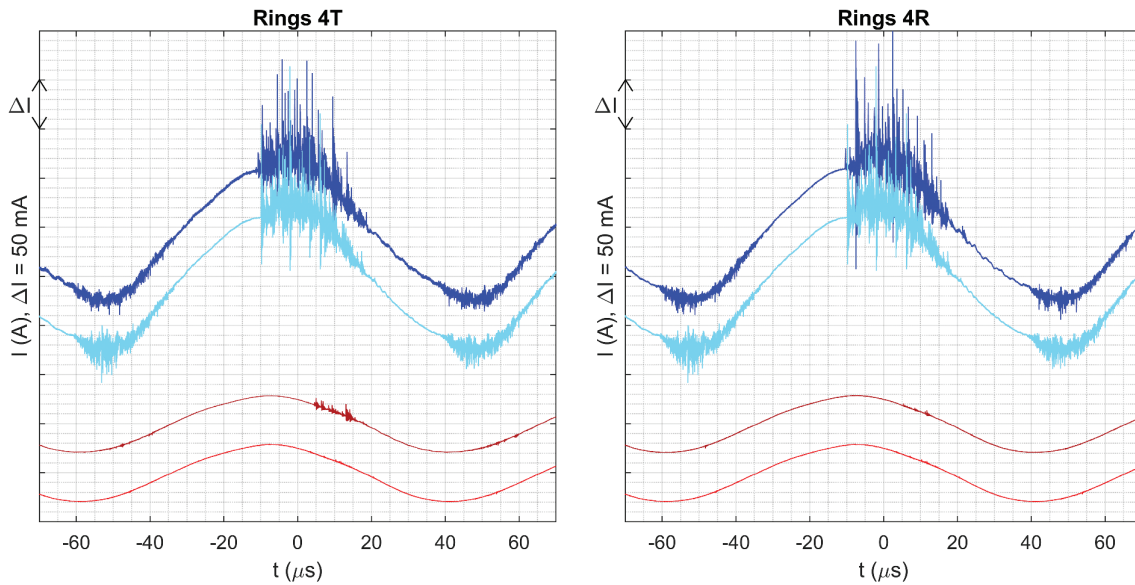
For lower voltages (red current curves in Figures 16 and 13), the airflow helps to increase the number of microdischarges. This can be caused by a better distribution of accumulated charged and high-energy particles (Wei et al. 2018b).

The effect of the number of air input nozzles and temperature on discharge ozone production

From the previous results, it can be concluded that the number of nozzles for radial, tangential or axial air input into the discharge chamber has a strong impact on the discharge ozone production. For the constant airflow, this number determines not only the air velocity at the particular input to the discharge chamber but mainly the uniformity of the streamline distribution. This distribution influences the number of microdischarges that are the most effectively affected by the flow. Besides, it also has an impact on the temperature field distribution in the discharge chamber.

For illustrative purposes, we show ozone concentrations and production yields for the number of air input nozzles and their types (axial, radial, or tangential) giving the most extreme changes of these two quantities. These dependences are given for both the strips and the rings active electrode and for two temperatures, 10 °C or 20 °C, respectively.

The ozone production yield α is defined as a mass of ozone produced by 1 kWh of energy. This quantity is for our experimental conditions calculated from the following expression:

$$\alpha = \frac{0.771 \cdot O_3}{P} \qquad [8]$$

where α is in g/kWh, ozone concentration O_3 is in ppm and discharge power P is in W.

The numerical constant 0.771 in this expression involves the density of ozone as well as all conversion factors of the airflow rate, power, and energy.
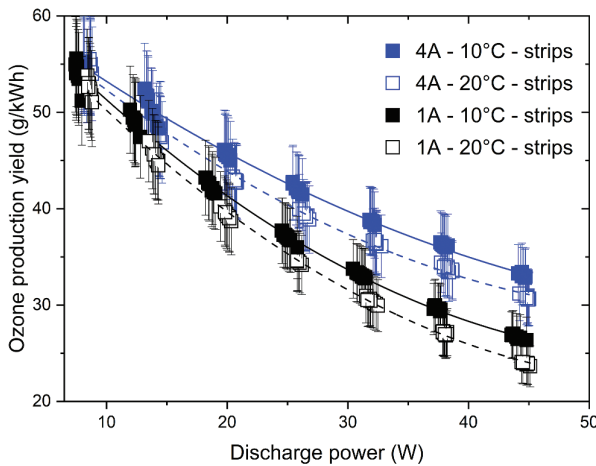
For the strips active electrode, the most marking difference in ozone concentration is for 1A and 4A input nozzles. For this versions of air inputs, the ozone concentration and production yield for two temperatures, 10 °C and 20 °C are shown in Figures 17 and 18.

According to our modeling study for 1A air input (see Figure 6), the flow looks like a "beam" filling a relatively small part of the discharge chamber volume. Because of this, only a relatively small number of microdischarges are effectively influenced by the flow. Thus, for the temperature 10 °C can be from Figure 17 seen that for the discharge power of 44.6 W, the concentration of generated ozone is 1502 ppm.

From Figure 7 can be seen that, in the case of 4A inputs, the streamlines occupy a more significant part of the discharge chamber volume, and turbulent flow in the initial part of the discharge chamber gradually changes into a uniform flow, mainly in the second part of the discharge chamber. As a result of this flow interaction with the microdischarges, the concentration of generated ozone, for the same discharge power as for 1A air input and temperature, is increased to 1920 ppm,
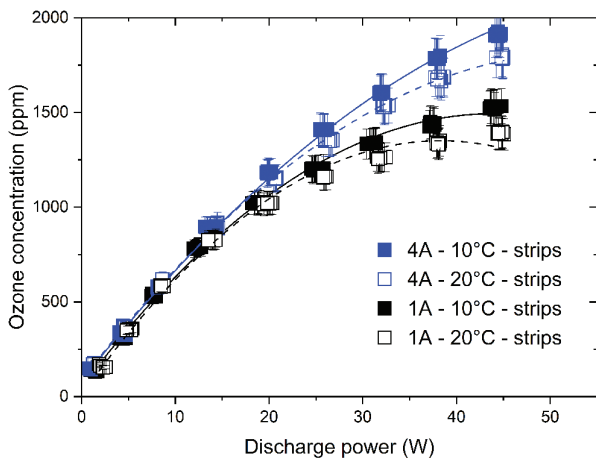
Figure 17. Ozone concentration for the strips active electrode, air inputs 1A and 4A and temperatures 10 °C (full symbols) or 20 °C (empty symbols).

Figure 18. Ozone production yield for the strips active electrode, air inputs 1A and 4A and temperatures 10 °C (full symbols) and 20 °C (empty symbols).

representing the increment of 26%. From this figure, it is also nicely seen, that for higher power, the increase in temperature decreases ozone concentration.

The effect of the change of air input nozzles on ozone production yield for the same version of air inputs 1A and 4A, the same strips active electrode and temperatures 10 °C and 20 °C is shown in Figure 18.

From this, Figure 18 can be seen that for the strips active electrode the increase in the ozone production yield for 10 °C when the air input changes from 1A to 4A for power of 44.6 W represents approximately 27%. Similar result is obtained also for the temperature of 20 °C. For the rings active electrode, the most marking difference in ozone concentrations was obtained for 1A and 4 T air input nozzles. For this versions of air inputs

the ozone concentrations and production yields for temperatures 10 °C and 20 °C are shown in Figures 19 and 20, respectively. These results can be explained on the base of the same considerations as in the case of the strips active electrode.

From this, Figure 19 can be seen that for the rings active electrode the ozone concentration for the power of 49.5 W and temperature 10 °C when the air input changes from 1A to 4 T increases from 1341 to 1684 ppm, which represents approximately 26%. Similar results were obtained also for the temperature of 20 °C.

From Figure 20, it can be seen that for the rings active electrode the increase in the ozone production yield for temperature 10 °C when the air input changes from 1A
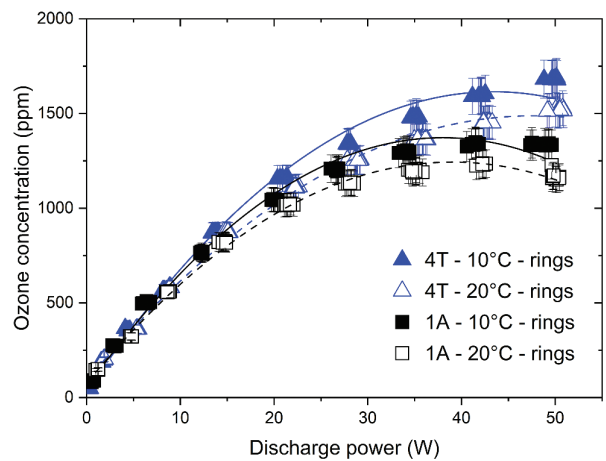
Figure 19. Ozone concentration for the rings active electrode, air inputs 1A and 4A and temperatures 10 °C (full symbols) and 20 °C (empty symbols).
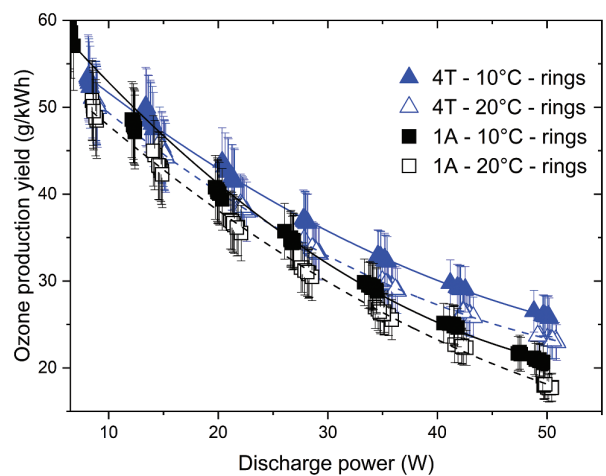
Figure 20. Ozone production yield for the rings active electrode, air inputs 1A and 4 T and temperatures 10 °C (full symbols) and 20 °C (empty symbols). There was wrong y axis.

to 4 T and for power of 49.6 W represents approximately 25%. Similar result is obtained also for temperature of 20 °C.

To demonstrate the effect of air inputs into the discharge chamber on the distribution of the temperature field, we used IR camera Flir E6.

In Figure 21(a), it is shown the thermographic image of the discharge chamber without the discharge, airflow 6 slm and input cap 1A at the bottom. Due to this way of air input, the air in the discharge chamber moves axially, and the temperature field distribution along the discharge tube length is uniform.

The thermographic image of the chamber after 2 minutes of discharge duration is shown in the Figure 21(b). This image is taken for the same airflow and position of the input cap as in the Figure 21(a). In this case the discharge power was 39.1 W. Because of the discharge the air was heated and consequently the temperature in the discharge chamber was increased. Heating the air along the discharge chamber caused the highest air temperature at the output (at the top). From Figure 21 (b) can be concluded, that the temperature distribution is also uniform.

The following two figures in Figure 22 are also for the rings active electrode and 4 T air input cap.

The Figure 22(a) shows the thermographic image of the discharge chamber without the discharge, airflow 6 slm, and the input cap 4 T at the bottom. The

thermographic image of the chamber after 2 minutes of discharge duration is shown in the Figure 22(b). This image Figure 22(b) is taken for the same airflow and position of the air input cap as in the Figure 22(a). In this case, the discharge power was 39.5 W. If we look on the results of modeling study of streamlines patterns for 4 T air input, shown in Figure 7(c), we can see a vortex flow that develops in the input part of the discharge chamber. In the thermographic image, the existence of this vortex flow is reflected by the inclined bright and dark regions.

From these results, it can be concluded that the temperature field distribution in the discharge chamber is affected by the airflow regime in the chamber, and the way of the air input determines this regime.

Discussion

The obtained results could be understood at least qualitatively based on the following considerations. The typical property of DBDs is that in most gases at about atmospheric pressure, the breakdown is initiated by a large number of independent current filaments or microdischarges. These microdischarges can be characterized as weakly ionized plasma channels with properties resembling those of transient high-pressure glow discharges. The number of microdischarges per unit of electrode area and time depends on the discharge voltage. The strength of the microdischarge, which can be
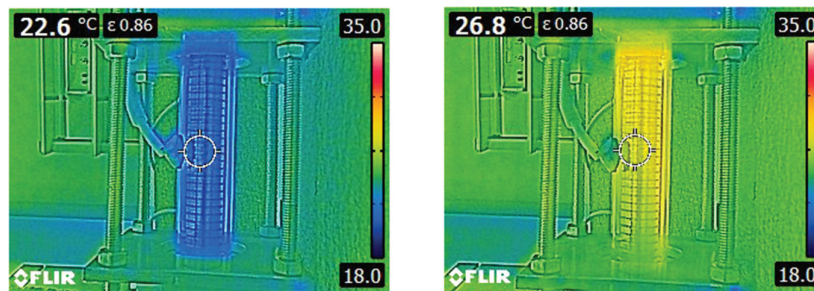

Figure 21. Thermographic images for 1A input nozzle for the discharge with the rings active electrode.
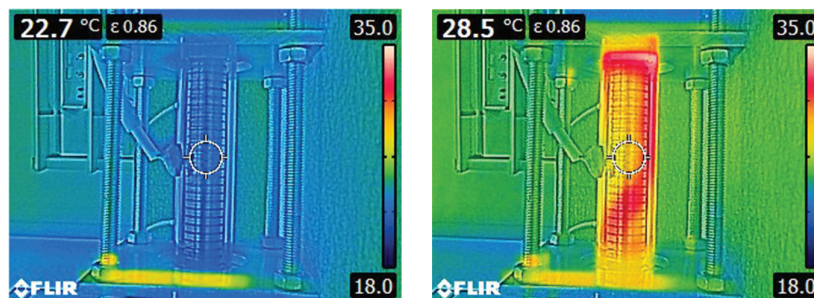

Figure 22. Thermographic images for 4 T input nozzle for the discharge with the rings active electrode.

characterized by the energy deposition in the micro-discharge channel, is determined by discharge energizing, the type and properties of the feeding gas, the gap spacing, and properties of the dielectric or the metal electrode. Besides radiation and collisional gain and loss, drift, diffusion, the convection of particles due to the neutral gas flow also contributes to the particle balance of charged and excited species in the micro-discharge. Thus, the gas flow is also an important control parameter of the microdischarges.

Since ozone is formed only in these microdischarges and not in space between (Kogelschatz 2003), the change in the number of the microdischarges and their properties will result in the change of discharge ozone production. The control of the plasma conditions inside the microdischarge columns is therefore of great importance for optimizing the reaction kinetics of ozone formation.

The overall yield of plasma processes in DBDs is determined by the multitude of discharges, but the properties of the single discharge determine the main processes. Therefore, it can be said that the DBD is characterized by conversion of electric field energy to chemical or physical processes or heating of the gas or surfaces and the effectiveness of a special application of DBDs crucially depends on the dynamics of charge transfer within the discharge (Gibalov and Pietsch 2000). While the energy of the electrons is used for chemical and physical purposes, the energy of the ions is, in general, useless, but controls the stability of the discharge. This energy conversion efficiency is determined by the total amount of energy released in the discharge volume per unit of time. This quantity, expressed as a power density, depends on the electric field strength and current density, or

$$p = \mathbf{j}.\mathbf{E} \ \ [W/m^3] \quad\quad [9]$$

The current density $\mathbf{j}$ can be expressed by the following equation:

$$\mathbf{j} = \pm\mu N\mathbf{E} - D \ \ N + \mathbf{v}N \ \ [A/m^2] \quad\quad [10]$$

In this expression, $N = e.n$, is the density of charged particles, μ is charged particles mobility, $\mathbf{E}$ is the electric field, $\mathbf{v}$ is a local velocity, and D is the diffusion coefficient. Application of the flow on the discharge can affect all three terms in the expression for the current density and, consequently, energy transformations in the microdischarges. The airflow through collisions of the neutral particles with ions affects microdischarge dimensions as well as the mixing of the gas. In this way, it is influenced by the size of the region in which the plasmachemical processes occur. Obviously, in these processes important

role is played by the velocity of the flow, uniformity of the flow in the discharge chamber, number of microdischarges (which is determined by the electrical parameters of the discharge and geometry of the active electrode), and also the orientation of the flow concerning the microdischarges. When the airflow is oriented perpendicularly to the microdischarges, their radius is effectively influenced, and, based on our results, there is a maximum impact of the flow on plasmachemical processes. Unfortunately, as it is often the case in plasmas, one external parameter, such as the orientation of the gas flow with respect to the microdischarges, affects multiple aspects of the discharge simultaneously (Bruggeman, Iza, and Brandenburg 2017). Thus, the overall yield of plasmachemical processes in the discharge is given by the synergy among all the above-mentioned properties.

The ozone generation by DBD from the air is a complex process involving many ozone formation and destruction reactions. There exist different models of this mechanism, which differ mainly by the number of species and reactions involved (Kim et al. 2013; Kitayama and Kuzumoto 1999; Kogelschatz, Eliasson, and Hirth 1988; Yagi and Tanaka 1979).

Speaking generally, the mechanism of ozone generation by electrical discharge in the air is rather complex due to the presence of nitrogen in the air. The presence of nitrogen causes ozone destruction processes because of the existence of nitrogen oxides. A simple model of ozone formation from air involves the following reactions. The initial step is the electron impact dissociation of molecular O_2 and N_2.

The initial step in the formation of O_3 and NO_x is the electron impact dissociation of molecular O_2 and N_2:

$$e + O_2 \ \rightarrow \ O + O + e \quad\quad [11]$$

$$e + N_2 \ \rightarrow \ N + N + e \quad\quad [12]$$
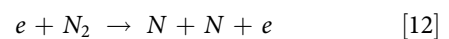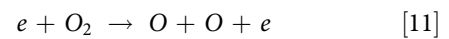
The threshold electron energy for molecular oxygen dissociation is 6 eV or 8.4 eV. Similarly, the threshold electron energy for nitrogen molecular dissociation is 6.17 eV or 7.35 eV (Wei et al. 2019).

Atomic nitrogen reacts with O_2 and O_3 to form NO by reactions:

$$N + O_2 \ \rightarrow \ NO + O \qu\quad [13]$$

$$N + O_3 \ \rightarrow \ NO + O_2 \quad\quad [14]$$
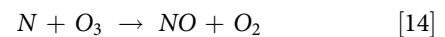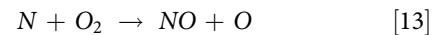
NO and NO_2 form a cycle for ozone destruction by reactions:

$$O + NO_2 \ \rightarrow \ NO + O_2 \quad\quad [15]$$

$$NO + O_3 \rightarrow NO_2 + O_2 \qquad [16]$$

NO_2 is consumed by the following reactions:

$$NO_2 + O_3 \rightarrow NO_3 + O_2 \qquad [17]$$

$$NO_2 + NO_3 \rightarrow N_2O_5 \qquad [18]$$
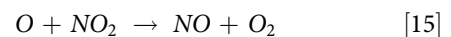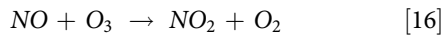
and regenerated by reactions:

$$NO + NO_3 \rightarrow NO_2 + NO_2 \qquad [19]$$

$$N_2O_5 \rightarrow NO_2 + NO_3 \qquad [20]$$

$$O + N_2O_5 \rightarrow NO_2 + NO_2 + O_2 \qquad [21]$$

The main ozone formation reaction dominant at high pressures is reaction:

$$O + O_2 + M \rightarrow O_3 + M \qquad [22]$$

Undesirable reaction, which determines the upper limit of O concentration is:

$$O + O + M \rightarrow O_2 + M \qquad [23]$$

In case of the discharge in air M represents molecular oxygen or nitrogen. There are certainly other different reactions destroying ozone. One example of catalytic reaction destroying ozone is:

$$NO_2 + O_3 \rightarrow NO_3 + O_2 \qquad [24]$$

$$O + NO_3 \rightarrow O_2 + NO_2 \qquad [25]$$
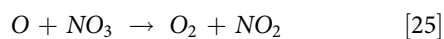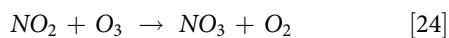
The presented model is very simple because it does not include the reactions involving excited species, other molecules or other ozone self-destruction reactions.
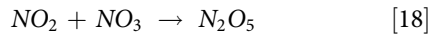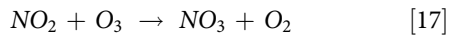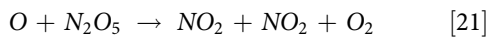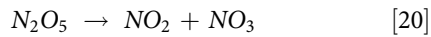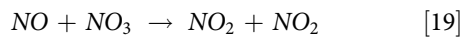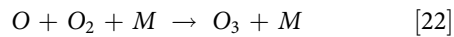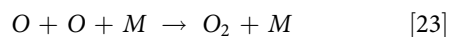
Reaction rates of individual reactions depend on various parameters, for example, on electric field, temperature, or pressure. The temperature, or more precisely the temperature distribution in the discharge chamber, can be affected by varying air input into the discharge chamber. Thus, for example, the main ozone formation reaction dominant at atmospheric pressure is reaction No. (22), where M represents molecular oxygen or nitrogen. In this case, the reaction rate dependence of the gas temperature T_g is given by the following expression:

$$k = 2.5 \cdot 10^{-35} \cdot \exp^{\left(\frac{970}{T_g}\right)} \qquad [26]$$

where k is in $cm^6 \cdot s^{-1}$.

From this expression, it is seen that the reaction rate of ozone generation decreases with increasing gas temperature.

Contrary to ozone, NO_x formation is favored by heat and linked with the discharge path temperature. Thus, for example, the reaction No. (16) is significantly enhanced by increasing the gas temperature

$$k = 1.5 \cdot 10^{-12} \cdot \exp^{\left(\frac{-1300}{T_g}\right)} \qquad [27]$$

where k is in $cm^3 \cdot s^{-1}$.

For example, for the ozone formation reaction No. (22), the increase in the temperature from 10 °C to 20 °C causes the 10% decrease of this reaction rate. On the other hand, the same change of temperature for the NO_x formation reaction No. (16) causes increase of this reaction rate by 16%. Certainly, the discharge ozone production results from the reaction rates of all individual reactions involved in the process. Increasing gas temperature substantially reduces ozone generation processes.

The effect of temperature on the concentration and production yield of generated ozone is nicely demonstrated in Figures 17, 18, 19, 20 in the section *The effect of the number of air input nozzles and temperature on discharge ozone production*.

Conclusions

In this paper, we studied the effect of airflow orientation concerning the microdischarges and the impact of air input nozzle number on ozone production and electrical parameters of the surface dielectric barrier discharge in a cylindrical configuration. The experiments were performed with constant airflow through the discharge chamber and two temperatures. Our findings can be summarized as follows:

- For the maximum effect of the flow on ozone concentration produced by the surface dielectric barrier discharge, the streamlines patterns should be predominantly oriented perpendicular to the majority of microdischarges.
- The streamlines patterns should be uniformly distributed in the discharge chamber volume. Their distribution can be controlled by the number and orientation of the input nozzles.
- An illustrative example of these two conclusions is the increase in ozone concentrations and production yield of circa 26% for the discharge with the strips active electrode, power of 44.6 W when the air input into the discharge chamber was changed from 1A to 4A. For the rings active electrode, the similar results were obtained for air inputs 1A and 4 T.
- Electrical parameters of the discharge are not strongly affected by air input for a particular geometry of the active electrode.
- The increase in temperature decreases discharge ozone production.

To obtain the best yield of plasmachemical processes in the discharge, the number and orientations of the input nozzles together with the geometry of the active electrode should be optimized, considering the above-mentioned results. We hope that our findings can contribute to a better understanding of the interaction between the flow and microdischarges, which will help to design more efficient ozone generators.

Disclosure statement

No potential conflict of interest was reported by the author(s).

Funding

ORCID

J. Mikeš http://orcid.org/0000-0003-2219-4320
S. Pekárek http://orcid.org/0000-0002-7171-9341
O. Hanuš http://orcid.org/0000-0001-7869-5744

References

Brandenburg, R. 2017. "Dielectric Barrier Discharges: Progress on Plasma Sources and on the Understanding of Regimes and Single Filaments." *Plasma Sources Science and Technology* 26 (5): 053001. doi:10.1088/1361-6595/aa6426

Bruggeman, P. J., F. Iza, and R. Brandenburg. 2017. "Foundations of Atmospheric Pressure Non-equilibrium Plasmas." *Plasma Sources Science and Technology* 26 (12): 123002. doi:10.1088/1361-6595/aa97af

Choudhury, B., S. Portugal, J. Johnson, and S. Roy. 2020. *Performance Evaluation of Fan and Comb Shaped Plasma Reactors for Distribution of Generated Ozone in a Confined Space*. Florida, Orlando: American Institute of Aeronautics and Astronautics.

Draou, A., S. Nemmich, K. Nassour, Y. Benmimoun, and A. Tilmatine. 2018. "Experimental Analysis of a Novel Ozone Generator Configuration for Use in Water Treatment Applications." *International Journal of Environmental Studies* 76 (2): 338–50. doi:10.1080/00207233.2018.1499698

Fan, Z., H. Yan, Y. Liu, H. Guo, Y. Wang, and C. Ren. 2018. "Investigation of Airflow Effects on the Dielectric Barrier Discharge with Single/double Discharge Channel Arrangement." *Physics of Plasmas* 25 (5): 053519.

Fridman, A. 2008. *Plasma Chemistry*. New York: Cambridge University Press.

Gibalov, V. I., and G. J. Pietsch. 2000. "The Development of Dielectric Barrier Discharges in Gas Gaps and on Surfaces." *Journal of Physics D: Applied Physics* 33 (20): 2618–36. doi:10.1088/0022-3727/33/20/315

Gibalov, V. I., and G. J. Pietsch. 2012. "Dynamics of Dielectric Barrier Discharges in Different Arrangements." *Plasma Sources Science and Technology* 21 (2): 024010. doi:10.1088/0963-0252/21/2/024010

Höft, H., M. M. Becker, and M. Kettlitz. 2016. "Impact of Gas Flow Rate on Breakdown of Filamentary Dielectric Barrier Discharges." *Physics of Plasmas* 23 (3): 033504. doi:10.1063/1.4943278

Jodzis, S., T. Smolinski, and P. Sowka. 2011. "Ozone Synthesis under Surface Discharges in Oxygen: Application of a Concentric Actuator." *IEEE Transactions on Plasma Science* 39 (4): 1055–60. doi:10.1109/TPS.2011.2105285

Kim, H. Y., S. K. Kang, H. C. Kwon, H. W. Lee, and J. K. Lee. 2013. "Gas Temperature Effect on Reactive Species Generation from the Atmospheric Pressure Air Plasma." *Plasma Processes and Polymers* 10 (8): 686–97. doi:10.1002/ppap.201200163

Kitayama, J., and M. Kuzumoto. 1999. "Analysis of Ozone Generation from Air in Silent Discharge." *Journal of Physics D: Applied Physics* 32 (23): 3032–40. doi:10.1088/0022-3727/32/23/309

Kogelschatz, U., B. Eliasson, and M. Hirth. 1988. "Ozone Generation from Oxygen and Air: Discharge Physics and Reaction Mechanisms." *Ozone: Science & Engineering* 10 (4): 367–77. doi:10.1080/01919518808552391

Kogelschatz, U. 2003. "Dielectric-barrier Discharges: Their History, Discharge Physics, and Industrial Applications." *Plasma Chemistry and Plasma Processing* 23 (1): 1–46. doi:10.1023/A:1022470901385

Machala, Z., K. Hensel, and Y. Akishev. 2012. *Plasma for Bio-Decontamination, Medicine and Food Security*. Netherlands, Dodrecht: Springer.

Malik, M. A., and D. Hughes. 2016. "Ozone Synthesis Improves by Increasing Number Density of Plasma Channels and Lower Voltage in a Nonthermal Plasma." *Journal of Physics D: Applied Physics* 49 (13): 135202. doi:10.1088/0022-3727/49/13/135202

Mikeš, J., S. Pekárek, and I. Soukup. 2016. "Experimental and Modelling Study of the Effect of Airflow Orientation with respect to Strip Electrode on Ozone Production of Surface Dielectric Barrier Discharge." *Journal of Applied Physics* 120 (17): 173301. doi:10.1063/1.4966603

Pavón, S. (2008). *Interaction between a Surface Dielectric Barrier Discharge and Transonic Airflows*. PhD thesis, École polytechnique fédérale de Lausanne, École poly- technique fédérale de Lausanne.

Pavón, S., J.-L. Dorier, C. Hollenstein, P. Ott, and P. Leyland. 2007. "Effects of High-speed Airflows on a Surface Dielectric Barrier Discharge." *Journal of Physics D: Applied Physics* 40 (6): 1733–41. doi:10.1088/0022-3727/40/6/021

Pekárek, S., J. Mikeš, M. Červenka, and O. Hanuš. 2021. "Air Supply Mode Effects on Ozone Production of Surface Dielectric Barrier Discharge in a Cylindrical Configuration." *Plasma Chemistry and Plasma Processing* 41 (3): 779–92. doi:10.1007/s11090-021-10154-x

Pipa, A., and R. Brandenburg. 2019. "The Equivalent Circuit Approach for the Elec- Trical Diagnostics of Dielectric Barrier Discharges: The Classical Theory and Recent Developments." *Atoms* 7 (1): 14. doi:10.3390/atoms7010014

Sedláček, M. 2003. "Digital Measurement of Phase Difference of Lf Signals–a Comparison of Dsp Algorithms." Proceedings of XVII IMEKO World Congress (Croatia, Dubrovnik), 639–44.

Sedláček, M., and M. Krumpholc. 2005. "Digital Measurement of Phase Difference – A Comparative Study of Dsp Algorithms." *Metrology and Measurement Systems* 12 (4): 427–48.

Uytdenhouwen, Y., J. Hereijgers, T. Breugelmans, P. Cool, and A. Bogaerts. 2021. "How Gas Flow Design Can Influence the Performance of a DBD Plasma Reactor for Dry Reforming of Methane." *Chemical Engineering Journal* 405:126618. doi: 10.1016/j.cej.2020.126618.

Volkoff, S. J., T. J. Carlson, K. Leik, J. J. Smith, D. Graves, P. Dennis, T. Aris, D. Cuthbertson, A. Holmes, K. Craig, et al. 2020. "Demonstrated SARS-CoV-2 Surface Disinfection Using Ozone." *Ozone: Science & Engineering* 43(4): 296–305 doi:10.1080/01919512.2020.1863770.

Wei, L., H. Deng, G. Neretti, and Y. Zhang. 2019. "Ozone Yield Limit in Low temperature Plasmas Based on Thermodynamics." *The European Physical Journal D* 73 (7). doi:10.1140/epjd/e2019-90560-y.

Wei, L., X. Liang, and Y. Zhang. 2018a. "Numerical Investigation on the Effect of Gas Parameters on Ozone Generation in Pulsed Dielectric Barrier Discharge." *Plasma Science and Technology* 20 (12): 125505. doi:10.1088/2058-6272/aadca6

Wei, W., S. He, S. Wang, X. Yan, and G. Gao. 2018b. "Effects of Airflow on At- Mospheric Pressure Surface Dielectric Barrier Discharge." 2018 IEEE International Conference on High Voltage Engineering and Application (ICHVE). Athens: IEEE.

Xie, S., Y. He, D. Yuan, Z. Wang, S. Kumar, Y. Zhu, and K. Cen. 2019. "The Effects of Gas Flow Pattern on the Generation of Ozone in Surface Dielectric Barrier Discharge." *Plasma Science and Technology* 21 (5): 055505. doi:10.1088/2058-6272/aafc50

Yagi, S., and M. Tanaka. 1979. "Mechanism of Ozone Generation in Air-fed Ozonisers." *Journal of Physics D: Applied Physics* 12 (9): 1509–20. doi:10.1088/0022-3727/12/9/013

Yousfi, M., N. Merbahi, J. P., O. Eichwald, A. Ricard, J. Gardou, O. Ducasse, and M. Benhenni. 2011. "Non Thermal Plasma Sources of Production of Active Species for Biomedical Uses: Analyses, Optimization and Prospect." In *Biomedical Engineering - Frontiers and Challenges* Fazel, Reza, United Kingdom, London: InTech 99–124 doi:10.5772/19129 .

A.9 Catalytic and time stability effects of photocatalysts on ozone production of a surface dielectric barrier discharge in air
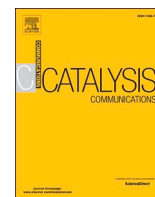
Catalytic and time stability effects of photocatalysts on ozone production of a surface dielectric barrier discharge in air

J. Mikeš [a,*], S. Pekárek [a], P. Dzik [b]

[a] *Czech Technical University in Prague, Faculty of Electrical Engineering, Technická 2, 166 27 Prague 6, Czech Republic*
[b] *Brno University of Technology, Faculty of Chemistry, Purkyňova 464/118, 612 00 Brno, Czech Republic*

A B S T R A C T

We investigated the effect of various photocatalysts - titanium, zinc, barium, and tungsten oxides on ozone generation of the surface dielectric barrier discharge in air. The layers of these catalysts were deposited on the side of the glass plate opposite the active electrode so that the emission from the discharge irradiated them. We found that TiO_2, ZnO, and $BaTiO_3$ catalysts increase the concentration of ozone generated by the discharge. On the other hand, the presence of WO_3 in the discharge does not affect the ozone concentration. All these catalysts show no substantial effect on the electrical parameters of the discharge.

1. Introduction

Ozone, due to its wide range of applications, such as water treatment, medicine for wound decontamination and fast healing, sterilization, inactivation of bacteria and viruses, food and vegetable storage, restoration of buildings and other objects after fire or floods, or in agriculture, is at the center of extensive research [1–3]. It is usually produced by electrical discharges, electrochemical processes, or ultraviolet radiation. Most ozone for the above applications is generated by electrical discharges, corona, and dielectric barrier discharge [4,5].

To increase the efficiency of its production, various approaches involve the choice of discharge energization, proper design of the electrodes, or optimization of the gas flow in the discharge chamber.

An interesting alternative to these approaches is using various catalysts that trigger plasma-catalyst interactions [6].

The ozone generation by electrical discharges from the air is a complex process involving a chain of various reactions occurring in the discharge volume. In the case of discharges with the presence of photocatalysts, the contribution of the surface reactions due to the activation of the photocatalysts by ultraviolet radiation emitted by the discharge should be added to the volume reactions. These surface catalytic reactions refer to breaking chemical bonds on the catalyst surface. As long as the photocatalysts are used mostly semiconductor materials, the energies of photons triggering catalytic reactions should be higher than the forbidden energy gap. Consequently, the electrons from the valence band can promote to a largely vacant conduction band, and

positive holes with strong oxidizing capability are formed. The electrons are capable of carrying out reduction reactions, and holes can carry out oxidation reactions [7]. These reactions affect the mechanism of the discharge ozone production. The mechanism of photocatalysis is shown in Fig. 1.

Our previous paper [8] tested the titanium dioxide TiO_2 and zinc oxide ZnO effects of discharge ozone production. Now, besides these two photocatalysts, we also examine the usage of barium titanate $BaTiO_3$ and tungsten trioxide WO_3 for these purposes. Our attention is also focused on the time stability of ozone generation processes.

The most frequently used photocatalyst for the enhancement of discharge ozone generation is TiO_2. This photocatalyst is an *n*-type semiconductor that can exist in several phases: TiO_2 in an anatase phase has a forbidden energy gap of 3.2 eV, TiO_2 in a rutile phase has a forbidden energy gap of 3.02 eV, and TiO_2 in a brookite phase has a forbidden energy gap of 2.96 eV [9]. The energy gaps of 3.2 eV and 2.96 eV correspond to electromagnetic radiation of wavelengths 387 nm and 414 nm, respectively.

Zinc oxide ZnO is an *n*-type semiconductor with an energy gap of 3.37 eV at room temperature [10]. This energy gap corresponds to electromagnetic radiation at a wavelength of 376 nm.

Barium titanate, $BaTiO_3$, is an electrical insulator in its pure form. However, when doped with small amounts of metals, it becomes an *n*-type semiconductor with an energy gap of 3.3–3.5 eV [11,12]. This energy gap corresponds to the electromagnetic radiation wavelength of 375–353 nm.
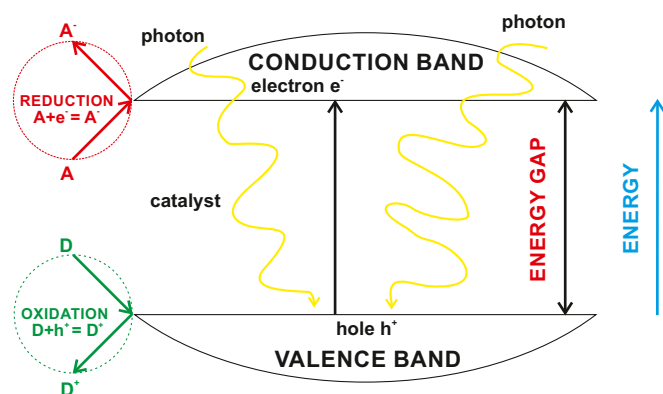

Fig. 1. The mechanism of photocatalysis.

Tungsten trioxide WO$_3$ is an *n*-type semiconductor with a bandgap of 2.6 eV (highly crystalline) to 3.3 eV (amorphous) [13]. Corresponding wavelengths are 476 and 374 nm. Moreover, the electrical and optical properties of the WO$_3$ can be changed by adding the dopants, including metallic.

From what has been said, it is obvious that the photocatalytic activity of the catalysts is triggered if the catalyst is irradiated by electromagnetic radiation from the discharge of wavelengths, which corresponds to the above-given forbidden energy bandgaps. In Fig. 3, we, therefore, show the emission spectrum of the investigated discharge together with the wavelength of radiation required for triggering the photocatalytic reactions for different photocatalysts.

The stability of photocatalytic activity is one of the most important parameters in ozone generation by electrical discharges with the presence of photocatalysts. Literature dealing with this problem is not too numerous. On the other hand, the problem of stability of photocatalysts, e.g., for the textile industry or water treatment, is treated in various papers. The photocatalytic degradation of methyl orange using TiO$_2$, WO$_3$, and mixed thin films has been investigated in [14]. The stability of the photocatalytic films in long-time running processes was examined in a series of experiments using contact periods of up to 9 days. The results show that the thin films maintained their photocatalytic properties confirming their stability and viability for up-scaling. The paper [15] presents the results obtained with heterogeneous catalytic ozonation in model and natural waters in the presence of TiO$_2$ supported on alumina. In this work, the stability of the process with the catalyst was investigated for a contact time of 30 min.

A comprehensive review of the interaction of the plasma produced by the dielectric barrier discharge with different catalysts is given in [16]. Thus, for TiO$_2$ and BaTiO$_3$ catalysts used for CO$_2$ decomposition, the time dependence of the temperature of the catalyst surface during the transition process lasting 25 min and its impact on CO$_2$ conversion was studied.

However, a comparative study of catalytic activity and the stability of various catalysts in low-temperature plasma produced by the dielectric barrier discharge is still missing. We used the concentration of ozone generated by the discharge as an indicator of these two quantities. We choose ozone because of the wide range of its applications.

Our paper studies various photocatalysts, TiO$_2$, BaTiO$_3$, ZnO, and WO$_3$, to compare their effects on ozone generation by the surface dielectric barrier discharge in air. For this purpose, we developed a measuring and control experimental system to ensure that the observed effects can be attributed to the catalyst. Our attention was also focused on the time dependence of the concentration of generated ozone. In this context, we conducted a series of experiments devoted to the discharge ozone production in a time period lasting 12 h. Apart from the ozone produced by the discharge, we were also able to detect the effects, which are in the majority of papers not observed, particularly small variations

in the discharge's electrical parameters, which are usually hidden in the temperature dependences of the experimental parameters.

2. Experimental arrangement

The experimental arrangement, shown in Fig. 2, consists of a discharge chamber, power supply system, electrical diagnostics, control system, spectrometer, ozone monitor, air feeding unit, water cooling system, and thermobox.

The flat discharge chamber, produced by fused deposition modeling, was printed by Prusa I3 - 3D printer from the polylactic acid filament. It contains the electrode system on the ceramic plate. The dimensions of the plate are 49.7 × 103.7 × 1.1 mm. The active electrode, on the upper side of the plate, is formed by 19 interconnected parallel strips, each with a length of 36.7 mm. The grounded electrode, in the form of a parallelepiped, is made on the lower side of the plate. The capacitance of the electrode system for the frequency of 10 kHz is 169.8 pF.

The upper side of the discharge chamber is closed by the glass window. On the inner part of this window, exposed to the active electrode, is deposited the layer of the photocatalyst.

The air input into the discharge chamber is through ten openings in the tube on one side of the active electrode. An identical tube with the same number of openings is on the other side of the active electrode for air output.

The power supply system consisted of the function generator KEYSIGHT 33500B, wideband AC power amplifier AL-1400-HF-A (1000 W, frequency response 5 Hz to 800 kHz), and a high-frequency high-voltage transformer AL-T1000.7 (1000 W, frequency response 3.5 to 11 kHz). The discharge's electrical parameters were recorded by a digital four-channel oscilloscope Tektronix MDO4054B-3 (3 GHz, 2.5 GS/s).

The voltage at the power supply's output was measured by a high-voltage probe Pintek HVP-28HF (division ratio 1000/1, frequency up to 200 MHz) and recorded on the first channel of this oscilloscope. The voltage drop on the measuring capacitor was recorded on the second channel. The discharge current, monitored by a Pearson current monitor (PCM - model 2877, bandwidth up to 200 MHz), was recorded on the third channel of the oscilloscope. In Fig. 2, the high voltage probe is denoted as HVP, Pearson current monitor is PCM, and the probe for measuring the voltage drop on the measuring capacitor is CVP.

To keep the temperature of the discharge chamber constant, the chamber was placed in a thermobox, offering the possibility of regulating the temperature from +3 to +70 °C with an accuracy of ±0.1 °C.

The grounded electrode was cooled by water flowing through the thermostat. The temperature T$_W$ of the water was adjusted to the same value as the temperature in the thermobox T$_T$.

The air into the discharge chamber was supplied from an oil-free compressor through a membrane dryer MD and mass flow controller MFC. The relative humidity RH, temperature T1, and air pressure P in the discharge chamber input were also monitored. At the output from the discharge chamber, we measured the temperature T2 of air by the optical fiber thermometer and ozone concentration by a BMT 964 ozone monitor.

The emission spectrum of the discharge in the range of 300–500 nm was recorded using an HR2000 High-Speed Miniature Fiber Optic Spectrometer. An optical fiber collected the spectrum through the opening in the upper side of the discharge chamber, perpendicular to the strip electrode.

To measure electrical as well as non-electrical quantities simultaneously, we developed a control system. All instruments were connected - using voltage outlets (0–10 V) or by means of a current loop (0/4–20 mA) - into an automated computer-controlled measuring system. This system consists of a central computer Raspberry Pi 4 for which the control software was written in Python language. Individual measurements consisted of predefined steps performed autonomously to retain the identical character of all the measurements. The first step was aimed at checking the system's integrity, and the setup of all the elements of the
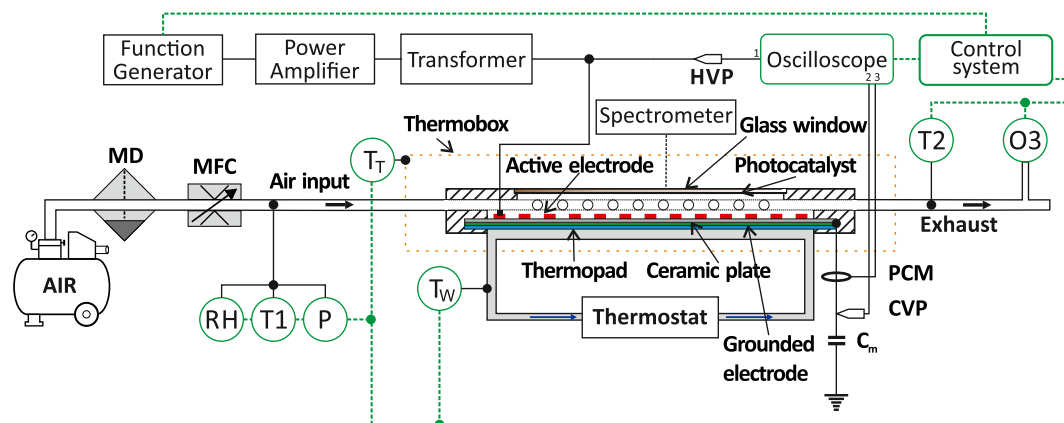
Fig. 2. Experimental arrangement.

measuring chain was checked back to the initial stage. Signals were taken not only from individual sensors but also directly from the oscilloscope. Data were saved into CSV files and later processed and analyzed.

2.1. Preparation of photocatalysts layers

All oxide coatings were deposited from the liquid phase by inkjet material printing performed with the Fujifilm Dimatix DMP-2831 experimental printer. This technique is superior due to its versatility, scalability, the efficiency of ink used, and its inherent direct patterning capability. The ink used for printing contained nanoparticles of the functional oxides and our proprietary oligomeric siloxane condensate acting as dispersing and suspension stabilizing agents in the liquid ink and a binding agent in the dry layer. As reported in our previous paper [17] it provides excellent stability and flawless printability of the ink and adequate adhesion and cohesion of the printed layer after solvent evaporation. The functional oxidic nanoparticles were of various origins but generally, all were prepared by the top-down approach, i.e., coarse crystalline materials were mechanically disintegrated into fine particles the size of which was in the range of a few hundred nanometers which ensured a reliable passage through the 20-μm nozzle orifices of the printer.

All printing inks were prepared following a common procedure: 2 ml of stock polysiloxane binder solution (20 wt% in anhydrous ethanol) were mixed with 6 ml of stock oxide dispersion (20 wt% in Dowanol PM solvent) and 6 ml of isobutanol and 14 ml of n-hexanol. Thus, the total dry mass loading of the printing ink was 5 wt% and the oxide/binder ratio was 3:1 by weight. The stock dispersions of employed oxides were prepared in the following way: ZnO nanoparticles were supplied by Sigma-Aldrich as ethanolic suspension. The suspension was lyophilized and resuspended into Dowanol PM by means of sonification. TiO_2 was the Evonik P-25 grade, also supplied by Sigma-Aldrich. After a 20 wt% suspension in Dowanol PM was prepared, 6 ml of it was combined with approx. 2 cm^3 of 1-mm glass balls in a 20 ml glass vial. The vial was then placed overnight on an oscillating lab shaker set to 1000 rpm. This gentle improvised ball-milling step proved surprisingly effective and resulted in the disintegration of larger multigrain titania aggregates which constitute the raw P-25. WO_3 and $BaTiO_3$ were provided in the form of coarse powders by Sigma-Aldrich, too. As determined by SEM imaging, the powders consisted of large compact grains rather than multigrain aggregates, so a more powerful milling method was employed. Twenty wt% coarse suspensions in Dowanol PM were subject to ball milling and regular sampling until the mean particle size determined by DLS dropped below 200 nm. Once this particle size was reached, the printing ink was prepared following the procedure described above.

The prepared printing inks were loaded into the Dimatix printer ink reservoirs, clamped onto the 10 pl print head, and mounted into the printer. The patterns of 65 × 26 mm size were printed onto microscope slides (glass windows) of dimensions 76 × 26 × 1.1 mm with a drop spacing of 40 μm. Four layers were overprinted, and the thickness of the dry layers was 500 ± 50 nm.

Further details of the catalyst layer deposition processes can be found in our previous papers [18,19].

3. Experimental results

The experiments were performed with the sinusoidal driving voltage of a frequency 10 kHz. The airflow through the discharge chamber was 4 standard liters per minute (slm), and the relative humidity of the air was 11%. The temperature of the cooling water, as well as the temperature in the thermobox, were adjusted to 20 °C.

3.1. Emission spectrum of the discharge

Photocatalytic activity of the photocatalyst is triggered if it is irradiated by electromagnetic radiation of wavelengths corresponding to its forbidden energy gap. The forbidden energy gaps of investigated catalysts TiO_2, ZnO, $BaTiO_3$, and WO_3 vary, according to the *Introduction section*, in the range of wavelengths from 353 to 476 nm.
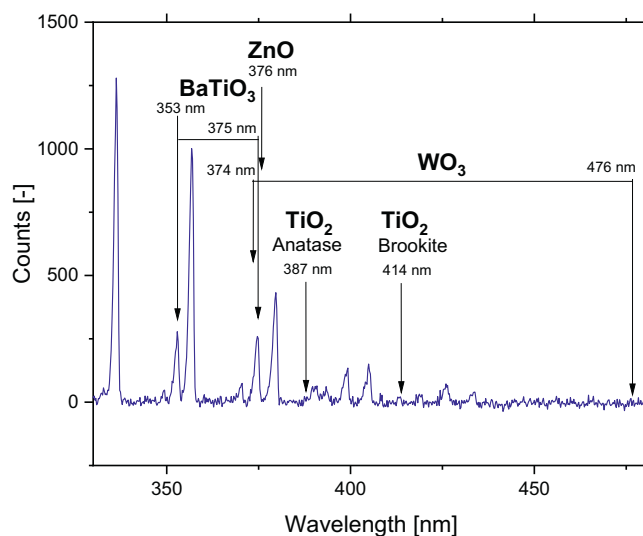

Fig. 3. The surface dielectric barrier discharge spectrum in the air for the effective voltage of 2800 V for the wavelengths of 330 to 480 nm.

In Fig. 3, we show for the discharge voltage of 2800 V the emission spectrum of the discharge from the air for the wavelengths of 330 to 480 nm, together with the wavelengths of the radiation corresponding to the forbidden energy gaps of different photocatalysts. The strong emission at a wavelength of 337.1 nm originates from the second positive system of nitrogen ($C_3\Pi_u \to B_3\Pi_g$). Weaker radiation of a wavelength of 391.4 nm is due to the first negative system ($B_2\Sigma_u^+ \to X_2\Sigma_g^+$) of N_2^+.

When the UV light of suitable wavelengths illuminates the photocatalyst, it becomes activated. The electron and positive hole can then react with the molecules in the vicinity of the catalyst. An example of the reaction of an electron with an oxygen molecule is the formation of the superoxide anion O_2^-:

$$e^- + O_2 \to O_2^- \tag{1}$$

In addition to superoxide anions, other active oxygen species, such as O^-, O_3^-, O_2^{--}, [20], etc., could also be produced. These active oxygen species then enter plasma-chemical reactions leading to ozone generation and destruction. The resulting concentration of ozone then represents the dynamic balance of these two types of reactions.

Based on the discharge spectrum and the forbidden energy gap width, different photocatalytic materials can be chosen to enhance discharge ozone production.

3.2. Electrical measurements

The electrical parameters of the discharge play a key role in the evaluation of the discharge ozone production efficiency. Besides, the knowledge of various catalysts' effects on these parameters can help better understand the ozone generation process.

3.2.1. Discharge power evaluation

The discharge power is a key quantity used in the study of discharge ozone production. In general, the average value of the discharge power can be expressed as:

$$P_{av} = \frac{1}{T}\int_0^T V_j(t)I_j(t)dt \tag{2}$$

The numerical calculation involves discharge current and voltage multiplication. The result is obtained by *trapz* function providing trapezoidal numerical integration and dividing by period. The procedure is described in the following pseudocode:

$$P_{av} = \frac{trapz(time\ interval, discharge\ current \bullet discharge\ voltage)}{period} \tag{3}$$

Therefore, it is necessary to determine the discharge voltage $V_j(t)$ and current $I_j(t)$ to evaluate discharge power. The discharge voltage is usually measured using a high-voltage probe, and the discharge current is determined differently. The most frequently used is a current monitor or a measuring capacitor.

The current monitor is an electrical transducer used for measuring ac currents. In our experiments, we used the Pearson current monitor PCM, see Fig. 2. The main advantage of this method is the galvanic separation between the electric signal from the current monitor and the discharge electrical circuit, which increases the safety of measurements. On the other hand, the drawback of this method is the limited bandwidth of the current monitor and a small phase shift between discharge voltage and current signals.

The second method of the discharge current evaluation is based on the measurement of the voltage drop $V_m(t)$ on the measuring capacitor C_m. The discharge power is calculated from the following equation:

$$P = f \cdot \oint V_j(t)\cdot\frac{dQ}{dt}dt = f\cdot C_m \oint V_j(t)dV_m, \tag{4}$$

The voltage drop across this capacitor is proportional to the transferred charge. The area of a closed loop of the applied voltage versus charge, the so-called Lissajous figure, represents the energy transferred in one period [21,22]. The capacitance of the measuring capacitor must be chosen to be significantly larger than the capacitance of the electrode system, usually by a factor of 1000 [23]. In our experiments, this capacitance was 101.8 nF, and the capacitance of the electrode system was 169.8 pF. This method requires the same safety features as the first one but needs more complex data processing to compute power. Both the discharge voltage and the voltage drop on the measuring capacitor must be smoothened. Otherwise, any noise that causes overlays of the Lissajous figures distorts the calculated average power. The area of the figure is calculated by the *polyarea* function multiplied by the capacitance of the measuring capacitor C_m and frequency f. The integer number of measured periods is denoted as N. The procedure can be described as the following pseudocode:

$$P_{av} = f \bullet C_m \bullet polyarea\left(smooth(V_j), smooth(V_m)\right)/N \tag{5}$$

Our experiments were performed for six values of the effective voltages calculated from the discharge voltages. For the lowest value of this effective voltage was chosen 2380 V. For this voltage, the discharge covered all area of the active electrode. The electrical parameters of the active electrode material gave the highest value of this voltage of 2800 V. This voltage span was divided into six equal intervals.

Fig. 4 shows average power calculated from the Pearson current monitor (PCM) or the voltage drop on the measuring capacitor (CVP) for the discharge with the TiO$_2$ (full symbols) or the discharge without a photocatalyst (empty symbols). An evaluated error of power measurement is 7%.

From Fig. 4, we can see that for each measuring interval within the full range of investigated effective voltage values, the power evaluated from the voltage drop on the measuring capacitor is slightly higher than the power calculated from the Pearson current monitor. These results are the same for the discharge without the photocatalyst and the discharge with TiO$_2$. Besides, all four dependencies follow the same trend. The discharges with ZnO and BaTiO$_3$ photocatalysts show similar effects. The dependence of ozone concentration versus voltage for the discharge with WO$_3$ shows the same trend as for the discharge without the catalyst.

To compare these two methods of power evaluation, in Fig. 5 is shown the ratio of the average discharge power for all measuring intervals calculated from the data obtained from the Pearson current monitor and data from the voltage drop on the measuring capacitor. Similarly, as in the preceding case, the results for the discharge without the photocatalyst and with TiO$_2$ are shown.
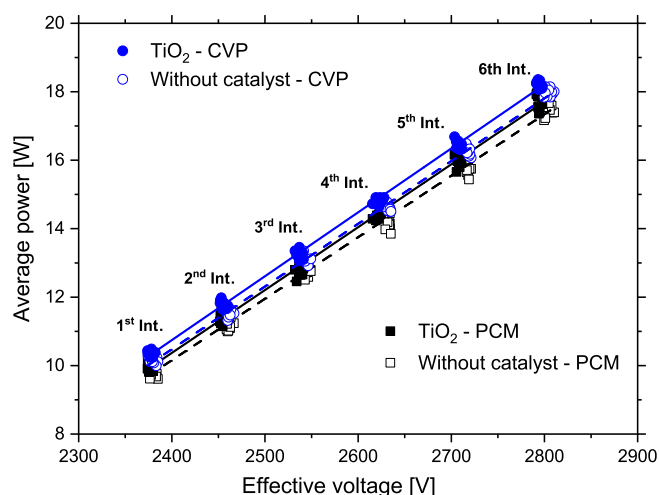

Fig. 4. Average power calculated from the Pearson current monitor (PCM) or the measuring capacitor (CVP) for the discharge with TiO$_2$ or the discharge without a photocatalyst.
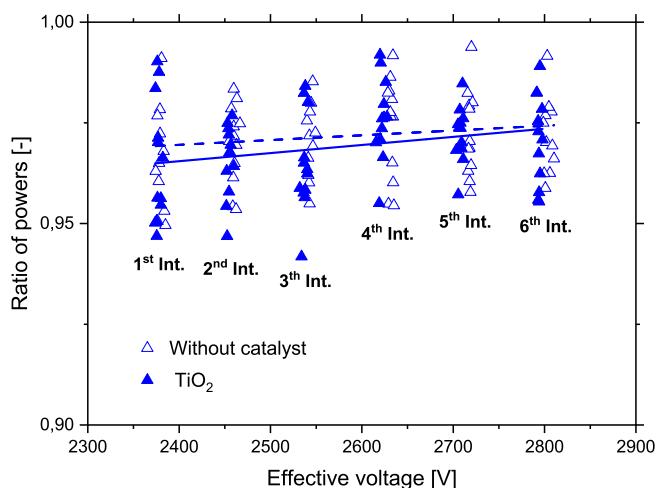
Fig. 5. The power ratio calculated from the Pearson current monitor and the measuring capacitor for the discharge with TiO_2 and without the photocatalyst.

This figure shows that the ratio of powers calculated by these two methods is practically the same for the discharge without and with the photocatalyst. Based on these results and the fact that the usage of the voltage drop on the measuring capacitor (Lissajous figures) is the approach that does not require high bandwidth probes and oscilloscopes [23], we used for evaluation of the discharge ozone production efficiency average discharge power calculated from the Lissajous figures.

3.2.2. Effect of photocatalysts on electrical parameters of the discharge

To eliminate the possible role of the photocatalysts position on the discharge parameters, we performed our experiments with their fixed position. All catalysts were deposited on the inner part of the glass window and exposed to the active electrode.

The ozone generation by the electrical discharges is, among other factors, determined by their electrical parameters. These parameters include discharge voltage, current, and discharge power. The discharge voltage, determined by the power source, is assumed not to change. On the contrary, the discharge current is affected by the type of discharge. The surface dielectric barrier discharge involves displacement current and a current due to a series of peaks reflecting the existence of microdischarges. To have a deeper insight into the role of photocatalysts on the discharge's electrical parameters, we give in Fig. 6 an illustrative example of voltage and current waveforms for the discharge without and with different photocatalysts for the 4th measuring interval.

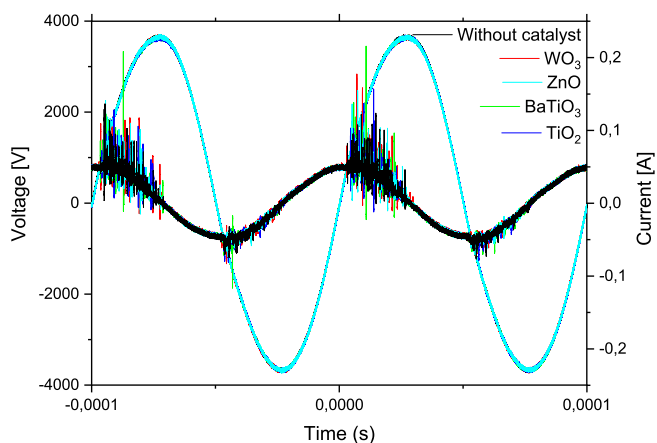From Fig. 6, it is seen that the discharge current consists of the above-mentioned displacement current and a series of current peaks. These peaks have different amplitudes and are randomly distributed for the discharge without the photocatalyst and with photocatalysts. Most of the authors working with the photocatalysts and their role in the generation of discharge products focus on studying these current peaks. Thus, in [24], the TiO_2 photocatalyst was deposited on the side of the dielectric barrier, which was opened to the high-voltage electrode. It was shown that the amplitudes, density, or distribution function of current peaks might be affected by the presence of the TiO_2 photocatalyst.

Since our attention was also focused on the time stability of investigated catalysts and the duration of these experiments was 12 h, we used the average effective current in our analysis of results. This current was calculated in the following way. In each measuring interval, we performed 12 measurements, and we determined the effective value of current for each of these measurements. For each of these intervals, we, therefore, had 12 values of effective current. From these 12 values of effective current, we determined the average effective current, shown in the vertical axis of Fig. 7. Evaluated current measurement error is 1%.

From Fig. 7 can be seen that the presence of the photocatalysts for a particular voltage does not substantially affect the discharge current.

Finally, the discharge power is given by the discharge voltage and current product. For a capacitive load, it also depends on the phase shift between applied voltage and current. Based on the analysis of the discharge voltage and current waveforms, we calculated the phase shift for the discharge without and with different photocatalysts. The dependence of the phase shift versus the effective value of the discharge voltage for different photocatalysts is shown in Fig. 8.

From Fig. 8 can be concluded that the effect of catalysts on the phase shift between voltage and current waveforms can be grouped into two families; the first one involves the discharge with TiO_2, $BaTiO_3$, and ZnO photocatalysts. The second group is for the discharge without the photocatalyst and with WO_3. For each of these groups, the effect of photocatalysts is the same, but for the discharge without the photocatalyst and the discharge with WO_3, the phase shift is higher than for the discharge with TiO_2, $BaTiO_3$, and ZnO photocatalysts.

Thus, we can say that for our experimental conditions, for the constant discharge voltage, the photocatalysts have no substantial effect on the effective value of the discharge current, but the presence of TiO_2, ZnO, and $BaTiO_3$ slightly increases discharge power and also decreases the phase shift between voltage and current.

Besides, the agreement between the results presented in Fig. 8 and the results dealing with ozone concentrations shown in Fig. 9 and Fig. 10 suggests that the phase shift between the applied voltage and current waveforms could also be added to the quantities influencing discharge
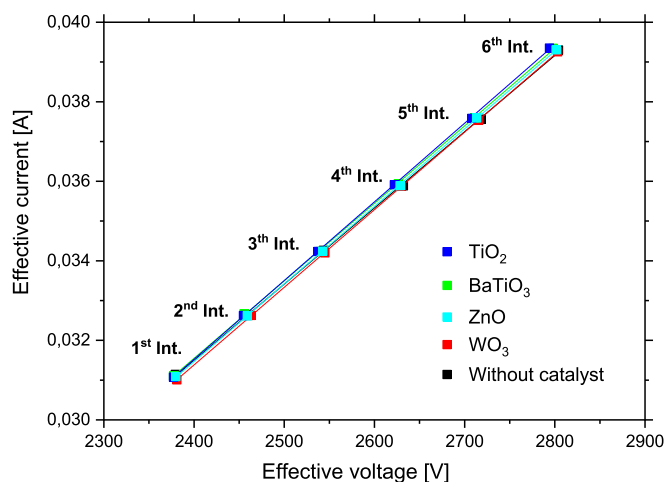

Fig. 6. Current and voltage waveforms for the discharge without and with different photocatalysts.

Fig. 7. Effective current versus voltage for the discharge without and with photocatalysts.
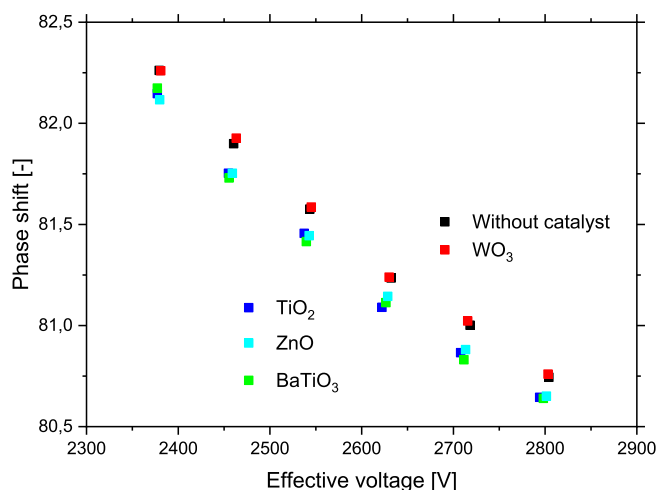
Fig. 8. Phase shifts between applied voltage and current for the discharge without and with various photocatalysts as a function of the effective voltage.
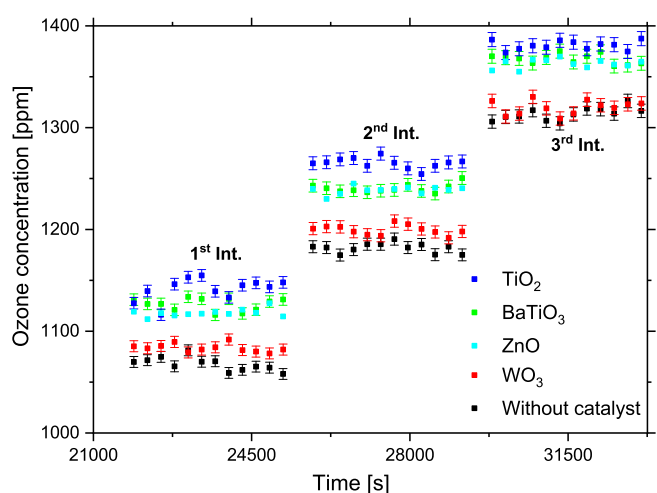

Fig. 9. Time dependences of ozone concentrations generated by the discharge without and with the photocatalysts for the first, second, and third measuring intervals.
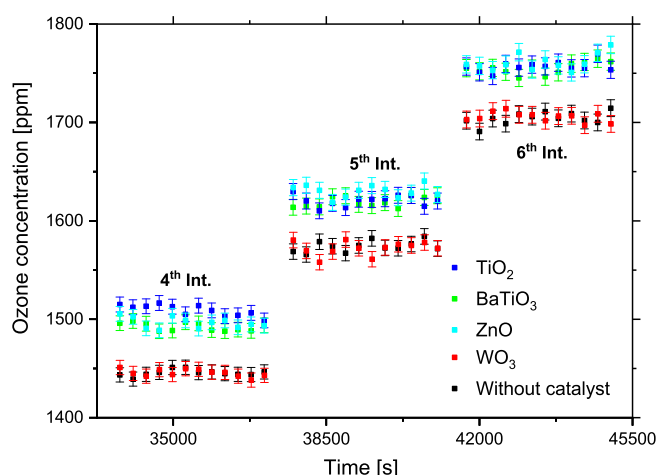

Fig. 10. Time dependences of ozone concentrations generated by the discharge without and with the photocatalysts for fourth, fifth, and sixth measuring intervals.

ozone production in the presence of photocatalysts.

In this situation, a certain role can be played by the change in the contribution of the charge transferred by the plasma filaments when different photocatalysts are used. This contribution is affected by the charged species generated by the surface reactions, which are associated with the internal structure of photocatalysts (e.g., the width of the forbidden energy gap). We can therefore assume that their impact on discharge ozone production can be attributed mainly to photocatalysis.

3.3. Time stability and catalytic effects of photocatalysts on discharge ozone production

We investigated the effect of the TiO_2, ZnO, $BaTiO_3$, and WO_3 photocatalysts on the concentration of ozone produced by the discharge, together with the time stability of this process. To be sure that the discharge parameters, as well as the concentration of generated ozone, are stable, we conducted two series of experiments lasting 12 h. The methodology of measurements was in both series the same. Thus, for the first measuring interval, we adjusted the discharge voltage to 2380 V; the data were collected for 3600 s, then the discharge was switched off, and after 300 s, we increased the voltage for the second interval. The first series, therefore, lasted six hours, that is 21,600 s. The corresponding values of the average discharge power for different voltages (that is, for individual measuring intervals) were shown in Fig. 4.

The ozone concentrations generated by the discharge without and with the photocatalysts presented in Fig. 9 and Fig. 10 are the results obtained in the second series of experiments in the time interval from 21,600 to 45,500 s (6 to 12 h). The time dependences of ozone concentrations for the first, second, and third measuring intervals are shown in Fig. 9. The error of ozone concentration, shown in these two figures, was determined from the technical specification of ozone monitor BMT-964 as the sum of 0.4% of measurement plus 0.1% of scale.

The time dependences of ozone concentrations for the fourth, fifth and sixth measuring intervals are shown in Fig. 10.

From Fig. 9 and Fig. 10 can be taken following conclusions. Considering the effect of investigated photocatalysts on ozone generation of the discharge, the catalysts can be divided into two groups. First, the TiO_2, ZnO, and $BaTiO_3$ catalysts increase in each measuring interval concentration of ozone generated by the discharge. There are only small differences in these concentrations for these three catalysts. On the other hand, the presence of WO_3 in the discharge does not affect the concentration of generated ozone compared with the discharge without the catalysts. Approximately the same increase of ozone concentration produced in the discharge, which was observed in the presence of TiO_2 and ZnO catalysts, agrees with our earlier results [8].

For all measuring intervals, concentrations of ozone generated by the discharge with and without the photocatalysts show good time stability.

Figs. 9 and 10 show that in contrast to TiO_2, ZnO, and $BaTiO_3$, the presence of WO_3 does not increase the concentration of ozone generated by the discharge. This result can be explained on the base of the following considerations. The WO_3 behaves as a typical *n*-type semiconductor, with a bandgap of 2.6 eV (highly crystalline) to 3.3 eV (amorphous). These bandgaps correspond to the electromagnetic radiation of wavelengths 476 and 374 nm, respectively. In our case, the layer of WO_3 is formed by highly crystalline nanoparticles of dimensions 100–200 nm. Consequently, the forbidden bandgap corresponds to the radiation wavelength of 476 nm. Considering the spectrum emitted by the discharge, see Fig. 3, it is seen that the intensity of radiation of this wavelength is negligibly small in comparison with the radiation emitted at shorter wavelengths. It can be consequently concluded that ozone generation processes will not be enhanced by the presence of the WO_3 layer.

Fig. 11 shows the dependence of average ozone concentration on the average discharge power for each measuring interval. These values of ozone concentrations were determined from the results presented in Fig. 9 for the first three measuring intervals and from Fig. 10 for the
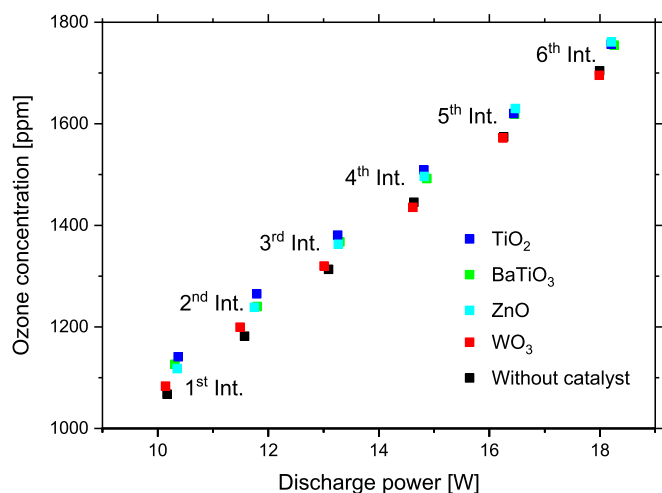
Fig. 11. Ozone concentration versus average discharge power.

fourth, fifth, and sixth intervals. Each of these average ozone concentrations for each measuring interval was calculated from 12 measurements, similar to the average discharge current.

From this figure, besides the conclusions dealing with the effect of catalysts on ozone concentrations shown in Figs. 9 and 10, there appear other interesting effects. Considering that for each measuring interval for the discharge without and with various catalysts was adjusted the same discharge voltage, it is seen that the presence of TiO_2, ZnO, and $BaTiO_3$ slightly increases discharge power. This is not true for the discharge with WO_3. Apart from it, for higher discharge powers (e.g., 5th and 6th intervals), the difference in ozone concentrations for the discharge with TiO_2, ZnO, and $BaTiO_3$ decreases.

Besides this effect, Fig. 11 shows that the ozone concentration can be grouped into two families, similar to the case of the phase shift presented in Fig. 8. The first one involves the discharge with TiO_2, $BaTiO_3$, and ZnO photocatalysts, and the second one is for the discharge without the photocatalyst and with WO_3.

The efficiency of the ozone generation process is evaluated based on ozone production yield α, which is defined as a mass of ozone produced by 1 kWh of energy:

$$\alpha = \frac{21.44 \bullet (Ozone\ concentration) \bullet Airflow \bullet 6 \bullet 10^{-3}}{P_{av}}\ [g/kWh] \qquad (6)$$

In this expression concentration of ozone produced by the discharge is substituted in ppm, airflow in slm, and average discharge power in W. For our experimental conditions, α is calculated from the following expression:

$$\alpha = \frac{0.515 \bullet O_3}{P_{av}}\ [g/kWh] \qquad (7)$$

The numerical constant 0.515 involves the density of ozone as well as all conversion factors of the airflow rate, power, and energy.

The dependences of ozone production yield as a function of the average discharge power for the discharge without the catalyst and the discharge with TiO_2, ZnO, $BaTiO_3$, or WO_3 catalysts are shown in Fig. 12. The ozone production yield error was estimated as 9%.

From this figure, we can take the following conclusions. Within the investigated power range, the highest ozone production yield is obtained for the discharge with the TiO_2 photocatalyst. The lowest ozone production yield is attained for the discharge without any photocatalyst. For the highest discharge power, there is only a small difference in ozone production yield for the discharge with TiO_2, $BaTiO_3$, or ZnO. For these power values, the WO_3 has no substantial effect on the ozone production yield.

Important quantities for practical applications of generated ozone
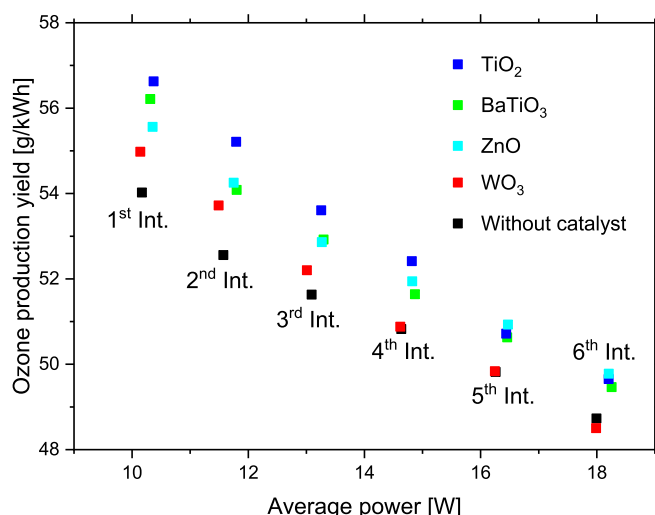
Fig. 12. Ozone production yield as a function of the average discharge power for the discharge without and with the catalysts.

are its concentration and production yield. The optimum situation involves the highest production yield and simultaneously the highest concentration of generated ozone. However, in certain respects, these two quantities are represented by conflicting requirements.

The role of individual photocatalysts on the concentration of ozone produced by the discharge simultaneously with the production yield is demonstrated in Fig. 13. Thus, for example, for a certain yield of 54 g/kWh for the discharge without any catalyst, an ozone concentration of 1050 ppm can be obtained. For the same production yield and the discharge with TiO_2 can be obtained ozone concentration of 1373 ppm, representing an increase of 30%. Similarly, for ozone concentration, e. g., 1700 ppm for the discharge without the catalyst or discharge with WO_3 can be attained production yield 48.6 g/kWh and for the discharge with TiO_2, $BaTiO_3$ or ZnO almost 50 g/kWh.

Based on the results from Figs. 11, 12, and 13 can be attempted to answer a question dealing with the proper choice of the photocatalyst for the enhancement of ozone generation for a particular application. It is seen that simultaneously having high ozone concentration and production yield is impossible. Thus, to have the highest ozone concentrations (see Fig. 11; 5th and 6th intervals), there is no difference in using TiO_2, $BaTiO_3$, or ZnO. However, these highest ozone concentrations are

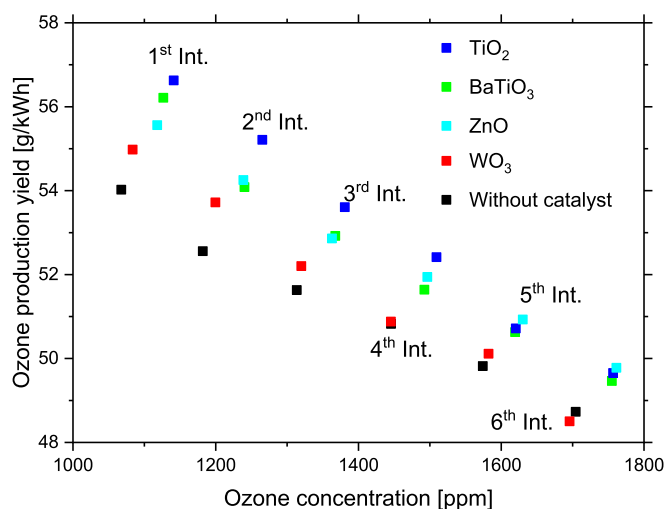**Fig. 13.** Ozone production yield as a function of ozone concentration for the discharge without and with the catalysts.

obtained for the higher discharge powers. The discharge power is involved in the ozone production yield. From Fig. 12, it is seen that for smaller discharge powers, ozone production yield depends on the type of the catalyst, and the best results are obtained for the discharge with TiO$_2$. It is also seen that even WO$_3$ increases ozone production yield for the smallest powers.

Finally, the detailed insight into the role of individual photocatalysts on ozone production yield simultaneously with ozone concentration gives Fig. 13. It can be concluded that for smaller ozone concentrations, each of investigated photocatalysts affects in different ways ozone production yield. For the highest ozone concentrations, these differences decrease.

The final decision on which catalysts to use for a particular application represents a balance between the physics of the discharge, the mechanism of photocatalysis, and the economy of choice.

4. Conclusions

We investigated the effect of TiO$_2$, ZnO, BaTiO$_3$, and WO$_3$ photocatalysts on the concentration of ozone generated by the surface dielectric barrier discharge in air and the time stability of its generation process. The catalysts were deposited from the liquid phase by inkjet material printing and situated on the glass window opposite the active electrode. We also studied these catalysts' effect on the discharge's electrical parameters and on the phase shift between the applied voltage and current waveforms. To have reasonable values of the ozone production yield, we measured the discharge power by two methods. The first used the Pearson current monitor, and the second used the measuring capacitor.

Our findings can be summarized as follows:

The layers of catalysts show no substantial effects on the electrical parameters of the discharge.

The layers of TiO$_2$, ZnO, and BaTiO$_3$ catalysts for particular discharge power increase the ozone concentration generated by the discharge. There are only small differences in the effect of these catalysts on ozone concentration.

For particular discharge power, the layer of WO$_3$ in the discharge does not affect the concentration of generated ozone.

For the time interval lasting 12 h, the concentration of ozone generated by the discharge with individual catalysts and the discharge without the catalyst show good time stability.

For the highest discharge power, there is only a small difference in ozone production yield for the discharge with TiO$_2$, BaTiO$_3$, or ZnO. For these values of power, particularly WO$_3$ has no substantial effect on the ozone production yield.

It can be therefore concluded that investigated photocatalysts from the standpoint of their effects on ozone generation of the discharge can be divided into two groups. First, the TiO$_2$, ZnO, and BaTiO$_3$ catalysts increase the concentration of ozone generated by the discharge. Secondly, the presence of WO$_3$ in the discharge has no substantial effect on the concentration of generated ozone.

The obtained results could contribute to a deeper understanding of discharge-catalyst interaction. Still, they can also have a direct application impact, for example, in plasma medicine for wound decontamination and fast healing, sterilization, inactivation of bacteria and viruses, and food and vegetable storage.

CRediT authorship contribution statement

J. Mikeš: Conceptualization, Methodology, Investigation, Formal analysis, Visualization, Project administration, Funding acquisition, Writing - original draft, Writing - review & editing. **S. Pekárek:** Conceptualization, Methodology, Investigation, Supervision, Formal analysis, Visualization, Writing - original draft, Writing - review & editing. **P. Dzik:** Investigation, Supervision, Formal analysis.

Declaration of Competing Interest

The authors declare that they have no known competing financial interests or personal relationships that could have appeared to influence the work reported in this paper.

Data availability

No data was used for the research described in the article.

Acknowledgements

References

[1] M.A. Malik, A. Ghaffar, S.A. Malik, Plasma Sources Sci. Technol. 10 (2001) 82–91, https://doi.org/10.1088/0963-0252/10/1/311.

[2] Ch. Morrison, A. Atkinson, A. Zamyadi, F. Kibuye, M. McKie, S. Hogard, P. Mollica, S. Jasim, E.C. Wert, Ozone Sci. Eng. 43 (1) (2021) 2–20, https://doi.org/10.1080/01919512.2020.1839739.

[3] R. Mohanapriya, R. Kalpana, K.V. Aravinth, Ind. J. Nutr. Dietetics 59 (2) (2022) 232–249, https://doi.org/10.21048/IJND.2022.59.2.29211.

[4] M.A. Malik, Plasma Chem. Plasma Process. 30 (2010) 21–31, https://doi.org/10.1007/s11090-009-9202-2.

[5] U. Kogelschatz, B. Eliasson, M. Hirth, Ozone Sci. Eng. 10 (1988) 367–377, https://doi.org/10.1080/01919518808552391.

[6] H.H. Kim, Y. Teramoto, A. Ogata, Plasma Catalyst Interact. 106 (2019) 47–68, https://doi.org/10.1007/978-3-030-05189-1_3.

[7] G. Magesh, B. Viswanathan, R.P. Viswanath, T.K. Varadarajan, Environ. Energy Fuel 21 (2007) 1–37.

[8] S. Pekárek, J. Mikeš, J. Krýsa, Appl. Catal. A Gen. 502 (2015) 122–128, https://doi.org/10.1016/j.apcata.2015.06.003.

[9] A. Fujishima, T.N. Rao, D.A. Tryk, J Photochem Photobiol C: Photochem Rev 1 (2000) 1–21.

[10] A. Janotti, Ch.G. Van de Walle, Rep. Prog. Phys. 72 (2009), 126501.

[11] K. Suzuki, K. Kijima, Jpn. J. Appl. Phys. 44 (2005) 2081–2082, https://doi.org/10.1143/JJAP.44.2081.

[12] B. Ertuǧ, Am. J. Eng. Res. 02 (2013) 01–07.

[13] A. Rydosz, K. Dyndał, K. Kollbek, W. Andrysiewicz, M. Sitarz, K. Marszałek, Vacuum 177 (2020), https://doi.org/10.1016/j.vacuum.2020.109378.

[14] R.A. Carcel, L. Andronic, A. Duta, Mater. Charact. 70 (2012) 68–73, https://doi.org/10.1016/j.matchar.2012.04.021.

[15] R. Gracia, S. Cortés, J. Sarasa, P. Ormad, J.L. Ovelleiro, Ozone Sci. Eng. 22 (5) (2000) 461–471, https://doi.org/10.1080/01919510009408790.

[16] J. Li, C. Ma, S. Zhu, F. Yu, B. Dai, D. Yang, Nanomaterials 9 (10) (2019) 1–34, https://doi.org/10.3390/nano9101428.

[17] T. Svoboda, M. Veselý, R. Bartoš, T. Homola, P. Dzik, Catalysts 11 (1) (2021) 50, https://doi.org/10.3390/catal11010050.

[18] S. Pekárek, J. Mikeš, I. Beshajová Pelikánová, F. Krčma, P. Dzik, Plasma Chem. Plasma Process. 36 (2016) 1187–1200, https://doi.org/10.1007/s11090-016-9723-4.

[19] T. Vidmar, M. Topič, P. Dzik, U.O. Krašovec, Sol. Energy Mater. Sol. Cells 125 (2014) 87–95, https://doi.org/10.1016/j.solmat.2014.02.023.

[20] K. Yanallah, F. Pontiga, A. Fernández-Rueda, C. Castellanos, J. Phys. D. Appl. Phys. 42 (6) (2009) 1–8, https://doi.org/10.1088/0022-3727/42/6/065202, 065202.

[21] T.C. Manley, Trans. Electrochem. Soc. 84 (1) (1943) 83–96, https://doi.org/10.1149/1.3071556.

[22] U. Kogelschatz, Plasma Chem. Plasma Process. 23 (2003) 1–46, https://doi.org/10.1023/A:1022470901385.

[23] R. Brandenburg, Plasma Sources Sci. Technol. 26 (2017), 053001, https://doi.org/10.1088/1361-6595/aa6426.

[24] O. Guaitella, F. Thevenet, Ch. Guillard, A. Rousseau, J. Phys. D. Appl. Phys. 39 (14) (2006) 2964–2972, https://doi.org/10.1088/0022-3727/39/14/015.

A.10 Effect of TiO_2 on Various Regions of Active Electrode on Surface Dielectric Barrier Discharge in Air

S. Pekárek, J. Mikeš, I. Beshajová-Pelikánová *et al.*, 'Effect of TiO_2 on various regions of active electrode on surface dielectric barrier discharge in air,' *Plasma Chemistry and Plasma Processing*, vol. 36, no. 5, pp. 1187–1200, Jun. 2016. DOI: 10.1007/s11090-016-9723-4.

CrossMark

ORIGINAL PAPER

Effect of TiO$_2$ on Various Regions of Active Electrode on Surface Dielectric Barrier Discharge in Air

S. Pekárek[1] · J. Mikeš[1] · I. Beshajová Pelikánová[1] ·
F. Krčma[2] · P. Dzik[2]

Abstract For surface dielectric barrier discharge in air, we examined the effect of titanium dioxide on various regions of the active electrode on the electrical parameters of discharge, on its emission spectra, and for demonstration of the obtained results also on the concentration of ozone produced by the discharge. We used the active electrode in the form of nine interconnected parallel strips and a square counter electrode. The TiO$_2$ layer covered either only the strips, the region between the strips, or all active electrode. As reference discharge we used the discharge without any layer of TiO$_2$. We found that direct application potential has a version when the strips of the active electrode are covered with a layer of TiO$_2$, because the concentration of ozone produced by the discharge is the highest in all investigated cases. This finding could therefore be used for construction of more efficient ozone generators.

Keywords Surface dielectric barrier discharge · Photocatalysis · Titanium dioxide · Ozone

Introduction

Plasma catalysis holds great promise for a wide range of environmental applications of corona or dielectric barrier discharge at atmospheric pressure. These applications involve e.g. cleaning water, volatile organic compounds decomposition, increasing storage time of food and vegetables, surface treatment, medical applications, production of ozone etc. Plasmachemical processes occurring in non-equilibrium plasma of this discharge are responsible for the generation of various active species, as well as electromagnetic radiation of various wavelengths. These discharge products affect the efficiency of the

✉ S. Pekárek
  pekarek@fel.cvut.cz

1 FEE, Czech Technical University in Prague, Prague, Czech Republic

2 FCH, Brno University of Technology, Brno, Czech Republic

aforementioned applications, and the process viability should be maximised in terms of energy efficiency and product selectivity.

In order to optimise the processes' viability, different factors could be varied. These factors include e.g. the nature of the gas, asymmetry in the geometry of the active and grounded electrode, applied voltage and frequency or presence of conductive coating on the dielectric walls of the reactor. One of the most promising techniques is however the usage of various catalysts or photocatalysts in the discharge [1–5].

Heterogeneous catalysts can be combined with non-thermal plasma produced by electrical discharge in two ways: by introducing the catalyst in the discharge zone [6–10], or by placing the catalyst after the discharge zone [11, 12]. In both cases, the catalyst material can be in the form of coating, powder, granulates, coated fibers or pellets. In these cases the catalyst is placed in the discharge chamber usually on the walls of the chamber or in the inter-electrode space but the active electrode is catalyst free.

In contrast with these studies, as well as with our previous results published in [5, 9, 10, 13] we present the results of a systematic experimental study of the effect of a TiO_2 photocatalyst layer on different regions of the active electrode of surface dielectric barrier discharge (SDBD) in air. We used the active electrode in the form of nine inter-connected parallel strips and a square counter electrode. The TiO_2 layer covered either only the strips, the region between the strips, or all active electrode. As long as the discharge develops along the surface of the active electrode we substantially affected discharge properties. We studied the effect of this TiO_2 layer in these different regions of the active electrode on electrical parameters of the discharge, on its emission spectra and also on discharge ozone production. We chose discharge ozone production because it has a large application potential, and therefore has been the subject of extensive research [14–19].

Experimental Setup and TiO_2 Photocatalyst

Experimental Setup

The experimental arrangement, shown in Fig. 1, consists of a discharge chamber, electrical and optical diagnostics, an air feeding system, and an ozone monitor.
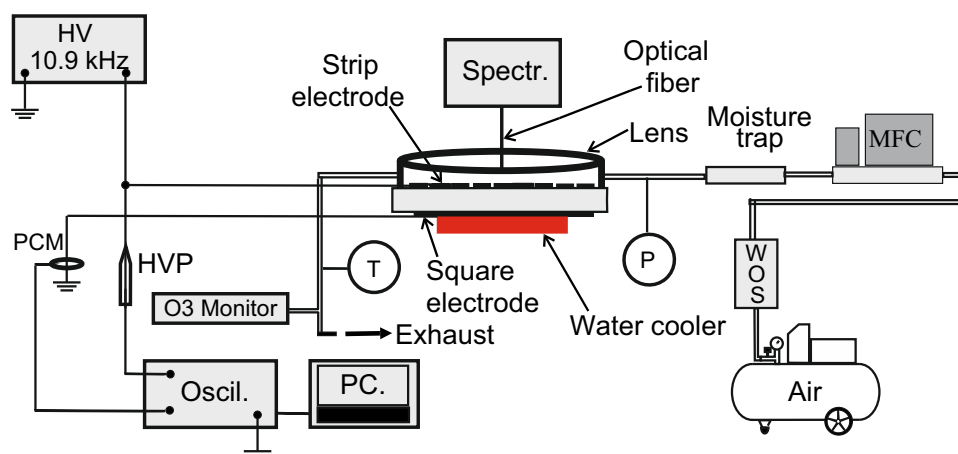
Fig. 1 Experimental arrangement

The discharge chamber was created by the polymethyl methacrylate Plexiglas box of inner dimensions $38 \times 38 \times 4.8$ mm, which was placed on an alumina plate of dimensions $50 \times 50 \times 0.635$ mm. On the side of the alumina plate covered by the plexiglass box, the active electrode of the SDBD was screen printed. This electrode consisted of nine interconnected strips. The width of each strip was 1 mm, its length was 36 mm and the gap between the strips was 3 mm. The area of the active electrode was 324 mm^2. On the other side of the alumina plate, the square electrode of dimensions 36×36 mm was screen printed. The area of this grounded electrode was 1296 mm^2. The layout of electrodes, which was also used in our previous paper [13], is shown in Fig. 2.

In order to remove the heat generated by the discharge and to stabilise the temperature, the square counter electrode was placed on a copper water-cooled plate. To better see the discharge, in the upper side of the discharge chamber we placed a lens.

We used a white coloured alumina plate with a content of Al_2O_3 of 96 %, mass density of 3.7 g/cm^3, roughness 0.25–0.7 μm, a dielectric constant for 1 MHz of 9.6, electric strength of 14 kV/mm and the heat conductivity for temperature of 25 °C of 24 W/m.K.

The electrode system was produced by screen printing using the DuPont nickel-based paste 9538. The sheet resistivity of the layer made from this paste is 30–60 mΩ/sq at 25 μm thickness.

The air into the discharge chamber was supplied from a compressor through a water and oil separator (WOS), mass flow controller (MFC) and through a moisture trap. The input/output of air into/out of the discharge chamber was through three tubes, so that the flow of air was parallel to the strips. The square grounded electrode was placed on the water cooler.

To investigate the effect of TiO_2 on various regions of the active electrode, we made four identical discharge chambers, which differed only by presence (or lack thereof) of TiO_2 on various regions of the active electrode.

The experiments were performed with a sinusoidal driving voltage of 10.9 kHz and a peak-to-peak voltage of up to 9 kV. On the first channel of an ADS 1102CM digital storage oscilloscope (150 MHz) we sampled and recorded the discharge voltage through the high-voltage probe (HVP-28HF, Pintek; division ratio: 1000/1; frequency: up to 200 MHz). To determine the discharge current, we used a signal obtained from a Pearson current monitor (PCM, model 2877) with a bandwith of up to 200 MHz. Average discharge power was calculated on the basis of the following equation:

Fig. 2 Layout of electrodes. Upper side of the alumina plate—active strip electrode; lower side of this plate—grounded square electrode (*grey region*)
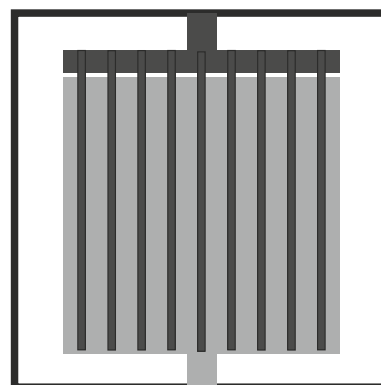
$$P_{av} = \frac{1}{T} \int_0^T V(t)I(t)dt,$$

where T is the period, and $V(t)$ and $I(t)$ are voltage and current signals respectively.

The ozone concentration was measured by absorption of the 254 nm UV spectral line using an API 450 ozone monitor.

The discharge emission spectra in the range of 249–697 nm were recorded using a HR2000+ High-Speed Miniature Fiber Optic Spectrometer. The spectral resolution of the spectrometer was 0.5 nm. The spectra were collected by an optical fiber directly through the opening in the upper side of the discharge chamber, perpendicular to the strip electrode.

A photograph of the discharge without any layer of TiO_2 on the active electrode for discharge voltage 3.2 kV and airflow through the discharge chamber 1.8 slm is shown in Fig. 3.

Preparation of the Photocatalyst and Geometry of the Active Electrode Regions with TiO_2

The layout of electrodes on the dielectric plate is shown in Fig. 2. To investigate the effect of TiO_2 on various regions of the active strip electrode on properties of the discharge, the TiO_2 layer covered either only the strips, the region between the strips, or all active electrode. In Fig. 4 are shown regions on the side of the dielectric plate carrying the active electrode covered by the TiO_2 photocatalyst.

Preparation of Silica Binder

The hybrid organosilica binding agent was prepared through the sol–gel process according to the procedure described in [20]. Methyltriethoxysilane (MTEOS, supplied by ABCR) was used as the silica precursor and was subjected to acid-catalysed hydrolysis and condensation. During the reaction, the methyl groups are much more resistant to hydrolytic scission than the oxyethyl ones, so the structure of the resulting product can be described as methyl-substituted amorphous silica. The residual methyl groups ensure solubility in polar anhydrous solvent, so a stock solution of 20 wt% in anhydrous ethanol was prepared and used for the mixing of the printing ink.

Fig. 3 Photograph of the discharge in air without any layer of TiO_2 on the active electrode. Discharge voltage 3.2 kV and airflow through the discharge chamber 1.8 slm

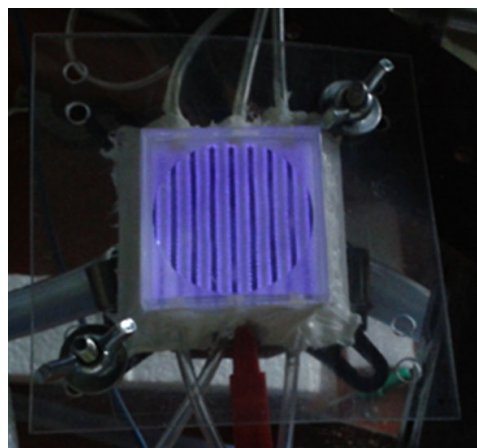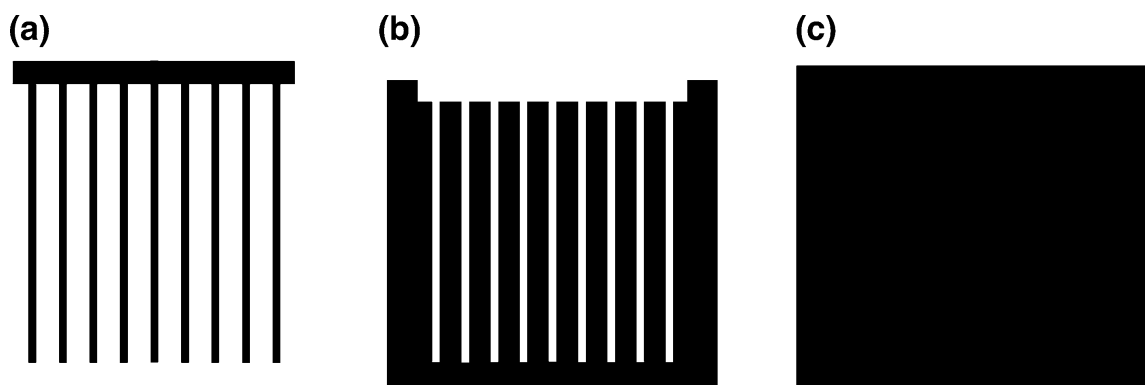**Fig. 4** Regions covered by TiO_2 on the side of the dielectric plate carrying the active strip electrode. **a** TiO_2 on the strips; **b** TiO_2 between the strips; **c** TiO_2 on all areas

Preparation of the Ink

A stock dispersion of titanium dioxide (Evonik P-25) in Dowanol PM (1-Methoxy-2-propanol), having the same dry mass content as the silica binder solution (i.e., 20 wt%), was mixed. The printing formulation was then prepared by mixing 2 mL of the silica binder solution, 6 mL of the titania dispersion and 6 mL of a viscosity-controlling solvent (butanol) in a 20 mL glass vial. Thus the dry mass content was set to 0.114 g/mL and the titania/silica ratio was 3:1. Approximately 3 g of 1 mm diameter glass balls were added to the vial, and it was shaken for 1 day on an oscillating plate shaker set to 900 rpm. After the ball-milling phase was finished, the ink was further diluted by 6 mL of *n*-hexanol, and the printing ink was obtained.

Printing

The TiO_2 layers on the side of the dielectric plate carrying the active electrode were created with an experimental inkjet printer Fujifilm Dimatix 2831. The printer features a disposable 16-nozzle piezoelectric jetting printhead coupled with a 2 mL polyethylene ink tank. It is capable of printing on A4 size substrates with a resolution of up to 5080 dpi, i.e. 5 μm. Both substrate and printhead can be heated in order to speed up solvent evaporation and reduce ink viscosity, respectively. A stroboscopic camera provides still images or slowed-down video for observation of drop formation process, while another fiducial camera is used for precise substrate positioning and aligning of subsequent print layers. The printer has been successfully employed for the deposition of a wide variety of functional and auxiliary layers, and during the past few years has become the *de facto* industrial standard tool for ink development and testing.

Generally, the following procedure was repeated for each tested formulation: the prepared ink was loaded into a syringe and a blunt needle was attached to the syringe lure ports. The ink was filled into the Dimatix ink tank and the Dimatix 10 pL printing head was attached to the tank; the set was mounted into the Dimatix printer. The drop formation characteristics of all formulations were checked by means of the built-in stroboscopic camera, and the interaction of the printed material with the substrate was observed by an optical microscope. The following printer settings were used: Dimatix Model fluid 2 waveform, 18 V driving voltage, nozzle temperature 30 °C, substrate temperature 40 °C. The nozzle span was set to 40 μm (i.e. 25 drops per mm, 625 drops per mm^2). Printing was

performed twice to ensure complete coverage of the substrate and to reduce layer porosity. Complete drying took place after printing each layer, so that the following layer was printed in the "wet-to-dry" manner. The deposition process was finalised by curing. The printed samples were annealed at 450 °C in air (heating ramp of 3 °C/min and 30 min sustained at the target temperature).

Experimental Results

Our experiments were performed with a sinusoidal driving voltage of frequency 10.9 kHz. The airflow through the discharge chamber was adjusted to 1.8 slm. The experiments were performed in a range of temperatures of air at the output from the discharge chamber of 23 ± 2 °C.

Effect of TiO_2 on Various Regions of the Active Electrode on Electrical Characteristics of the Discharge

In order to compare the effect of TiO_2 on various regions of the active electrode on electrical parameters of the discharge, we recorded voltage-current waveforms for: the discharge with active electrode without TiO_2, the discharge with active electrode with a layer of TiO_2 on the strips, the active electrode with a layer of TiO_2 between the strips and finally for the active electrode with a layer of TiO_2 on all areas. Covering different regions of the active electrode with a layer of TiO_2 changes capacitance of the electrode system. Thus the capacitance of the system changes from 99.6 pF for the system without any TiO_2 on the active electrode to 102.6 pF for case when there was a layer of TiO_2 on the strips, to 109.6 pF when a layer of TiO_2 was on all area and finally to 115.6 pF when there was a layer of TiO_2 between strips.

For illustrative purposes, Fig. 5 shows voltage-current waveforms for the discharge without TiO_2 on active electrode for the discharge voltage 3.2 kV. From this figure, the asymmetry in current waveforms for positive and negative half-periods of the driving
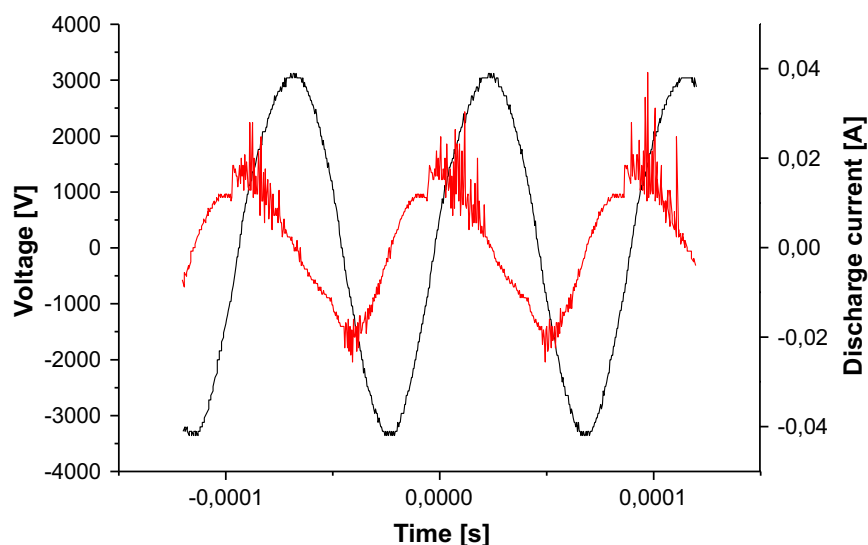

Fig. 5 Voltage current waveforms for the discharge without any TiO_2 on active electrode. Discharge voltage 3.2 kV

voltage can be seen. This asymmetry, which is associated with different microdischarge activities, is an inherent property of surface dielectric barrier discharge caused by asymmetry in the geometry of active and grounded electrodes [21].

We also found that the presence of TiO_2 on various regions on the side of dielectric plate carrying the active electrode neither influences the shape of voltage waveform nor the phase shift between voltage and current waveforms.

In order to make the comparison of the effect of TiO_2 on various regions of this electrode on electrical parameters of the discharge more illustrative, in Fig. 6 we therefore show only current signals for the same discharge voltage of 3.2 kV. Thus Fig. 6a shows the current signal for the discharge with active electrode without TiO_2; Fig. 6b shows the current signal for the discharge with active electrode with a layer of TiO_2 on the strips only; Fig. 6c is for the active electrode with a layer of TiO_2 between the strips; and finally Fig. 6d shows the current signal for the discharge with a layer of TiO_2 on all areas of the active electrode.

From Fig. 6, it is clear that covering various regions of the active electrode with a layer of TiO_2 electrical parameters of the discharge differently. As long as the discharge current for different cases shows multiple current peaks we take as the main criterion for the comparison of the effect of TiO_2 on various regions of the active electrode on the discharge the average discharge current. From Fig. 6 it is seen that average current for discharge without any TiO_2 was ~ 2.0 mA, while for the case when TiO_2 was on the strips, the average discharge current was ~ 2.2 mA. For the case when TiO_2 was between the strips
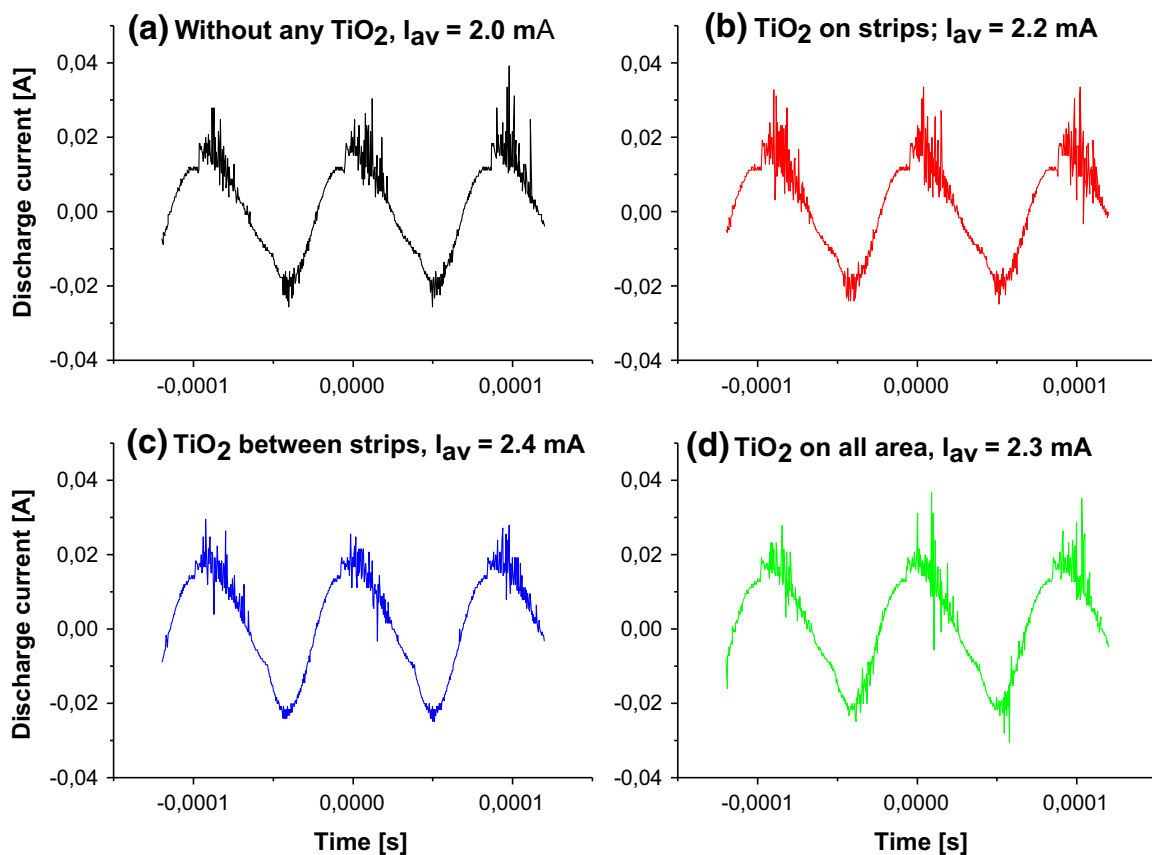
Fig. 6 Discharge current waveforms. **a** active electrode without TiO_2; **b** active electrode with a layer of TiO_2 on the strips; **c** active electrode with a layer of TiO_2 between the strips; **d** layer of TiO_2 on all areas of the active electrode. Discharge voltage 3.2 kV

the average discharge current was ~ 2.4 mA and when TiO$_2$ was on all areas of the active electrode, the average discharge current was ~ 2.3 mA. This comparison was made for the discharge voltage of 3.2 kV.

Similar effects of various materials in the discharge chamber on the electrical parameters of the discharge are also described in [22, 23]. Thus in [22] it is shown that for DBD with a sinusoidal driving voltage, large current amplitude peaks depend on the presence of photocatalytic porous materials containing TiO$_2$. The fact that the electrical characteristics of the dielectric barrier discharge depend on the surface conductivity of the reactor walls is also demonstrated in [23].

Effect of TiO$_2$ on Various Regions of the Active Electrode on Discharge Emission

An illustrative example of the discharge spectra for the discharge with a layer of TiO$_2$ on the strips, layer of TiO$_2$ between strips, layer of TiO$_2$ on all areas of the active electrode, and finally for discharge without any TiO$_2$ on the active electrode is shown in Fig. 7. In all cases the discharge voltage is 3.2 kV.

From Fig. 7, it can be concluded that for all four situations, the emission spectra contain the same spectral lines, however with varying intensities. These observed spectral lines could be attributed to the second positive system of N$_2$ [C$^3\Pi_u$ − B$^3\Pi_g$]. For this system the most intense peak is observed at the wavelength of 336.7 nm. The numerical values of intensities, shown in Fig. 7, are given in arbitrary units and these values are valid only for
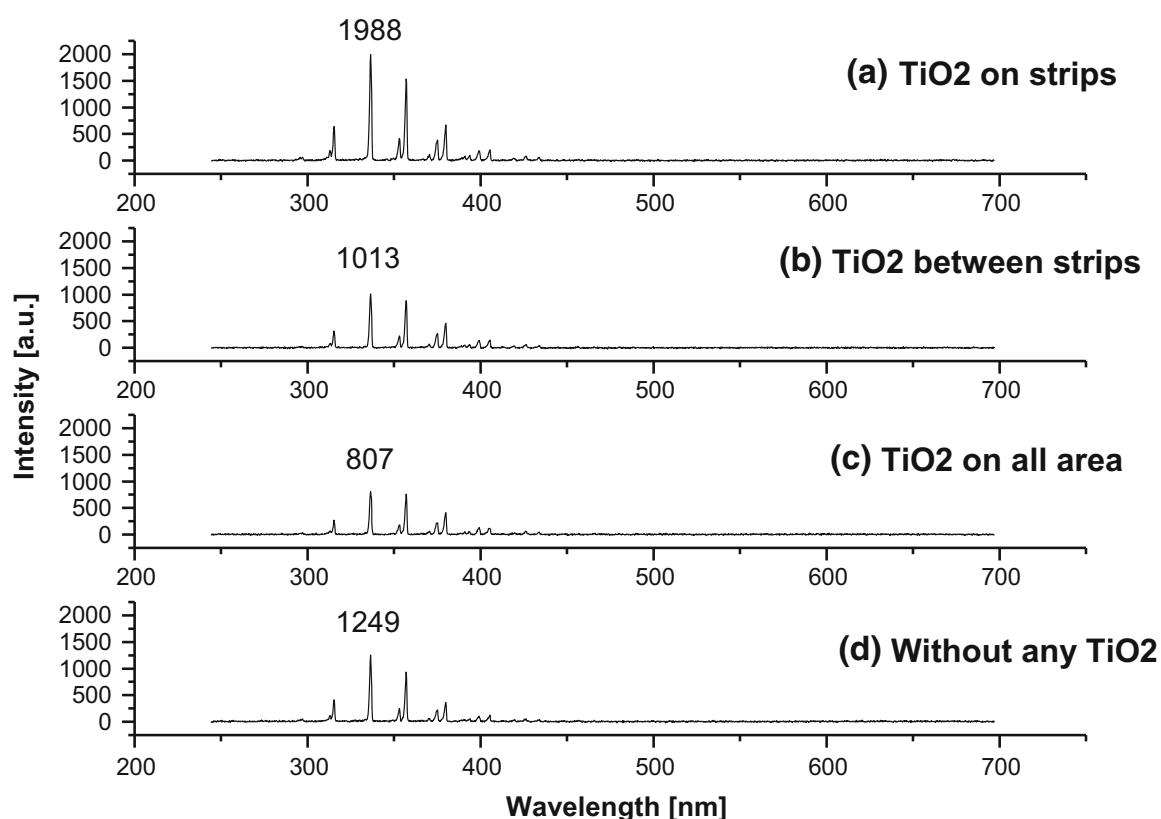
Fig. 7 Emission spectra of the discharge with various regions of the active electrode covered by TiO$_2$. **a** active electrode with a layer of TiO$_2$ on the strips only; **b** active electrode with a layer of TiO$_2$ between the strips; **c** layer of TiO$_2$ on all areas of the active electrode; **d** active electrode without any TiO$_2$. Discharge voltage 3.2 kV

spectral line of 336.7 nm. From this figure it is seen, that the highest intensity is obtained for discharge with a layer of TiO_2 on the strip electrode (1988 a.u.); the second highest intensity is for discharge without any TiO_2 on the active electrode (1249 a.u.); then discharge with a layer of TiO_2 between strip electrodes (1013 a.u.); and the smallest intensity is obtained for the discharge with a layer of TiO_2 on all areas of the active electrode (807 a.u.).

This smallest intensity of UV radiation for the discharge with a layer of TiO_2 on all areas could be explained by absorption of this UV emission. This finding corresponds with the result presented in [24]. In this paper were observed the UV–Vis emission spectra from the outside of envelope tube containing surface discharge plasma. When the envelope with TiO_2 coating was used, the UV light was not detected. This indicates that UV light from plasma was absorbed by TiO_2.

Effect of TiO_2 on Various Regions of the Active Electrode on Discharge Ozone Production

Ozone is formed by plasmachemical processes occurring in the discharge volume. There could be a contribution to ozone production due to the photocatalytic process caused by the presence of TiO_2 on various regions of the active electrode. As an illustrative example of the effect of TiO_2 on various regions of the active electrode, we show in Fig. 8 the dependence of concentration of ozone produced by the discharge versus discharge power for the four aforementioned cases.

From Fig. 8 it can be seen that the concentration of ozone produced by the discharge is affected by placement of TiO_2 on various areas of the active electrode differently. Thus for a particular average discharge power, the highest concentration of produced ozone is obtained for the case when the layer of TiO_2 is on the strip electrode. It is also seen that the trend of the dependence of ozone concentration versus average discharge power for this
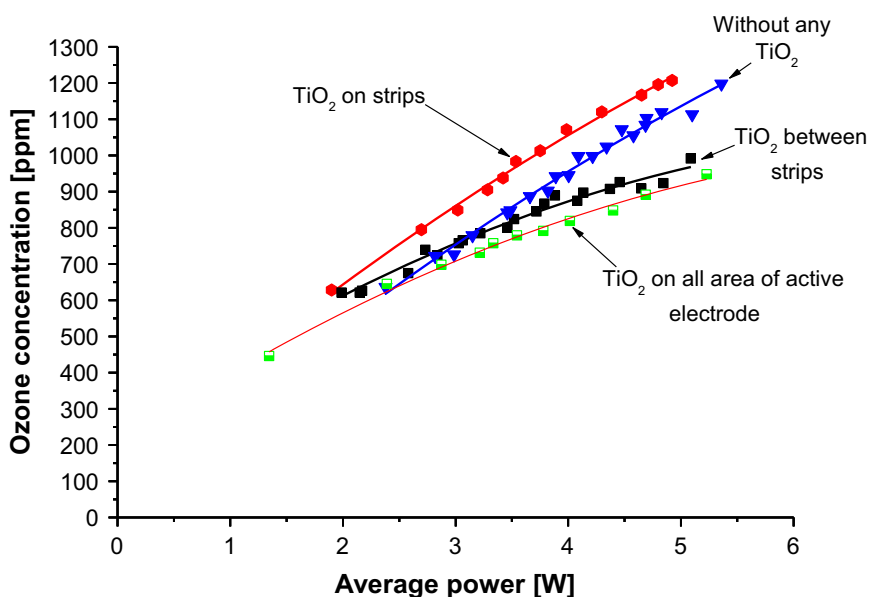
Fig. 8 Ozone concentration versus average discharge power. **a** Active electrode without TiO_2; **b** active electrode with a layer of TiO_2 on the strips only; **c** active electrode with a layer of TiO_2 between the strips; **d** layer of TiO_2 on all areas of the active electrode

case is similar to the trend of the dependence of ozone concentration versus average discharge power for the case without any TiO_2 on the active electrode.

The situation is different for the case when the layer of TiO_2 is on regions between the strips and on all areas of the active electrode. In both cases, the ozone concentration for average powers exceeding $\sim$ 3 W is decreased compared to the discharge when there is no TiO_2 on the active electrode. The smallest ozone concentration for any particular power is produced when the layer TiO_2 is on all areas of the active electrode. From Fig. 8 is can also be seen that the trend of the curve showing the dependence of ozone concentration on discharge power is similar when TiO_2 is in the region between the strips and when TiO_2 is on all areas of the active electrode.

Discussion

The effect of TiO_2 on various regions of the active electrode on electric parameters of the discharge, discharge emission and discharge ozone production, involves variety of factors such as differences in material properties of alumina, nickel conductor paste and TiO_2 (dielectric constant and resistivity), consequent changes of electric field distribution, interaction of the microdischarges with the surface through the surface charge, emission of electrons, or even the difference in areas covered by TiO_2.

The first quantities, which determine the discharge functioning, are therefore material properties of alumina, TiO_2 and the conducting electrode. The dielectric alumina plate has a content of Al_2O_3 of 96 %, mass density of 3.7 g/cm^3, roughness 0.25–0.7 μm, a dielectric constant for 1 MHz of 9.6, electric strength of 14 kV/mm and a heat conductivity for temperature of 25 °C of 24 W/m.K.

The electrode system was screen printed on this alumina plate using nickel conductor paste DuPont 9538. The sheet resistivity of the layer made from this paste is 30–60 mΩ/sq at 25 μm thickness.

The TiO_2 photocatalyst in the anatase phase is an n-type semiconductor with a forbidden energy gap of 3.2 eV and dielectric permittivity $\varepsilon_r = 85$–110 (depending on the manufacturer). This high dielectric permittivity enhances the electrical energy transferred to the gas phase. TiO_2 exhibits photocatalytic properties when it is activated by UV radiation. The series of its energy levels is associated with covalent bonds among atoms composing valence band and a second series of spatially diffuse higher energy levels, which are associated with the conduction band. Both series are separated by a forbidden energy gap of 3.2 eV. The electron of the valence band becomes excited when illuminated by UV radiation of wavelength 388 nm and shorter. As seen from Fig. 7, the discharge in air is a source of radiation of various wavelengths. In the UV range, the most intense spectral lines are of wavelengths 336.7 nm, 356.5 nm and 379.2 nm. This radiation could therefore cause TiO_2 activation, which can contribute to the processes leading to the discharge ozone generation.

In order to understand at least qualitatively obtained results, we can consider the following cases.

No TiO_2 on the Active Electrode

Our reference experiment was an experiment when there was no TiO_2 layer on the active—strip electrode. This was the situation of the classical dielectric barrier discharge.

Comprehensive reviews of this discharge are given in [25, 26]. According to these papers, the classical DBD develops along the conductive electrode on the dielectric surface, and plasma does not come into direct contact with the strips. The discharge consists of distinct parallel channels that originate at the conductive electrode and terminate somewhere on the dielectric surface. The channels seem to appear simultaneously and develop independently of their neighbours. The preceding channels influence the succeeding ones by surface charges left on the dielectric surface. Apart from these charges, there exist also charges in the discharge volume and charges on the conductive electrode. All these charges certainly depend on the material properties of the alumina plate, as well as on the properties of the material of the strip electrode. The discharge performance, involving its emission as well as ozone generation, is therefore affected by the properties of these two materials.

The ozone generation in non-equilibrium discharges in air at atmospheric pressure is a two-step process [13], which starts from dissociation of molecular oxygen and nitrogen by electron impact reactions. The dissociation rates coefficients of O_2 and N_2 are functions of reduced electric field (E/n), which is defined as the ratio of electric field strength E per unit gas density n. The second step in the ozone formation is the reaction of atomic oxygen with O_2 and a third body to create an ozone molecule. Thus the main ozone-generating reaction dominant at atmospheric pressure is:

$$O + O_2 + M \rightarrow O_3^* + M \rightarrow O_3 + M,$$
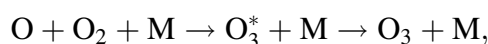
where M is a third-body collision partner (in air O_2, N_2), or a solid metallic/dielectric surface. According to [27], the optimum reduced electric field for ozone generation from air at atmospheric pressure is about 200 Td; this process takes about 100 μs.

Layer of TiO_2 is Only on the Strips of the Active Electrode

In this case, the conductive strip discharge electrode is covered by a layer of TiO_2 semiconductor. As mentioned earlier, the discharge develops along the conductive electrode on the dielectric surface; therefore the plasma does not come into direct contact with the layer of TiO_2 on the strips.

As seen from comparison of Fig. 6a, b, electrical parameters of the discharge are changed, which results in the change of emission spectra and finally in the change in discharge ozone production. In this case, to the production of ozone due to the volume processes in the discharge should be added ozone production due to the processes caused by the activation of the TiO_2 photocatalyst on the strips by ultraviolet radiation emitted from the discharge. When the TiO_2 photocatalyst absorbs ultraviolet radiation produced by de-excitation processes in the discharge, the electron of the valence band of titanium dioxide becomes excited. The excess energy of this excited electron promotes the electron to the conduction band of TiO_2, therefore creating the negative-electron (e−) and positive-hole (h+) pair:

$$TiO_2 + hf \rightarrow h^+ + e^-$$
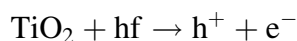
If a suitable scavenger in the vicinity of the catalyst is available to trap the electron or hole, subsequent redox reactions can occur. The electrons are capable of carrying out reduction reactions, while the holes can carry out oxidation reactions. Thus, active oxygen species O–, O_3–, and superoxide anion O_2– are produced from reactions of electrons with O_2 in air. These active oxygen species together with other radicals should be added to plasma components produced by the discharge. All these species at different levels contribute to

the processes leading to the discharge ozone production. It is therefore reasonable to expect that covering the strip electrode with a layer of TiO_2 should contribute to the discharge ozone production.

From Fig. 8 it can be seen that when the layer of TiO_2 covers the strip electrode, the discharge ozone production is the highest in all four investigated cases. This finding could have important application impacts, which could be utilised in the construction of more efficient ozone generators.

TiO_2 Layer Only in the Regions Between the Strips of the Active Electrode

As long as the discharge develops in this region, the change in electrical properties of this region will affect the discharge properties. For propagation of the discharge in this region, an important role is played by the distribution of the electric field. One of the quantities that affects electric field distribution is the dielectric constant, ε_r. In the case of alumina, $\varepsilon_r = 9.6$. When the surface of alumina is covered by the layer of TiO_2 with the dielectric constant $\varepsilon_r = 85\text{--}110$, the electric field distribution of the gap will be changed compared to the case of field distribution without the TiO_2 layer. According to [28–30] the increase in dielectric constant makes the electric field in the gap increase at the fixed applied voltage. The change of the dielectric constant in the region between the strips of the active electrode also acts on the expansion of the positive ion cloud in the positive half-period of the driving voltage [31].

As was already mentioned, for efficient ozone generation from air, a reduced electric field $(E/n) \sim 200$ Td is required. As long as this reduced electric field has a certain optimum, it is reasonable to suppose that ε_r has also some optimum value. This conclusion is supported by the results presented in [29], where it is indicated that there exists an optimum ε_r for ozone generation.

TiO_2 Layer on all Area of the Active Electrode

This case differs from the preceding case when the layer of TiO_2 was only in the region between the strips of the active electrode only by the surface area covered by TiO_2, namely an increase in area due to the covering of the sides of the dielectric plate with TiO_2. This surface does not take any substantial part in the discharge development. The discharge develops in the region between the strips, and its properties are therefore mainly given by the properties of the region between the strips and those of conductive electrode. These two regions are the same as in the case of the layer between the strips of the active electrode. It could therefore be expected that the electrical parameters of the discharge will not be substantially different. This conclusion is supported by the results in Fig. 6, where it is seen that for the same discharge voltage the average discharge current for the discharge with a layer of TiO_2 between the strips is only slightly higher than for the discharge with TiO_2 on all areas.

From Fig. 7, it is seen that intensities of spectral lines for the case when TiO_2 is on all area of the active electrode are the smallest from all investigated cases. This result can be explained by the largest absorption area for discharge emission. As long as these intensities of UV radiation are the smallest, the photocatalyst́s contribution to the discharge ozone production will be small. This conclusion is in agreement with the results the concentration of ozone produced by the discharge, which are shown in Fig. 8.

The assumption with higher absorption of UV radiation when TiO_2 was on all areas of the active electrode is also supported by the following experimental fact. The active

electrode as well as the square electrode was screen printed on the alumina plate using the same procedure. In our preliminary experiments, the cooling of the grounded electrode for all four investigated cases was performed only by flowing air. We performed the experiment with TiO_2 on the strips, TiO_2 between the strips, TiO_2 on all areas of the active electrode, and finally with the active electrode without any TiO_2. All experiments lasted for the same time. It was found that from all four cases, only for the electrode system with TiO_2 on all areas of the active electrode was the square counter electrode stripped away. This result can be explained by excessive heating of the alumina plate with a layer of TiO_2 on all areas of the active electrode, caused by adsorption of UV radiation in the range 300–400 nm.

Conclusions

In order to better understand the influence of TiO_2 photocatalyst on electrical characteristics, emission and ozone production of surface dielectric barrier discharge, we examined the effect of placement of this catalyst on various regions of the active electrode. If we take as a reference discharge the discharge without any layer of TiO_2 on the active electrode, our findings can be summarized as follows:

- Covering the strips of the active electrode with a layer of TiO_2 increases average discharge current, increases the intensity of spectral lines, and increases the concentration of ozone produced by the discharge. The concentration of ozone produced by the discharge as well as discharge emission is the biggest from all investigated cases.
- Covering the region between the strips of the active electrode with a layer of TiO_2 increases average discharge current, decreases the intensity of spectral lines, and decreases the concentration of ozone produced by the discharge. The average discharge current is the biggest in all investigated cases.
- Covering all area of active electrode with a layer of TiO_2 increases average discharge current. Intensity of the spectral lines, as well as the concentration of ozone produced by the discharge, are the smallest from all investigated cases.

The obtained results could contribute not only to a deeper understanding of discharge catalyst interaction, but can also have direct application impact; for example, in the construction of more efficient ozone generators.

References

1. Van Durme J, Dewulf J, Leys Ch, Van Langenhove H (2008) Appl Catal B 78:324–333
2. Neyts EC, Bogaerts A (2014) J Phys D Appl Phys 47:224010. doi:10.1088/0022-3727/47/22/224010
3. Jodzis S (2003) Ozone Sci Eng 25:63–72
4. Malik MA, Minamitani Y, Schoenbach KH (2005) IEEE Trans Plasma Sci 33:50–56
5. Pekárek S (2008) Eur Phys J D 50:171–175
6. Guaitella O, Thevenet F, Guillard C, Rousseau A (2006) J Phys D Appl Phys 39:2964–2972
7. Kim HH, Ogata A, Futamura S (2008) Appl Catal B 79:356–367
8. Weidong H, Tingting R, Weidong X (2007) Ozone Sci Eng 29:107–112
9. Pekárek S (2012) J Phys D Appl Phys 45:075201

10. Pekárek S, Mikeš J, Krýsa J (2015) Appl Catal A 502:122–128
11. Roland U, Holzer F, Kopinke FD (2015) Appl Catal B 58:217–226
12. Thevenet F, Sivachandiran L, Guaitella O, Barakat C, Rousseau A (2014) J Phys D Appl Phys 47:224011. doi:10.1088/0022-3727/47/22/224011
13. Pekárek S, Mikeš J (2014) Eur Phys J D 68:310. doi:10.1140/epjd/e2014-50393-x
14. Kogelschatz U, Eliasson B, Hirth M (1988) Ozone Sci Eng 30:367–378
15. Park SL, Moon JD, Lee SH, Shin SY (2006) J Electrostat 64:275–282
16. Hong D, Rabat H, Bauchire JM, Chang MB (2014) Plasma Chem Plasma Proc 34:887–897
17. Malik MA (2014) Ind Eng Chem Res 53:12305–12311
18. Jodzis S, Patkowski W (2016) Ozone Sci Eng 38:86–99
19. Malik MA, Hughes D (2016) J Phys D Appl Phys 49:135202. doi:10.1088/0022-3727/49/13/135202
20. Gregori D, Benchenaa I, Chaput F, Therias S, Gardette JL, Leonard D, Guillard C, Parola S (2014) J Mater Chem A 2:20096–20104
21. Pekárek S (2013) Eur Phys J D. doi:10.1140/epjd/e2013-30723-4
22. Guaitella O, Thevenet F, Guillard C, Rousseau A (2006) J Phys D Appl Phys 39:2964–2972. doi:10.1088/0022-3727/39/14/015
23. Belov I, Paulussen S, Bogaerts A (2016) Plasma Sources Sci Technol 25:015023. doi:10.1088/0963-0252/25/1/015023
24. Sano T, Negishi N, Sakai E, Matsuzawa S (2006) J Mol Catal A Chem 245:235–241
25. Gibalov VI, Pietsch GJ (2012) Plasma Sources Sci Technol 21:024010. doi:10.1088/0963-0252/21/2/024010
26. Gibalov VI, Pietsch GJ (2000) J Phys D Appl Phys 33:2618. doi:10.1088/0022-3727/33/20/31
27. Kogelschatz U, Eliasson B, Egli W (1997) J Phys IV (France 7) Colloque C4, Suppl J Phys III 47–63
28. Murata T, Tatsukawa M, Okita Y, Yasuoka K (1996) Trans Inst Elect Eng Jpn 116-A:937)
29. Chen HL, Lee HM, Chen SH, Chang MB (2008) Ind Eng Chem Res 47:2122–2130
30. Neyts EC (2016) Plasma Chem Plasma Process 36:185–212
31. Lagmich Y, Callegari T, Pitchford LC, Boef JP (2008) J Phys D Appl Phys. doi:10.1088/0022-3727/41/9/095205

A.11 Comparative study of TiO_2 and ZnO photocatalysts for the enhancement of ozone generation by surface dielectric barrier discharge in air

Comparative study of TiO$_2$ and ZnO photocatalysts for the enhancement of ozone generation by surface dielectric barrier discharge in air

S. Pekárek [a,*], J. Mikeš [a], J. Krýsa [b]

[a] Czech Technical University in Prague, Faculty of Electrical Engineering, Technická 2, 166 27 Prague 6, Czech Republic
[b] Institute of Chemical Technology Prague, Technická 5, 166 28 Prague 6, Czech Republic

A B S T R A C T

We examined the possibility of finding an alternative to the photocatalyst titanium dioxide for enhancement of ozone generation by electrical discharges. As a rough indicator of the photocatalytic activity of the catalysts, we took the concentration of the ozone produced by the surface dielectric barrier electrical discharge in air. This discharge is, apart from the source of the charged and excited species, also the source of ultraviolet radiation, which could be used for the activation of photocatalysts. From various photocatalysts we have chosen zinc oxide. We compared the effect of ZnO and TiO$_2$ on the enhancement of discharge ozone production and we found that for this application ZnO shows almost the same effect as TiO$_2$ photocatalyst.

1. Introduction

Photocatalysis is a chemical reaction occurring in photoirradiated mostly semiconductor materials. The principle of this reaction, see Fig. 1, consists of the irradiation of the photocatalyst by electromagnetic radiation with the energy of photons higher than the forbidden energy gap. This irradiation can promote electrons from the valance band to the largely vacant conduction band. Simultaneously, a positive hole with strong oxidising capability is formed. The electrons are capable of carrying out reduction reactions and holes can carry out oxidation reactions [1]. The chemical structure of the photocatalyst remains unchanged.

Due to these properties, photocatalysis has been found to be useful in a wide range of important applications such as solar cells, self-cleaning materials for residential or office buildings, air pollution control, water purification, sterilisation and medicine, and environmental applications [2].

Starting from 1972 one of the most studied photocatalysts has been titanium dioxide, TiO$_2$ [3]. TiO$_2$ is an n-type semiconductor, which can exist in several phases: TiO$_2$ in an anatase phase has a forbidden energy gap of 3.2 eV, TiO$_2$ in a rutile phase has a forbidden energy gap of 3.2 eV, TiO$_2$ in a rutile phase has a forbidden

energy gap of 3.02 eV, and TiO$_2$ in a brookite phase has a forbidden energy gap of 2.96 eV. The energy gaps of 3.2 eV and 2.96 eV correspond to electromagnetic radiation at wavelengths of 387 nm and 414 nm, respectively.

The principal task of this paper is to examine the possibility of finding an alternative to, or maybe a substitute for, TiO$_2$ for the enhancement of ozone generation by surface dielectric barrier electrical discharge in air. As a rough indicator of the photocatalytic activity of catalysts, we measured the concentration of produced ozone. Generally speaking, ozone generation by electrical discharge from air is a rather complex process involving a chain of various reactions [4–6].

In the case of ozone generation by electrical discharge only, ozone is mainly produced by reactions occurring in the discharge volume. The initial step is the electron impact dissociation of molecular O$_2$ and N$_2$ followed by other reactions among oxygen and nitrogen species. The main ozone formation reaction dominant at atmospheric pressure is:

$$O + O_2 + M \rightarrow O_3 + M, \tag{1}$$

where M is the third collision partner.

In the case of electrical discharge with the presence of catalysts, the contribution of the surface reactions due to the activation of the photocatalysts by ultraviolet radiation emitted by the discharge should be added to the volume reactions that lead to ozone generation. For the discharges in air, the strongest emissions originate

* Corresponding author. Fax: +420 233337031.
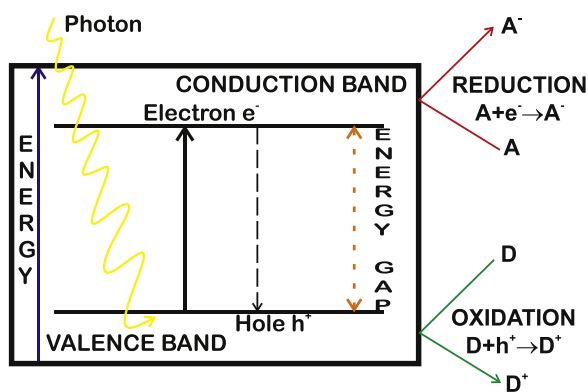E-mail addresses: pekarek@fel.cvut.cz (S. Pekárek), mikes.jan@fel.cvut.cz (J. Mikeš), Josef.Krysa@vscht.cz (J. Krýsa).

Fig. 1. Principle of photocatalysis.

from the second positive system of nitrogen $(C_3 \Pi_u \to B_3 \Pi_g)$, which emits photons at a wavelength of 337.1 nm. The first negative system $(B_2 \Sigma_u^+ \to X_2 \ \Sigma_g^+)$ of N_2^+ emits radiation at a wavelength of 391.4 nm. Thus, when the photocatalyst is illuminated by the UV light of these wavelengths, it becomes activated and the electron and positive hole can then react with the molecules in the vicinity of the catalyst. An example of the reaction of an electron with an oxygen molecule is the formation of the superoxide anion O_2^-:

$$e^- + O_2 \to \ O_2^-. \qquad (2)$$

In addition to superoxide anions, other active oxygen species such as O^-, O_3^{--}, O_2^{--} [6], etc. could also be produced. These active oxygen species then enter plasma-chemical reactions leading to the generation as well to the destruction of ozone. The resulting concentration of ozone then represents the dynamic balance of these two types of reactions.

Based on the spectrum of electrical discharges in air and the corresponding width of the forbidden gap, different materials exist which could be suitable alternatives to TiO_2 for the enhancement of discharge ozone production.

The most promising candidate is probably zinc oxide, ZnO. ZnO is an n-type semiconductor with a band gap of $\sim$3.37 eV at room temperature [7]. This energy gap corresponds to electromagnetic radiation at a wavelength of 376 nm. An important property of ZnO is that its band gap can further be tuned to $\sim$3–4 eV through its alloying with magnesium oxide or cadmium oxide. This property suggests the possibility of sensitising ZnO to particular wavelengths emitted by the discharge. Another interesting property of ZnO is that pointed tips of ZnO nanorods result in the strong enhancement of an electric field. As long as the electric field distribution affects the reduced electric field, it could lead to the increase of discharge ozone generation. Given that ZnO is relatively inexpensive and commercially available, this material is therefore very promising.

In addition to TiO_2 and ZnO, other materials which combine the contribution of photocatalysis together with the effect of a local enhancement of the electric field, as well as processes associated with adsorption on the surface of these materials or processes associated with thermal activation, could also be placed into the discharge volume.

One of these materials is strontium titanium oxide, $SrTiO_3$. In its stoichiometric form $SrTiO_3$ is a good insulator. Doping of $SrTiO_3$ can confer semiconducting properties to it. In the case of n-type conductivity, $SrTiO_3$ is a wide-gap semiconductor with a band gap $\sim$3.2 eV [8]. This energy gap corresponds to the electromagnetic radiation wavelength of 387 nm, which is closer to the wavelength emitted by the first negative system N_2^+ than TiO_2 is. $SrTiO_3$ finds applications in varistors or in high temperature superconducting microwave filters.

Another interesting material for our purposes is stannic oxide, SnO_2. It is a transparent metal-oxide n-type semiconductor with an energy gap of 3.6 eV [9,10]. This energy gap corresponds to the electromagnetic radiation wavelength of 344 nm, which is the closest to radiation emitted from the second positive system of nitrogen. In conjunction with vanadium oxide, SnO_2 is used as a catalyst for the oxidation of aromatic compounds in the synthesis of carboxylic acids and acid anhydrides.

Barium titanate, $BaTiO_3$, is an electrical insulator in its pure form. However, when doped with small amounts of metals it becomes an n-type semiconductor with an energy gap 3.3–3.5 eV [11,12]. This energy gap corresponds to the electromagnetic radiation wavelength of 376 nm. $BaTiO_3$ is frequently used in in nonlinear optics or in uncooled thermal imagers.

Aside from these materials, other possibilities exist, such as silica Al_2O_3 or $CaTiO_3$. For example, silica can also exhibit catalytic properties in ozone synthesis under silent discharge conditions [13].

Given that the most commercially available material is ZnO and that its energy gap corresponds to the wavelength of the radiation emitted by the discharge in air, we have therefore decided to choose it from the above-mentioned materials for the purposes of ozone generation as a possible alternative to TiO_2. This choice is also motivated by the results presented in [14], where it is stated that ZnO photocatalytic performance for processes such as photodegradation of dyes is superior to Degussa P25 TiO_2.

As a rough indicator of the photocatalytic activity of these two catalysts, we measured the concentration of ozone produced by the surface dielectric barrier electrical discharge in air. We have therefore compared the effect of TiO_2 or ZnO on the electrical parameters of the discharge for various experimental conditions. We first tested discharge ozone production without any photocatalyst, followed by discharge ozone production with TiO_2 and finally discharge ozone production with ZnO. Finally we compared the increments of ozone concentration due to the presence of the photocatalyst in the discharge chamber as a function of the intensity of UV radiation emitted by the discharge.

It should also be mentioned that for other environmental applications such as volatile organic compound decomposition, catalysts other than TiO_2 or ZnO, for example those mentioned in this section, could also be more effectively used when sensitised to the particular emitted spectra.

2. Experimental arrangement

The experimental arrangement, shown in Fig. 2, consists of an ozone generator together with electrical diagnostics, an air feeding system, and an ozone monitor. The ozone generator is based on surface dielectric barrier discharge, which was used as a source of UV radiation for activation of the catalysts. The discharge chamber of the ozone generator is arranged in such a way that plates of different shapes without or with a layer of a catalyst can be placed there.

2.1. Ozone generator on the basis of surface dielectric barrier discharge

A flat ozone generator made from polymethyl methacrylate Plexiglas, comprises an electrode system screen-printed on a 50×50 mm high-purity alumina Al_2O_3 dielectric plate of 0.635 mm thickness. This plate divided the ozone generator into two parts. In the lower part there was a discharge chamber with dimensions of $40 \times 40 \times 4.8$ mm. This chamber was opened to nine interconnected active electrode strips on the alumina plate. On the other side of the plate a second square electrode was screen-printed. The layout of
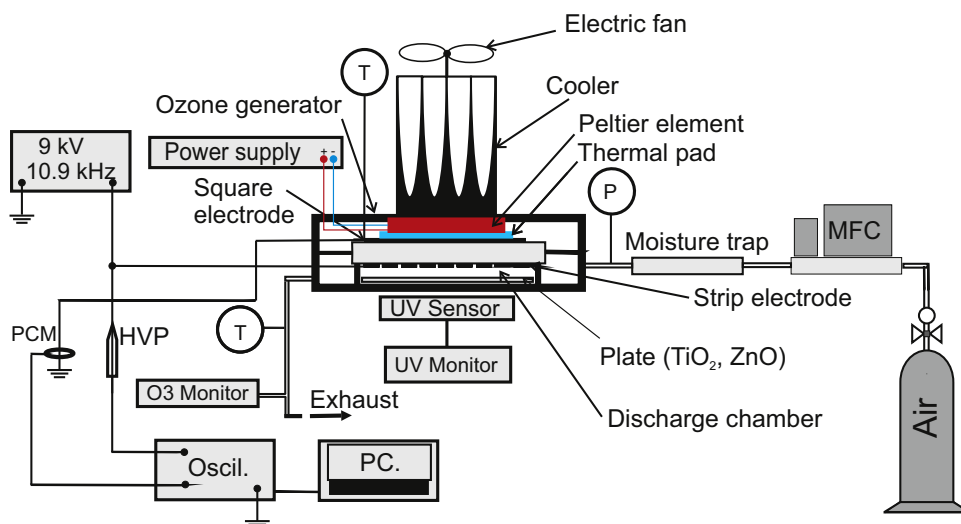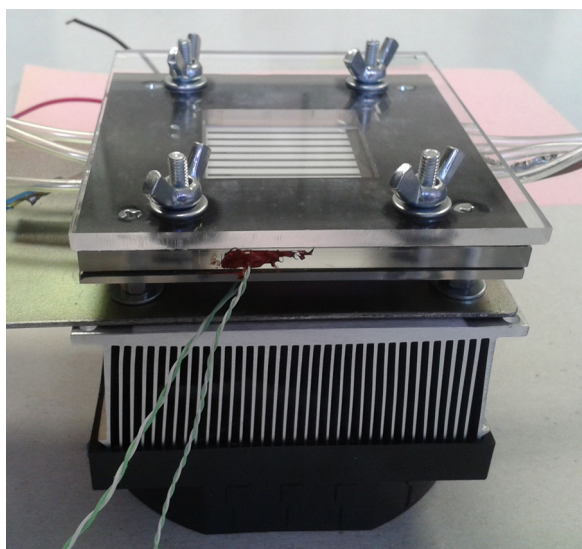
Fig. 2. Experimental arrangement.

Fig. 3. Photograph of the discharge ozone generator with the Peltier element.

the electrodes together with a photograph of the discharge is given in our earlier paper [15].

Reaction rates of processes leading to ozone generation and destruction strongly depend on temperature. For the stabilisation and control of temperature in the discharge chamber we used a Peltier element. One side of this element was in contact with square electrode through the thermal pad and the other side was in contact with a cooler with an electric fan. To control the Peltier element, its temperature was measured with a thermocouple placed between the square electrode and the thermal pad. Additionally, the temperature was measured at the output of the discharge chamber.

The discharge chamber was flushed by air from a cylinder, which was delivered through the moisture trap and the mass flow controller (MFC). The input/output of air into/out of the discharge chamber was through three tubes. A photograph of the ozone generator with the Peltier element is shown in Fig. 3.

The experiments were performed with a sinusoidal driving voltage of 10.9 kHz and a peak-to-peak voltage up to 9 kV. On the first channel of an ADS 1102CM digital storage oscilloscope (150 MHz) we sampled and recorded the discharge voltage through the high voltage probe (HVP-28HF, Pintek; division ratio: 1000/1; fre-

quency: up to 200 MHz) to determine the average discharge power. To determine the discharge current we used a signal obtained from a Pearson current monitor (PCM, model 2877) with a bandwith up to 200 MHz.

The ozone concentration was measured by absorption of the 254 nm UV spectral line using an API 450 ozone monitor.

Discharge UV emission measurements for the 365 nm wavelength were performed using an AccuMAX UV monitor with an XS-365 sensor through the UV transparent lower wall of the discharge chamber. For this measurement the discharge chamber was empty without plates inside. We registered the peak values of the radiation intensities emitted by the surface of the strip electrode.

2.2. Geometry of the plates with the photocatalysts

Our experiments were devoted to the comparison of the effect of TiO_2 or ZnO photocatalysts on the concentration of ozone and the ozone production yield of the discharge. For this purpose we placed in the discharge chamber of dimensions $40 \times 40 \times 4.8$ mm, in lower part of an ozone generator, see Fig. 2, either a clean plate or a plate carrying the layer of TiO_2 or ZnO photocatalyst. The side of the plate with the layer of photocatalyst was oriented to the strip electrode that is to the discharge. The plates were made from polymethyl methacrylate Plexiglas. Experiments devoted to the measurement of concentration of ozone produced by the discharge were performed either with the clean plate without any catalyst, or this plate was removed and exchanged by the plate of the same dimensions however with the layer of TiO_2 or ZnO.

Layer of ZnO or TiO_2 photocatalyst on the plate were prepared by sedimentation of an ultrasonically pretreated suspension of ZnO powder (zincite, crystalline size 35 nm, BET surface area roughly $29\,m^2/g$) produced by Umicore, or TiO_2 powder (78% of anatase, 14% of rutile, and 8% of amorphous phase, crystalline size 30 nm, BET surface area roughly $56\,m^2/g$) produced by Evonik Degussa.

In order to have various experimental conditions our experiments were performed with plates of two different geometries. As a first geometry we used a plate with dimensions of $39.5 \times 39.5 \times 2.0$ mm. In this case the area of the plate opened to the strip electrodes was $1560\,mm^2$. The surface density of both ZnO or TiO_2 photocatalyst was $0.5\,mg/cm^2$.

Given that the photocatalytic activity depends on the surface area of the photocatalyst [16], as a second geometry we used a plate with the same dimensions as the first one, i.e. 39.5×39.5, but of a height 2.8 mm. On the surface of this plate opened to the
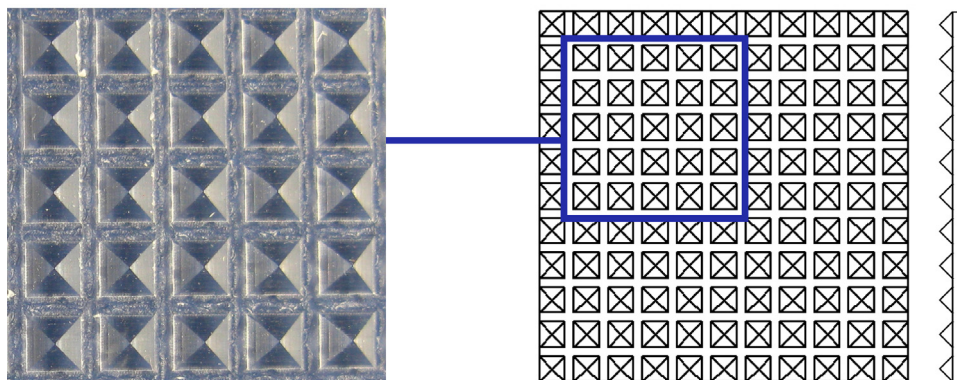
Fig. 4. Plate with pyramids. Central part of the figure – top view of the plate; left side – zoomed photograph of the part of the plate; right side – side view of the plate.

discharge, pyramids were created that had a height 1.4 mm and base dimensions of 2.7×2.7 mm. In this way, the area opened to the discharge was increased to 1946 mm^2. This represents a 2.5% increase in area in comparison with the plate without the pyramids. The surface density of each catalyst was 0.35 mg/cm^2.

A plate with pyramids is shown in Fig. 4. The figure at the center shows top view of the plate; figure at left shows zoomed photograph of the part of the plate; and finally right figure shows side view of the plate.

Another reason for using plates with pyramids is connected to the fact that ozone generation by the discharge is also affected by the residence time of particles involved in the ozone generation process. This residence time depends on the airflow patterns in the discharge chamber. In order to obtain the results for different air-flow patterns, we performed our experiments with two types of airflow – flow through a rectangular cross section chamber (when there was a plate in the discharge chamber) and flow through the cross section in which there are pyramids opened to the strip elec-trode. In each of these two cases we measured the concentration of ozone produced by the discharge for the clean plate as well as for the plates with the ZnO and TiO$_2$ layers. It should also be pointed out that the height of the plate in the form of the parallelepiped was chosen in such a way that the cross section of the discharge chamber through which the air was blowing was the same as the cross section of the chamber in the case where there was a plate with pyramids.

3. Experimental results and discussion

The experiments were performed with airflow through the discharge chamber 1.8 standard litres per minute and relative humidity of air 3%. The Peltier element was controlled in such a way that during the experiments the temperature of the square electrode was kept constant $18.2 \pm 0.2\,^\circ$C.

3.1. Electrical parameters of the discharge without and with photocatalysts

Ozone is first of all generated by the discharge itself and beside of it there is a contribution to the processes leading to its generation due to the presence of photocatalysts in the discharge chamber. The discharge ozone production is except of other quantities affected mainly by electrical parameters of the discharge. We therefore examined effect of placement of the plate, plate with pyramids or these plates covered by layer of TiO$_2$ or ZnO in the discharge chamber on electrical parameters of the discharge. Fig. 5 shows the dependence of the discharge power on the peak discharge voltage when clean plates, plates with pyramids, or the plates with TiO$_2$ or ZnO layers are placed in the discharge chamber.

Fig. 5. Discharge power as a function of the peak discharge voltage when clean plates, plates with pyramids, or the plates wit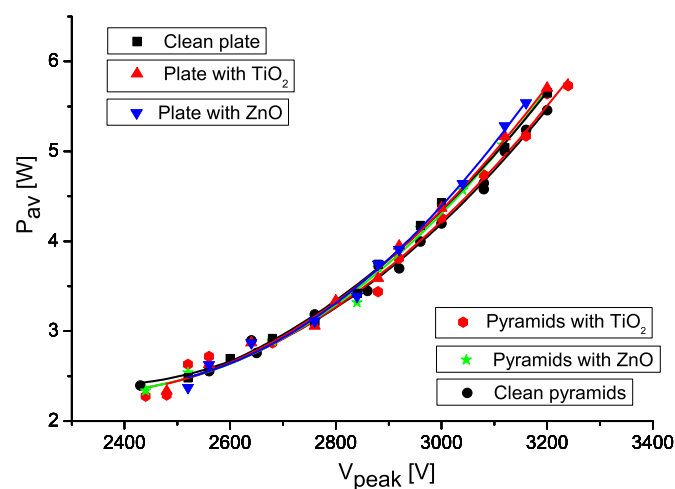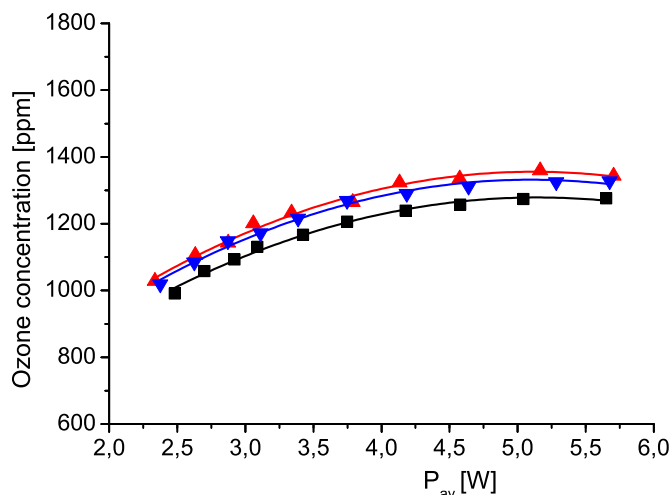h TiO$_2$ or ZnO layers are placed in the discharge chamber. Clean plate – black squares; plate with ZnO – blue down triangles; plate with TiO$_2$ – red up triangles. Clean plate with pyramids – black circles; plate with pyramids with ZnO – green stars; plate with pyramids with TiO$_2$ – red pentagons. (For interpretation of the references to color in this figure legend, the reader is referred to the web version of this article.)

It can be seen in Fig. 5 that the type of photocatalyst on the plate or the geometry of the plate in the discharge chamber does not substantially affect the electrical parameters of the discharge.

Similar dependence of injected power versus applied voltage for the barrier discharge in cylindrical configuration with presence of TiO$_2$ and UV irradiation was investigated in [17]. It was shown, that the presence of photocatalytic material increases the discharge power by a factor of 1.5. It should be however mentioned that in this case was investigated volume dielectric barrier discharge when TiO$_2$ was placed directly inside the plasma region and in our case we investigated surface dielectric barrier discharge when TiO$_2$ (or ZnO) was placed in the discharge chamber but on the side opposite to the active strip electrode and relatively far from it.

3.2. Discharge ozone production

As a rough indicator of the photocatalytic activity of TiO$_2$ or ZnO we measured the concentration of ozone produced by the surface dielectric barrier electrical discharge in air with and without the presence of these photocatalysts in the discharge chamber. In order to also take into consideration the energy required for the produc-tion of a certain mass of ozone in our analysis, we also calculated

Fig. 6. Ozone concentration versus average discharge power for plates placed inside the discharge chamber. Clean plate – black squares; plate with ZnO – blue down triangles; plate with TiO_2 – red up triangles. (For interpretation of the references to color in this figure legend, the reader is referred to the web version of this article.)
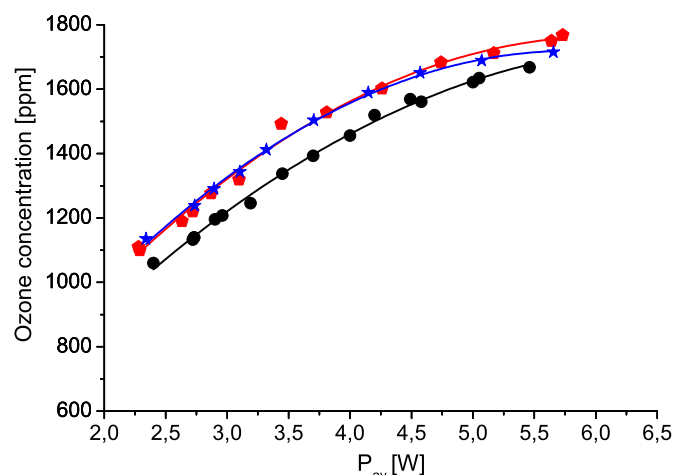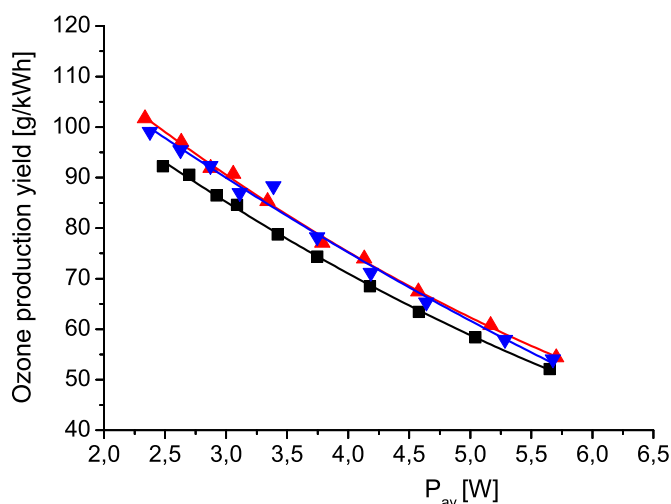

Fig. 8. Ozone concentration versus average discharge power for plates with pyramids. Clean plate – black circles; plate with ZnO – blue stars; plate with TiO_2– red pentagons. (For interpretation of the references to color in this figure legend, the reader is referred to the web version of this article.)

Fig. 7. Ozone production yield versus average discharge power for plates placed inside the discharge chamber. Clean plate – black squares; plate with ZnO – blue down triangles; plate with TiO_2 – red up triangles. (For interpretation of the references to color in this figure legend, the reader is referred to the web version of this article.)

Fig. 9. Ozone production yield versus average discharge power for plates with pyramids. Clean plate – black circles; plate with ZnO – blue stars; plate with TiO_2– red pentagons. (For interpretation of the references to color in this figure legend, the reader is referred to the web version of this article.)

the ozone production yield, α, which is defined in the following way:

$$\alpha = \frac{21.44 \times (\text{Ozone concentration}) \times \text{Airflow} \times 6 \times 10^{-3}}{P_{av}} \left[\text{g/kWh} \right], \qquad (3)$$

where the concentration of ozone produced by the discharge is substituted in parts per million, the airflow in standard liters per minute, and the average discharge power in watts.

3.2.1. Ozone production of the discharge with plates in the discharge chamber

The ozone concentration versus average discharge power for a clean plate, a plate with a layer of ZnO, and finally a plate with a layer of TiO_2 placed inside the discharge chamber is shown in Fig. 6. Analogical dependences for ozone production yield are shown in Fig. 7.

It can be seen in Fig. 6 that the concentration of ozone produced by the discharge with a plate in the discharge chamber is slightly higher for the plate with a layer of TiO_2 than for the plate with a
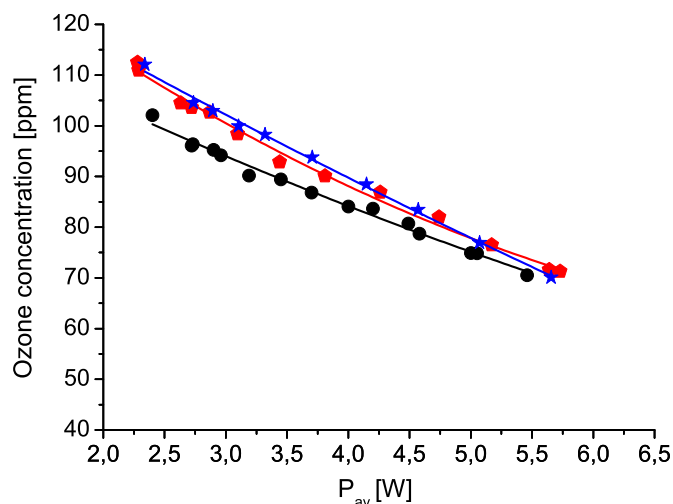
layer of ZnO, irrespective of the discharge power. As can be seen in Fig. 7, a similar conclusion can be made for ozone production yield.

3.2.2. Ozone production of the discharge for plates with pyramids in the discharge chamber

The ozone concentration versus average discharge power for the clean plate with pyramids placed inside the discharge chamber and for the plates with pyramids with a layer of ZnO or TiO_2 is shown in Fig. 8. Analogical dependences for the ozone production yield are shown in Fig. 9.

It can be seen in Fig. 8 that the concentration of ozone produced by the discharge with plates with pyramids in the discharge chamber is approximately the same for plates with a layer of TiO_2 or with a layer of ZnO, irrespective of the average discharge power. As can be seen in Fig. 9, a similar conclusion can be made for ozone production yield.

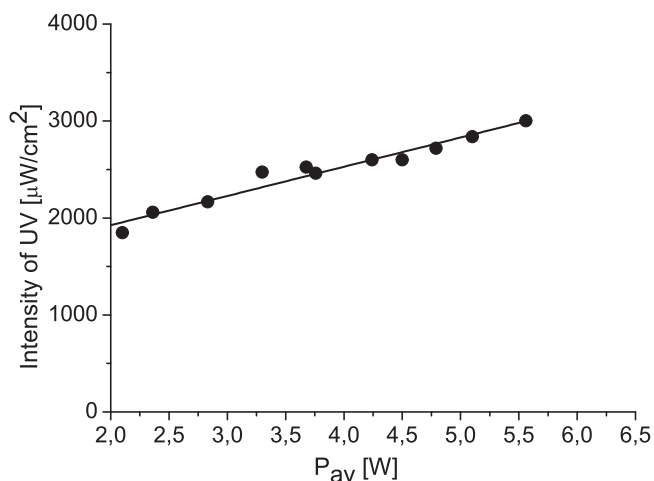It can also be concluded from a comparison of Figs. 6 and 8 for the ozone concentration produced by the discharge with a plate or with a plate with pyramids that ozone concentration increases faster as power increases in case of the plate with pyramids.

Fig. 10. Peak values of the UV emission intensities of the discharge for the 365 nm wavelength versus average discharge power.
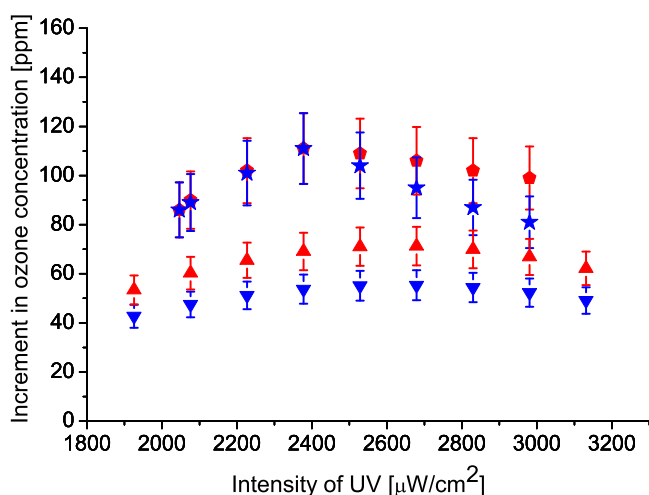
Fig. 11. Increment of the ozone concentration as a function of the intensity of the UV radiation emitted by the discharge for the 365 nm wavelength. Plate with TiO₂ – red up triangles; plate with ZnO – blue down triangles. Plate with pyramids with TiO₂ – red pentagons; plate with pyramids with ZnO – blue stars. (For interpretation of the references to color in this figure legend, the reader is referred to the web version of this article.)

3.2.3. Discharge UV emission and the photocatalytic activity of the catalysts

The triggering role for the activation of photocatalysts is played by UV radiation emitted by the discharge. This radiation can be described by its wavelength and intensity. For the range of investigated average power from 2 to 6 W the peak values of intensities of UV radiation for the 365 nm wavelength versus average discharge power are shown in Fig. 10. From this figure we can conclude that for the investigated range of average power the intensity of UV emission is a linear function of average discharge power.

To evaluate the photocatalytic activity of the catalysts, we compared the increment in the ozone concentration produced by the discharge when we had placed the photocatalyst in the discharge chamber compared with the situation when there was no photocatalyst. The experiments were performed with two different plates with catalysts, as mentioned in Section 2.2.

In Fig. 11 this increment of ozone concentration is shown as a function of the intensity of UV radiation emitted by the discharge for a plate with a layer of TiO₂ (red up triangles) or ZnO (blue down triangles). In the same figure the increment of the ozone concentration for the plates with pyramids with a layer of TiO₂ (red

pentagons) or ZnO (blue stars) is also shown. It should, however, be pointed out that the increment in the ozone concentration was obtained as the difference between two close large numbers, which means that this difference is subject to an important error. This is the reason why the obtained results should only be considered as indicative. For illustrative purposes estimated error bars are shown in this figure.

From Fig. 11 we can see that the increments of the ozone concentration produced by the discharge for the plates with pyramids (with a layer of TiO₂ or ZnO) is higher than the increments of the ozone concentration for plates without the pyramids (both with a layer of TiO₂ or ZnO). This difference in the ozone concentration could be explained by the increased surface area in the case of plates with pyramids and as well by the effect of the change in the airflow patterns on ozone generation in the discharge chamber.

Another conclusion could be taken from the dependence of this increment in the ozone concentration on the intensity of UV radiation for both catalysts. It can be seen that this increment for both catalysts varies with UV intensity. As long as data concerning the effect of intensity of UV on ozone generation for various photocatalysts do not yet exist, we tried to compare our results with the results presented in [18], where TiO₂ is used for the destruction of water contaminants. In this paper it was shown that at low intensities the quantum efficiency of the photocatalytic process (the number of molecules transformed per absorbed photon) is approximately constant, and at higher intensity levels it decreases. Our results could therefore be considered as being in qualitative agreement with the results presented in [16].

Finally, it can be concluded that from the standpoint of the discharge ozone generation the TiO₂ photocatalyst shows only slightly better performance than ZnO.

4. Conclusions

We examined the possibility of finding an alternative to the photocatalyst TiO₂ for ozone generation by electrical discharges. From various catalysts we selected ZnO because it is the most commercially available and its energy gap corresponds to the wavelength of the radiation emitted by the discharge in air. As an indicator of the photocatalytic activity of these two photocatalysts we took the concentration of ozone produced by the surface dielectric barrier electrical discharge in air. We measured the concentration of ozone produced by the discharge itself, and the discharge ozone concentration with the presence of TiO₂ or ZnO layers on plates of two different geometries, which were placed in the discharge chamber.

We found that the electrical parameters of the discharge were not substantially affected by the geometry of the plates or the presence of the catalysts on these plates. Our findings concerning the effect of TiO₂ or ZnO on the discharge ozone production can be summarised as follows:

- There is only a small difference in the concentration of ozone or ozone production yield for the discharge with plates with a layer of TiO₂ or ZnO.
- There is no reasonable difference in the concentration of ozone or ozone production yield for the discharge with plates with pyramids coated in a layer of TiO₂ or ZnO.
- The increment of the discharge ozone production is higher for plates with pyramids than for plates without pyramids.

Finally, we demonstrated that for the enhancement of the discharge ozone generation in air, the TiO₂ photocatalyst shows only slightly better performance than ZnO. It should, however, be pointed out that for other environmental applications, such as volatile organic compound decomposition, other catalysts, e.g.

those mentioned in the introduction, could be more effectively used when sensitised to the particular emitted spectra.

Acknowledgement

References

[1] G. Magesh, B. Viswanathan, R.P. Viswanath, T.K. Varadarajan, Environ. Energy Fuel 21 (2007) 1–37.
[2] H.H. Kim, Plasma Process. Polym. 1 (2004) 91–110.
[3] A. Fujishima, T.N. Rao, D.A. Tryk, J. Photochem. Photobiol. C: Photochem. Rev. 1 (2000) 1–21.
[4] U. Kogelschatz, B. Eliason, M. Hirth, Ozone Sci. Eng. 10 (1988) 367–378.
[5] F. Pontiga, C. Soria, A. Castellanos, J.D. Skalny, Ozone Sci. Eng. 24 (2002) 447–462.
[6] K. Yanallah, F. Pontiga, A. Fernandez-Rueda, C. Castellanos, J. Phys. D: Appl. Phys. 42 (2009) 1–8.
[7] A. Janotti, G. Ch. Van de Walle, Rep. Prog. Phys. 72 (2009) 126501.
[8] K. Van Benthem, C. Elsässer, R.H. French, J. Appl. Phys. 90 (2001) 6156.
[9] C. Kilic, A. Zunger, Phys. Rev. Lett. 88 (2002) 1–5.
[10] Y. Ch. Ji, H.X. Zhang, X.H. Zhang, Z.Q. Li, Phys. Status Solidi B 250 (2013) 2145.
[11] K. Suzuki, K. Kijima, Jpn. J. Appl. Phys. 44 (2005) 2081–2082.
[12] B. Ertuğ, Am. J. Eng. Res. 02 (2013) 01–07.
[13] S. Jodzis, Ozone Sci. Eng. 25 (2003) 63–72.
[14] Ch. Tian, Q. Zhang, A. Wu, M. Jiang, Z. Liang, B. Jiang, H. Fu, Chem. Commun. 48 (2012) 2858–2860.
[15] S. Pekárek, J. Mikeš, Eur. Phys. J. 68 (2014) 310, D.
[16] M. Kaneko, L. Okura, Photocatalysis – Science and Technology, Kodansha, Springer, Tokyo, 2002.
[17] O. Guaitella, F. Thevenet, C. Guillard, A. Rousseau, J. Phys. D: Appl. Phys. 39 (2006) 2964–2972.
[18] D.F. Ollis, F. Pelizzetti, N. Serpone, Environ. Sci. Technol. 25 (1991) 1522–1529.

A.12 Patent č. 308 279 – Způsob generování ozonu a dalších aktivních částic a zařízení k provádění tohoto způsobu

Patent No. 308 279 - Method of generating ozone and other active particles and the apparatus for carrying out the method.

PATENTOVÝ SPIS

(56) Relevantní dokumenty:
US 5147614 A; US 2003165411 A1; CN 204474327 U; EP 3205623 A1; JP H02293302 A.

(73) Majitel patentu:
České vysoké učení technické v Praze, Praha 6, Dejvice, CZ

(72) Původce:
Ing. Jan Mikeš, Ph.D., Praha 6, CZ
prof. Ing. Stanislav Pekárek, CSc., Praha 4, CZ

(74) Zástupce:
Ing. Lenka Bobková, patentový zástupce, Kosmická 755/37, 149 00 Praha 4

(54) Název vynálezu:

Způsob generování ozonu a dalších aktivních částic a zařízení k provádění tohoto způsobu

(57) Anotace:

Způsob generování ozonu, aktivních kyslíkových i dusíkových částic s dielektrickým bariérovým nebo koronovým výbojem a zařízení k provádění tohoto způsobu s válcovým systémem elektrod využívající na jedné straně tangenciální vstup (1) pracovního plynu a na opačné straně opatřený výstupem (2) pracovního plynu, ozonu, aktivních kyslíkových i dusíkových částic a dalších produktů výboje, přičemž na uzemněnou válcovou elektrodu (5) je nasunuta trubka (4) z dielektrického materiálu, na jejímž povrchu je vytvořena vysokonapěťová elektroda (3) a tato sestava je koaxiálně vložena do třetí trubky z dielektrického materiálu sloužící jako kryt (7) generátoru, čímž vznikne ve válcovém mezikruží ohraničeném vnitřní stěnou krytu (7) generátoru a vnější stěnou trubky (4) z dielektrického materiálu výbojový prostor (6), ve kterém je dosaženo orientovaného pohybu pracovního plynu vůči hraně vysokonapěťové elektrody (3).
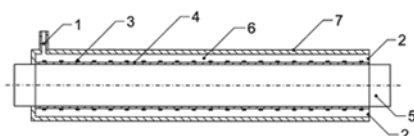
CZ 308279 B6

Způsob generování ozonu a dalších aktivních částic a zařízení k provádění tohoto způsobu

Oblast techniky

Předložené řešení se týká způsobu generování ozonu a dalších aktivních kyslíkových i dusíkových částic vznikajících dielektrickými nebo koronovými výboji využívající k jejich produkci orientovaný pohyb pracovního plynu vzhledem k vysokonapěťové elektrodě za pomoci tangenciálních vstupů tohoto plynu do komory generátoru a zařízení ke generování ozonu založené na tomto principu.

Dosavadní stav techniky

In situ sanační chemické oxidace jsou často založeny na principu oxidačně-redukčních reakcí. Oxidační činidlo je redukováno a polutant je oxidován. V praktických aplikacích jsou používána různá reakční činidla. Jsou jimi nejčastěji peroxid vodíku, manganistan draselný, manganistan sodný, Fentonovo činidlo, ale i například ozon.

Ozon neboli trikyslík je anorganická molekula chemického vzorce O_3, je to bledě modrý plyn s výrazně štiplavým zápachem. Je to allotropická modifikace kyslíku, který je mnohem méně stabilní než diatomický allotrop O_2, rozpadající se v atmosféře na O_2 neboli dikyslík. Ozon v atmosféře Země je tvořen z dikyslíku působením ultrafialového světla a elektrických výbojů. Je přítomen ve velmi nízkých koncentracích ve všech vrstvách atmosféry včetně přízemní, přičemž jeho nejvyšší koncentrace lze nalézt v ozonové vrstvě stratosféry, která absorbuje většinu ultrafialového záření ze Slunce.

Ozon je nestabilní plyn, který se okamžitě začíná rozkládat. Jeho poločas rozpadu se v závislosti na podmínkách pohybuje od několika sekund až do řádu hodin. Rozkládá se na kyslík, přičemž nevznikají žádné škodlivé produkty. Podmínky vedoucí k rozkladu ozonu jsou především zvýšená vlhkost, zvýšená teplota, případně přítomnost některých kovů jako je měď, stříbro nebo železo. Při zvýšené teplotě a za přítomnosti některých katalyzátorů jako je vodík, železo, měď, chrom může být proces rozkladu výbušný.

V souvislosti s touto nestabilitou nelze ozon skladovat a musí se proto vyrábět na místě, kde bude používán.

Lidé mají schopnost detekovat přítomnost ozonu při koncentracích 0,003 ppm, přičemž při koncentracích okolo 0,15 ppm se stává toxickým. Vystavení osob působení ozonu o těchto koncentracích způsobuje dýchací problémy, slzení očí, případně kašel.

Aktivní kyslíkové částice, například ozon, atomy kyslíku, peroxid vodíku atd., jsou oxidačními činidly, které ve styku s plísněmi, sporami nebo s bakteriemi tyto kontaminanty ničí. Vzhledem k těmto vlastnostem se dodáváním výše uvedených aktivních kyslíkových, případně dusíkových, částic do prostoru, ve kterém jsou skladovány nebo přepravovány potraviny, zelenina nebo ovoce, dosahuje prodloužení jejich trvanlivosti.

Ozonizace patří k často využívaným sanačním technikám, jako taková však vykazuje při masovém použití relativně vysoké náklady na vlastní provoz. Zvýšení účinnosti ozonizace a snížení její ekonomické náročnosti jsou předmětem navrhovaného vynálezu. V sanačních technologiích existují i jiné metody, které však jsou ve srovnání s ozonizací málo účinné či vůbec neúčinné.

Ozon se vyrábí třemi hlavními způsoby: elektrochemickým generováním, kdy elektrický proud prochází elektrolytem, přičemž vzniklá směs plynů obsahující ozon, ultrafialovými paprsky - k tomuto procesu dochází např. v horních vrstvách atmosféry a v netermálním plazmatu

generovaném elektrickými výboji.

Ozon je pro praktické aplikace obvykle generován elektrickými výboji za atmosférického tlaku. Nejčastěji se jedná o dielektrický bariérový výboj, případně o výboj koronový. Aktivní kyslíkové a dusíkové částice jsou generovány plazmochemickými procesy, které jsou spouštěny energetickými elektrony generovanými výbojem. Elektrony disociují molekuly kyslíku a dusíku přítomné ve vzduchu a spouštějí soustavu reakcí vedoucích jak k produkci, tak i k rozkladu výše uvedených částic. Výsledná koncentrace aktivních kyslíkových a dusíkových částic je dána dynamickou rovnováhou uvedených reakcí.

Jedná se o komplikovaný fyzikálně-chemický proces, který se skládá z disociačních, excitačních a ionizačních reakcí. Z řady všech těchto reakcí je pro generování ozonu ze vzduchu za atmosférického tlaku nejdůležitější reakce:

$$O + O_2 + \mathrm{M} \rightarrow O_3 + M$$

kde M je buď molekula kyslíku nebo dusíku. Z uvedené rovnice je tedy zřejmé, že pro nastartování reakcí vedoucích ke generaci ozonu ze vzduchu je nutná přítomnost kyslíkových atomů. Ke vzniku těchto atomů dochází v důsledku disociace kyslíkových molekul obsažených ve vzduchu.

Vzhledem k tomu, že generování ozonu i ostatních aktivních kyslíkových a dusíkových částic samotnými elektrickými výboji již téměř dosáhlo teoretických mezí, jsou hledány cesty, jak tuto produkci zvýšit, například optimalizací systému elektrického napájení, použitím dalších fotokatalytických látek aplikovaných do výboje, ovlivněním či stabilizací výboje elektromagnetickými či akustickými poli.

Známé je řešení výroby ozonu ve válcových generátorech podle přihlášky vynálezu, např. US 2009/0211895 A1, kde vysokonapěťová elektroda je řešena formou spirály na povrchu či uvnitř dielektrické trubky umístěné koaxiálně s vodivou válcovou uzemněnou elektrodou. Korona či povrchový dielektrický výboj potom vznikají ve stacionárním vzduchu či kyslíku. Pracovní plyn tedy není nijak veden ani orientován vůči elektrodovému systému. Elektrony ze streamerových mikrovýbojů disociují molekuly pracovního plynu a dochází ke vzniku ozonu a dalších kyslíkových, případně dusíkových částic, které nejsou ze zařízení řízené odváděny. Proces generování aktivních částic je tak nahodilý a silně závislý na environmentálních podmínkách.

Známé je řešení podle dokumentu US 2009/0283399 A1, kde je pracovní plyn axiálně vháněn do prostoru mezi aktivní napěťovou a zemnicí elektrodu, vzájemně oddělených dielektrickou bariérou, a to v jejich různých polohových variacích. Návazně patentové řešení US 7514377 B2 specifikuje typy a polohy jednotlivých elektrod. Řešení popsaná v dokumentech US 2009/0283399 A1 i US 7514377 B2 využívají ke svému provozu dielektrický objemový výboj, který má obecně nízkou účinnost. Požadované výsledné koncentrace ozonu tak dosahují pouze uspořádáním více takových generátorů do jednoho zařízení.

Dále je známé řešení podle dokumentu GB 424691 A, které využívá tangenciální vstup pracovního plynu do výbojové komory generátoru ozonu, avšak neorientuje vzniklé proudění vůči elektrodovému systému, kterým je v konkrétním případě kovový elektricky vodivý povlak, či páska nanesené na skleněné trubici.

Je známé i řešení podle dokumentu US 5501845 A, kde se jedná o válcový generátor využívající k výrobě ozonu opět dielektrický bariérový objemový výboj s plošnými elektrodami neorientovanými vůči proudění. Nevýhodou obou uvedených řešení je vytvoření objemového dielektrického výboje, který má obecně nižší produkci ozonu, nižší výtěžnost, vyšší elektrický příkon než povrchový dielektrický výboj vytvořený prostřednictvím elektrod, které jsou vhodně orientovány vůči směru proudění pracovního plynu uvnitř komory generátoru. Velký vliv na účinnost uvedeného zařízení mají environmentální podmínky, ve kterých je zařízení provozováno.

<u>Podstata vynálezu</u>

5   Výše definované nevýhody popsané ve stavu techniky snižuje či eliminuje způsob výroby ozonu a zařízení specifikované podle tohoto vynálezu. Zvýšení koncentrace ozonu a aktivních kyslíkových i dusíkových částic generovaných dielektrickým bariérovým nebo koronovým výbojem v porovnání se stávajícím stavem techniky umožňuje potom zařízení podle předkládaného řešení.

10   V hlavním provedení se jedná o způsob generování ozonu a dalších aktivních kyslíkových i dusíkových částic s dielektrickým bariérovým nebo koronovým výbojem využívající k jejich produkci orientovaný pohyb pracovního plynu vzhledem k vysokonapěťové elektrodě za pomoci tangenciálních vstupů tohoto plynu do komory generátoru.

15   Při způsobu generování ozonu, aktivních kyslíkových a dusíkových částic elektrickým výbojem v systému s válcovými elektrodami prochází výbojovým prostorem tvaru válcového mezikruží pracovní plyn o teplotě od -40 do +50 °C. Válcové mezikruží je ohraničeno vnitřní stěnou krytu generátoru a do ní koaxiálně umístěnou vnější stěnou trubky z dielektrického materiálu, opatřenou na povrchu vysokonapěťovou elektrodou tvořenou paralelně spojenými vodivými pásky ve formě 20 prstenců nebo vodivým páskem ve formě válcové spirály. Vnitřní stěna trubky doléhá na koaxiálně vloženou uzemněnou válcovou elektrodu. Pracovní plyn vchází vstupem tangenciálně vůči hraně vysokonapěťové elektrody a dále se orientovaně pohybuje za přetlaku 100 až 300 kPa výbojovým prostorem paralelně s hranou vysokonapěťové elektrody směrem k výstupu. Postupuje válcovým mezikružím a působením výboje, vybraného ze skupiny povrchový dielektrický bariérový výboj, 25 koronový výboj, vzniká disociačními, excitačními a ionizačními reakcemi směs pracovního plynu, ozonu, aktivních kyslíkových i dusíkových částic a dalších produktů výboje, která na protilehlé straně výstupem odchází do sanovaného pracovního prostoru nebo k dalšímu zpracování. Frekvence napájení vysokonapěťové elektrody pro dielektrický bariérový výboj je výhodně od 50 do 20 kHz.

30

    Zařízení pro generování ozonu, aktivních kyslíkových i dusíkových částic elektrickým výbojem v systému s válcovými elektrodami sestává z uzemněné válcové elektrody, na kterou je nasunuta trubka z dielektrického materiálu. Uzemněná válcová elektroda je tedy nosnou částí generátoru a je to elektricky i tepelně vodivá trubka, případně tyč, která slouží i pro odvod tepla. Na povrchu 35 trubky z dielektrického materiálu je vytvořena vysokonapěťové elektroda. Uvedená sestava je koaxiálně vložena do třetí trubky z dielektrického materiálu, která slouží jako kryt generátoru, čímž je vytvořen výbojový prostor ve tvaru válcového mezikruží ohraničeného vnitřní stěnou krytu generátoru a vnější stěnou trubky z dielektrického materiálu, kde jedna strana zařízení je opatřena tangenciálním vstupem pracovního plynu orientovaného vůči hraně vysokonapěťové elektrody a 40 na protilehlé straně výstupem směsi pracovního plynu, ozonu, aktivních kyslíkových i dusíkových částic a dalších produktů výboje.

    Tangenciální vstup pracovního plynu do výbojového prostoru je s výhodou umístěný uprostřed výbojového prostoru a je orientován vůči hraně vysokonapěťové elektrody. Na obou koncích jsou 45 pak axiální výstupy.

    Zařízení podle vynálezu je výhodně opatřeno *N* tangenciálními vstupy pracovního plynu do výbojového prostoru, které jsou umístěny ve vnější stěně krytu generátoru a rozmístěny po axiální ose výbojového prostoru.

50

    Zařízení podle vynálezu je výhodně opatřeno *N* tangenciálními vstupy pracovního plynu do výbojového prostoru, které jsou umístěny ve vnější stěně krytu generátoru a jsou rozmístěny ve směru válcové spirály po axiální ose výbojového prostoru.

55   Válcové mezikruží výbojového prostoru má s výhodou radiální šířku od 0,1 do 10 mm, délku

elektrod od 30 do 3000 mm a tloušťku stěny trubky z dielektrického materiálu od 0,01 do 3 mm. Vysokonapěťová elektroda je ve výhodném provedení z elektricky vodivého materiálu o tloušťce od 0,001 do 1,5 mm.

Orientovaného proudění pracovního plynu lze pro danou geometrii vysokonapěťové elektrody dosáhnout například vírovým pohybem pracovního plynu způsobeného tangenciálním vstupem tohoto plynu do komory generátoru. Směr proudění pracovního plynu je podél hrany vysokonapěťové elektrody. Ve výbojovém prostoru vznikne vírový pohyb plynu s proudnicemi kolmými k mikrovýbojům vznikajícími od prstenců či válcové spirály vysokonapěťové elektrody.

V porovnání s dosud známými řešeními představuje zařízení podle vynálezu pro generování ozonu a aktivních kyslíkových i dusíkových částic dielektrickým bariérovým nebo koronovým výbojem zařízení s vyšší účinností, vyšší výtěžností ozonu, a přitom s menší energetickou náročností, a to díky orientovanému proudění pracovního plynu vůči geometrii vysokonapěťové elektrody.

Objasnění výkresů

Využití výše zmíněného způsobu generování ozonu a uspořádání válcového generátoru ozonu a dalších aktivních kyslíkových i dusíkových částic využívajícího tento způsob je schematicky rozkresleno na přiložených výkresech, přičemž na obrázku 1 je sestava generátoru s jedním tangenciálním vstupem a výstupy pracovního plynu. Obrázek 2 ukazuje v řezu tangenciální vstup pracovního plynu do výbojového prostoru generátoru. Obrázek 3 potom definuje středovou polohu jednoho tangenciálního vstupu. Obrázek 4 znázorňuje válcový generátor s N tangenciálními vstupy. Závislost koncentrace ozonu na středním příkonu generátoru s různými variantami vstupu pracovního plynu do výbojového prostoru je uvedena v grafu na obrázku 5. Křivka 1 znázorňuje řešení podle vynálezu a odpovídá tangenciálnímu vstupu pracovního plynu. Křivka 2 odpovídá radiálnímu vstupu a znázorňuje řešení ze stavu techniky. Křivka 3 znázorňuje řešení ze stavu techniky s axiálním vstupem pracovního plynu. Střední příkon do výboje je udáván ve W a koncentrace ozonu je v ppm. Z grafu je zřejmé významné zvýšení koncentrace generovaného ozonu při tangenciálním vstupu pracovního plynu.

Příklady uskutečnění vynálezu

Dále popsaná, zobrazená a specifikovaná vhodná provedení vynálezu jsou ilustrativní a pouze příkladem možného uskutečnění jak způsobu, tak provedení, avšak nejsou omezením příkladů provedení vynálezu na uvedené případy. Odborná komunita najde nebo bude schopna identifikovat za použití rutinního experimentování další ekvivalentní provedení specifických uskutečnění vynálezu, která jsou zde explicitně popsána.

Navržené technické řešení se týká způsobu generování ozonu a válcového generátoru ozonu a dalších aktivních kyslíkových i dusíkových částic, pro které existují dvě možné varianty elektrodového uspořádání. V prvním je vysokonapěťová elektroda tvořena paralelně spojenými tenkými pásky ve formě prstenců, ve druhém pak je vysokonapěťová elektroda tvořena tenkým páskem ve formě válcové spirály. Směr proudění pracovního plynu je podél hrany vysokonapěťové elektrody. Orientovaný vstup pracovního plynu do komory generátoru může být řešen následujícími provedeními.

Příkladným způsobem generování ozonu, aktivních kyslíkových a dusíkových částic elektrickým výbojem je generování v systému s válcovými elektrodami, kde do výbojového prostoru 6 tvaru válcového mezikruží ohraničeného vnitřní stěnou krytu 7 generátoru a do ní koaxiálně umístěnou vnější stěnou trubky 4 z dielektrického materiálu, opatřenou na povrchu vysokonapěťovou elektrodou 3 tvořenou paralelně spojenými vodivými pásky ve formě prstenců nebo vodivým páskem ve formě válcové spirály, přičemž vnitřní stěna trubky 4 z dielektrického materiálu doléhá

na koaxiálně vloženou uzemněnou válcovou elektrodu 5, vstupem 1 vchází tangenciálně vůči hraně vysokonapěťové elektrody 3 pracovní plyn, který se o teplotě od -40 do +50 °C orientovaně pohybuje za přetlaku 100 až 300 kPa výbojovým prostorem 6 paralelně s hranou vysokonapěťové elektrody 3 směrem k výstupu 2, postupuje válcovým mezikružím výbojového prostoru 6, přičemž působením výboje, vybraného ze skupiny povrchový dielektrický bariérový výboj, koronový výboj, vzniká disociačními, excitačními a ionizačními reakcemi směs pracovního plynu, ozonu, aktivních kyslíkových i dusíkových částic a dalších produktů výboje, která na protilehlé straně výstupem 2 odchází do sanovaného pracovního prostoru nebo k dalšímu zpracování.

Dalším příkladným způsobem generování ozonu, aktivních kyslíkových a dusíkových částic elektrickým výbojem je systém s válcovými elektrodami s frekvencí napájecího napětí vysokonapěťové elektrody 3 pro dielektrický bariérový výboj od 50 do 20 kHz.

Jedním z příkladných provedení vynálezu je řešení, kdy je pracovní plyn do komory generátoru dodáván jedním tangenciálním vstupem 1 a na opačné straně válcového generátoru je axiální výstup 2 ozonu, aktivních kyslíkových i dusíkových částic a dalších produktů výboje, přičemž na uzemněnou válcovou elektrodu 5 je nasunuta trubka 4 z dielektrického materiálu, na jejímž povrchu je vytvořena vysokonapěťová elektroda 3 a tato sestava je koaxiálně vložena do třetí trubky z dielektrického materiálu sloužící jako kryt 7 generátoru, čímž vznikne ve válcovém mezikruží ohraničeném vnitřní stěnou krytu 7 generátoru a vnější stěnou trubky 4 z dielektrického materiálu výbojový prostor 6 s tím, že tangenciálním vstupem 1 pracovního plynu do výbojového prostoru 6 je dosaženo jeho vírového pohybu a proudnice pracovního plynu jsou tak kolmé na mikrovýboje vznikající od vysokonapěťové elektrody 3 tvořené paralelně spojenými tenkými pásky ve formě prstenců nebo tvořené tenkým páskem ve formě válcové spirály.

Následujícím vhodným provedením vynálezu je řešení, kdy je pracovní plyn dodáván do komory generátoru jedním tangenciálním vstupem 1 umístěným uprostřed komory generátoru, a na obou koncích jsou axiální výstupy 2 ozonu, aktivních kyslíkových i dusíkových částic a dalších produktů výboje, přičemž na uzemněnou válcovou elektrodu 5 je nasunuta trubka 4 z dielektrického materiálu, na jejímž povrchu je vytvořena vysokonapěťová elektroda 3 a tato sestava je koaxiálně vložena do třetí trubky z dielektrického materiálu sloužící jako kryt 7 generátoru, čímž vznikne ve válcovém mezikruží ohraničeném vnitřní stěnou krytu 7 generátoru a vnější stěnou trubky 4 z dielektrického materiálu výbojový prostor 6 s tím, že tangenciálním vstupem 1 pracovního plynu do výbojového prostoru 6 je dosaženo jeho orientovaného pohybu vůči hraně vysokonapěťové elektrody 3.

Dalším vhodným provedením vynálezu je řešení, kdy je pracovní plyn dodáván do komory generátoru na jedné straně N tangenciálními vstupy 1, které jsou umístěny ve vnější stěně krytu 7 generátoru a rozmístěny po axiální ose generátoru a na opačné straně válcového generátoru je axiální výstup 2 ozonu, aktivních kyslíkových i dusíkových částic a dalších produktů výboje, přičemž na uzemněnou válcovou elektrodu 5 je nasunuta trubka 4 z dielektrického materiálu, na jejímž povrchu je vytvořena vysokonapěťová elektroda 3 a tato sestava je koaxiálně vložena do třetí trubky z dielektrického materiálu sloužící jako kryt 7 generátoru, čímž vznikne ve válcovém mezikruží ohraničeném vnitřní stěnou krytu 7 generátoru a vnější stěnou trubky 4 z dielektrického materiálu výbojový prostor 6 s tím, že tangenciálními vstupy 1 pracovního plynu do výbojového prostoru 6 je dosaženo jeho orientovaného pohybu vůči hraně vysokonapěťové elektrody 3.

Podstatou další varianty je řešení pro dodávání pracovního plynu do výbojového prostoru N tangenciálními vstupy 1, které jsou umístěny ve vnější stěně krytu 7 generátoru a rozmístěny ve směru válcové spirály po axiální ose válcového generátoru ozonu a aktivních kyslíkových i dusíkových částic generovaných dielektrickým bariérovým nebo koronovým výbojem. Opačná strana je opatřena výstupem 2 ozonu, aktivních kyslíkových i dusíkových částic a dalších produktů výboje, přičemž na uzemněnou válcovou elektrodu 5 je nasunuta trubka 4 z dielektrického materiálu, na jejímž povrchu je vytvořena vysokonapěťová elektroda 3 a tato sestava je koaxiálně vložena do třetí trubky z dielektrického materiálu sloužící jako kryt 7 generátoru, čímž vznikne ve

válcovém mezikruží ohraničeném vnitřní stěnou krytu 7 generátoru a vnější stěnou trubky 4 z dielektrického materiálu výbojový prostor 6 s tím, že tangenciálními vstupy 1 pracovního plynu do výbojového prostoru 6 je dosaženo jeho orientovaného pohybu vůči hraně vysokonapěťové elektrody 3.

Pro ověření funkčnosti navrhovaného řešení zvýšení koncentrace ozonu, aktivních kyslíkových i dusíkových částic a dalších produktů výboje bylo také sestrojeno experimentální zařízení sestávající z uzemněné válcové elektrody 5 vyrobené z mosazi o vnějším průměru 17,6 mm, síle stěny 1 mm a celkové axiální délce 150 mm.

Na tuto elektrodu byla těsně nasunuta skleněná trubka 4 o vnějším průměru 20 mm a síle stěny 1,2 mm a celkové axiální délce 150 mm. Na povrchu této skleněné trubky byla vytvořena vysokonapěťová elektroda 3 ve formě vodivě spojených prstenců s šířkou jednoho prstence 1 mm a vzájemnou mezerou mezi prstenci o velikosti 3 mm. V druhém případě byla jako vysokonapěťová elektroda 3 vytvořena válcová spirála o tloušťce 1 mm a se stoupáním 3 mm. Materiálem vysokonapěťové elektrody 3 byla v obou případech měděná folie o tloušťce 0,04 mm. Koaxiálně byla tato sestava uložena do třetí trubky vyrobené z polymethylmetakrylátu PMMA o vnějším průměru 30 mm a síle stěny 2 mm. Mezi prostorem skleněné trubky 4 s vysokonapěťovou elektrodou 3 a vnitřní stěnou třetí trubky z PMMA byl vytvořen výbojový prostor 6 v podobě válcového mezikruží o středním průměru 22,5 mm. Pracovní plyn byl do výbojového prostoru dodáván tangenciálně vstupem 1 a ozon, aktivní kyslíkové i dusíkové částice a další produkty výboje byly axiálně odváděny na opačném konci válcového generátoru ozonu a dalších kyslíkových i dusíkových částic výstupem 2.

V tomto uspořádání je možné dosáhnout vlivem vírového pohybu pracovního plynu bez dalších energetických nároků zvýšení koncentrace ozonu o 40 %, absolutně pak o více než 600 ppm.

Průmyslová využitelnost

Výše popsaným způsobem generování ozonu a dalších kyslíkových i dusíkových částic a zařízení vynálezu využívající k jejich produkci orientovaný pohyb pracovního plynu vzhledem k vysokonapěťové elektrodě za pomoci tangenciálních vstupů tohoto plynu do komory generátoru a zařízení ke generování ozonu založené na tomto principu oproti generátoru s běžně používaným axiálním, laterálním či radiálním vstupem pracovního plynu je možné zvýšit účinnost, výtěžnost zmiňovaných produktů a následně snížit energetickou náročnost generátoru.

Uvedené výhody umožňují konstrukci výkonnějších, menších, mobilních a kompaktních zdrojů ozonu a dalších aktivních kyslíkových i dusíkových částic pro celou řadu aplikací, například pro potravinářský, chemický, biochemický průmysl i pro zdravotnictví. Tyto generátory dále naleznou uplatnění pro zvyšování kvality vzduchu, vody a půdy, v odpadovém hospodářství, v zařízeních pro dekontaminaci a sterilizaci látek atd.

PATENTOVÉ NÁROKY

1.   Způsob generování ozonu, aktivních kyslíkových a dusíkových částic elektrickým výbojem v systému s válcovými elektrodami, **vyznačující se tím**, že do výbojového prostoru (6) tvaru válcového mezikruží ohraničeného vnitřní stěnou krytu (7) generátoru a do ní koaxiálně umístěnou vnější stěnou trubky z dielektrického materiálu, opatřenou na povrchu vysokonapěťovou elektrodou (3) tvořenou paralelně spojenými vodivými pásky ve formě prstenců nebo vodivým páskem ve formě válcové spirály, přičemž vnitřní stěna trubky (4) z dielektrického materiálu doléhá na koaxiálně vloženou uzemněnou válcovou elektrodu (5), vstupem (1) vchází tangenciálně vůči hraně vysokonapěťové elektrody (3) pracovní plyn, který se při teplotě od -40 do +50 °C orientovaně pohybuje za přetlaku 100 až 300 kPa výbojovým prostorem (6) paralelně s hranou vysokonapěťové elektrody (3) směrem k výstupu (2), postupuje válcovým mezikružím výbojového prostoru (6), přičemž působením výboje, vybraného ze skupiny povrchový dielektrický bariérový výboj, koronový výboj, vzniká disociačními, excitačními a ionizačními reakcemi směs pracovního plynu, ozonu, aktivních kyslíkových i dusíkových částic a dalších produktů výboje, která na protilehlé straně výstupem (2) odchází do sanovaného pracovního prostoru nebo k dalšímu zpracování.

2.   Způsob generování ozonu, aktivních kyslíkových a dusíkových částic elektrickým výbojem v systému s válcovými elektrodami podle nároku 1, **vyznačující se tím,** že vysokonapěťová elektroda (3) je pro dielektrický bariérový výboj napájena s frekvencí od 50 do 20 kHz.

3.   Zařízení pro provádění způsobu generování ozonu, aktivních kyslíkových i dusíkových částic elektrickým výbojem v systému s válcovými elektrodami, podle nároků 1 a 2, **vyznačující se tím**, že na uzemněnou válcovou elektrodu (5) je nasunuta trubka (4) z dielektrického materiálu, na jejímž povrchu je vytvořena vysokonapěťová elektroda (3), celá tato sestava je koaxiálně vložena do třetí trubky z dielektrického materiálu sloužící jako kryt (7) generátoru, čímž je vytvořen výbojový prostor (6) ve tvaru válcového mezikruží ohraničeném vnitřní stěnou krytu (7) generátoru a vnější stěnou trubky (4) z dielektrického materiálu, jedna strana zařízení je opatřena tangenciálním vstupem (1) pracovního plynu orientovaným vůči hraně vysokonapěťové elektrody (3) a protilehlá strana výstupem (2) směsi pracovního plynu, ozonu, aktivních kyslíkových i dusíkových částic a dalších produktů výboje.

4.   Zařízení pro generování ozonu, aktivních kyslíkových a dusíkových částic elektrickým výbojem v systému s válcovými elektrodami podle nároku 3, **vyznačující se tím**, že je opatřeno jedním tangenciálním vstupem (1) pracovního plynu, umístěným uprostřed výbojového prostoru (6) a na obou koncích axiálními výstupy (2).

5.   Zařízení pro generování ozonu, aktivních kyslíkových a dusíkových částic elektrickým výbojem v systému s válcovými elektrodami podle nároku 3, **vyznačující se tím**, že tangenciálních vstupů (1) je N a jsou umístěny na jedné straně ve vnější stěně krytu (7) generátoru a rozmístěny po axiální ose výbojového prostoru (6).

6.   Zařízení pro generování ozonu, aktivních kyslíkových a dusíkových částic elektrickým výbojem v systému s válcovými elektrodami podle nároku 3, **vyznačující se tím**, že tangenciálních vstupů (1) je N a jsou umístěny ve vnější stěně krytu (7) generátoru a rozmístěny ve směru válcové spirály po axiální ose výbojového prostoru (6).
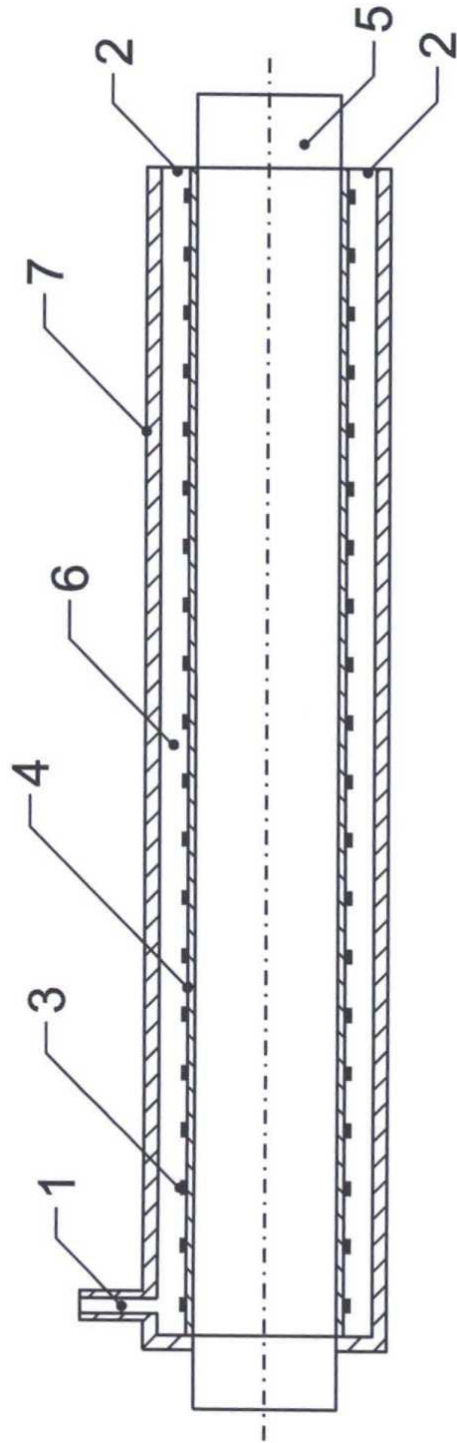
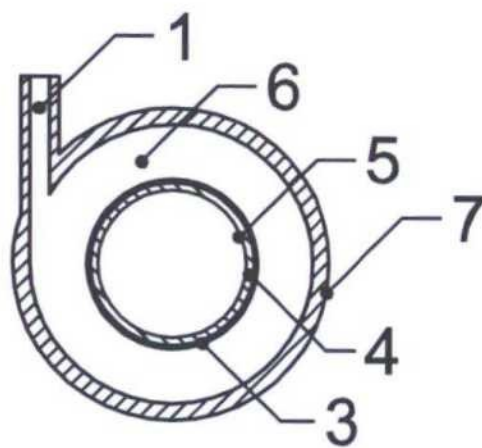7.   Zařízení pro generování ozonu, aktivních kyslíkových i dusíkových částic elektrickým výbojem v systému s válcovými elektrodami podle nároků 3 až 6, **vyznačující se tím**, že výbojový prostor (6) je tvořený válcovým mezikružím o radiální šířce od 0,1 do 10 mm, s délkou elektrod (3), (5) od 30 do 3000 mm a tloušťkou stěny trubky (4) z dielektrického materiálu od 0,01 do 3 mm.

8.   Zařízení pro generování ozonu, aktivních kyslíkových i dusíkových částic elektrickým výbojem v systému s válcovými elektrodami podle nároků 3 až 7, **vyznačující se tím**, že vysokonapěťová elektroda (3) je z elektricky vodivého materiálu o tloušťce od 0,001 do 1,5 mm.
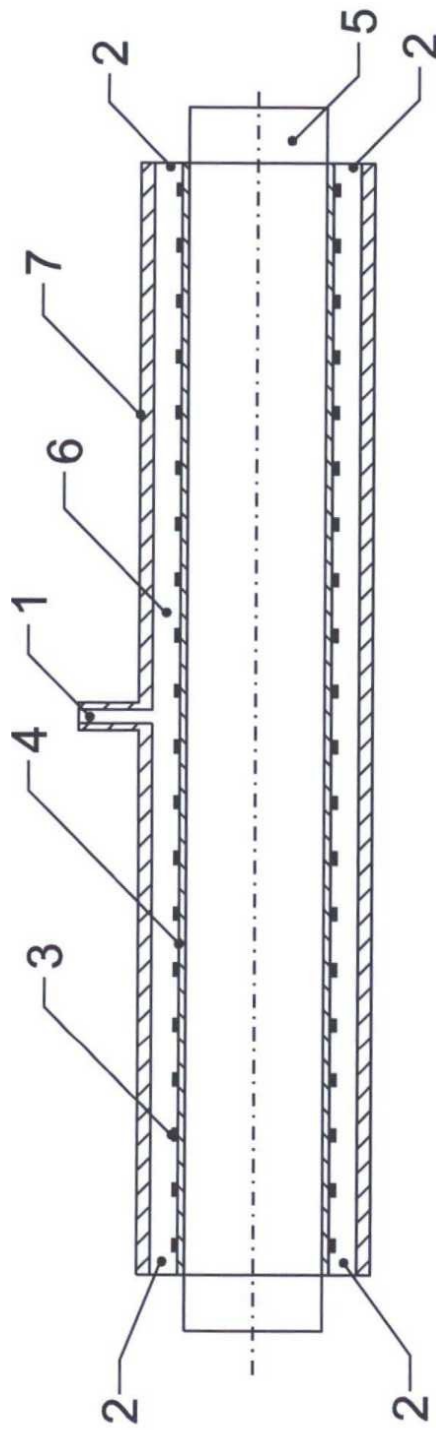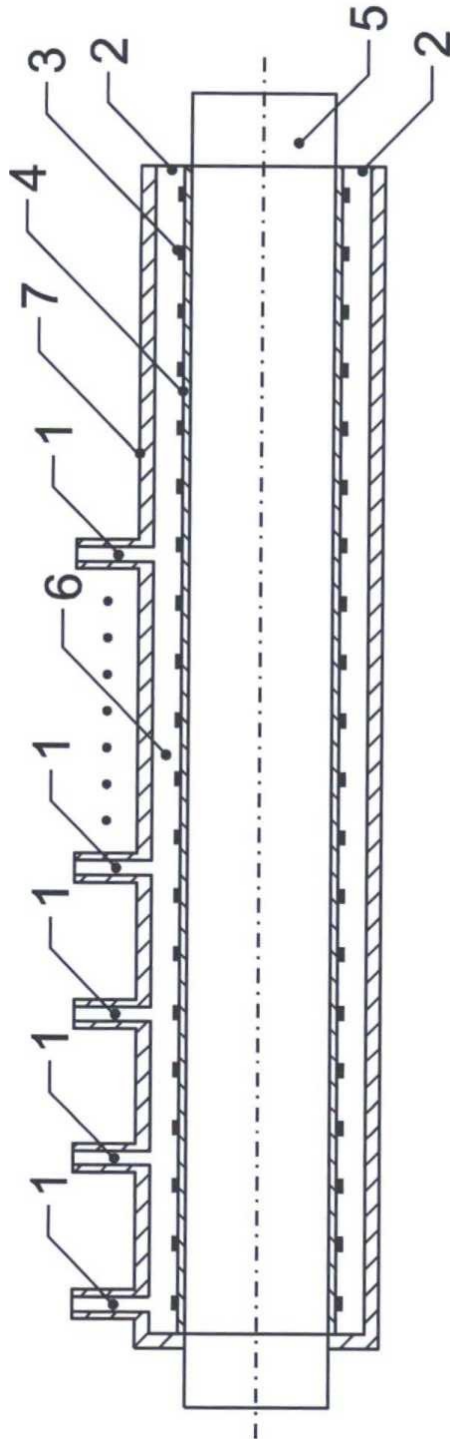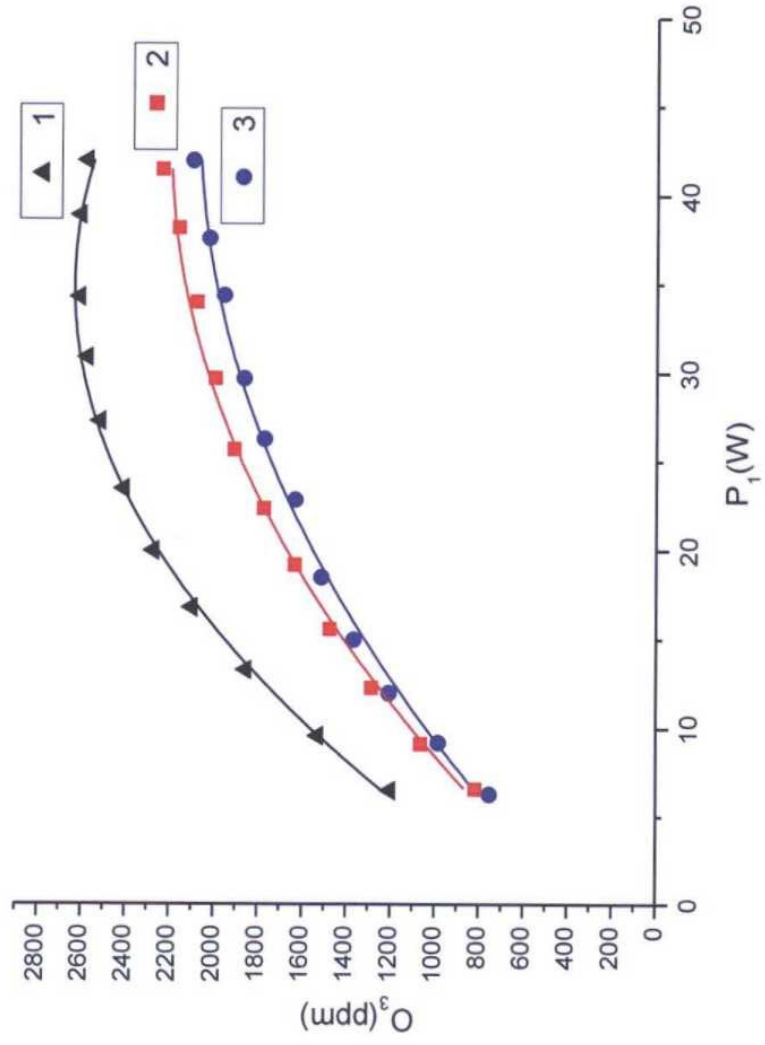
5

5 výkresů

Obr. 1

Obr. 2

Obr. 3

Obr. 4

Obr. 5